SCUOLA DI DOTTORATO
UNIVERSITÀ DEGLI STUDI DI MILANO - BICOCCA

Facoltà di Scienze Matematiche, Fisiche e Naturali

PhD program: Fisica e astronomia **Cycle:** XXIX

Search for heavy resonances decaying to VW in the semi-leptonic final state with the CMS detector

Surname: Brianza **Name:** Luca

Registration number: 731792

Tutor: Prof. Alessio Ghezzi

Co-tutor: Dott. Pietro Govoni

Coordinator: Prof. Marta Calvi

ACADEMIC YEAR 2015-2016

Summary

The data collected by the CMS detector during the first run of LHC at a centre-of-mass energy of $\sqrt{s} = 7$ and 8 TeV have shown the existence of a new particle with a mass of 125 GeV [1, 2]. The spin properties and the measured production and decay rates of the discovered particle have been found to be consistent with those of the Higgs boson predicted by the Standard Model (SM).

These results suggest that the discovered particle is indeed the SM Higgs boson. A crucial question is whether there is only one Higgs doublet as postulated by the SM, or whether the Higgs sector is extended, leading to more than one Higgs boson of which one has SM-like properties, as predicted in many beyond the Standard Model (BSM) theories. Some scenarios, such as the Electroweak Singlet model [3], predict for example that the SM Higgs boson mixes with a heavy scalar singlet, implying the existence of an additional resonance at high mass with couplings similar to the SM Higgs boson. It is therefore important to continue to investigate the region around the TeV scale of the mass spectrum.

Moreover, the SM fails to provide an explanation for other open questions of particle physics, such as the integration of the gravity into the SM itself. Several BSM theories try to address this problem, such as the bulk graviton model [4] [5] [6], which predicts spin-2 resonances decaying into pair of vector bosons. Another class of models predict the existence of heavy spin-1 resonances, such as W' and Z' bosons. The phenomenological description of these additional resonances is obtained by adding BSM mass and interaction terms to the SM Lagrangian, as done in the composite heavy vector triplet (HVT) model [7]. Experimental results are used to set limits on the coefficients of these additional terms.

In order to probe these theories, this work focuses on the search for heavy resonances decaying into a VW final state, where V denotes either a W or a Z boson, with the CMS detector. The investigated final state is the semi-leptonic channel, where the W boson decays into a lepton-neutrino pair while the V boson decays into a pair of quarks. One of the challenges of this analysis is the reconstruction of the highly energetic decay products. Since the resonances under study have masses of O(TeV), the bosons have on average transverse momenta of several hundred GeV. Therefore, the quarks from the V boson decay tend to be very collimated and they are reconstructed as a single ("merged") jet in the detector. Dedicated techniques have been developed to improve the reconstruction of these merged jets, exploiting their different spatial and energy distribution of the jet constituents with respect to QCD jets. In addition, the presence of an isolated and high energetic lepton in

the final state coming from the leptonically decaying W boson contributes to reduce the contamination from the QCD background, allowing the semi-leptonic channel to be one of the most performing signature for this class of searches.

The strategy of the analysis is to reconstruct the diboson invariant mass of the events (m_{VW}) and to search for a local excess in the m_{VW} spectrum, which could indicate the presence of a new resonance. Therefore, the precise estimate of the contribution of the background processes is of paramount importance and it is one of the challenges of the work. The production of a W boson in association with quarks and gluon jets that are falsely identified as the hadronically decaying V boson is the main background of the analysis, due to the large cross section of the process. The correct estimate of this background contribution depends crucially on the ability to reconstruct the merged jet emerging from the hadronic V decay. Since the clustering process in the detector and parton shower effects are not perfectly simulated in the Montecarlo, the analysis employs a data-driven algorithm [8] to extrapolate the background shape and yield directly from data, allowing the analysis to be robust against disagreements between data and simulation.

In this work, these techniques are used to probe some of the theoretical models described above. A first analysis using LHC Run I data is presented, searching for heavy Higgs bosons in the mass range $0.6 - 1.0$ TeV. The results have been also interpreted within the Electroweak Singlet framework. The main feature of this analysis is the categorization of the events based on the number of jets, introducing a dedicated search for Higgs production via the Vector Boson Fusion (VBF) channel, which improves the sensitivity with respect to a previous version of the analysis [8]. With the achieved sensitivity, it has been possible to set upper limits on the production cross section of the model considered, excluding the existence of a SM-like Higgs boson with a cross section (times the branching fraction to WW) larger than 0.3459 pb and than 0.0348 pb for masses of 0.6 and 1 TeV, respectively. The analysis has been published in [9, 10].

In the summer of 2015, the LHC has restarted operating with a higher centre-of-mass energy (13 TeV). The same analysis approach described above has been applied to the LHC Run II data. In this case, the higher center-of-mass energy with respect to Run I allowed to probe a larger part of the mass spectrum, between 0.6 and 4.0 TeV. One of the main features of this analysis is the categorization of the events using the mass of the merged jet from the V boson, to achieve a better separation between a W-like and a Z-like jet, and allowing to better discriminate between a charged and a neutral interpretation, respectively. Results have been interpreted in the bulk graviton model and the HVT model. For the bulk graviton case, upper limits on the production cross section times the branching fraction to WW have been set. These limits span from 2 pb to 0.02 pb for masses between 0.6 TeV and 4.0 TeV, respectively. For the HVT case, the achieved sensitivity is enough to exclude the existence of W' and Z' resonances with masses below $\sim 1.5-2.0$ TeV, depending on the particular model considered. The analysis has been published in [11, 12].

An accurate reconstruction of high energy electrons is another crucial aspect of this analysis, for which the Electromagnetic CALorimeter (ECAL) of the CMS detector plays a major role. In order to ensure an excellent energy resolution, a precise calibration of the channel-by-channel response (known as inter-calibrations) of the ECAL is required. This is achieved through different methods. One of them provides inter-calibrations exploiting energetic electrons from W and Z boson decays, comparing their energy measured in the

ECAL with the momentum measured from the silicon tracker. Electrons from W and Z decays are also used to monitor the stability of the energy response of the ECAL as a function of the time. In this work, these techniques are described and applied using LHC Run II data.

Contents

Chapter 1

Theoretical introduction

The fundamental theory which describes elementary particles and their interactions is called the Standard Model (SM). Its numerous predictions, including the existence of the Higgs boson arising from the Brout-Englert-Higgs (BEH) mechanism, have been confirmed by several experiments, from the precision measurements performed at the Large Electron Positron (LEP) collider [13], to the most recent results from the Large Hadron Collider (LHC) [1, 2, 14, 15, 16]. In this chapter, the SM is briefly presented in section 1.1, followed by an overview of the gauge symmetries and the spontaneous symmetry breaking (section 1.2 and 1.3). The BEH mechanism, which explains the origin of the masses of the elementary particles, is described in section 1.4, while the experimental confirmations of the theory, with the discovery of an Higgs-like boson at LHC, are presented in section 1.5. Despite its phenomenological success, however, the SM fails in providing an explanation to some observed physical phenomena, for which other Beyond-the-Standard-Model (BSM) scenarios have been proposed. Some of these models are described in section 1.6, and their validity is tested through the analyses presented in chapters 4, 5 and 6.

1.1 The Standard Model

The Standard Model, formulated in the 1970s, describes all elementary particles and their interactions. According to this model, particles are grouped into two categories: *fermions* and *bosons*. The former have spin $\frac{1}{2}$ and are the building blocks of matter, while the latter have integer spin and are the carriers of the forces acting between the fermion constituents. All matter is built from a small number of fermions: six *leptons* and six *quarks*. For each of them, a respective anti-particle exists, with identical mass but opposite electric charge.

Among the leptons, the *electron* (e), with unit negative charge, was discovered in 1897 by J.J.Thomson during his experiments with cathode rays [17]. The *muon* (μ) and the *tauon* (τ), heavy versions of the electron carrying the same charge, were discovered respectively in 1936 by C.D.Anderson in cosmic rays and in 1977 at the SLAC accelerator. The lepton family includes also three neutral-charged *neutrinos* (ν), each one paired with one of the charged leptons (ν_e, ν_μ, ν_τ). Neutrinos were first postulated by W.Pauli in 1930 to explain the missing energy and momentum in nuclear β-decay, and subsequently discovered in 1956 by F.Reines and C.Cowan (while the ν_τ was observed only in 2000).

Quarks are grouped into pairs differing by one unit of electric charge. There are six different quark "flavours": *up* (u), *down* (d), *strange* (s), *charm* (c), *bottom* (b), *top* (t). The up, charm and top quarks carry an electric charge of $+\frac{2}{3}|e|$, while down, strange and bottom quarks carry a charge of $-\frac{1}{3}|e|$. The up and down quarks are the fundamental constituents of the *proton* and the *neutron*, and they were theorized (together with the strange quark) for the first time in 1964 by M.Gell-Mann and G.Zweig. The s quark is the constituent of the so-called "strange particles" observed in the cosmic rays, long before quarks were postulated. The c quark was discovered in 1974 with the J/Ψ resonance (a $c\bar{c}$ bound state), simultaneously at SLAC and BNL. The bottom quark was observed for the first time three years later, with the Υ resonance (a $b\bar{b}$ state) at Fermilab. The top quark was discovered in 1995, again at Fermilab, and it is the heaviest elementary particle currently known. Quarks also have an additional type of charge, called "colour", that can have three different values. While leptons exist as free particles, quarks do not; they exists only in bound states composed by three quarks (or three antiquarks) called *baryons* or by a pair of quark and an antiquark, called *mesons*.

The list of fermions described in the SM is reported in table 1.1, with the mass and the electric charge of each particle [18].

	1st gen.		2nd gen.		3rd gen.		Q
leptons	ν_e	< 2.2 eV	ν_μ	< 0.17 MeV	ν_τ	< 15.5 MeV	0
	e	511 KeV	μ	105.7 MeV	τ	1.777 GeV	-1
quarks	u	~ 2.3 MeV	c	~ 1.275 GeV	t	~ 173.07 GeV	2/3
	d	~ 4.8 MeV	s	~ 95 MeV	b	~ 4.18 GeV	-1/3

Table 1.1: Table of fundamental fermions

A fermion of mass m is described by the following free Lagrangian [19]:

$$L_{Dirac} = i\bar{\psi}\gamma_\mu\partial^\mu\psi - m\bar{\psi}\psi \tag{1.1}$$

from which the following equation of motion, called Dirac equation, is derived:

$$i(\gamma_\mu\partial^\mu - m)\psi = 0 \tag{1.2}$$

where ψ is the four-components Dirac spinor, which describes the quantum field operators associated to the fermion, and γ_μ are the Dirac matrices.
The Dirac spinor ψ is usually split into a left-handed and a right-handed part:

$$\psi = \psi_L + \psi_R$$

with

$$\psi_L = P_L\psi = \frac{1}{2}(1-\gamma_5)\psi \qquad \psi_R = P_R\psi = \frac{1}{2}(1+\gamma_5)\psi$$

Particles interact with each other through four different forces, or *interactions*. These interactions are mediated by the exchange of other particles called *gauge bosons*:

- The *electromagnetic* interaction acts only between particles with electric charge different from zero. This force is responsible for the phenomena outside the nuclei: the bound states of electrons with nuclei, i.e. atoms and molecules, and for the intermolecular forces in liquids and solids. This interaction is mediated by the *photon*, a massless particle with spin 1 and no electric charge. The theory that describes this type of interactions is called QED (Quantum Electro-Dynamics).

- The *strong* interaction acts between particles with colour charge, i.e. quarks, through the exchange of massless particles called *gluons*, with spin 1. The strong interaction keeps the quarks bounded inside protons and neutrons ("quark confinement"). Moreover, the same force keeps protons and neutrons bounded inside the nuclei. The theory that describes strong interactions is named QCD (Quantum Cromo-Dynamics).

- The *weak* interaction is responsible for radioactive decays and neutrino interactions, like the β-decay. The carrier of this force are three massive bosons: the W^-, the W^+ and the Z boson. They were discovered in 1983 at the Super Proton Synchrotron (SPS) located at CERN, and they have masses of order 100 times the proton mass.

- The *gravitational* interaction acts between particles with mass. Since its relative strength is small compared to the other forces, its effects become relevant only in presence of large masses, like planets or stars. The hypothetical boson which carries this force is the *graviton*, that has not been observed yet.

The list of interactions with their corresponding bosons is reported in table 1.2.

Interaction	Relative strength	Mediator	Spin	Q
Strong	1	gluon, g	1	0
Electromagnetic	10^{-2}	photon, γ	1	0
Weak	10^{-7}	$W^{\pm}$, Z	1	$\pm$1,0
Gravity	10^{-39}	graviton*, G	2	0

Table 1.2: Table of fundamental forces and mediator bosons.
*Not observed yet.

A spin 0 boson with mass m is described by the Klein-Gordon Lagrangian [19]:

$$L_{KG} = (\partial_\mu \phi)^\dagger (\partial^\mu \phi) - m^2 \phi^\dagger \phi$$

from which the correspondent equation of motion can be derived:

$$(\Box + m^2)\phi = 0$$

where ϕ is a complex scalar field describing the particle.
For a vector (i.e. spin 1) boson, the dynamics is described by the following Proca Lagrangian:

$$L_{Proca} = -\frac{1}{2} F_{\mu\nu} F^{\mu\nu} + \frac{1}{4} m^2 A_\mu A^\mu$$

and the corresponding equation of motion is:

$$(\Box + m^2)A_\mu = 0$$

where A_μ is the vector field describing the particle and $F_{\mu\nu} = \partial_\mu A^\nu - \partial_\nu A^\mu$ is the Faraday antisymmetric tensor.

In the 1970s, experiments showed that at very high energies the weak and electromagnetic interactions are different aspects of the same force, called *electroweak* interaction; at lower energies the symmetry is broken and they appear as two different forces. The unified description of these two forces is based on a $SU(2)_L$ x $U(1)_Y$ symmetry group. The W^+, W^-, Z bosons and the photon arise from the invariance of the Lagrangian under this transformation group, as shown in section 1.2.
The strong interactions are described by a $SU(3)_C$ symmetry group: quarks appear in three different colour charges ("triplets"), and the gluons arise from the invariance of the Lagrangian under $SU(3)_C$ transformation.

1.2 Gauge symmetries

The interactions between particles arise from the requirement of a symmetry in the Lagrangian that describes the free-particle fields. In the Noether theorem, each simmetry in the Lagrangian is associated to a conserved current. This leads to the introduction of new fields and interactions.
In QED the free-field Lagrangian describing the fermionic field

$$L_0 = i\bar{\psi}\gamma_\mu\partial^\mu\psi - m\bar{\psi}\psi$$

is invariant under the global phase transformations [19]

$$\begin{cases} \psi(x) \to \psi'(x) = \psi(x)e^{-iqf} \\ \bar{\psi}(x) \to \bar{\psi}'(x) = \psi(x)e^{+iqf} \end{cases} \tag{1.3}$$

and this leads to the conservation of the electromagnetic current

$$J^\mu = q\bar{\psi}(x)\gamma^\mu\psi(x) \tag{1.4}$$

The transformations of equation 1.3 are named "global" because the phase factor f does not depend from space or time.
A generalization is the definition of the "local phase" (or gauge) transformations:

$$\begin{cases} \psi(x) \to \psi'(x) = \psi(x)e^{-iqf(x)} \\ \bar{\psi}(x) \to \bar{\psi}'(x) = \psi(x)e^{+iqf(x)} \end{cases} \tag{1.5}$$

where $f(x)$ is an arbitrary function space or time dependent. Under these transformations, the free-field Lagrangian L_0 becomes

$$L_0 \to L_0{}' = L_0 + q\bar{\psi}(x)\gamma^\mu\psi(x)A_\mu(x) \tag{1.6}$$

The Lagrangian is no longer invariant, due to the presence of the last term in equation 1.6. One way to restore invariance is to introduce the covariant derivative:

$$D_\mu\psi(x) = [\partial_\mu + iqA_\mu(x)]\psi(x) \tag{1.7}$$

with a new field $A_\mu(x)$ (i.e. the electromagnetic field) that transforms under gauge transformations in the usual way:

$$A_\mu(x) \to A'_\mu(x) = A_\mu(x) + \partial_\mu f(x) \tag{1.8}$$

The crucial feature is that the covariant derivative transforms in the same way as the matter field $\psi(x)$; in fact, combining equation 1.5 and 1.8, one obtains:

$$D_\mu \psi(x) \to e^{-iqf(x)} D_\mu \psi(x)$$

Therefore, it is possible to build a Lagrangian that is invariant under gauge transformations, replacing the ordinary derivative ∂_μ with the covariant one of equation 1.7, obtaining:

$$L = i\bar{\psi}\gamma^\mu D_\mu \psi - m\bar{\psi}\psi = L_0 - q\bar{\psi}(x)\gamma^\mu \psi(x) A_\mu(x) \tag{1.9}$$

Hence, the requirement of the Lagrangian to be invariant under simple $U(1)$ gauge transformations leads to the presence of a new term (the last one in equation 1.9) describing a new interaction between the fermionic field $\psi(x)$ and this new field A_μ. The quantum associated to this new field is the photon. This new boson should be massless in order to preserve the symmetry.

The same concepts can be applied also to the weak interactions. The starting point is the free-lepton Lagrangian density

$$L_0 = i[\bar{\psi_l}(x)\gamma^\mu \partial_\mu \psi_l(x) + \bar{\psi_{\nu_l}}(x)\gamma^\mu \partial_\mu \psi_{\nu_l}(x)] \tag{1.10}$$

where l means the sum over all kinds of leptons (e,μ,τ).
The fermionic field ψ can be divided in its left-handed and right-handed parts; moreover, the fields ψ_l^L and $\psi_{\nu_l}^L$ can be combined in a two-components field:

$$\Psi_l^L(x) = \begin{pmatrix} \psi_{\nu_l}^L(x) \\ \psi_l^L(x) \end{pmatrix}$$

and, correspondingly,

$$\bar{\Psi_l}^L(x) = \left(\bar{\psi}_{\nu_l}^L(x), \bar{\psi}_l^L(x)\right)$$

Hence, the Lagrangian can be written in term of the left-handed and the right-handed components:

$$L_0 = i[\bar{\Psi}_l^L(x)\gamma^\mu \partial_\mu \Psi_l^L(x) + \bar{\psi}_l^R(x)\gamma^\mu \partial_\mu \psi_l^R(x) + \bar{\psi}_{\nu_l}^R(x)\gamma^\mu \partial_\mu \psi_{\nu_l}^R(x)] \tag{1.11}$$

For the right-handed parts, no two-components field are introduced; this left-right asymmetry of the weak interactions can be described in terms of different transformation properties of the left and right-handed fields, as it is shown later.
Now, a set of $SU(2)$ transformations (called isospin transformations) is defined as follows:

$$\begin{cases} \Psi_l^L(x) \to \Psi_l^{L'}(x) = e^{\frac{i}{2}\alpha_j \tau_j} \Psi_l^L(x) \\ \bar{\Psi}_l^L(x) \to \bar{\Psi}_l^{L'}(x) = \bar{\Psi}_l^L(x) e^{-\frac{i}{2}\alpha_j \tau_j} \\ \Psi_l^R(x) \to \Psi_l^{R'}(x) = \Psi_l^R(x) \qquad \Psi_{\nu_l}^R(x) \to \Psi_{\nu_l}^{R'}(x) = \Psi_{\nu_l}^R(x) \\ \bar{\Psi}_l^R(x) \to \bar{\Psi}_l^{R'}(x) = \bar{\Psi}_l^R(x) \qquad \bar{\Psi}_{\nu_l}^R(x) \to \bar{\Psi}_{\nu_l}^{R'}(x) = \bar{\Psi}_{\nu_l}^R(x) \end{cases} \tag{1.12}$$

where τ_j are the Pauli matrices. It is clear that these transformations act only on the left-handed lepton fields, while the right-handed components are scalars under them.

The Lagrangian 1.11 is invariant under these transformations, so there are three conserved currents

$$J_{i\mu} = \frac{1}{2}\bar{\psi}_L \gamma_\mu \tau_i \psi_L \qquad \text{with} \qquad i = 1, 2, 3 \tag{1.13}$$

which are called weak isospin currents, leading to the conservation of the weak isospin quantum numbers, $\{I_i^W\}_{i=1,2,3}$.
Moreover, a new set of transformations, called hypercharge transformations, is defined as follows:

$$\psi(x) \to \psi'(x) = e^{i\beta Y}\psi(x), \qquad \bar{\psi}(x) \to \bar{\psi}'(x) = e^{i\beta Y}\bar{\psi}(x) \tag{1.14}$$

where $\psi(x)$ denotes any type of lepton field, and Y is called weak hypercharge and takes a different value depending on the field type. These are $U(1)$ transformations, and they leave the Lagrangian invariant, as before. This leads to the conservation of the hypercharge current, defined by

$$J_Y^\mu = J_{em}^\mu(x)/e - J_3^\mu(x) \tag{1.15}$$

with the corresponding weak hypercharge Y that is related to the electric charge Q and the weak isocharge I_3^W by

$$Y = Q/e - I_3^W$$

hence, Y takes the value $-\frac{1}{2}$ for the left-handed fields, -1 for the right-handed states of leptons and 0 for the right-handed neutrino.

Thus, the Lagrangian is invariant under these $SU(2)_L$ x $U(1)_Y$ global phase transformations. The last step is to generalize from global to local phase transformations. The set of $SU(2)_L$ transformations of equation 1.12 are replaced by the following ones:

$$\begin{cases} \Psi_l^L(x) \to \Psi_l^{L'}(x) = e^{\frac{i}{2}g\tau_j\omega_j(x)}\Psi_l^L(x) \\ \bar{\Psi}_l^L(x) \to \bar{\Psi}_l^{L'}(x) = \bar{\Psi}_l^L(x)e^{-\frac{i}{2}g\tau_j\omega_j(x)} \\ \Psi_l^R(x) \to \Psi_l^{R'}(x) = \Psi_l^R(x) \qquad \Psi_{\nu_l}^R(x) \to \Psi_{\nu_l}^{R'}(x) = \Psi_{\nu_l}^R(x) \\ \bar{\Psi}_l^R(x) \to \bar{\Psi}_l^{R'}(x) = \bar{\Psi}_l^R(x) \qquad \bar{\Psi}_{\nu_l}^R(x) \to \bar{\Psi}_{\nu_l}^{R'}(x) = \bar{\Psi}_{\nu_l}^R(x) \end{cases} \tag{1.16}$$

while the $U(1)_Y$ transformations become:

$$\psi(x) \to \psi'(x) = e^{ig'Yf(x)}\psi(x), \qquad \bar{\psi}(x) \to \bar{\psi}'(x) = e^{ig'Yf(x)}\bar{\psi}(x) \tag{1.17}$$

The Lagrangian is no longer invariant under these gauge transformations; as in the previous case, it is necessary to replace the ordinary derivative with a covariant one, which in this case is defined by

$$D_\mu = (\partial_\mu - ig\frac{\tau_i W_{\mu_i}}{2} - ig'YB_\mu) \tag{1.18}$$

where g and g' are new coupling constants, and there are in total four new fields: three components for $W_{\mu i}$, and B_μ.
The Lagrangian density can be rewritten in the form

$$L = L_0 + L_I = L_0 - gJ_i^\mu(x)W_{\mu i} - g'J_Y^\mu(x)B_\mu \tag{1.19}$$

where L_0 is the free-lepton Lagrangian density of equation 1.11, while L_I represents the interaction of the weak isospin currents (equation 1.13) and the weak hypercharge current (equation 1.15) with these new fields $W_{\mu i}$ and B_μ.
To better understand the interaction term, the first two components of $W_{\mu i}$ can be rewritten as follows

$$W^{\pm}{}_\mu(x) = \frac{1}{\sqrt{2}}[W_{1\mu}(x) \mp iW_{2\mu}(x)] \tag{1.20}$$

and $W_{3\mu}$ and B_μ as linear combinations of two different Hermitian fields A_μ and Z_μ, defined by

$$\begin{pmatrix} W_{3\mu} \\ B_\mu \end{pmatrix} = \begin{pmatrix} \cos\theta_W & \sin\theta_W \\ -\sin\theta_W & \cos\theta_W \end{pmatrix} \begin{pmatrix} Z_\mu \\ A_\mu \end{pmatrix} \tag{1.21}$$

where θ_W is called *Weinberg angle*, and its value is determined by experiments: $sin^2\theta_W = 0.23153 \pm 0.00016$.
With these substitutions, the interaction term of the Lagrangian becomes

$$\begin{aligned} L_I = &- J^\mu_{em} A_\mu(x) - \frac{g}{2\sqrt{2}}[J^\dagger_\mu(x) W^\mu(x) + J^\mu(x) W^\dagger_\mu(x)] \\ &- \frac{g}{cos\theta_W}[J^\mu_3(x) - sin^2\theta_W J^\mu_{em}/e] Z_\mu \end{aligned} \tag{1.22}$$

where

$$g \sin\theta_W = g' \cos\theta_W = e$$

Three terms can be identified in equation 1.22:

- The first one is the familiar interaction of QED between the electromagnetic current and the photon field $A_\mu(x)$;
- the second one represents the interaction between two weak charged currents with two fields $W_\mu(x)$; the quanta of these fields are the W^+ and W^- bosons;
- the last term represents an interaction between a neutral current and the vector field $Z_\mu(x)$; the quantum of this field is the Z boson.

The Lagrangian density of equation 1.19 describes the free leptons and their interactions between the gauge bosons. The complete Lagrangian must include also a free bosons term, when no fermions are present. Clearly the new term must be invariant under the $SU(2)_L \times U(1)_Y$ transformations, and is the following:

$$-\frac{1}{4} W_{i\mu\nu} W^{\mu\nu}_i - \frac{1}{4} B_{\mu\nu} B^{\mu\nu} \tag{1.23}$$

where the tensor fields are defined by

$$\begin{cases} W^{\mu\nu}_i = \partial^\mu W^\nu_i - \partial^\nu W^\mu_i + g\epsilon_{ijk} W^\mu_j W^\nu_k \\ B^{\mu\nu} = \partial^\mu B^\nu - \partial^\nu B^\mu \end{cases} \tag{1.24}$$

The last term in $W^{\mu\nu}_i$ contains the interactions of the gauge bosons $W^\pm$ and Z, represented by the Feynman diagrams of Figure 1.1; these terms arise because the W^μ_i fields (i.e. the $W^\pm$ bosons) carry weak isospin charge. This is in contrast to QED, where the interaction is transmitted through the photon that carries no electric charge.

Until now, all fermions and bosons in the theory were considered massless. It is not allowed to introduce mass terms in the Lagrangian, since these terms would not be invariant under the gauge transformations and they would break the symmetry. However, all these particles introduced up to now (except for the photon) are observed experimentally to have non-zero masses. This is the major issue with this theory, and it is controlled by the spontaneous symmetry breaking mechanism, described in the next section.

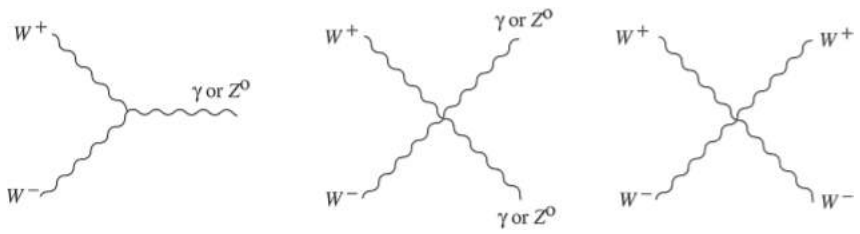

Figure 1.1: Feynman diagrams representing the interaction terms of the gauge bosons among themselves.

1.3 Spontaneous symmetry breaking

Considering a system with a Lagrangian L with a particular symmetry (invariant under a group of transformations), and the ground state of this system, i.e. the state with the lowest energy, two situations can occur:

- the ground state is non-degenerate, hence it is unique and it has the symmetry of the Lagrangian, being invariant under the symmetry transformation of L;

- the ground state is degenerate: in this case there are more eigenstates that represent the lowest energy state. Selecting arbitrarily one of the degenerate states, the ground state is no longer symmetric under the same transformations that leave L invariant; this phenomenon is called *spontaneous symmetry breaking*.

There are many examples of spontaneous symmetry breaking in physics. One of them is ferromagnetism: in ferromagnetic materials, at high temperatures the system shows a $SO(3)$ rotational symmetry, since the dipoles are randomly oriented in all the directions, giving a total null magnetization $\mathbf{M}$. Instead, at low temperatures (and therefore in the ground state) the dipoles are aligned in a definite direction resulting in a non-zero magnetization $\mathbf{M}$. This is a clear case of degeneracy, since the orientation of $\mathbf{M}$ can be in any direction and all the system properties would remain unchanged. In this case, the symmetry under rotations is broken.
The same mechanism can be applied to the electroweak theory. In quantum field theory, the state of lowest energy is the vacuum. If the vacuum state is non-unique, the spontaneous symmetry breaking can happen. In particular, it implies the existence of some quantity in the vacuum that is not-vanishing and not invariant under the symmetry transformations of the system. An example of a field theory with a spontaneous symmetry breaking is the Goldstone model [20].
Consider a scalar field ϕ with the following Lagrangian density

$$L(x) = [\partial^\mu \phi^*(x)]\,[\partial_\mu \phi(x)] - \mu^2|\phi(x)|^2 - \lambda|\phi(x)|^4 \tag{1.25}$$

that is invariant under global $U(1)$ phase transformations.
The first term of equation 1.25 is the kinetic one, while the last two terms represent the negative of the potential energy density of the field: $V(\phi) = \mu^2|\phi(x)|^2 + \lambda|\phi(x)|^4$. Since the energy of the field must be bounded from below to have a ground state, λ should be positive. Depending on the sign of μ^2, two different situations occur:

- $\mu^2 > 0$: in this case the two terms of $V(\phi)$ are positive definite, so the absolute minimum of the potential appears in the unique value $\phi(x) = 0$. Therefore, spontaneous symmetry breaking cannot occur.

- $\mu^2 < 0$: $V(\phi)$ has a local minimum at $\phi(x) = 0$ and a circle of absolute minima at

$$\phi(x) = \phi_0 = \left(\frac{-\mu^2}{2\lambda}\right)^{\frac{1}{2}} e^{i\theta}$$

with $0 \leq \theta \leq 2\pi$, where the θ angle defines a direction in the complex plane.

The second case is the interesting one, since spontaneous symmetry breaking occurs if a particular direction θ is chosen. Due to the Lagrangian invariance under global phase transformations, the value of θ is not significant; so, taking $\theta = 0$, the ground state is represented by

$$\phi_0 = \left(\frac{-\mu^2}{2\lambda}\right)^{\frac{1}{2}} = \frac{1}{\sqrt{2}}v$$

It is convenient to introduce two new real fields $\sigma(x)$ and $\eta(x)$ and rewrite the field $\phi(x)$ as ϕ_0 plus small deviations from the ground state:

$$\phi(x) = \frac{1}{\sqrt{2}}[v + \sigma(x) + i\eta(x)]$$

In term of these fields, the Lagrangian density becomes

$$\begin{aligned} L(x) = &\frac{1}{2}\left[\partial^\mu \sigma(x)\right]\left[\partial_\mu \sigma(x)\right] - \frac{1}{2}(2\lambda v^2)\sigma^2(x) \\ &+ \frac{1}{2}\left[\partial^\mu \eta(x)\right]\left[\partial_\mu \eta(x)\right] \\ &- \lambda v \sigma(x)\left[\sigma^2(x) + \eta^2(x)\right] - \frac{1}{4}\lambda\left[\sigma^2(x) + \eta^2(x)\right]^2 \end{aligned} \tag{1.26}$$

The first three terms of equation 1.26 contain the free-field Lagrangian, while the remaining ones are interaction terms. The quantity $\sigma(x)$ represents a spin 0 boson with a positive mass of $\sqrt{2\lambda v^2}$ (due to the presence of the second term), while $\eta(x)$ represents a spin 0 boson with no mass, since there are no terms in η^2, that is thermed a *Goldstone boson*.
Therefore, the spontaneous symmetry breaking leads to the presence of Goldstone bosons with zero mass, which are not observed in nature. This problem is solved with the Higgs model.

1.4 The Higgs model

The Goldstone model is generalized requiring the Lagrangian 1.25 to be invariant under $U(1)$ gauge transformations. Introducing the covariant derivative with the field A_μ, the Lagrangian density becomes [19]

$$L(x) = \left[D^\mu \phi(x)\right]^* \left[D_\mu \phi(x)\right] - \mu^2|\phi(x)|^2 - \lambda|\phi(x)|^4 - \frac{1}{4}F_{\mu\nu}(x)F^{\mu\nu}(x) \tag{1.27}$$

where $F_{\mu\nu}(x)$ is the usual tensor field.
This Lagrangian is invariant under the usual $U(1)$ gauge transformations

$$\left\{ \begin{array}{c} \phi(x) \to \phi'(x) = \phi(x)e^{-iqf(x)} \\ \psi^*(x) \to \phi^{*'}(x) = \phi^*(x)e^{+iqf(x)} \\ A_\mu(x) \to A'_\mu(x) = A_\mu(x) + \partial_\mu f(x) \end{array} \right. \tag{1.28}$$

To avoid the presence of the Goldstone boson η, it is possible to find a particular gauge of the form 1.28, called *unitary gauge*, that transforms the complex field $\phi(x)$ into a real field of the form

$$\phi(x) = \frac{1}{\sqrt{2}}\left[v + \sigma(x)\right] \tag{1.29}$$

Substituting 1.29 into 1.27 gives

$$L(x) = L_0(x) + L_I(x) \tag{1.30}$$

where $L_0(x)$ contains the free-field terms

$$\begin{aligned} L_0(x) = &\frac{1}{2}\left[\partial^\mu \sigma(x)\right]\left[\partial_\mu \sigma(x)\right] - \frac{1}{2}(2\lambda v^2)\sigma^2(x) \\ &- \frac{1}{4}F_{\mu\nu}(x)F^{\mu\nu}(x) + \frac{1}{2}(qv)^2 A_\mu(x)A^\mu(x) \end{aligned} \tag{1.31}$$

while L_I contains higher-order interaction terms.
Starting from the Lagrangian density of 1.27 for a complex scalar field and a massless real vector field, the final result is the Lagrangian density of 1.30 with a real scalar field and a massive vector field. So, of the two degrees of freedom of the complex field $\phi(x)$, one has been taken up by the vector field $A_\mu(x)$ which has become massive, the other shows up as the real field $\sigma(x)$. This is the *Higgs mechanism* [21, 22]: the vector boson acquires mass without destroying the gauge invariance of the Lagrangian. It should be noticed this mechanism does not generate any massless Goldstone bosons.

Finally, the Higgs mechanism can be applied to the electroweak model defined in section 1.2, to generate masses for the $W^\pm$ and Z bosons and for the fermions.
This time the symmetry to be broken is $SU(2)$, therefore it is necessary to introduce a field with several components (the Higgs field):

$$\Phi = \begin{pmatrix} \phi_a(x) \\ \phi_b(x) \end{pmatrix} \tag{1.32}$$

where $\phi_a(x)$ and $\phi_b(x)$ are scalar fields under Lorentz transformations. $\Phi(x)$ transforms under $SU(2)_L$ x $U(1)_Y$ transformations in the same way as the left-handed fermionic field $\Psi_l^L(x)$ does, following the laws of equation 1.16 and 1.17.
The Lagrangian to be included in the electroweak one is the following:

$$L^{\mathrm{H}} = \left(\mathcal{D}^\mu \Phi\right)^\dagger \left(\mathcal{D}_\mu \Phi\right) - \mu^2 \Phi^\dagger \Phi - \lambda\left(\Phi^\dagger \Phi\right)^2 \tag{1.33}$$

with the invariant property under $SU(2)_L$ x $U(1)_Y$ gauge transformations.
For $\lambda > 0$ and $\mu^2 < 0$, the Higgs field shows a circle of degenerate minima at

$$\Phi_0 = \begin{pmatrix} \phi_a^0(x) \\ \phi_b^0(x) \end{pmatrix} \tag{1.34}$$

with

$$\Phi_0^\dagger \Phi_0 = |\phi_a^0|^2 + |\phi_b^0|^2 = \frac{-\mu^2}{2\lambda}$$

Spontaneous symmetry breaking happens if a particular value of Φ_0 is chosen as ground state, for example

$$\Phi_0 = \begin{pmatrix} \phi_a^0(x) \\ \phi_b^0(x) \end{pmatrix} = \begin{pmatrix} 0 \\ \frac{v}{\sqrt{2}} \end{pmatrix} \tag{1.35}$$

where

$$v = \left(\frac{-\mu^2}{\lambda}\right)^{\frac{1}{2}}$$

The Higgs field in the vacuum state is no longer invariant under $SU(2)$ x $U(1)$ gauge transformations, breaking the symmetry; instead, it is invariant under $U(1)$ electromagnetic gauge transformations, in order to maintain the photon massless.
The Higgs field can again be parameterized in terms of its deviations from the ground state:

$$\Phi(x) = \frac{1}{\sqrt{2}} \begin{pmatrix} \eta_1(x) + i\eta_2(x) \\ v + \sigma(x) + i\eta_3(x) \end{pmatrix} \tag{1.36}$$

The interpretation of the three fields η_1, η_2, η_3 leads to the same difficulties met before (the presence of unobserved Goldstone bosons), but the problem can be avoided by employing again the unitary gauge, and rewriting the Higgs field in the following way:

$$\Phi(x) = \frac{1}{\sqrt{2}} \begin{pmatrix} 0 \\ v + \sigma(x) \end{pmatrix} \tag{1.37}$$

In this special gauge, the three unphysical fields $\eta_i(x)$ are "absorbed" and disappear, giving mass to the $W^{\pm}$ and Z bosons, while the photon remains massless since no electromagnetic gauge symmetry is broken. In contrast, the field $\sigma(x)$ survives, and after the quantization gives rise to a massive and spin-0 particle with no electric charge, the *Higgs boson.*
Using equation 1.37, the Higgs Lagrangian (equation 1.33) becomes

$$\begin{aligned} L^H =& \frac{1}{2}(\partial^\mu\sigma)(\partial_\mu\sigma) - \frac{1}{2}(2v^2\lambda)\sigma^2 - \lambda v\sigma^3 - \frac{1}{4}\lambda\sigma^4 \\ &+ \frac{1}{4}v^2g^2W_\mu^\dagger W^\mu + \frac{1}{8}\frac{v^2g^2}{\cos\theta_W}Z_\mu Z^\mu \\ &+ \frac{1}{2}vg^2W_\mu^\dagger W^\mu\sigma + \frac{1}{4}g^2W_\mu^\dagger W^\mu\sigma^2 + \frac{1}{4}\frac{vg^2}{\cos^2\theta_W}Z_\mu Z^\mu\sigma + \frac{1}{8}\frac{g^2}{\cos^2\theta_W}Z_\mu Z^\mu\sigma^2 \end{aligned} \tag{1.38}$$

where:

- the first line represents the kinetic term for the Higgs boson, its mass term (with $m_H = \sqrt{2v^2\lambda}$), and self-interaction terms between three and four Higgs bosons;
- in the second line there are the mass terms for the W boson (with $m_W = \frac{1}{2}vg$) and for the Z boson ($m_Z = \frac{m_W}{\cos\theta_W}$);
- the last line contains the interaction terms between the Higgs boson and the W and Z bosons.

The theory does not predict the value of the Higgs boson mass, since it depends on the two unknown parameters v and λ. Nevertheless, since m_W was measured at LEP, the value of v can be estimated from the Fermi coupling constant: $v = \sqrt{2G_F} \simeq 247$ GeV.
Up to now, only bosons have acquired mass; it is necessary also to give mass to fermions. This is done by adding a term which couples the Higgs and the fermion field to the Lagrangian:

$$L^{LH}_{\text{Yukawa}} = -g_l\left[\bar{\Psi}_l^L(x)\psi_l^R(x)\Phi(x) + \Phi^\dagger(x)\bar{\psi}_l^R(x)\Psi_l^L(x)\right] \tag{1.39}$$

This term is called the *Yukawa interaction*, and it is $SU(2)_L$ x $U(1)_Y$ gauge invariant. g_l is a dimensionless coupling constant. After the breakdown of the symmetry, inserting equation 1.37 into 1.39, one finds

$$\begin{aligned} L^{LH}_{\text{Yukawa}} &= -\frac{g_l}{\sqrt{2}}\left[(\bar{\psi}^L_{\nu_l}, \bar{\psi}^L_l)\begin{pmatrix} 0 \\ v+\sigma \end{pmatrix}\psi^R_l + \bar{\psi}^R_l\,(0, v+\sigma)\begin{pmatrix} \psi_{\nu_l} \\ \psi_l \end{pmatrix}\right] \\ &= -\frac{g_l}{\sqrt{2}}\left[v(\bar{\psi}^L_l\psi^R_l + \bar{\psi}^R_l\psi^L_l) + (\bar{\psi}^L_l\psi^R_l + \bar{\psi}^R_l\psi^L_l)\sigma\right] \\ &= -\frac{g_l}{\sqrt{2}}\left[v\bar{\psi}_l\psi_l + \bar{\psi}_l\psi_l\sigma\right] \end{aligned} \tag{1.40}$$

The first term can be interpreted as the mass term for the leptons, defining

$$m_l = \frac{g_l v}{\sqrt{2}}$$

while the second one is an interaction term between the Higgs and the leptonic fields. So, this mechanism allows mass to be given to leptons and down-like quarks, while neutrinos and up-like quarks get the mass from their interaction with the Higgs doublet charge conjugate:

$$\Phi_C(x) = -i\tau_2\Phi^*(x)$$

1.5 Higgs-like boson discovery at LHC

The main four production mechanisms of the Higgs boson at LHC are illustrated in Figure 1.2:

- **Gluon Fusion (ggH or gg→H)**: it is the dominant production process over the entire range of m_H accessible to LHC. The Higgs boson is produced through annihilation of a gluon pair, via a heavy quark triangle loop. The Higgs couplings to fermions are proportional to the square of their masses, so the main contribution in the loop comes from the top quark. The inclusive cross section of this process is known at NNLO+NNLL QCD and NLO EWK accuracy [23].

- **Vector Boson Fusion (qqH or qq→qqH)**: it is the second largest production mechanism, with a cross section that is about one order of magnitude below the gluon fusion one for $m_H \sim O(100$ GeV$)$. In this process, two quarks inside the protons radiate a pair of W or Z bosons, that annihilate producing a Higgs boson. The main characteristic of the VBF mechanism is the presence of two jets produced from the hadronization of the quarks which radiate the bosons. These jets are characterized by a large separation in pseudorapidity and large invariant mass and permit the identification of Higgs events produced via VBF. They are usualy called "tag jets" or "VBF jets". Another property is the reduced hadronic activity in the central region between the tag jets, since they are colour disconnected. The cross section of this process is known at NNLO QCD and NLO EWK accuracy [23].

- **Higgs-strahlung ($\mathbf{q\bar{q}'}$ →WH and $\mathbf{q\bar{q}'}$ →ZH)**: in this process two quarks annihilate producing a W or Z boson, which radiates a Higgs boson. The strength of this process is more than one order of magnitude below the gluon fusion one [24]. This process, as in the case of VBF, is directly sensitive to the Higgs couplings to vector bosons. The cross section of the process is known at NNLO QCD and NLO EWK accuracy [23].

- **t$\bar{\text{t}}$ associated production (gg→ t$\bar{\text{t}}$H and q$\bar{\text{q}}'$ → t$\bar{\text{t}}$H)**: in this process, a pair of gluons or quarks annihilates producing two top quarks, which radiate a Higgs boson [25]. This process is directly sensitive to the coupling between the Higgs boson and the top quark. Its cross section is known at NLO QCD accuracy [23].

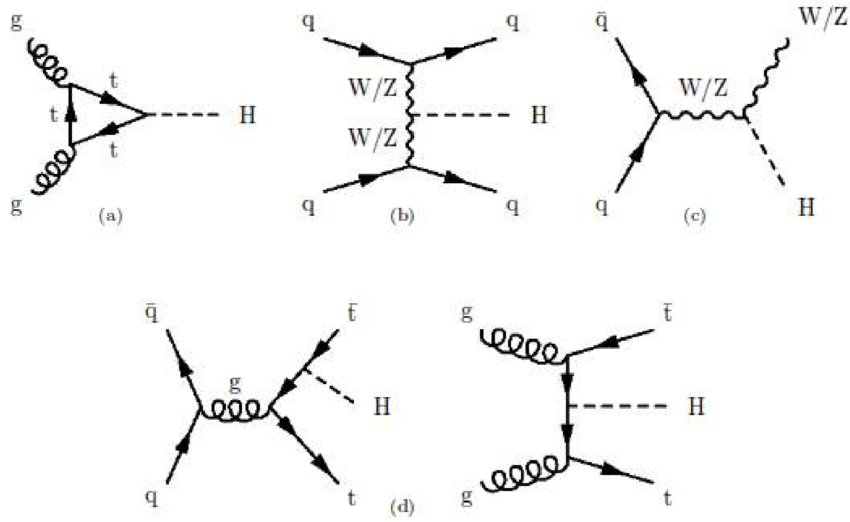

Figure 1.2: Feynman diagrams at tree-level for the most important production processes of a SM Higgs boson: (a) gluon fusion, (b) vector boson fusion, (c) Higgs-strahlung, (d) $t\bar{t}$ associated production.

The total production cross section for different center-of-mass energies and the cross section values for each production mode are shown in Figure 1.3 [26].

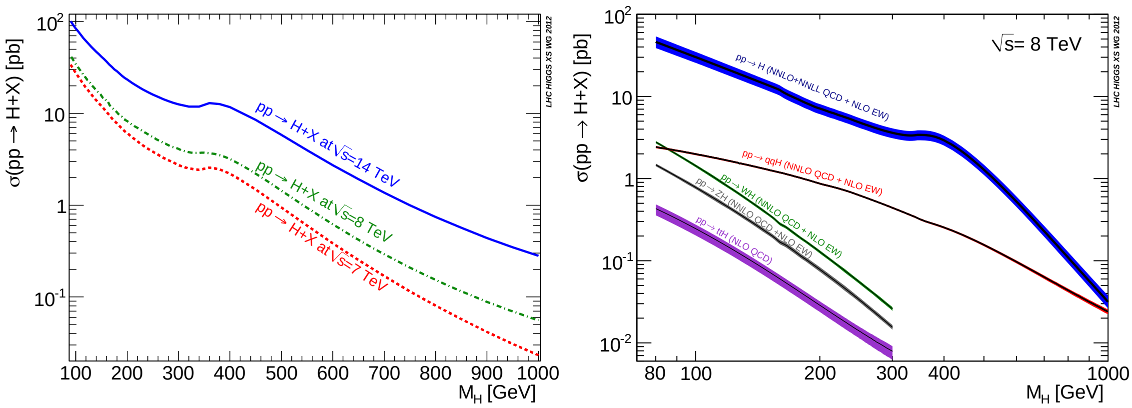

(a) **(b)**

Figure 1.3: (Left) SM Higgs total production cross section, as a function of the Higgs mass, for three different center of mass energy: $\sqrt{s} = 7$, 8 and 14 TeV. (Right) SM Higgs production cross sections at $\sqrt{s} = 8$ TeV for the different production mechanisms: gluon fusion (blue), vector boson fusion (red), Higgs-strahlung with a W/Z boson (green/grey), tt associated production (purple).

In the search for the Higgs boson, different decay channels can be exploited. The Higgs total width and decay branching ratios depend on the Higgs couplings to fermions and bosons, and are shown in Figure 1.4a. At low mass the main channel is H→ b$\bar{\text{b}}$, because channels with W/Z bosons pairs are suppressed. Above $m_H \simeq 160$ GeV the WW channel becomes the dominant one, and at higher mass the decay into a pair of Z bosons and

(above $m_H \simeq 350$ GeV) into a top quarks pair are possible as well. The Higgs boson does not couple with gluons or photons at tree level, so the decay into these particles can happen only via fermion loops.
The total width is shown in Figure 1.4b; it quickly increases with the Higgs mass due to the opening of new channels and the phase space increase. At $m_H \simeq 1$ TeV the width is as large as the Higgs mass itself.
The most sensitive decay channels at the LHC are the following:

- H$\rightarrow \gamma\gamma$: despite the very low branching ratio (since this decay can proceed only via fermion loops), at low mass ($m_H \lesssim 140$ GeV) this is one of the main channels of discovery due to the clear experimental signature: the presence of two high-E_T isolated photons, which results in a narrow peak above a falling background distribution in the diphoton invariant mass. The background comes from the SM production of prompt photon pairs or from the misidentification of jets or electrons.

- H$\rightarrow$ZZ: this is one of the "golden modes" for the discovery of the Higgs boson, in particular in the fully leptonic final state H$\rightarrow$ZZ$\rightarrow \ell\bar{\ell}\ell\bar{\ell}$ due to the very clean signature with four isolated leptons. Under $m_H \simeq 180$ GeV one Z boson is virtual. The backgrounds to this channel are the irreducible SM production of ZZ, and the $\mathrm{t\bar{t}}$ and $\mathrm{Zb\bar{b}}$ processes, that can be suppressed by requirements on the lepton isolation, transverse momentum and invariant mass (requiring the invariant mass of a lepton pair to be around m_Z) and by requirements on the event vertex.

- H$\rightarrow$WW: in the low mass region the search in this channel is performed in the fully leptonic mode WW$\rightarrow \ell\nu\ell\nu$; the signature is the presence of two isolated and opposite-charge leptons and missing energy. Since the mass peak can not be reconstructed due to the presence of the undetected neutrinos, the search strategy is based on event counting, for which an accurate knowledge of the backgrounds is needed.
  Instead, in the high-mass region (above $m_H \simeq 160$ GeV) this is the channel with the highest branching ratio; the search in the semi-leptonic mode WW$\rightarrow \ell\nu \mathrm{q\bar{q}}$ has some advantages with respect to the fully leptonic one, in particular a larger branching ratio and the possibility to reconstruct the mass peak, due to the presence of only one neutrino in the final state. The price to pay is the larger background, since in a hadron collider the final states with jets are more likely to occur. The main backgrounds for this channels are described in section 4.1.

The discovery (or the exclusion) of the SM Higgs boson has been one of the main goals of the LHC project. In 2012, both the CMS and ATLAS experiments reported the observation of a new boson with a mass of about 125 GeV [1, 2]. The properties of this new resonance have been extensively measured using the full statistics of 5.1 fb^{-1} at 7 TeV and 19.7 fb^{-1} at 8 TeV, collected in 2011 and 2012. Final results were published by both experiments in 2015 [27, 28]. For CMS, the measurements have been performed in several decay modes (H$\rightarrow \gamma\gamma$, H$\rightarrow$ZZ, H$\rightarrow$WW, H$\rightarrow \mathrm{\bar{b}b}$ and H$\rightarrow \tau\tau$) and targeting different production modes described above. The reported measured value for the mass of the new particle, obtained combining all these measurements, is $125.02^{+0.26}_{-0.27}$(stat.)$^{+0.14}_{-0.15}$(syst.) GeV, with event yields obtained in the different decay channels being compatible with those predicted by the SM, as shown in Figure 1.5. In the same figure, the 68% CL confidence regions, obtained from a two-dimensional likelihood scan, for the Higgs signal strength relative to the SM expectation ($\mu = \sigma/\sigma_{SM}$) and its mass (m_H) are shown for the H$\rightarrow \gamma\gamma$ and H$\rightarrow$ZZ channels, as well as for their combination. Only these two decay modes were used for the mass measurement due to their optimal resolution. The couplings of the new

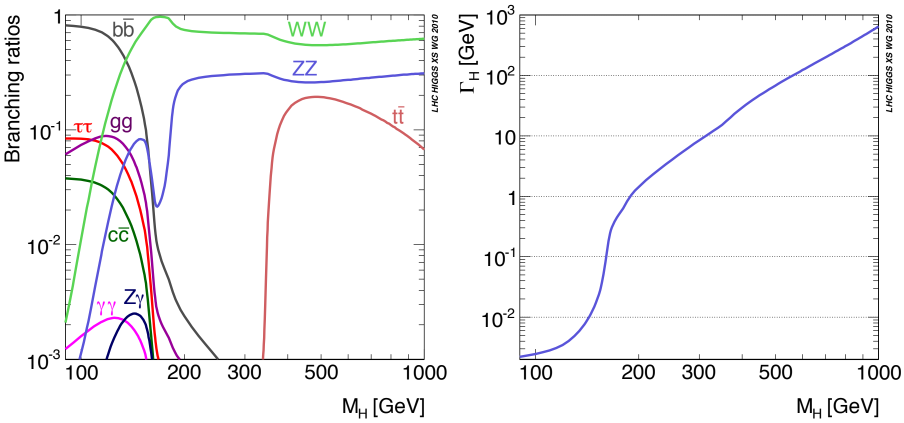

(a) (b)

Figure 1.4: Left: branching ratios of the SM Higgs boson in different decay channels. Right: total decay width of the SM Higgs boson, as a function of the Higgs mass.

boson to the SM particles were also measured, and no significant deviations from the SM prediction were found. Similar results were obtained by ATLAS [29].

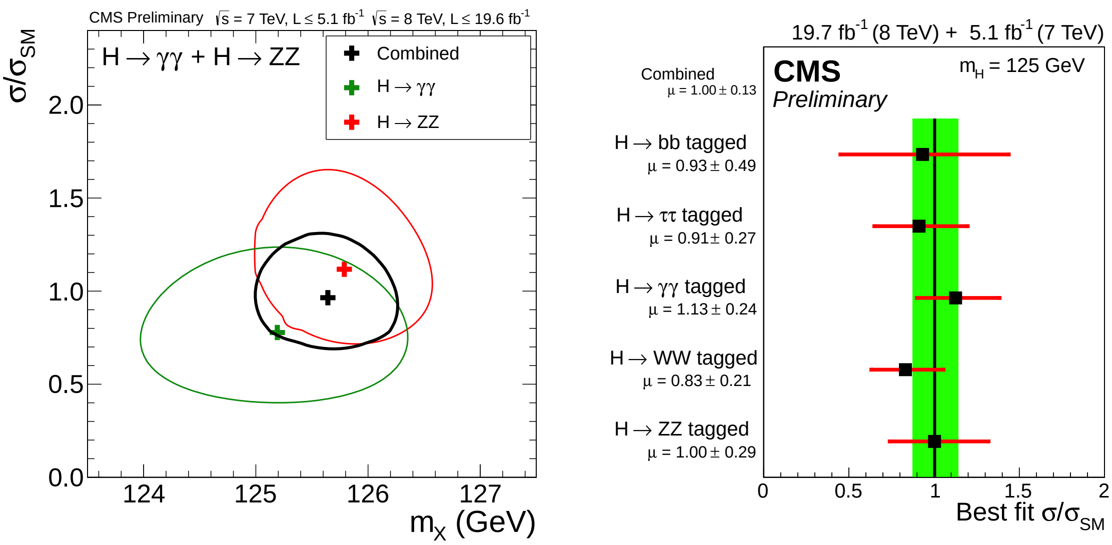

(a) (b)

Figure 1.5: Left:The 68% CL confidence regions for the signal strength σ/σ_{SM} versus the mass of the boson m_H for the H$\to$ $\gamma\gamma$ and H $\to$ ZZ $\to 4\ell$ final states and their combination. Right: Values of the best-fit σ/σ_{SM} for the combined analysis (solid vertical line) and for separate decay modes.

1.6 Beyond the Standard Model

The discovery of the Higgs boson was the last missing piece in the puzzle of particles of the SM. Despite its phenomenological success, however, this theory has some shortcomings, and it fails to provide an explanation to several physical phenomena. The main open questions are:

- No explanation is provided for important cosmological observations, such as the origin of dark matter and the matter-antimatter asymmetry [30].

- Hierarchy problem: no explanation is provided on why the Higgs mass/EWKB scale and the Planck scale ($M_p = 1.221 \times 10^{19}$ GeV) are several orders of magnitude different.

- The electroweak vacuum is unstable in the SM, without the introduction of new physics [31].

- No description of the cosmological inflation is included in the SM [32].

- The gravitational interaction is not included in the SM and no quantum theory of gravity exists.

There exists several Beyond-the-SM (BSM) models which tries to address some of these unsolved issues. In the following sections, some of these models are briefly presented. In section 1.6.1 a simple extension of the SM, with an addition of a singlet scalar field, is described. In section 1.6.2 and section 1.6.3 two other models, which mainly try to address the hierarchy problem, are presented. The same models are then tested in the analyses presented in chapter 4, 5 and 6.

1.6.1 The electroweak singlet model (EWSM)

As mentioned in section 1.5, the properties of the Higgs-like boson discovered at LHC are compatible with the SM expectations. However, the current limited theoretical and experimental uncertainties do not exclude the possibility that the observed resonance is only partially responsible for the EWSB, being only a piece of a more extended Higgs sector. Several BSM extensions have been proposed following this direction, such as the electroweak singlet model (EWSM) [3, 33, 34, 35, 36]. This model proposes the existence of an "hidden sector" of particles, which the SM Higgs field couples to. In this case, the couplings of the Higgs to the other SM particles are modified as well. In addition, decays into the hidden sector may generate an invisible decay mode affecting the total width.

In the EWSM, a minimal extension of the SM is obtained by adding a singlet scalar field ϕ_H to the SM Lagrangian. Denoting with ϕ_h the SM Higgs doublet field (corresponding to the observed boson at 125 GeV), the new Higgs potential can be written as [34]:

$$V = \mu_h^2|\phi_h|^2 + \lambda_h|\phi_h|^4 + \mu_H^2|\phi_H|^2 + \lambda_H|\phi_H|^4 + \eta_\chi|\phi_h|^2|\phi_H|^2 \tag{1.41}$$

where the last term represents the interaction between the two fields. As already shown in section 1.4, both the Higgs doublet ϕ_h and the singlet ϕ_H can be expanded around their ground state:

$$\phi_h = \frac{1}{\sqrt{2}}\begin{pmatrix} \eta_1(x) + i\eta_2(x) \\ v_h + h(x) + i\eta_3(x) \end{pmatrix} \qquad \phi_H = \frac{1}{\sqrt{2}}[H(x) + v_H + i\eta_4(x)] \tag{1.42}$$

and the respective Vacuum Expectation Values (VEV) are

$$v_h = \frac{1}{\lambda_h}(\mu_h^2 - \frac{1}{2})\eta_\chi v_H^2 \qquad v_H = \frac{1}{\lambda_H}(\mu_H^2 - \frac{1}{2})\eta_\chi v_h^2 \tag{1.43}$$

This means that the SM Higgs and the new scalar are mixed. Diagonalizing the Higgs mass matrix

$$M = \begin{pmatrix} 2\lambda_H^2 v_H^2 & \eta_\chi v_H v_h \\ \eta_\chi v_H v_h & 2\lambda_h^2 v_h^2 \end{pmatrix} \tag{1.44}$$

one obtains the following eigenstates $M_{1,2}$ and mixing angle χ:

$$\begin{aligned} M_{1,2}^2 &= (\lambda_H v_H^2 + \lambda_h v_h^2) \pm \sqrt{(\lambda_H v_H^2 - \lambda_h v_h^2)^2 + (\eta_\chi v_H v_h)^2} \\ \tan 2\chi &= \eta_\chi v_H v_h / (\lambda_H v_H^2 - \lambda_h v_h^2) \end{aligned} \tag{1.45}$$

with the following eigenvalues:

$$\begin{aligned} H_1(x) &= \cos\chi h(x) + \sin\chi H(x) \\ H_2(x) &= -\sin\chi h(x) + \cos\chi H(x) \end{aligned} \tag{1.46}$$

Both H_1 and H_2 couple to the Standard Model fields through $h(x)$ and to the hidden sector through the $H(x)$. It can be assumed that the potential parameters (λ_h, λ_H) and (v_h, v_H) are of similar size, and that the diagonal term η_χ is moderate. In this case, the properties of H_1 then remain dominated by the Standard Model component, while the properties of H_2 are characterized primarily by the hidden Higgs component.

An interesting scenario is obtained assuming that H_1 is light and matches the observed Higgs boson at 125 GeV, mainly decaying into Standard Model particles, at a rate reduced by the mixing parameter. The new scalar H_2 is instead much heavier than H_1, and decays primarily into particles of the hidden sector, and only in a small fraction to Standard Model particles and to light H_1 pairs.
The mixing reduces the production cross sections of the H_1, H_2 bosons to [35]:

$$\sigma_{1,2} = \cos^2\chi\{\sin^2\chi\}\ \sigma_{1,2}^{SM} \tag{1.47}$$

with respect to the cross sections of the Standard Model for equivalent masses, the expressions within the curly brackets for *index* = 2 substituting the corresponding expressions for *index* = 1.
The total widths of H_1, H_2 are modified correspondingly:

$$\Gamma_{1,2}^{\text{tot}} = \cos^2\chi\{\sin^2\chi\}\ \Gamma_{1,2}^{SM} + \sin^2\chi\{\cos^2\chi\}\ \Gamma_{1,2}^{hid} + \Delta_2\Gamma_2^{H_1H_1} \tag{1.48}$$

where $\Gamma_{1,2}^{SM}$ are the partial decay widths to SM particles, $\Gamma_{1,2}^{hid}$ are the partial decay widths into the hidden sector, and $\Delta_2 = 0, 1$ for *index* $= 1, 2$, respectively. The partial width $\Gamma_2^{H_1H_1}$ accounts for potential $H_2 \to H_1H_1$ decays if $M_2 > 2M_1$.
It is common to study the properties of H_2 in terms of the free parameters $\sin^2\chi$ (in the following indicated as C'^{2}), which expresses the signal strenght of the H_2 boson, and of the branching ratio into the hidden sector $\text{BR}_{\text{new}} = \Gamma_2^{hid}/\Gamma_2^{SM}$. While measurements on the $h(125)$ GeV boson at LHC set indirect limits on $\cos\chi$, a direct search on the H_2 boson is presented in chapter 5.

1.6.2 Warped Extra Dimensions model

Among the other open questions of the SM is the hierarchy problem, i.e. why gravity is so weak compared to the other interactions, or in other terms, why the Planck scale

($\bar{M_{pl}} = M_{pl}/8\pi = 2.4\times10^{18}$ GeV) is so different from the mass scale of the weak mediators, which is around 100 GeV. The so-called warped extra-dimension (WED) model, also known as Randall-Sundrum (RS) model [37, 38] tries to address this problem. The RS model predicts that the spacetime has a finite spatial dimension in addition to the standard 3+1 space-time. Particles of the SM are generally confined in the (3+1)-dimensional subspace, while the gravity propagates also in the additional dimension. Formally, the setup is a space S^1/Z_2 orbifold, where S^1 is the one-dimensional sphere (i.e. the circle) and Z_2 is the multiplicative group $\{-1, 1\}$. This construction leads to two fixed points at the two extremities of the circle, $\phi = 0, \pi$, each of them being the location of a 3+1-dimensional world (like the one we live in), called "3-branes". The 5-dimensional space, called "bulk", is enclosed by these two 3-branes. A graphical representation is shown in Figure 1.6.

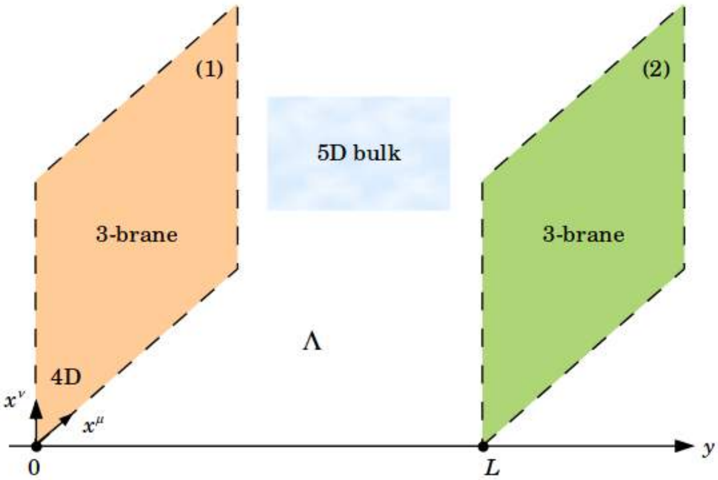

Figure 1.6: Graphical representation of the RS setup

The 3-branes couple to the four-dimensional component of the bulk:

$$g_{\mu\nu}^{\text{brane}}(x^\mu) \equiv G_{\mu\nu}(x^\mu, \phi = \pi) \qquad g_{\mu\nu}^{\text{brane'}}(x^\mu) \equiv G_{\mu\nu}(x^\mu, \phi = 0) \tag{1.49}$$

where G_{MN}, M, $N = \mu, \phi$, is the five-dimensional metric. x^μ are the coordinates of the 4-dimensional space, while ϕ is the coordinate of the 5th-dimension.
The classical action describing this setup is given by:

$$\begin{aligned} S =& S_{\text{gravity}} + S_{\text{brane}} + S_{\text{brane'}} \\ S_{\text{gravity}} =& \int d^4x \int_{-\pi}^{\pi} d\phi \sqrt{-G}\left(-\Lambda + 2M^3 R\right) \\ S_{\text{brane}} =& \int d^4x \sqrt{-g_{\text{brane}}}\left(L_{\text{brane}} - V_{\text{brane}}\right) \\ S_{\text{brane'}} =& \int d^4x \sqrt{-g_{\text{brane'}}}\left(L_{\text{brane'}} - V_{\text{brane'}}\right) \end{aligned} \tag{1.50}$$

where G is the determinant of $G_{\mu\nu}$, Λ is the 5D cosmological constant (which, unlike the effective 4D cosmological constant, does not need to be vanishing or small), M is the fundamental 5D mass scale, R is the 5D Ricci scalar, and g_{brane} and $g_{\text{brane'}}$ are the determinants of the metrics of the 3D-branes in Eq. 1.49. In each of the 3-brane actions in Eq. 1.50, the V term represents a constant "vacuum energy" which acts as a gravitational source even in the absence of particle excitations. The detailed form of the 3-brane Lagrangians L instead is not relevant for determining the classical five-dimensional metric in the ground state, and therefore is not considered in the following. The five-dimensional Einstein equation for the above action is:

$$\sqrt{-G}\left(R_{MN}-\frac{1}{2}G_{MN}R\right)=-\frac{1}{4M^3}[\Lambda\sqrt{-G}G_{MN}+V_{\text{brane}}\sqrt{-g_{\text{brane}}}g^{\text{brane}}_{\mu\nu}\delta^\mu_M\delta^\nu_N\delta(\phi-\pi)+ \\ +V_{\text{brane'}}\sqrt{-g_{\text{brane'}}}g^{\text{brane'}}_{\mu\nu}\delta^\mu_M\delta^\nu_N\delta(\phi)] \tag{1.51}$$

Since the solution to the 5D Einstein equations should fit the real 4D world, the metric should respect the four-dimensional Poincaré invariance along x^μ (i.e. the 4D universe derived from this theory should be flat and static). A five-dimensional metric which satisfies this ansatz is

$$ds^2=e^{-2\sigma(\phi)}\eta_{\mu\nu}dx^\mu dx^\nu+r_c^2d\phi^2 \tag{1.52}$$

where r_c is the "compactification radius" of the extra dimensional circle. This means that the usual four-dimensional metric is multiplied by a "warp" factor, which is a rapidly changing function which describes the additional dimension. Using this ansatz, the Einstein equations of Eq. 1.51 reduce to

$$\frac{6\sigma'^2}{r_c^2}=\frac{-\Lambda}{4M^3}\,\frac{3\sigma''}{r_c^2}=\frac{V_{\text{brane}}}{4M^3r_c}\delta(\phi-\pi)+\frac{V_{\text{brane'}}}{4M^3r_c}\delta(\phi) \tag{1.53}$$

whose solution consistent with a $\phi\to-\phi$ symmetry is

$$\sigma=r_c|\phi|\sqrt{\frac{-\Lambda}{24M^3}} \tag{1.54}$$

which implies also $\Lambda<0$. The metric should be a periodic function in ϕ; this implies that Eq. 1.53 can be solved only if $V_{\text{brane'}}$, V_{brane} and Λ are related in terms of a single scale factor k, as

$$V_{\text{brane'}}=-V_{\text{brane}}=24M^3k \qquad \Lambda=-24M^3k^2 \tag{1.55}$$

where k is called "curvature parameter". Therefore, the solution for the warp factor of Eq. 1.52 is

$$\sigma(\phi)=kr_c|\phi| \tag{1.56}$$

In order to evaluate the effect of this theory in our world, one can derive a 4-dimensional effective theory by substituting the metric of Eq. 1.49 into the gravity action of Eq. 1.50:

$$S_{eff}\supset\int d^4x\int_{-\pi}^{\pi}d\phi 2M^3r_ce^{-2kr_c|\phi|}\sqrt{-g_{\text{4D}}}R_{\text{4D}} \tag{1.57}$$

where g_{4D} and R_{4D} are the metric determinant and the Ricci tensor of the 4D space. This represents the 4D action. Integrating over the extra-dimension ϕ, one can derive the effective 4D Planck mass scale:

$$M_{Pl}^2=\frac{M^3}{k}[1-e^{-2kr_c\pi}] \tag{1.58}$$

This relation tells that M_{Pl}, which sets the energy scale of the gravity, depends only weakly on the size of the extradimension r_c, provided that kr_c is not too small. Moreover, one can rewrite the Lagrangian of the Higgs field using the action of Eq. 1.50, obtaining the following relation between the four-dimensional VEV of the Higgs field and the five-dimensional VEV located at the Planck scale:

$$v_{eff} = e^{-kr_c\pi} v_{Pl} \tag{1.59}$$

This implies that, if the value of the bare Higgs mass is of the order of the Planck scale, the physical Higgs mass is warped down to the weak scale by the exponential factor $e^{-kr_c\pi}$. For this reason, the first brane at $\phi = 0$ is often called the "Planck" brane, whereas the second brane is called the "TeV" brane. The relations 1.58 and 1.59 show how the hierarchy between the weak and the gravitational scale arises naturally from the theory: while the weak scale is exponentially suppressed along the extra dimension, the gravitational scale is mostly unaffected by it. In particular, in order to produce physical masses at the order of the TeV from fundamental parameters at the Planck scale, it is required $kr_c \sim 50$. A graphical representation of this phenomenon is shown in Figure 1.7.

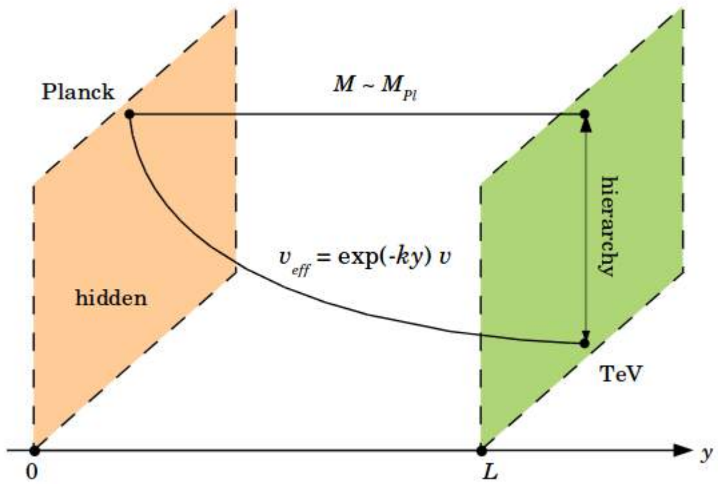

Figure 1.7: Graphical visualization of the exponential hierarchy

In addition, the quantum fluctuations of the metric solution of Eq. 1.49 are interpreted as particles: fluctuations around the four-dimensional part of the metric correspond to the Graviton field (spin-2), while the ones around the fifth dimension correspond to a spin-0 boson called Radion. Moreover, the finitness of the fifth dimension introduces excitation modes in the four dimensional effective theory, which appear as heavy resonances called Kaluza-Klein (kk) modes. The interesting fact is that the mass of the lightest kk mode of the graviton field (spin-2 field) depends only on the ratio between the curvature of the extra dimension and the Planck mass ($k/\bar{M}_{Pl} \equiv \tilde{k}$), and it is expected to be in the TeV range, therefore accessible to LHC searches. Two different scenarios are possible, depending on the coupling limits:

- RS1 scenario: the SM fields are confined in the TeV brane
- Bulk scenario: the SM fields can propagate also in the bulk

RS1 graviton

The RS1 graviton is the simplest resonance predicted by the RS model. It is characterized by a low branching fraction to massive vector bosons ($\sim 7\%$ for ZZ and $\sim 15\%$ for WW), and it decays mainly (90% of the time) into transverse polarized bosons. The model is defined in terms of two parameters only:

- The mass of the graviton resonance, M_G
- $\tilde{k}$, which acts as the coupling constant of the model, with the production cross-sections and widths of the graviton depending quadratically on it. Figure 1.8 shows the cross-section of the process pp $\rightarrow$ G* at a center of mass energy of 8 and 13 TeV.

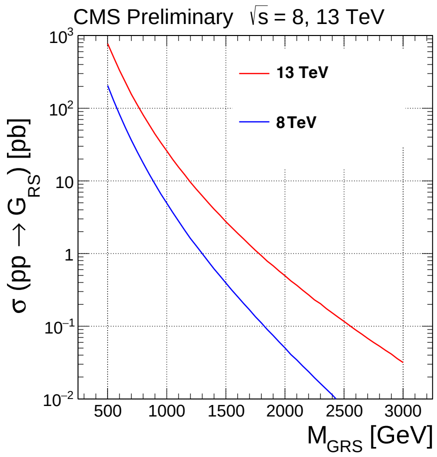

Figure 1.8: Cross-section of the process pp $\rightarrow$ G* at a center of mass energy of 8 and 13 TeV, in the original RS1 model, for $\tilde{k} = 0.1$.

Bulk graviton

The bulk graviton model [4, 5, 6] is an extension of the RS framework which proposes that the SM fields also propagate in the bulk. Phenomenologically, the main differences of the bulk graviton with respect to the original RS1 model are:

- the much smaller production cross-section, by a factor of 10^4
- the much larger branching fractions to WW, ZZ and hh channels
- the polarization of the produced W and Z bosons. Given the G* $\rightarrow ZZ$ process, the original RS1 graviton will decay to transverse polarized bosons 90% of the time, while the bulk graviton will decay to longitudinal polarized bosons more than 99% of the time. This leads to differences in the efficiency of the jet substructure techniques used for identifying the bosons (see section 2.4).

Direct searches of bulk gravitons with LHC data are presented in chapter 6.

1.6.3 Heavy vector triplet (HVT) model

HVT generalises a large number of explicit models, such as Composite Higgs [39, 40, 41], Little Higgs [42, 43] or Sequential Standard Model (SSM) [44], predicting spin-1 resonances. A convenient parameterisation of the HVT couplings was proposed in [7], which considers a real vector $V_\mu^a, a = 1, 2, 3$ in addition to the SM fields and interactions. This vector describes one charged and one neutral heavy spin-one particle with the charge eigenstate defined by the relation

$$V^{\pm}{}_\mu = \frac{1}{\sqrt{2}}[V_\mu^1 \mp iV_\mu^2]$$

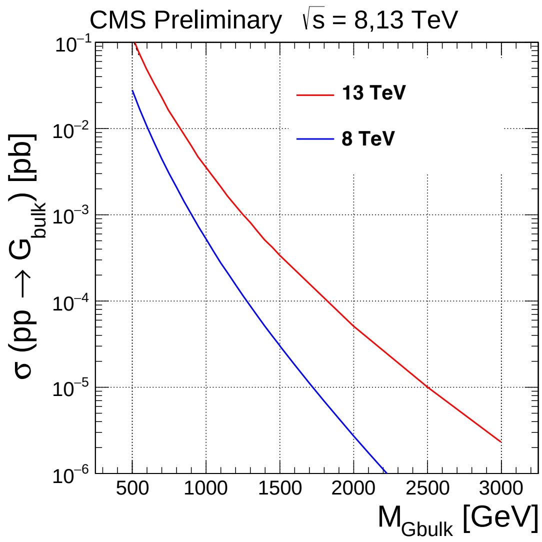

Figure 1.9: Cross-section of the process pp $\to$ G* at a center of mass energy of 8 and 13 TeV, in the bulk graviton model, for $\tilde{k} = 0.1$.

$$V^0_\mu = V^3_\mu$$

The dynamic of this new vector is described by the following Lagrangian:

$$\begin{aligned} L_V = &-\frac{1}{4}D_{[\mu}V^a_{\nu]}D^{[\mu}V^{\nu]a} + \frac{m_V^2}{2}V^a_\mu V^{\mu a} \\ &+ ig_V c_H V^a_\mu H^\dagger \tau^a \overleftrightarrow{D}^\mu H + \frac{g^2}{g_V}c_F V^a_\mu J^{\mu a}_F \\ &+ \frac{g_V}{2}c_{VVV}\epsilon_{abc}V^a_\mu V^b_\nu D^{[\mu}V^{\nu]c} + g_V^2 c_{VVHH}V^a_\mu V^{\mu a}H^\dagger H \quad -\frac{g}{2}c_{VVW}\epsilon_{abc}W^{\mu\nu a}V^b_\mu V^c_\nu \end{aligned} \tag{1.60}$$

The first line of the above equation contains the V kinetic and mass term, plus trilinear and quadrilinear interactions with the SM vector bosons from the covariant derivatives

$$D_{[\mu}V^a_{\nu]} = D_\mu V^a_\nu - D_\nu V^a_\mu$$

$$D_\mu V^a_\nu = \partial_\mu V^a_\nu + g\epsilon^{abc}W^b_\mu V^c_\nu$$

where g denotes the $SU(2)_L$ gauge coupling. The V^a_μ fields are not mass eigenstates, since they mix with W^a_μ after EWSB, so the parameter m_V does not coincide with the physical mass of the resonance.
The second line describes the interaction between the V and the Higgs current:

$$iH^\dagger\tau^a\overleftrightarrow{D}^\mu H = iH^\dagger\tau^a D^\mu H - iD^\mu H^\dagger\tau^a H$$

and with the SM left-handed fermionic currents

$$J^{\mu a}_F = \sum_f \bar{b}_L\gamma^\mu\tau^a f_L$$

where $\tau^a = \sigma^a/2$. The Higgs current term c_H leads to vertices involving the physical Higgs field and the three unphysical Goldstone bosons. By the Equivalence Theorem [45], the Goldstone bosons represent the longitudinally polarized SM vector bosons W and Z

in the high-energy regime. Thus c_H controls the V interactions with the SM vectors and with the Higgs boson, and in particular its decays into bosonic channels. Similarly, c_F describes the direct interaction with fermions, which is responsible for both the resonance production by Drell-Yan and for its fermionic decays.
Finally, the third line of Eq. 1.60 contains three new operators and free parameters, c_{VVV}, c_{VVHH} and c_{VVW} . None of them, however, contains vertices of one V with SM fields, thus they do not contribute directly to V decays and single production processes. They do affect the above processes only through the mixing of V with the W, but since the mixing is typically small their effect is marginal.
Therefore, to a first approximation the operators in the third line can be disregarded and the phenomenology described entirely by four parameters:

- c_H: describes the interactions involving the Higgs boson or longitudinally polarized SM vector bosons
- c_F: describes the direct interactions of the new resonance with fermions
- g_V: the typical strength of the new interaction
- M_V: mass of the new resonance

By scanning these parameters the generic Lagrangian describes a large class of models. Furthermore, the two couplings $g^2 c_F/g_V$ and $g_V c_H$ control all the relevant production rates and branching ratios in all the relevant channels.
Two benchmark models are also proposed in [7], called model A and model B. Model A predicts $g_V c_H \simeq g^2 c_F/g_V \simeq g^2/g_V$ thus resulting in comparable branching ratios into fermions and bosons. In model B, c_H is unsuppressed $g_V c_H \simeq -g_V$ $g^2 c_F/g_V \simeq g^2/g_V$ and the consequence is that fermionic decays are strongly suppressed, and the dominant branching ratios are into di-bosons.
Figure 1.10 shows the branching ratios for the two-body decays of the charged, W, and neutral resonance, Z', as a function of the resonance mass in Model B. As shown in the figure, the branching fractions of W' and Z' are expected to be of the same order of magnitude, since the charged and the neutral resonances are practically degenerate, with the W' boson mainly decaying into WZ and WH while the Z' boson into WW and ZH.
Figure 1.11 shows the production cross sections of the neutral and charged resonances as a function of the resonance in Model B. For comparison the predicted cross sections at both centre of mass energies of 8 TeV and 13 TeV are shown.
Searches which probe the HVT model using LHC data are presented in chapter 6.

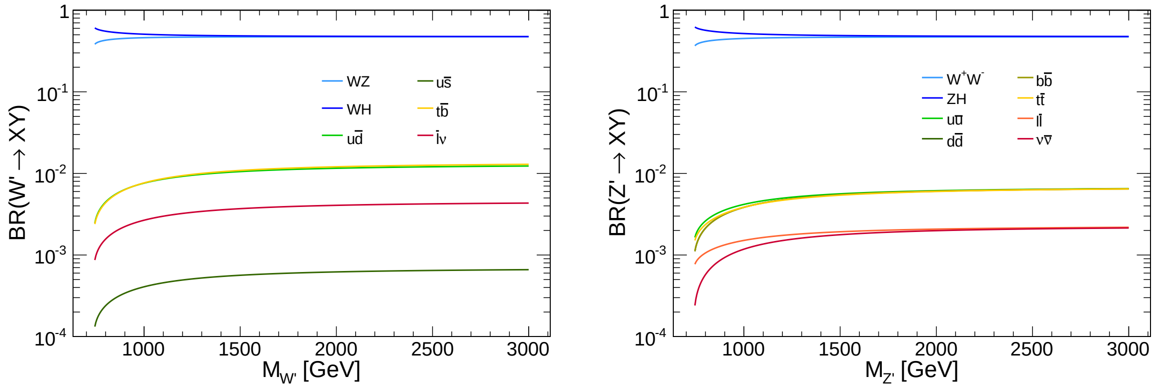

Figure 1.10: Branching Ratios for the two-body decays of the charged W' (left) and of the neutral resonance Z' (right) in the HVT Model B. The charged and the neutral resonances are practically degenerate.

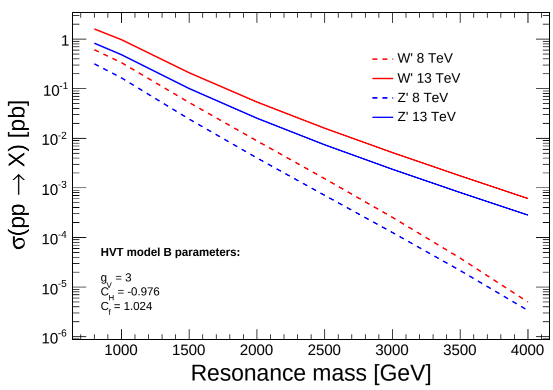

Figure 1.11: Production cross sections of the neutral and charged resonances as a function of the resonance mass in Model B. For comparison the predicted cross sections at centre of mass energies of 8 TeV and 13 TeV are shown.

Chapter 2

The LHC and the CMS Experiment

One of the main goals of the Large Hadron Collider was the discovery of the Higgs boson. However, despite the observation of the new resonance at 125 GeV, several open questions (described in section 1.6) of physics remain still open. It is therefore important to continue to search for phenomena beyond the SM. Hadron colliders are the most effective way to do that: the high center-of-mass energy and luminosity of these machines allow to probe higher parts of the energy spectrum. In this chapter, an overview of the Large Hadron Collider is given in section 2.1, together with the description of the CMS experiment with its sub-detectors in section 2.2. The description and reconstruction of the high-level physics objects used in the CMS analyses is presented in section 2.3. Finally, the algorithms used to improve the identification of boosted W and Z boson decays, are described in section 2.4. These techniques are extensively used in the analyses presented in chapter 5 and 6.

2.1 The Large Hadron Collider

The Large Hadron Collider (LHC) [46] is a proton-proton and heavy ions collider built by the European Organization for Nuclear Research (CERN) under the border between France and Switzerland, near Geneva. It consists of a 27 km ring, located 100 m underground, where two high-energy proton beams travel in opposite directions and collide at specific interaction points. LHC facilitates the investigation of the high-energy domain of particle physics with an accuracy never reached before, exploiting a nominal luminosity of $L = 10^{34}$ cm^{-2} s^{-1} and a center-of-mass energy of 14 TeV at full capacity, one order of magnitude higher than the previous generation of particle accelerators.

The beam is delivered to the LHC for its final acceleration by a multiple stage injection chain, shown in Figure 2.1.
Protons are firstly extracted from a bottle of hydrogen gas and accelerated up to 50 MeV by a linear machine (LINAC). Bunches of protons are then prepared and accelerated up to energies of 26 GeV in the Proton Synchrotron (PS), before being injected in the Super Proton Synchrotron (SPS), where they reach an energy of 450 GeV. Finally, they are injected into the main LHC ring, which consists of two adjacent parallel beamlines where the two beams travel in opposite directions. Eight radio-frequency resonant cavities which oscillate at 400 MHz accelerate the bunches to their final energy.
The beams are guided around the accelerator ring by a strong magnetic field provided by 1232 dipole magnets that keep the beams on their circular path, and by 392 quadrupole

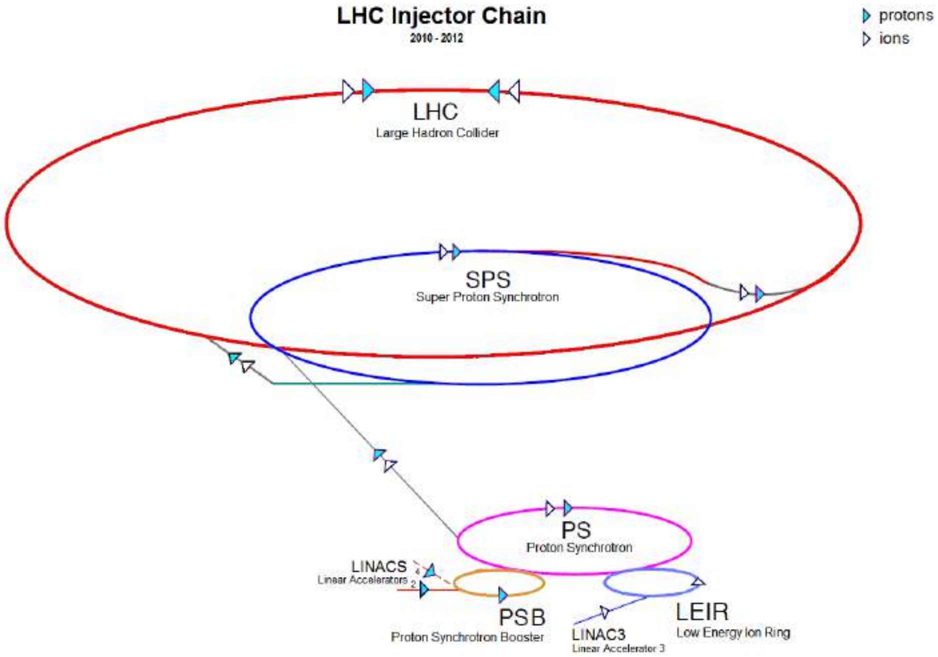

Figure 2.1: LHC injection scheme.

magnets that focus the beams in order to maximize the chances of interaction between the particles at the intersection points, where the two beams cross. The magnets are made of a Niobium-Titanium alloy and must work in a superconducting regime. Indeed, they are kept at a temperature of 1.9 K by means of superfluid Helium. At the design istantaneous luminosity, the beam is composed of approximately 3×10^3 bunches, each one containing 10^{11} protons, separated in time by 25 ns. The two beamlines intersect at four points around the ring, allowing collisions between the two beams. In these four points, the main experiments have been installed: CMS (Compact Muon Solenoid, [47]) and ATLAS (A Toroidal Lhc ApparatuS [48]), general purpose detectors hunting for the Higgs boson and looking for sign of new Physics; LHCb [49], investigating CP violation and B-physics; and ALICE (A Large Ion Colliding Experiment [50]), devoted to the investigation of high energy ion physics.

At the end of March 2010 the first collisions took place between beams of 3.5 TeV each, giving a total center-of-mass energy of 7 TeV (half of the nominal one). The same energy was kept for all the 2011 run, when a total integrated luminosity of 6.1 fb^{-1} was collected. In 2012 the energy of the beams was increased to 4 TeV each (8 TeV in the center of mass), delivering a total integrated luminosity of 20 fb^{-1} by the end of the year, and reaching a peak instantaneous luminosity of 7×10^{33} cm^{-2} s^{-1}. The 2011 and 2012 data taking is referred to as "Run I". During 2013 and 2014 several maintenance interventions have been performed to upgrade the machine, in order to reach an energy of 6.5 TeV per beam (13 TeV in the center-of-mass). This period is referred to as "Long-Shutdown 1" (LS1). LHC collisions restarted in spring 2015 at the new energy, delivering a total integrated luminosity of 4.2 fb^{-1} by the end of the year. The same beam energy has been kept for the whole 2016, collecting a total integrated luminosity of 41.1 fb^{-1} with a record peak instantaneous luminosity of 1.5×10^{34} cm^{-2} s^{-1}, surpassing the design luminosity. The 2015 and 2016 data taking is usually referred to as "Run II". The evolution of the integrated and the instantaneous luminosity versus time is shown in Figure 2.2 and 2.3, respectively.

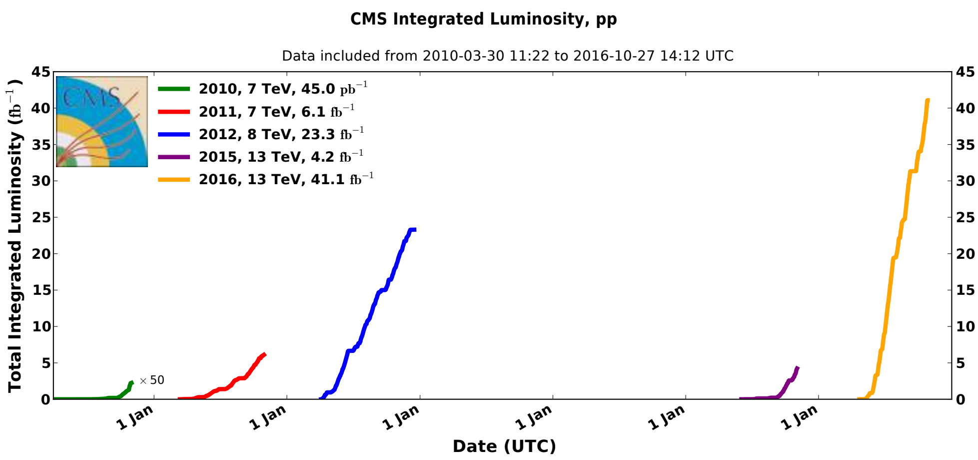

Figure 2.2: Evolution of the total integrated luminosity versus time from 2010 to 2016.

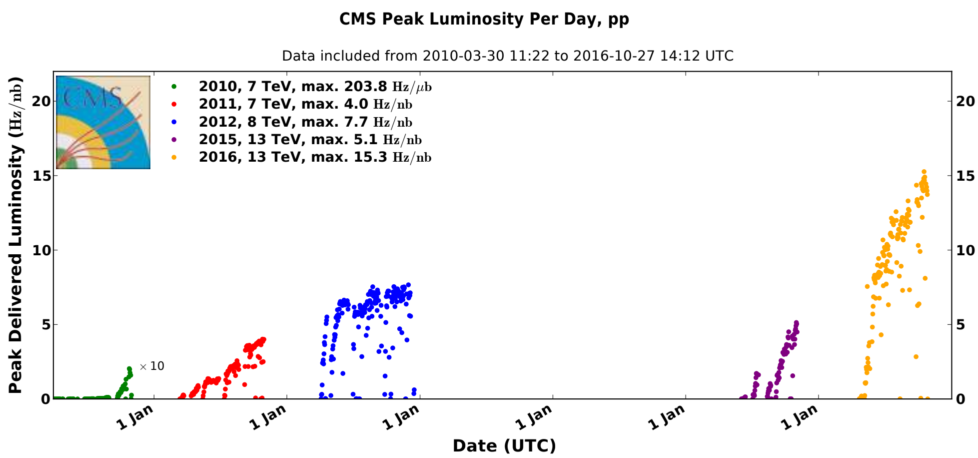

Figure 2.3: Evolution of the instantaneous luminosity versus time from 2010 to 2016.

2.2 The CMS experiment

The Compact Muon Solenoid [47] is a general purpose detector located at the interaction point number 5 along the LHC ring. It has an overall length of 22 m and a diameter of 15 m, with a cylindrical symmetry around the beam pipe; it consists of a sequence of subdetectors that allow the measurement of energy and momentum of all the particles generated in the collisions (except for the neutrinos). Starting from the inner one, the main subdetectors of CMS are the tracking system, the electromagnetic calorimeter (ECAL), the hadronic calorimeter (HCAL) and the muon chambers. The tracker and the two calorimeters are built inside a superconducting solenoid of 13 m length and 6 m diameter, giving the name “compact”, while the muon system is placed outside, embedded in an iron magnetic yoke that supports the structure and provides the return path for the 3.8 T magnetic field produced by the solenoid.
Every subdetector has been designed with a different function: the tracking system allows the reconstruction of the momentum particles and the interaction vertex; the two

calorimeters are designed to measure the energies of electrons and photons (ECAL) and hadrons (HCAL), while the muon system measures the muon momentum. Due to the huge collision frequency at the LHC, a trigger system is present as well, to reduce the output rate down to a substainible level. The system is based on two levels: a first hardware "Level-1 trigger" (L1), and a second software "High Level Trigger" (HLT), running on ordinary computer farms.

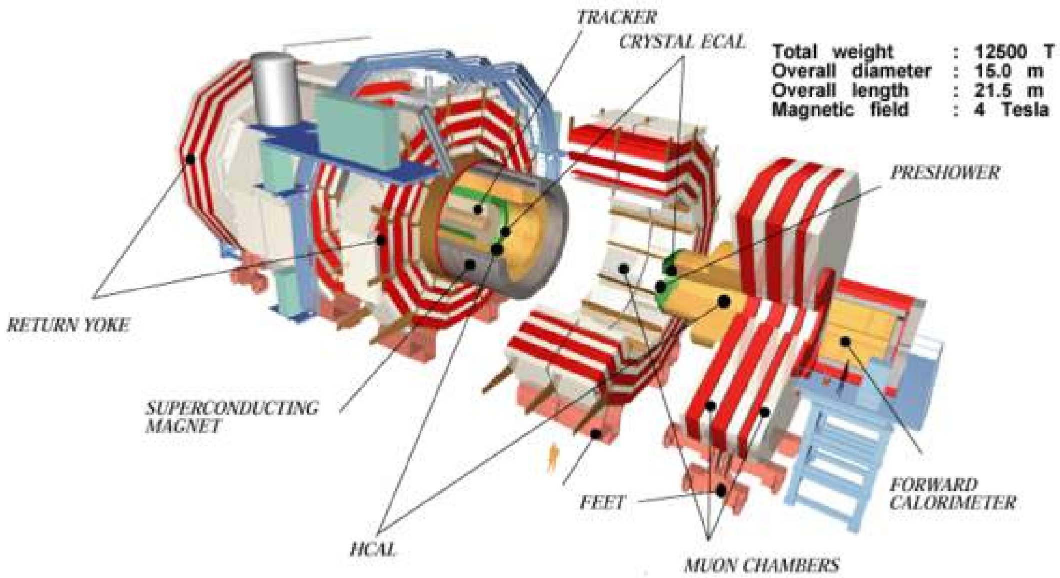

Figure 2.4: General view of the Compact Muon Solenoid experiment

In a typical proton-proton collision, the fractions of the parent proton momentum carried by the interacting partons are unknown, and the rest frame of the hard collision is boosted along the beam line with respect to the laboratory frame. The reconstruction of the boost of the system requires the full reconstruction of the remnants of the colliding protons, which is in practice not possible, because of the presence of the beam-pipe. Because of the unknown energy balance along the beam-line direction, proton collisions are usually studied in a convenient coordinate system which has been established such that the origin is centered at the nominal collision point inside the experiment, the z-direction is parallel to the beam line, the y-direction is vertical and the x-direction is horizontal, pointing toward the center of the ring. The azimuthal angle ϕ is measured around the beam line in the xy plane, starting from the x-axis, while the polar angle θ is measured from the z-axis. The polar angle is usually expressed in terms of the pseudorapidity η, defined by

$$\eta = -\log\left(\tan\frac{\theta}{2}\right)$$

The advantage of this coordinate frame is the Lorentz invariance of transverse quantities and differences in η, under Lorentz boosts along the beam-line. As a consequence, a solid angle in (η, ϕ) is also invariant under longitudinal boosts.
In the following, a more complete description of the CMS sub-apparatus is given.

2.2.1 Tracker

The tracker [51] is the innermost subdetector of CMS and it surrounds the interaction point, with a total length of 5.4 m and a diameter of 2.4 m. It consists of 1440 silicon pixel and 15148 silicon strip detector modules, divided into five main parts: the Tracker Outer Barrel (TOB), the Tracker Inner Barrel (TIB), the Tracker Inner Disks (TID), the Tracker End Caps (TEC), consisting of silicon strips; and the pixel detector (see Figure 2.5). The entire tracker covers the region of pseudorapidity $|\eta| < 2.5$, with a barrel-endcap transition region at $0.9 < |\eta| < 1.4$.

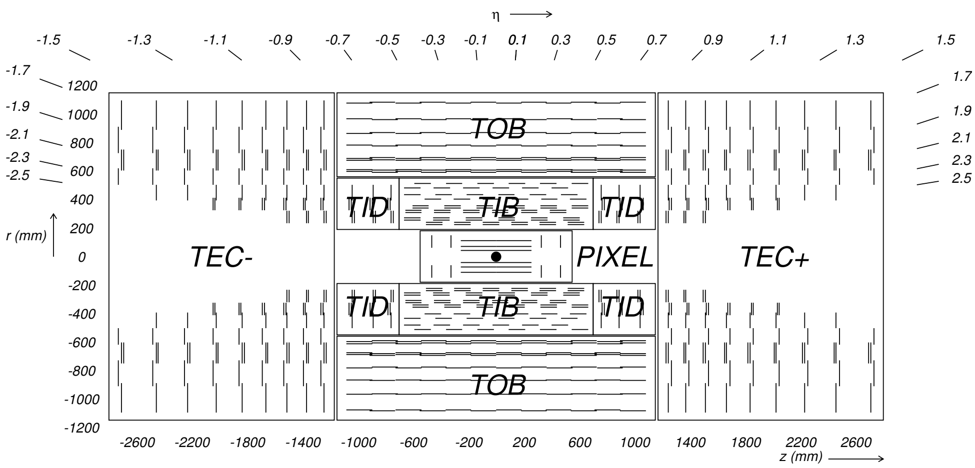

Figure 2.5: The different sub-systems of the silicon tracker.

At the LHC design luminosity, an average of about 1000 particles coming from more than 20 overlapping proton-proton interactions are present for each bunch crossing. Therefore, silicon was chosen as building material for the tracker, given its properties: high granularity and fast response, that are properties required to identify the right trajectories and attribute the correct bunch crossing, and radiation hardness, to avoid radiation damage to the system caused by the intense particle flux.
The tracker can reconstruct the paths of high-energy muons, electrons and charged hadrons as well as identify tracks coming from the decay of very short-lived particles, such as τ or b quarks. Given the strong magnetic field, charged particles have a curved trajectory with a curvature proportional to one over the momentum, $1/p$. A very high accuracy is required to locate the interaction point. For the pixel detector, the spatial resolution on a single hit is 10 μm for the (r,ϕ) coordinate and 15 μm for z in the barrel, while it is 15 μm and 20 μm respectively in the endcaps. For the silicon strip detectors, the resolution grows to 50 μm in (r,ϕ) and 500 μm along the z coordinate.

Particles in the tracker also lose energy, due to their interaction with the silicon, depending on the amount of material traversed. For the central region of the detector the radiation length is about 0.4 X_0, but this number increases rapidly when moving to forward regions, as can be seen in Figure 2.6. A maximum of 2 X_0 is found for the barrel-endcap transition region. The material budget constitutes the main source of error in accurate calorimetric measurements of electrons (which emit bremsstrahlung radiation) and photons (which convert into e^+e^- pairs).

2.2.2 ECAL

The purpose of the Electromagnetic CALorimeter [52] is the measurement of the particle energies, in particular electrons and photons. The ECAL is made of approximately 76000 lead tungstate ($PbWO_4$) crystals arranged into a barrel structure which covers the pseu-

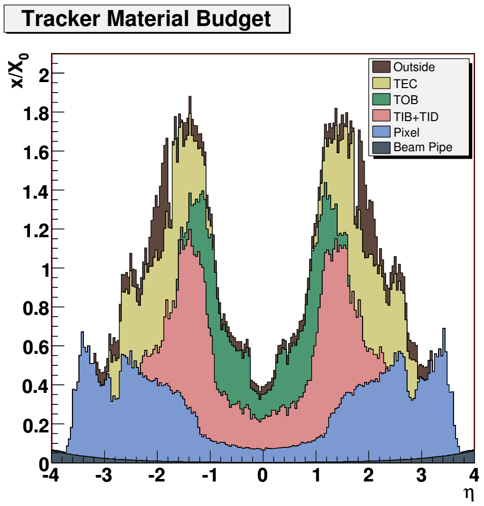

Figure 2.6: Tracker material budget as a function of the pseudorapidity in units of radiation length

dorapidity region $|\eta| < 1.479$ and two endcaps on both sides ($1.479 < |\eta| < 3$), as shown in Figure 2.7.

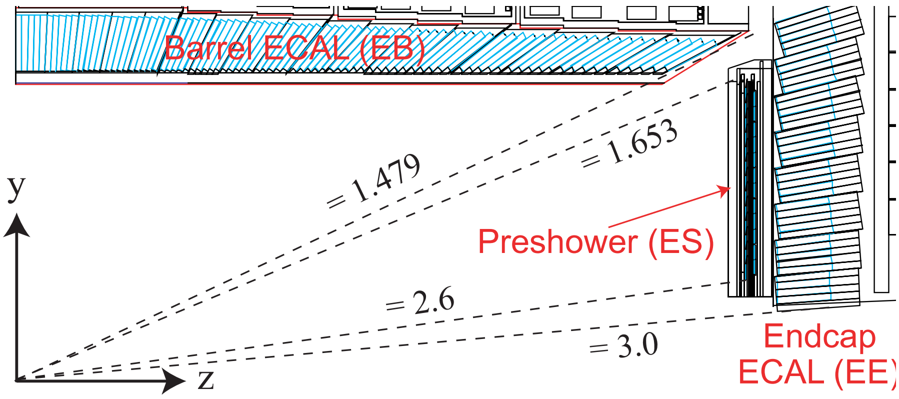

Figure 2.7: View in (r,z) of a quadrant of the ECAL

When a photon or electron traverses the crystals, an electromagnetic shower develops and every crystal emits an amount of light directly proportional to the energy released by the shower inside it. The description of the algorithms used to reconstruct the shower energy is discussed more in detailed in section 2.3.1 and chapter 3.2.

Lead tungstate has been chosen as scintillation material because of its radiation hardness, high density and fast response. The scintillation decay time is comparable with the LHC bunch crossing time: at the nominal rate of 40 MHz there is an interaction every 25 ns, which is the time required for a crystal to emit about 80 % of its scintillation light. However, $PbWO_4$ presents a low light-yield (from 50 to 80 γ/MeV) which makes it necessary to use intrinsic high-gain photodetectors, capable of operating in a high magnetic field. In the barrel region Avalanche PhotoDiodes (APDs) are used, while for the endcap crystals Vacuum PhotoTriodes (VPTs) are used. The ECAL barrel (EB) is made of 61200 crystals, arranged in a cylindrical shape with an inner radius of 1.29 m. Every crystal has a truncated pyramidal shape that points toward the interaction vertex, with a depth of 23 cm (corresponding to a radiation length of 25.8 X_0) and a front surface of about 22x22 mm^2. Crystals are grouped in arrays of 5x2 elements, called sub-modules, arranged in modules

of 400 or 500 crystals. 4 modules are assembled with metallic cross plates in between to form the biggest unit of the barrel part, the so-called supermodule. There are in total 36 supermodules, 18 for each side of the interaction point.
The two endcaps (EE) consist of identically shaped crystals having a larger front face of 29x29 mm^2 and a shorter length of 22 cm, corresponding to 25 X_0. They are grouped into carbon-fiber structures of 5x5 elements, called supercrystals. Each endcap is composed of a total of 7324 crystals, divided into 2 halves, or Dees.
A preshower (ES) is placed in front of EE crystals with the aim of providing position measurement of the electromagnetic shower to high accuracy and discriminating photons produced in a Higgs boson decay from photons produced in a π_0 decay. Thin lead radiators are used to initiate the shower; to measure the hit position of the shower, silicon strip sensors are used, placed beyond the radiators. The total material depth corresponds to about 3 X_0, covering the region $1.653 < |\eta| < 2.6$.

2.2.3 HCAL

The aim of the Hadron CALorimeter [51] is the measurement of charged and neutral hadrons, which produce jets of particles when they decay and interact with the CMS detector. In fact, when a hadron interacts with matter, an hadronic shower is developed by a sequence of inelastic scatterings, which produce a multi-particle final state. The HCAL is a sampling calorimeter: in this typology, alternating layers of “absorber” and fluorescent “scintillator” materials are used to measure particle energies. Hadrons interact with the absorber material, in this case brass or steel, producing many secondary particles which pass through the scintillator and the successive layers of absorber interacting again and producing an hadronic shower. When the particles of the shower pass through the scintillator material emits blue-violet light, that is collected using wavelength-shifting fibers (WLS). The WLS fibers shift the blue-violet light into green one, which is visible to the readout modules.
The general structure of HCAL consists of three main parts: an Hadron Barrel (HB and HO), an Hadron Endcap (HE) and a Very Forward calorimeter (HF), as shown in Figure 2.8.

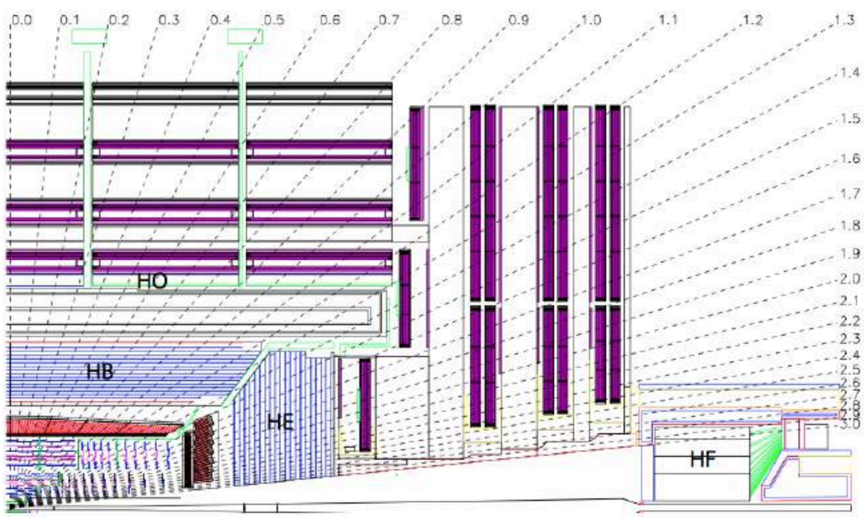

Figure 2.8: View in (r,z) of a quarter of the HCAL

The hadron calorimeter barrel is radially restricted between the outer extent of ECAL (r=1.77 m) and the inner extent of the magnet coil (r= 2.95 m), constraining the total amount of material which can be put in to absorb the hadronic showers. The total absorber thickness at $\eta = 0$ is 5.82 interaction lengths (λ_I). To complement the barrel calorimetry, an outer hadron calorimeter (HO) is placed outside the solenoid, increasing the interaction length to 10.6 λ_I. The endcap part extends until $|\eta| = 3$ while, beyond it, forward hadron calorimeters are placed at 11.2 m from the interaction point, extending the pseudorapidity coverage up to $|\eta| = 5$.
The barrel and the endcap parts are made of absorbing layers of brass and plastic scintillators, while the forward calorimeter is made of quartz fibers embedded in steel, with photomultipliers as readout detectors.
According to the test-beam results, the expected energy resolution for single pions interacting in the central part of the calorimeter is:

$$\frac{\sigma_E}{E} = \frac{94\%}{\sqrt{E}} \oplus 4.5\%$$

where the energy is measured in GeV. An important degradation of the resolution is expected at $|\eta| = 1.4$, due to the presence of services and cables. The performance of the very forward calorimeter is expected to be:

$$\frac{\sigma_E}{E_{em}} = \frac{100\%}{\sqrt{E_{em}}} \oplus 5\% \qquad\qquad \frac{\sigma_E}{E_{had}} = \frac{172\%}{\sqrt{E_{had}}} \oplus 9\%$$

where E_{em} and E_{had} refer to the energies of the electromagnetic and hadronic components of the shower, respectively.

2.2.4 Muon System

A muon detection system [53] is placed outside the magnetic coil, sustained by the iron return yoke of the magnet itself. For muons with energies of hundreds GeV or more, the tracker alone is not sufficient to measure their momentum with good precision, since the track curvature produced in the silicon strips is too small. The return magnetic field (with a value that goes from 1.8 T in the barrel region to 2.5 T in the endcaps) allows a complementary measurement of momentum and charge.
The system consists of four layers of muon chambers in the barrel part and four in the endcap region, each one providing track segments reconstruction from few distributed hits. These tracks are combined with the information coming from the tracker to form a complete muon track. A sketch of the muon system is represented in figure 2.9.

In the barrel part, the four layers of muon chambers follow the cylindrical geometry of CMS, arranged in such a way that a muon traverses at least three of them. They are segmented on the z coordinate by the 5 wheels of the yoke and divided in 12 sectors on the plane, covering the region from $|\eta| = 0$ to $|\eta| \sim 3$. Each chamber is made of 12 layers of Drift Tubes (DTs) grouped in 3 sub-units called superlayers. The CMS DTs are gaseous detectors consisting of a long aluminum cell filled with gas, with an anode wire in the center that collects ionization charges. Two of the superlayers have anode wires parallel to the beam line, providing a measurement of the r and ϕ coordinates; the third one is placed perpendicularly between the others and provides the z measurement. The spatial resolution of each chamber is 100 μm in the (r,ϕ) plane and 150 μm in the (r-z) plane.
The endcaps are composed of Cathode Strip Chambers (CSCs) that cover the pseudorapidity interval $0.9 < |\eta| < 2.4$. CSCs are multi-wire proportional chambers, with a

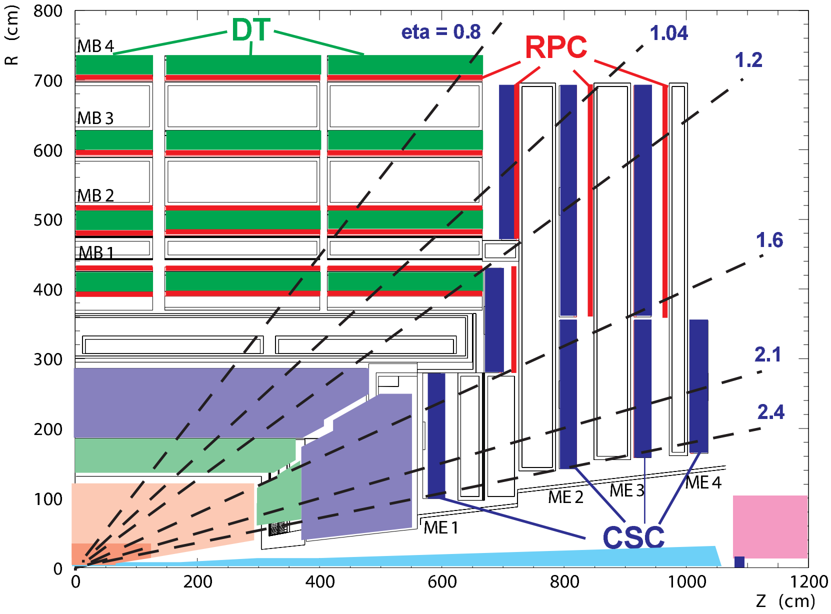

Figure 2.9: View in (r,z) of a quarter of the muon system

trapezoidal form which follows the endcap geometry. Inside the chambers each cathode plane is segmented into strips running across wires: when a muon crosses the chamber, the avalanche developed on a wire induces a charge on several strips of the cathode plane. Therefore, by detecting simultaneously the signal induced by the same particle on both wires and strips, two coordinates can be measured.
Resistive Plate Chambers (RPCs) are coupled to the barrel DTs and the CSCs of the endcaps. They are gaseous parallel-plate detectors made of bakelite and operating in avalanche mode. Their space resolution is poor, due to the large width of the strips in which each plane is segmented (from 2.3 to 4.1 cm), but they have an excellent time resolution (3 ns), allowing them to be used for triggering purposes and for the correct identification of the bunch crossing.

2.2.5 Trigger

At the nominal LHC luminosity, the expected event rate is about 10^9 Hz, too large to store all the collision events. Moreover, most of the events coming from the interaction point are not interesting, since they come from soft pp interactions. The trigger system [54] has the purpose of providing a large rate reduction factor, maintaining at the same time a high efficiency for potentially interesting events. Thanks to this system, the total output rate is reduced to about 10^4 Hz. It consists of a Level-1 (L1) Trigger, which consists of a hardware system with largely programmable electronics, and an High Level Trigger (HLT), which is a software system implemented in a farm of more than 1000 standard processors. The Level-1 Trigger is hardware-based and has been designed to analyze each 25 ns bunch crossing and take decisions in no more than 3.2 μs. Due to these short timescales, it employs only the calorimetric and muon informations, since the tracker algorithms are too slow for this purpose. Therefore, the L1 trigger is organized into a calorimeter and a muon trigger, whose information is transferred to the global trigger which takes the accept-reject decision. The calorimeter trigger is based on trigger towers, matrices of 5x5 ECAL crystals which match the granularity of the HCAL towers. The calorimeter trigger identifies the

best four candidates for each of the following classes: electrons and photons, central jets, forward jets and τ-jets. The information is then passed to the global trigger, together with the measured missing transverse energy ($\not{E}_T$), described in section 2.3.3. The muon trigger is performed separately for each muon detector. The information is then merged and the best four muon candidates are transferred to the global trigger. At the end, the rate of the selected events is reduced to about 100 kHz, and the accepted events are passed to be processed by the High Level Trigger.
The HLT software performs a first reconstruction of the entire event using information from different parts of the detector, and accept/reject events using three different virtual levels. The first one uses only the muon system and the calorimeters; in the second level, information coming from the tracker pixels are used, while the third one exploits the full event information. The High Level Trigger completes the reduction of the output rate down to about 1 kHz.

2.2.6 Superconducting magnet

The magnet is the central device around which the experiment is built, with a 4 T magnetic field. This field bends the path of the particles, allowing to measure their momentum: the more energetic the particle is, the smaller is the curvature, and vice-versa. The CMS magnet is a solenoid with a length of 13 m and a diameter of 6 m, and it is refrigerated by superconducting niobium-titanium coils [55].
The inductance of the magnet is 14 H and the nominal current for 4 T is 19500 A, giving a total stored energy of 2.66 GJ. There are dump circuits to safely dissipate this energy in the case of a magnet quench. The circuit resistance (essentially the cables from the power converter to the cryostat) has a value of 0.1 mΩ which leads to a circuit time constant of nearly 39 hours.
The tracker and calorimeter detectors (ECAL and HCAL) fit inside the magnet coil whilst the muon detectors are interleaved with a 12-sided iron structure that surrounds the magnet coils and contains and guides the field. Made up of three layers, this “return yoke” reaches out 14 metres in diameter. It also provides most of the experiment structural support.

2.3 Physics object reconstruction at CMS

An overview of the main physics objects used in CMS analyses is presented below.

2.3.1 Electrons

To first approximation, when a single electron reaches the ECAL surface, it starts an electromagnetic shower within the first few centimeters of the ECAL crystals and most of its energy is collected within a small matrix of crystals around the impact point. In general, the situation is much more complicated: electrons can loose part of their energy radiating photons by bremsstrahlung when traversing the tracker material. For electrons of low energy, the effect of the magnetic field is to enhance the bending of their trajectories, causing a spread of irradiated photons along the ϕ coordinate. Therefore, to obtain an accurate measurement of the electron energy in correspondence of the primary vertex, it is essential to collect bremsstrahlung photons.
In Run I, the so-called “standalone” approach was used, consisting of two clustering algorithms that were used in the ECAL barrel and endcap, respectively [56]. The ‘hybrid’

algorithm takes advantage of the fact that the crystals in the ECAL barrel are arranged in $\eta \times \phi$ geometry and that the shower is more spread out along ϕ due to the influence of the magnetic field. In the ECAL endcap, due to a different arrangement of the crystals, the 'multi 5×5' algorithm was used, which collects the energy deposit within clusters of 5×5 crystals around a crystal seed which are then grouped together into a supercluster if their total energy exceeds a certain threshold. In Run II, an alternative approach was used, that is part of the Particle Flow (PF) reconstruction algorithm described in section 2.3.3. In this approach, called 'mustache' clustering, clusters are reconstructed by grouping together all crystals contiguous to a seed crystal if their energy deposit is two standard deviations above the electronic noise. The requirement of a crystal to be taken as a seed is that its energy must be above these thresholds.

Once a supercluster is found, the following step is the track reconstruction. Under both $+1$ and -1 charge hypotheses, the supercluster energy and position are back-propagated in the magnetic field to the nominal vertex, to look for compatible hits in the pixel detector. Once a pair of compatible hits is found, an electron pre-track seed is built. Starting from seeds, compatible hits are searched for in the next available silicon layers. In this procedure, the probability of major energy losses due to bremsstrahlung emission has to be taken into account. Therefore, a dedicated algorithm has been developed, where the electron energy loss probability density function (PDF), well described by the Bethe-Heitler model [57], is approximated with a sum of Gaussian functions, in which different components model different degrees of hardness of the bremsstrahlung in the layer under consideration. This procedure, known as Gaussian Sum Filter (GSF) [58], is iterated until the last tracker layer, unless no hit is found in two subsequent layers. A minimum of five hits is finally required to create a track.

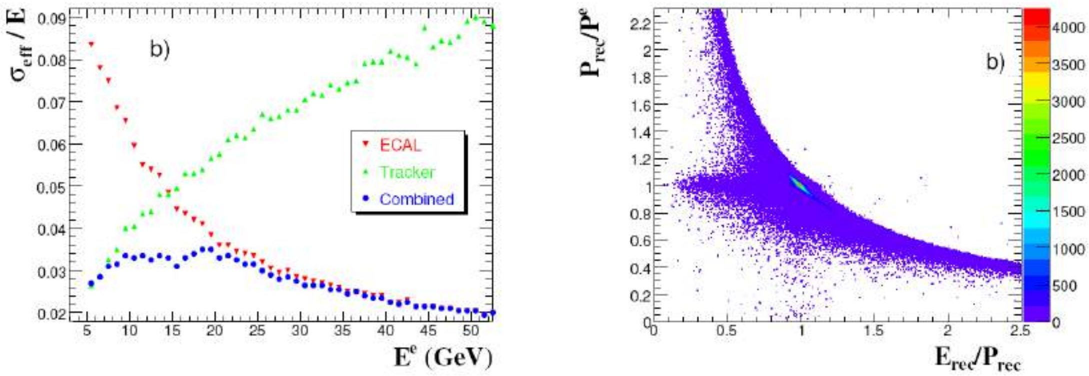

Figure 2.10: Left: fractional resolution (effective RMS) as a function of generated electron energy E^e measured with the ECAL supercluster (green arrows), the electron track (red arrows) and the combined track-supercluster (blue circles). Right: correlations between ECAL energy and tracker momentum measurements in the η range of the barrel [55].

In the final step, the supercluster and track information are merged. To improve the estimate of the electron momentum at the interaction vertex for low energy particles, the energy measurement E_{sc} provided by electromagnetic calorimeter and the tracker momentum measurement p_{tk} can be combined. The improvement comes from the opposite behavior of E of the intrinsic calorimetry and p of tracking resolutions, and from the fact that p_{tk} and E_{sc} are differently affected by the bremsstrahlung radiation (see Figure 2.10).

2.3.2 Muons

The standard muon reconstruction sequence is performed in three stages: a local reconstruction inside every muon subdetector, a standalone reconstruction in the muon chambers and a global reconstruction in the whole detector [55].
In the first step, local pattern recognition algorithms start from single hits and build track stubs separately in each subdetector (CSCs in the endcap and DTs in the barrel): the result is a three-dimensional segment associated with a single muon layer. In the second step, a track is propagated from the innermost layer to the outside, taking into account material effects and comparing the track with existing hits. A suitable χ^2 cut is applied to reject bad hits and the procedure is iterated until the outermost surface of the muon system is reached. In this step, the inclusion of RPC measurements helps in the reconstruction of low p_T muons and of those which escape through the module gaps, leaving only one fired DT station. The track is then extrapolated to the nominal interaction point and a vertex-constrained fit is performed. Due to the large amount of material traversed to reach the muon spectrometers, the momentum resolution as measured in the muon chambers is degraded by multiple scattering. In the last stage (global reconstruction), muon trajectories are extended up to the outermost layer of the tracker system (silicon strips + pixel). The compatibility between the muon track and the track parameters of the reconstructed silicon trajectories is checked on a χ^2 basis and, if the result is found in agreement, a global fit is performed with all the hits (tracker + muon).
Figure 2.11 shows how the additional information provided by the muon tracking system improves the momentum reconstruction of high-energy muons ($p \gtrsim 100$ GeV), for which the tracker-only momentum measurement degrades. For lower momenta, instead, the resolution of the tracking system dominates.

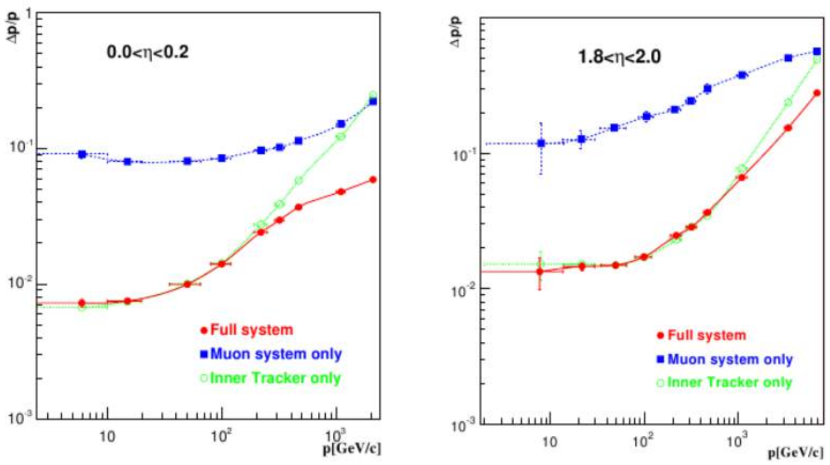

(a)

Figure 2.11: Muon momentum resolution versus p using the muon system only (blue), the inner tracker only (green) or the full system (red). Left: barrel, $|\eta| < 0.2$; right: endcap, $1.8 < |\eta| < 2$.

2.3.3 Jets and missing transverse energy: Particle Flow reconstruction

The Particle Flow (PF) is a whole-event reconstruction technique whose purpose is the reconstruction and identification of each particle produced in pp collisions with an optimized combination of all sub-detector information [59, 60]. In this process, the identification of

the particle type (photon, electron, muon, charged hadron, neutral hadron) plays an important role in the determination of the particle direction and energy.
While no substantial changes are expected for the reconstruction of high-energy electrons and muons, the Particle Flow significantly improves the resolution of jets and $\not{E}_T$ with respect to a standard, pure calorimetric jet reconstruction. Since only about the 15% of a jet energy is carried by neutral, long-lived hadrons (neutrons, Λ baryons, etc.), for the remaining 85% carried by charged particles the coarse HCAL information can be combined with the more precise tracker momentum measurements, thus allowing for a better jet reconstruction.

- Photons are identified as ECAL energy clusters not linked to the extrapolation of any charged particle trajectory to the ECAL. Their energy is directly obtained from the ECAL measurement.

- Electrons are identified as a primary charged particle track and ECAL energy clusters corresponding to this track extrapolation to the ECAL and to possible bremsstrahlung photons emitted along the way through the tracker material. Their energy is determined from a combination of the track momentum at the main interaction vertex, the corresponding ECAL cluster energy, and the energy sum of all bremsstrahlung photons attached to the track, as described in section 2.3.1.

- Muons are identified as a series of hits in the central tracker consistent with a track or several hits in the muon system, associated with an energy deficit in the calorimeters. Their energy is obtained from the corresponding track momentum, as described in section 2.3.2.

- Charged hadrons are identified as charged particle tracks that are not identified as electrons or muons; their energy is determined from a combination of the track momentum and the corresponding ECAL and HCAL energy.

- Neutral hadrons are identified as HCAL energy clusters not linked to any charged hadron trajectory, or as ECAL and HCAL energy excesses with respect to the expected charged hadron energy deposit. Their energy is obtained from the corresponding ECAL and HCAL energy.

The list of particles resulting from the operation of the PF algorithm on a whole event represents the best description of the event at the particle level, according to the information provided by the CMS detector and the intrinsic energy and position resolutions of the different sub-detectors. Figure 2.12 shows the composition of a typical minimum-bias event in terms of different particle types. In the central part of the detector, where the tracker allows for charge measurements, the largest fraction of an event energy is carried by charged hadrons ($\sim$ 65%). Only about 2% is carried by electrons, with neutral hadrons and photons almost equally sharing the remaining part. Outside the tracker acceptance, no distinction can be made between charged and neutral particles. Here, the vast majority of the event energy is carried by hadronic candidates, with purely electromagnetic objects contributing 10% or less.
The PF approach to the event reconstruction also allows for a natural definition of the "jet" object. Once well-isolated leptons and prompt photons are excluded from the particle list, all the remaining particles are clustered into jets, as further explained in the following paragraph. In this approach, jets and leptons are naturally disentangled, since the same energy deposits or tracker hits cannot contribute to the reconstruction of distinct objects.

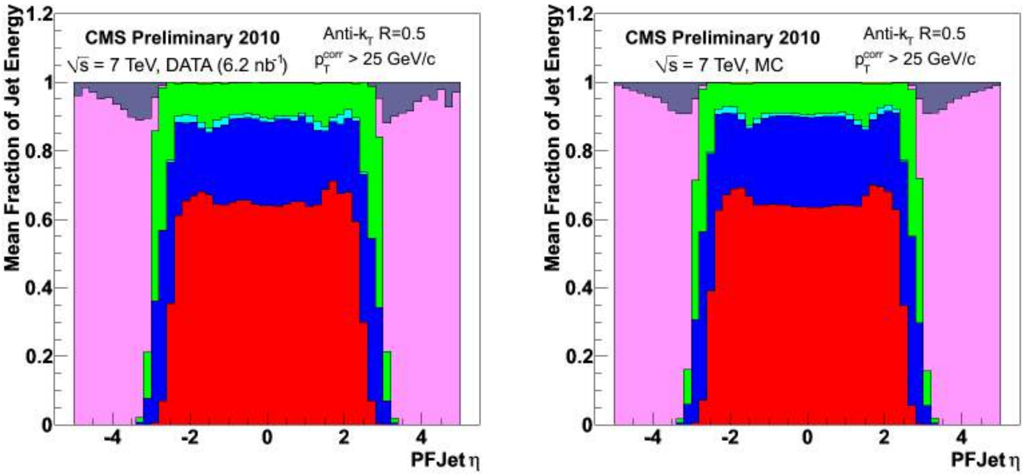

Figure 2.12: Reconstructed jet energy fractions as a function of pseudorapidity (a) in data (b) and in Monte Carlo. From bottom to top in the central region: charged hadrons (red), photons (blue), electrons (light blue), and neutral hadrons (green). In the forward regions: hadronic deposits (pink), electromagnetic deposits (grey).

Jets

The high-energy quarks and gluons emitted in hard proton-proton collisions do not appear in the detector. As they reach large distances from the proton relics, the strong force potential favors the radiation of softer or collinear gluons and quarks, until a point is reached where a non-perturbative transition causes the partons to combine into colorless hadrons. The result is a spray of more-or-less collimated particles, called jet, which, due to energy conservation, reflects at some level the energy and the flight direction of the initial parton.

Jets are detectable in modern experiments as a cluster of tracks and energy deposits in a defined region of the detector. Due to the intrinsic compositeness of such objects, jets are defined using algorithmic procedures to recombine different daughter particles into a single mother jet.
Given the infinite probability of a collinear or soft gluon to be emitted by a parton, jet algorithms must satisfy a few requirements, so that they can be used to provide finite theoretical predictions. The two conditions to be respected are the following:

- collinear safety: the result of the jet algorithm must not change if a particle of momentum p is substituted by two collinear particles of momentum $p/2$;

- infrared safety: the result of the jet algorithm must not change if a particle with $p \to 0$ is added (or subtracted) to the list of particles to be clustered.

Two main clustering algorithms have been widely used for the LHC phenomenology: the so-called anti-k_T [61] and the Cambridge-Aachen [62].

The anti-k_T algorithm proceeds via the definition of two distances for each particle i in the list of particles, namely

$$\begin{aligned} d_{ij} &= \min\left(\frac{1}{p_{Ti}^2}, \frac{1}{p_{Tj}^2}\right)\frac{\Delta R_{ij}^2}{R^2} \\ d_{iB} &= \frac{1}{p_{Ti}^2} \end{aligned} \tag{2.1}$$

In the above equation, d_{ij} can be interpreted as the "distance" between the particle i and a generic other particle j among those still to be clustered, while d_{iB} represents the "distance" between the particle i and the beam line. ΔR_{ij} is the distance between the two particles in the $\eta - \phi$ plane, while R is the algorithm radius parameter.
The algorithm determines, for each particle i, if there is another particle j such that d_{ij} is smaller than d_{iB}. If this happens, then particles i and j are recombined by adding together their four-momenta, otherwise the i particle is promoted to jet. The whole procedure is iterated and the algorithm stops when only jets are left.
It can be easily seen that particles at a distance greater than R from the jet axis are not clustered together with the jet itself, thus leading to the construction of cone-shaped jets. The standard radius parameter adopted in CMS during Run I, corresponding to the approximate jet size in the $\eta - \phi$ plane, is 0.5, giving the name "AK5 jet". In Run II, this parameter has been changed to 0.4 ('AK4 jets').

In the Cambridge-Aachen algorithms, the starting point is a table of N primary objects, which is the set of the particle four-momenta. It starts clustering the pair of particles with the smallest opening angle, using the ordering variable v_{ij} defined by

$$v_{ij} = 2(1 - \cos\theta_{ij})$$

where θij is the opening angle between particle i and j.
A test variable y_{ij} decides when the iterative procedure is stopped. The test variable is defined as

$$y_{ij} = \frac{2\min(E_i, E_j)}{E_{\text{vis}}^2}(1 - \cos\theta_{ij})$$

where E_i and E_j denote the energies of particle i and j and E_{vis} the visible energy.
The algorithm proceeds as follows:

- If only one object remains, store this as a jet and stop.
- Select the pair of objects i and j that have the minimal value for their ordering variable v_{ij}.
- Inspect the test variable y_{ij}; if $y_{ij} < y_{\text{cut}}$ (where y_{cut} is the resolution parameter) then combine i and j in a new object with four momentum $p_i + p_j$, and remove particles i and j from the table of objects that remain; if $y_{ij} \geq y_{\text{cut}}$ then store the object i or j with the smaller energy as a separated jet and remove it from the table. The higher energetic object remains in the table.

The jet momentum is defined as the vectorial sum of all particle momenta in it. Although important corrections are already applied at particle level during PF reconstruction, a set of further corrections have to be applied on reconstructed jets so that they can be used as high-level Physics objects. The jet correction scheme adopted in CMS is factorized into subsequent steps, each of them addressing a different physic aspect.

- Level 1 (offset) corrections: the purpose of this first step is to remove from the jet the additional energy coming from spurious particles produced in secondary pp interactions within the same bunch crossing or from the underlying events that randomly overlap with the jet area ("pileup"). This correction is determined both in data and in Monte Carlo on a event-by-event basis. First of all, the charged component of a jet within the tracker acceptance can be removed from the jet calculating the impact parameter of all jet particles: those which are not compatible with the event primary vertex are not considered in the jet clustering algorithm. To further remove the contribution of neutral particles, or to correct jets with $|\eta| > 2.4$, a different technique is used. All Particle Flow candidates are re-clustered implementing a different algorithm (the k_T algorithm) and after adding a large number of very soft "ghost" particles uniformly to the event. The median energy density ($\rho_{\mathrm{PU}} = E/\Delta\eta/\Delta\phi$) of the many pseudo-jets so produced is taken as the estimate of the pileup plus underlying event energy density for that event, and is subtracted from real jets, after being multiplied for the jet area (roughly πR^2) [63];
- Level 2 (relative) corrections: these corrections are meant to correct for non-uniformities in the different CMS sub-detectors by equalizing the jet response along η to the center of the barrel;
- Level 3 (absolute) corrections: this last correction factor correctly sets the jet absolute energy scale, and is derived from γ+jet events, where the event energy balance allows to compare the jet energy to the photon, precisely measured in ECAL.

Level 2 and 3 corrections are derived in simulated events and further checked on real data. Potential differences between data and Monte Carlo are accounted for with residual correction factors for jets in real data.
Figure 2.13 reports the jet energy resolution expected from the simulation and measured in data for PF jets reconstructed with an anti-k_T algorithm ($R = 0.5$) within the tracker acceptance.

Missing transverse energy

The missing transverse energy ($\not\!\!E_T$) is reconstructed through the particle flow algorithm, and it is defined as the negative vector sum of the transverse energy of all particle flow candidates in a given event:

$$\not\!\!E_T^{PF} = -\sum_{i}^{\text{PF-cand}} \vec{E_T^i} \tag{2.2}$$

In the hypothesis that all detectable particles are properly reconstructed, $\not\!\!E_T$ coincides with the vector sum of the transverse energy of all undetectable particles, and it is therefore the physics observable used as signature of invisible particles like neutrinos, or BSM particles such as neutralinos in more exotic scenarios. The jet energy corrections described in the previous section are propagated also to the missing transverse energy computation, to improve its resolution.

2.4 Jet substructure

In the hadronic decay of heavy objects such as W, Z, or Higgs bosons, the decay products are produced with a significant Lorentz boost, and thus are highly collimated and

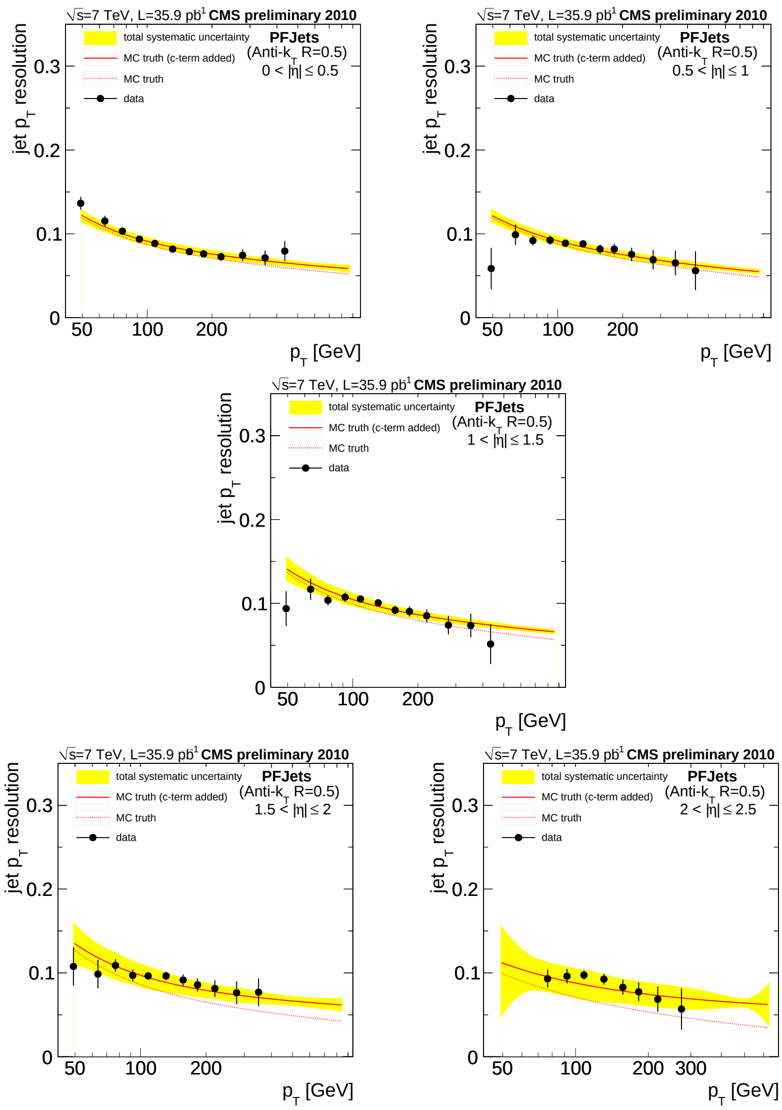

Figure 2.13: Data resolution measurements compared to the MC truth resolution before (red dashed line) and after (red solid line) corrections for the residual discrepancy between data and simulation for PF jets in different η ranges are applied.

reconstructed as a single jet in the detector. The typical variables used in analyses with jets are the jet direction and jet p_T. However, these are not sufficient in order to discriminate between jets from heavy object decays and jets produced from quarks and gluons. Several methods have been developed to exploit other jet information such as the spatial and the energy distribution of the constituents, and it is common to refer to them as "jet-substructure". In [64] and [65], studies of different substructure observables which improve the identification of heavy boson decays have been performed. Two of the most powerful observables are:

- The groomed jet mass, specifically using the pruning algorithm.
- The N-subjettiness variable τ_N.

In the following, these two variables are described. They are extensively used in the analyses presented in chapter 5 and 6.

Grooming

Jet grooming techniques are typically used to reduce the impact of underlying event (UE), pileup (PU) and soft QCD contributions to the jet. Several algorithms have been proposed and studied over the years. Among them, there are pruning [66], soft drop [67], filtering [66] and trimming [68].

- In pruning algorithms, the jet is reclustered using all the particles belonging to the original jet, ignoring in each recombination step the softer "protojet" if the recombination z_{ij} is softer than a given threshold $z_{\text{cut}} = 0.1$ or forms an angle ΔR_{ij} wider than $D_{\text{cut}} = \alpha \times \frac{m}{p_T}$ with respect to the previous recombination step, where $\alpha = 0.5$ and m and p_T are, respectively, the mass and the transverse momentum of the original jet. The hardness of the recombination z_{ij} is defined as:
$$z_{ij} = \frac{\min(p_{T,i}, p_{T,j})}{p_{T,(i+j)}} < z_{\text{cut}}$$
where $p_{T,i}$ and $p_{T,j}$ are the transverse momenta of the i and j protojets, while $p_{T,(i+j)}$ is the p_T of the combined jet. Then, the pruned jet mass is defined as the mass of the jet obtained using the pruning procedure.
The different distributions for the pruned jet mass for simulated samples of boosted W bosons and inclusive QCD jets are shown in Figure 2.14. It can be seen that the former shows a peak at m_W, while this is not the case for jets coming from quarks or gluons.
- Soft drop algorithms proceed instead in the opposite direction, declustering the original jet. Given a jet of radius R_0 with only two constituents, the soft drop procedure removes the softer constituent unless
$$\frac{min(p_{T1}, p_{T2})}{p_{T1} + p_{T2}} > z_{cut}(\frac{\Delta R_{12}}{R_0})^{\beta}$$
where p_{Ti} is the transverse momenta of the constituents with respect to the beam, ΔR_{12} is their distance in the rapidity-azimuth plane, z_{cut} is the soft drop threshold, and β is an angular exponent. By construction, this condition fails for wide-angle soft radiation, which is then discarded from the jet. Similarly to the pruned jet mass, the softdrop mass is defined as the mass of the jet obtained through the softdrop procedure.

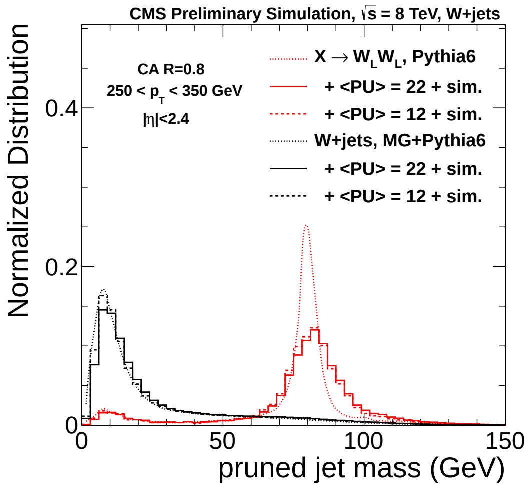

Figure 2.14: Pruned jet mass distribution in simulated samples of boosted W bosons (red) and inclusive QCD jets (black). MG denotes the Madgraph5 generator. Thick dashed lines represent the generator predictions without pileup interactions and without CMS simulation. The histograms are the distributions after CMS simulation with two different pileup scenarios corresponding to an average number of interactions of 12 and 22 respectively.

N-subjettiness

N-subjettiness τ_N was introduced in [69]. The first step of the procedure consists in identifying N subjets inside a given jet. These are selected by running the exclusive k_T algorithm, forcing it to return exactly N jets. Then, the N-subjettiness is defined as:

$$\tau_N = \frac{1}{d_0} \sum_k p_{T,k} \mathrm{min}\{\Delta R_{1,k}, \Delta R_{2,k}, ..., \Delta R_{N,k}\}$$

where k runs over all constituent particles. The normalization factor is $d_0 = \sum_k p_{T,k} R_0$ and R_0 is the original jet radius. The τ_N observable is a way to quantify to a certain degree how much a jet is likely to be composed of N subjets: the more it is close to zero, the more likely the jet is made of N subjets.

In particular, the ratio "2-subjettiness" over "1-subjettiness" (τ_2/τ_1) has excellent capability of separating jets coming from boosted vector bosons and jets coming from quarks and gluons. The τ_2/τ_1 distributions for simulated samples of boosted W bosons and inclusive QCD jets are shown in Figure 2.15. It can be seen that the two distributions have a different behavior, giving the possibility to discriminate jets from heavy boson decays from QCD jets.

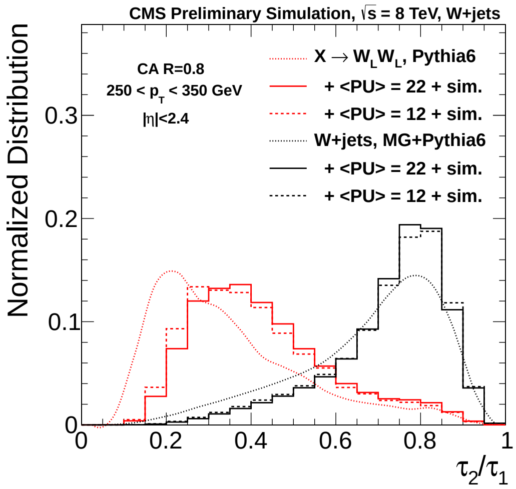

Figure 2.15: The n-subjettiness τ_2/τ_1 distribution in simulated samples of boosted W bosons (red) and inclusive QCD jets (black). MG denotes the Madgraph5 generator. Thick dashed lines represent the generator predictions without pileup interactions and without CMS simulation. The histograms are the distributions after CMS simulation with two different pileup scenarios corresponding to an average number of interactions of 12 and 22 respectively.

Chapter 3

Intercalibration of ECAL using electrons from W/Z bosons

The CMS experiment is designed to search for new physics at the TeV energy scale, with several searches involving the presence of electrons or photons in the final state.

One of the main channels which led to the discovery of the Higgs boson is the $H \rightarrow \gamma\gamma$ decay. One challenge of this channel is to reach an excellent resolution in the invariant di-photon mass, driven by the high resolution of the ECAL, which allows one to identify a narrow peak over an irreducible background with a falling spectrum.

Other examples are searches for heavy resonances decaying into diboson final states, described in chapter 5 and 6, where one of the V bosons decays leptonically, in the electron channel. The resolution on the diboson reconstructed invariant mass depends on many factors, one of them being the resolution on the electron energy, driven by ECAL.

In section 3.1, an overview of the techniques used to reconstruct photons and electrons in ECAL is given. In section 3.2, a description of the main methods used to calibrate the ECAL single channel response is presented. The second part of the chapter, starting from section 3.3, focuses on one of these methods, which uses high-energy electrons from W/Z boson decays for the calibration, presenting the event selection (section 3.3.1), the procedure used for the momentum calibration (section 3.3.2), several studies to improve the algorithm (section 3.3.3) and finally, showing the results with LHC Run II data in section 3.3.4. Furthermore, isolated electrons from W and Z decays are used not only for calibration purposes, but also as a good sample to study the stability of the channel response. The procedure is described in section 3.4, while the results with LHC Run II data are presented in section 3.4.1.

3.1 Electron and photon energy reconstruction

Electrons and photons deposit their energy over several ECAL crystals. Due to the combined effects of the CMS magnetic field and of the secondary interactions with the tracker material (bremsstrahlung or photon conversions), the energy deposits are spread along the azimuthal direction ϕ. A dynamic algorithm is used to merge clusters belonging to the same electromagnetic shower into superclusters (SC) [55], recovering the energy radiated via bremsstrahlung or photon conversions. The electron or photon energy is then estimated as follows:

$$E_{e/\gamma} = F_{e/\gamma} \cdot [G \cdot \sum_i S_i(t) C_i A_i] + E_{\mathrm{ES}} \tag{3.1}$$

where the sum is performed over the channels belonging to the cluster, and where:

- A_i represents the signal amplitude of the i-th channel measured in ADC counts.
- C_i are the inter-calibration coefficients used to equalize the channel-to-channel response.
- $S_i(t)$ corrects for the time variations of the channel response, mainly due to changes in the crystal transparency, discussed more in detail in section 3.4.
- G is a conversion factor from ADC To GeV.
- $F_{e/\gamma}$ includes corrections for imperfect clustering, material and geometry effects.
- E_{ES} is the energy measured in the preshower.

The effects of the supercluster procedure and of the corrections included in $F_{e/\gamma}$ are shown in Figure 3.1 using 2015 data. In the plot, the invariant mass of e^+e^- pairs in Z$\rightarrow$ e^+e^- events reconstructed using a fixed cluster of 5×5 crystals only, using the uncorrected supercluster energy (E_{raw}) and including also the $F_{e/\gamma}$ corrections ($E_{\mathrm{corrected}}$) are compared. The resolution is improved by using the supercluster algorithm and the $F_{e/\gamma}$ corrections.

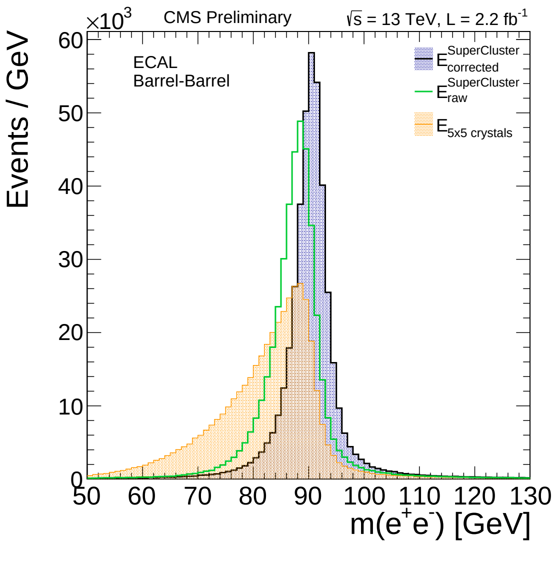

Figure 3.1: Invariant mass of e^+e^- pairs in Z$\rightarrow e^+e^-$ events with 2015 Run 2 ECAL data at B= 3.8 T, reconstructing the energy with different algorithms: using a fixed cluster of 5×5 crystals (orange), the uncorrected supercluster energy (E_{raw}, green) and including the $F_{e/\gamma}$ corrections ($E_{\mathrm{corrected}}$, black).

3.1.1 ECAL signal pulse reconstruction

The electrical signal coming from the photodetectors is amplified and shaped using a multi-gain preamplifier, which uses three parallel amplification stages. The output is digitized by a 12 bit ADC running at 40 MHz, which records a set of 10 consecutive samples, that are used to reconstruct the signal amplitude.

During LHC Run I a digital filtering algorithm was used, where the signal amplitude was estimated as the linear combination of the $N = 10$ samples S_i:

$$A = \sum_{i=1}^{N} w_i \times S_i \tag{3.2}$$

where the weights were calculated by minimizing the variance of A [70]. This method provides an optimal filtering of the electronics noise and of the fluctuations of the baseline, which are estimated event-by-event by using the average of the first three digitized pedestal-only samples, before the pulse shape of the signal develops. At the beginning of Run II, LHC started to run with more challenging pileup conditions, with an average of 40 collisions per bunch crossing during the highest intensity collisions in 2015. Furthermore, the spacing between two consecutive colliding bunches has been reduced from 50 to 25 ns, increasing the level of out-of-time pileup. To better deal with these new conditions, a new method, called "multi-fit", has been developed and used. This algorithm estimates the in-time signal amplitude and up to 9 out-of-time amplitudes by minimization of a χ^2:

$$\chi^2 = \sum_{i=1}^{N} \frac{\left(\sum_{j=1}^{M} A_j p_{ij} - S_i\right)^2}{\sigma_{S_i}^2} \tag{3.3}$$

where A_j are the amplitudes of up to $M = 10$ interactions. $\vec{p_j}$, the pulse templates of each bunch crossing j, have the same shape but are shifted in time by multiples of 25 ns within a range of -5 and +4 bunch crossings (BX) around the in-time signal (BX=0). The pulse templates for each crystal are measured using low pileup pp collision data. Dedicated runs with no colliding beams (called "pedestal runs") are used to measure S_i, the electronic noise and σ_{S_i}, its associated covariance matrix. The minimization of the χ^2 of eq. 3.3 is performed constraining the fitted amplitudes to be all positive.
Examples of one fit for signals in the barrel and in the endcaps are shown in Figure 3.2, for an average pileup of 20 and for 25 ns bunch spacing.
The new technique allowed an improvement in energy resolution with respect to the Run I reconstruction algorithm for collisions with 25 ns bunch spacing, especially for low p_T photons and electrons, which suffer more from the larger contribution of pileup to the total energy estimate.

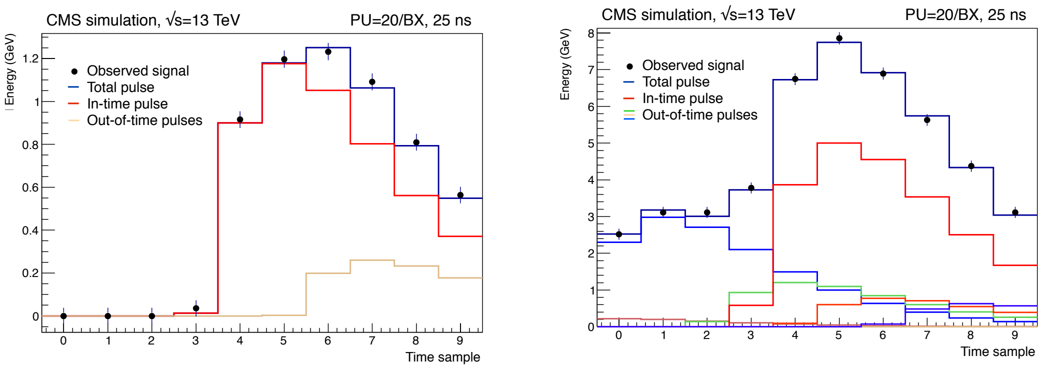

Figure 3.2: Example of fitted pulses for simulated events with 20 average pileup interactions and 25 ns bunch spacing, for a signal in the barrel (left) and in the endcap (right). Dots represent the 10 digitized samples, the red distributions (other light colors) represent the fitted in-time (out-of time) pulses with positive amplitude. The dark blue histograms represent the sum of all the fitted contributions.

3.2 ECAL calibration

The resolution for electrons in the ECAL barrel has been measured in test beams [71]:

$$\frac{\sigma_E}{E} = \frac{2.8\%}{\sqrt{E(GeV)}} \oplus \frac{12\%}{E(GeV)} \oplus 0.3\% \tag{3.4}$$

where the three terms represent, respectively:

- Stochastic term: includes the contributions from the shower containment, the number of photoelectrons and the fluctuations in the gain process.
- Noise term: accounts for all the effects of electronic noise which degrades the energy measurement. The value of 12% at 1 GeV corresponds to a single-channel noise of about 40 MeV.
- Constant term: includes several effects such as the non-uniformity of the longitudinal light collection, energy leakage from the back of the calorimeter, and the single-channel response uniformity and stability.

For electrons and photons in the range of interest of the analyses which target high-mass resonances, i.e. with energies of 100 GeV or more, the constant term becomes the dominant one. It is then of fundamental importance to keep this term under control. During CMS operation, the contributions to the resolution due to detector instabilities and to the channel-to-channel response spread must be kept to within 0.5%, in order to preserve the excellent resolution of the ECAL. The 'intercalibration constants' (IC), used to equalize the channel-to-channel response, must be measured with appropriate calibration procedures.
Three methods are used to measure intercalibration constants in ECAL:

- ϕ-symmetry is based on the expectation that, for a large sample of minimum bias events, the total deposited transverse energy should be the same in all crystals at the same pseudorapidity (same η ring in CMS). This method can provide a complete set of intercalibrations with a small amount of statistics, typically 100-500 nb^{-1}. The precision of this method is systematically limited to a few percent, due to the uncertainty in the knowledge of the material in front of ECAL. Since the systematic does not vary with time, the method can be used to track possible time dependencies of the IC values.
- Di-photon decays of π^0 and η mesons are used to intercalibrate channel response, by comparing the reconstructed diphoton invariant mass with the expected one. Also this method can provide intercalibration constants with a relatively short amount of statistics, due to the high production rate of π^0-η mesons. Its precision is limited by systematic effects due to dependences of the shower containment on the energy.
- E/p method: isolated electrons from W$\rightarrow$eν and Z$\rightarrow$ee decays are used to provide channel-to-channel calibrations, by comparing the electrons supercluster energy with their momentum measured by the tracker. Contrary to the previous methods, this needs a large amount of statistics, at least 10 fb^{-1}, due to the low production rate of W and Z bosons.

All these methods are used to intercalibrate channels placed at the same pseudorapidity (η-ring). The relative scale of the different η-ring is provided with an independent method, based on the comparison of the Z invariant mass distribution in Z$\rightarrow ee$ events in different η-rings.

3.3 The L3 calibration algorithm

The E/p method to intercalibrate the ECAL single channel response exploits an iterative algorithm developed to calibrate the electromagnetic calorimeter of the LEP L3 experiment. The main idea of the algorithm is to intercalibrate the ECAL channels using a sample of high-energetic and isolated electrons, by constraining their E_{sc}/p_{tk} ratio to be as close as possible to its physical target value $E/p \approx 1$. A key assumption of the method is that the electron momentum is measured without any bias. Therefore, any bias in the momentum measurement should be taken into account as a systematic effect after the calibration procedure. The inter-calibrations are calculated at each iterative step of the L3 algorithm, through the following formula:

$$ic_i^N(i\eta, i\phi) = ic_i^{N-1}(i\eta, i\phi) \times \frac{\sum_{j=1}^{N_e} \omega_{ij} \cdot f\left(\frac{E_{sc}}{p_{tk}}\right)\Big|_j \cdot \left(\frac{p_{tk}}{E_{sc}}\right)}{\sum_{j=1}^{N_e} \omega_{ij} \cdot f\left(\frac{E_{sc}}{p_{tk}}\right)\Big|_j} \tag{3.5}$$

where:

- N is the iteration index
- $ic_i(i\eta, i\phi)$ is the single crystal intercalibration coefficient, identified by a crystal index i that corresponds to specific coordinates $(i\eta, i\phi)$ in the barrel and (ix, iy) in the endcap.
- N_e is the total number of electrons used in the calibration procedure.
- ω_{ij} measures the fraction of energy carried by the crystal i, with respect to the total supercluster energy of the electron j:

$$\omega_{ij} = \frac{E_{ij}^{rechit}}{E_j^{SC}}$$

- $\frac{p_{tk}}{E_{sc}}{}_j$ is the ratio between the tracker momentum and the supercluster energy of the electron j.
- $f\left(\frac{E_{sc}}{p_{tk}}\right)$ is a weight, which expresses the probability of finding an electron with energy E_{sc} and momentum p_{tk} in a given η ring.

The algorithm is run independently for the barrel and for each endcap side (EE+ and EE-). The calibration is performed using the following procedure:

- Using all available electrons, the $\frac{E_{sc}}{p_{tk}}$ distributions are built for each η-ring, using the $i\eta$ value of the seed crystal (the crystal with the largest energy in the supercluster) as reference to assign an event to a specific ring. The supercluster energy is estimated, for each electron, summing over the energies of all the rechits:

$$E_j^{sc} = \left(\sum_{k=0}^{N_{hit}} E_{jk} \cdot ic_k(i\eta, i\phi)\right) \cdot F_e(\eta, p_T) \tag{3.6}$$

  where k is the rechit index, E_{jk} is the single crystal energy and $ic_k(i\eta, i\phi)$ is the corresponding intercalibration value. The final energy is then corrected by $F_e(\eta, p_T)$, which includes the corrections for imperfect clustering and material and geometry effects already introduced in section 3.1. In the calculation of E_{sc}, noisy or problematic channels are not considered.

- Once the $\frac{E_{sc}}{p_{tk}}$ distributions are obtained, they normalized such that their integral is 1, obtaining $f\left(\frac{E_{sc}}{p_{tk}}\right)$, and the intercalibration constants for each crystal are calculated through the formula 3.5, with the supercluster energy being estimated from the single crystal (rechits) energies using Eq. 3.6.
- After each iteration, the updated inter-calibration map $ic_i(i\eta, i\phi)$ is used to recalculate all the electron energies and re-build each E_{sc}/p_{tk} distribution.
- Finally, the procedure is repeated until convergence is reached. The convergence criteria is defined in the next section.

In the calibration procedure, not all the crystals are used. Crystals immediately close to dead ones or to dead Trigger Towers (TT) are skipped, and their intercalibration coefficients are set to zero. This means that regions of 3x3 clusters around dead crystals and of 7x7 clusters centered around dead TT are not calibrated with this method. The reason for such a choice is that the intercalibration value of crystals near dead ones is not reliable. In fact, an electron supercluster generally involves serveral crystals. If one of them is dead, the energy of the electron is underestimated and the calibration algorithm tries to compensate for this fact by increasing the intercalibration values of the other crystals involved in the supercluster. This effect is dramatic for the crystals located near dead ones or at the border of dead TT, for which the intercalibration coefficients become meaningless.

Convergence and statistical precision

The L3 algorithm follows an iterative procedure, where intercalibrations are re-calculated at each step. Therefore, it is necessary to define some convergence criterium to decide when to stop the algorithm. The level of convergence reached can be checked by looking at the variation of the constants with respect to the previous iteration. If the algorithm works properly, when the convergence is reached, this variation must be small. Quantitatively, at each iteration the distribution $ic_i^N - ic_i^{N-1}$ is built, using all the crystals used in the calibration procedure, and a Gaussian fit is performed to this distribution. The rms extracted from the fit quantifies the level of convergence. Generally, 15 iterations are sufficient in order to reach a level of convergence at the per-mille level, i.e. the spread of the distribution $ic_i^N - ic_i^{N-1}$ between two consecutive iterations is smaller than 0.1%.
Another important point that must be considered is the statistical precision of the method. This can be estimated by splitting the events in two sub-samples, containing odd and even events respectively, and running the calibration algorithm independently on the two sub-samples. At this point, one can define the following variable:

$$z = \frac{ic_{ev}(i\eta, i\phi) - ic_{odd}(i\eta, i\phi)}{ic_{ev}(i\eta, i\phi) + ic_{odd}(i\eta, i\phi)}$$

where $ic_{ev}(i\eta, i\phi)$ and $ic_{odd}(i\eta, i\phi)$ are the intercalibration coefficients obtained on the even and odd samples, respectively. In this variable, the systematic term cancels out in the subtraction $ic_{ev}(i\eta, i\phi) - ic_{odd}(i\eta, i\phi)$, leaving only the statistical part. The statistical precision can then be estimated through the rms σ_Z of the distribution of z in each η-ring, extracted via a Gaussian fit.

Normalization of the intercalibration constants

The outcome of the algorithm, after convergence is reached, are the intercalibration values for each crystal in the barrel and in the endcap. These intercalibration coefficients are rescaled by convention such that the mean value of the IC in the same η-ring is 1.0. This method therefore provides only a relative calibration along the ϕ direction, not along η.

3.3.1 Event selection

The calibration results presented here are based on proton-proton collision data at $\sqrt{s} =$ 13 TeV collected by the CMS experiment at the LHC during 2015 and corresponding to an integrated luminosity of 2.3 fb^{-1}.

Online selections

The datasets used are collected with triggers requiring either one electron (SingleElectron path) or two electrons (DoubleEG path). Different online selections are applied in the two cases. In the SingleElectron trigger, events are selected if they have one electron with $p_T > 27$ GeV which passes isolation requirements. In the DoubleEG trigger, events are required to have two electrons: the leading electron should have $p_T > 17$ GeV, the second one should have $p_T > 12$ GeV. Additional selections are applied on the cluster shape, on the isolation and on the matching between supercluster position and electron track.

Offline selections

Further selections are then applied at offline level. Events from W→ $e\nu$ decays are selected requiring:

- Exactly one electron with $E_T > 30$ GeV, and satisfying tight ID criteria (described in Tab. 3.1)
- The electron must lie within the tracker acceptance, i.e. should have $|\eta| < 2.5$
- A veto on the presence of additional electrons which satisfy loose ID criteria (described in Tab. 3.1) is applied
- Large missing energy due to the presence of the undetected neutrino: events are required to have $\not{E}_T > 25$ GeV
- Large W transverse mass, which is defined as $m_T = \sqrt{(2\not{E}_T E_T^e) \cdot (1 - cos\Delta\phi)}$. It is required that $m_T > 50$ GeV.

Events from Z→ ee are selected requiring:

- Two electrons, both satisfying loose ID criteria (described in Tab. 3.1). In case of more than two electrons, the pair of electrons with highest p_T is used
- A cut on the dielectron invariant mass: $m_{ee} > 55$ GeV

Tab. 3.1 summarizes the selections included in the electron loose and tight ID.
The variable listed in Tab. 3.1 are defined as follows:

- H/E: the ratio between the energy deposited in the HCAL and in the ECAL
- $\Delta\eta_{in}$: the difference in η between the track extrapolated position to the ECAL surface and the super-cluster position
- $\Delta\phi_{in}$: the difference in ϕ between the track extrapolated position to the ECAL surface and the super-cluster position

Variable	Loose ID	Tight ID
H/E <	0.104 (0.0897)	0.0597 (0.0615)
$\Delta\eta_{in}$ <	0.0105 (0.00814)	0.00926 (0.00724)
$\Delta\phi_{in}$ <	0.115 (0.182)	0.0336 (0.0918)
$\sigma_{i\eta i\eta}$ <	0.0103 (0.0301)	0.0101 (0.0279)
d_0 <	0.0261 (0.118)	0.0111 (0.0351)
d_z <	0.41 (0.822)	0.0466 (0.417)
Isolation <	0.0893 (0.121)	0.0354 (0.0646)
Expected missing inner hits <	2 (1)	2 (1)
Conversion veto	yes (yes)	yes (yes)

Table 3.1: Values of the cuts used on each variable in the loose and tight electron ID, in the barrel. The values in parentheses are for the endcap.

- $\sigma_{i\eta i\eta}$: the weighted energy cluster covariance, calculated along η using a 5×5 matrix centered in the position of the seed
- d_0: the transverse impact parameter of the electron track with respect to the selected primary vertex
- d_z: the longitudinal impact parameter of the electron track with respect to the selected primary vertex
- Isolation: the electron is required to be isolated simultaneously in the ECAL and in the HCAL. The isolation parameter is defined as:

  $$I = (I_n + I_{ch})/p_T$$

  where I_n is the neutral isolation, defined as $I_n = \max(0, I_{nh} + I_{em} - \rho \cdot A_{\text{eff}})$ with I_{nh} being the E_T sum of neutral hadrons, I_{em} the E_T sum of photons, ρ the average neutral particle energy density of the event and A_{eff} is the electron effective area, defined as a different number depending on the η region, while I_{ch} is the p_T sum of the charged hadrons in the event
- Expected missing inner hits: the number of inner tracker layers with no hits
- Conversion veto: the events in which an electron track is closed to another one, compatible with a photon conversion, are discarded. This condition is checked by imposing $|\text{dcot}| = |\Delta\text{cot}\theta| < 0.02$ and $|\text{dist}| < 0.02$, which are the distances between the two tracks in the longitudinal and in the transverse plane, respectively.

3.3.2 Momentum scale calibration

As stated in section 3.3, the basic assumption of the E/p method is that the tracker momentum measurement of the electron is unbiased. However, this is not perfectly true. This can be verified by looking at simulated data. For this purpose, a sample of W+jets is used, selecting events of W$\rightarrow e\nu$ by applying the same selections described in section 3.3.1. The calibration algorithm is run on these events, and the maps of the intercalibration coefficients obtained are shown in Figure 3.3.
It can be seen that a systematic effect is present, with periodic ϕ structures. This systematic effect is known and it is related to inaccuracies in the momentum measurement. The calibration algorithm is then run again on the simulation, but this time the ratio $\frac{E_{sc}}{p_{tk}}$

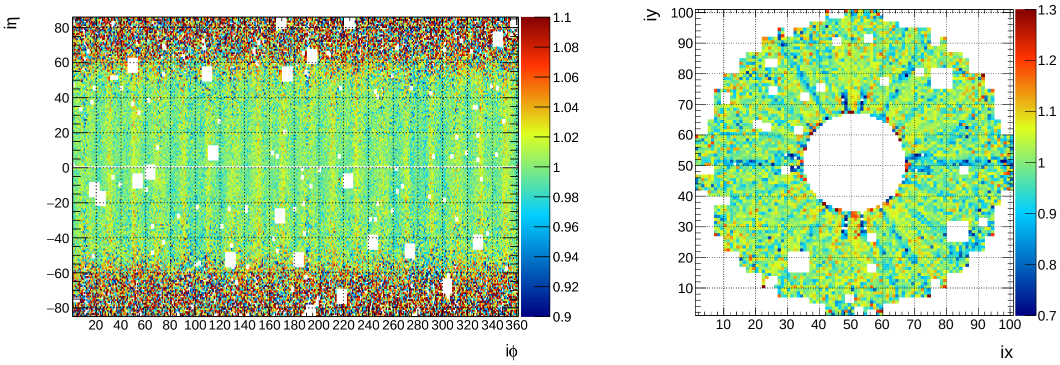

Figure 3.3: Maps of intercalibrations obtained running the algorithm on simulation. Left: EB, right: EE+.

in Eq. 3.5 is replaced by $\frac{E_{sc}}{E_{true}}$, where E_{true} is the true energy of the electron. In this way, no information on the tracker momentum is used in the calibration. The results of this test are shown in Figure 3.4, where the intercalibration constant maps are shown. As it can be observed, the effect is significantly reduced, and the values of the coefficients are uniform in ϕ.

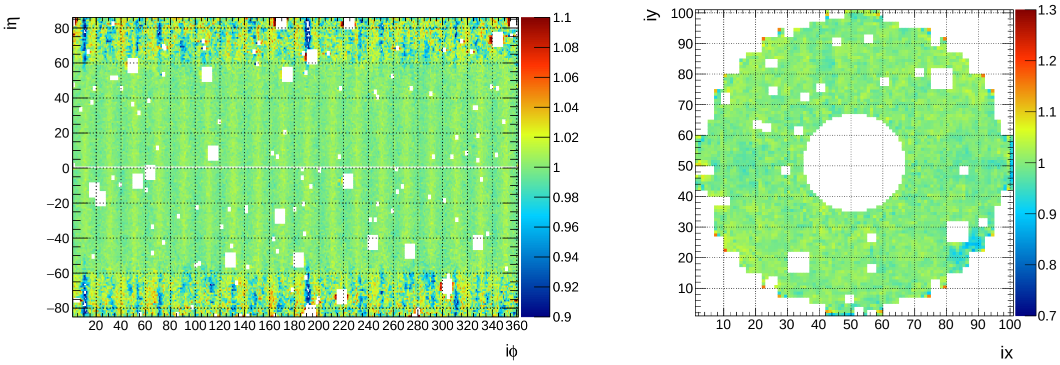

Figure 3.4: Maps of intercalibrations obtained running the algorithm on simulation, using $\frac{E_{sc}}{E_{true}}$ instead of $\frac{E_{sc}}{p_{tk}}$ in the calibration. Left: EB, right: EE+.

This proves effectively that the periodic ϕ structures are related to the momentum measurement; most likely they are related to the tracker structure modularity.
An accurate calibration of the momentum scale versus ϕ is therefore needed. For this purpose, Z$\rightarrow ee$ candidates are considered, assigning each event to a precise ϕ bin depending on the coordinate of the supercluster seed of the electron. A given event is therefore used twice, considering alternatively both electrons in their proper ϕ position. Then, the distribution of the dielectron invariant mass is built in each ϕ bin, using the momentum tracker p_{tk} for one electron and the supecluster energy of the other electron:

$$m_{ee}^2 = 4 \cdot E_{sc} \cdot p_{tk}(i\phi) \cdot \sin^2\theta/2$$

where $i\phi$ is the azimuthal index, which identify all the events with one electron whose seed lies in the $i\phi$ bin, while θ is the polar angle between the electron and the positron track.
A scale calibration factor for the momentum is then extracted from the relative m_{ee}^2/m_Z^2 scale, which is proportional to p_{tk}, using data. The following method is used:

- A reference distribution (referred to as "template") of m_{ee}^2/m_Z^2 is built using all the available events, integrating over all $i\eta$ and $i\phi$ bins. Two templates are created, one for the barrel, and one for the endcap.

- m_{ee}^2/m_Z^2 distributions are built for each $i\phi$ bin, using only electrons whose seed falls in that bin.

- Each distribution is fitted using a scaled version of the template, defined as follows:

$$f(x,k) = N \cdot k \cdot F(kx)$$

  where $x = m_{ee}^2/m_Z^2$, N is the number of events in the ϕ-bin considered, and k is a factor which tells how much the original template distribution $F(x)$ is drifting and scaling to fit the data in the subset of events considered.

The results of this procedure are shown in Figure 3.5, where the relative m_{ee}^2/m_Z^2 scale (proportional to the p_{tk} scale) is plotted versus ϕ for the barrel and for the endcap. It can be noticed that a modularity versus ϕ is clearly present, especially in the endcap. This scale factor is then used to correct the tracker momentum in the calibration. The algorithm is re-run, and for each electron, p_{tk} is divided by the relative scale of the corresponding ϕ-bin.

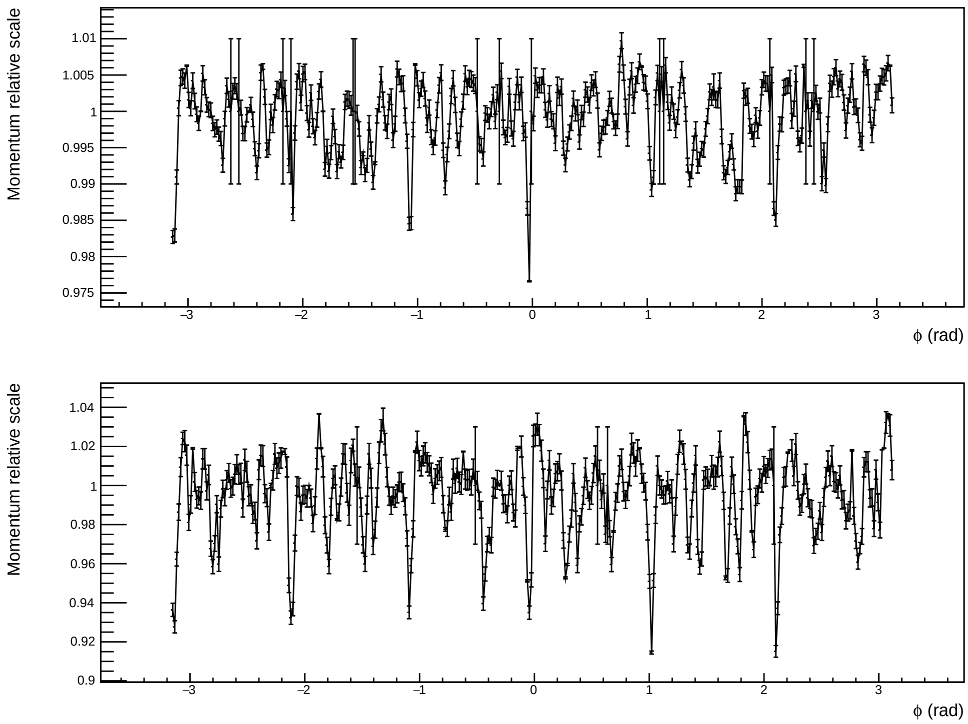

Figure 3.5: Relative momentum scale as a function of ϕ. Top: Barrel, bottom: endcap.

The final results are shown in Figure 3.6, where the intercalibration maps obtained in data after the momentum calibration are presented. Although the periodic ϕ structures are less evident, the modularity has not completely disappeared. In order to further correct this systematic effect, an additional selection is applied, which is described in the next section.

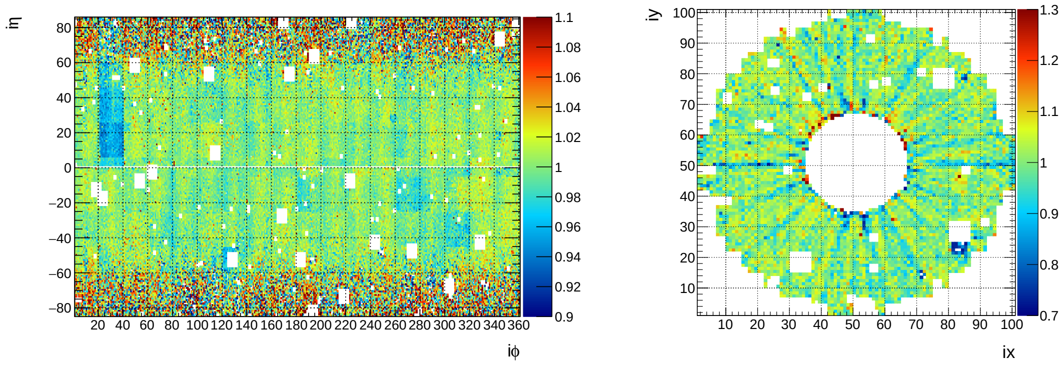

Figure 3.6: Maps of intercalibrations obtained running the algorithm on 2015 data, after applying the momentum scale correction. Left: EB, right: EE+.

3.3.3 Dynamic selection on E/p

The results of the calibration procedure depend crucially on the momentum measurement precision. This is strictly related to the shape of the E_{sc}/p_{tk} distribution: electrons with $E_{sc}/p_{tk} \approx 1$ have in general (supposing there are no large miscalibrations in the crystals) a well-measured momentum. On the contrary, when the quality of the momentum measurement is poor, the E_{sc}/p_{tk} ratio is generally far from 1. This situation is typical for electrons located in the tails of the E_{sc}/p_{tk} distribution. It is therefore possible to improve the accuracy of the calibration by selecting only events in the core of the E_{sc}/p_{tk} distribution, i.e. electrons with a well-measured momentum. Furthermore, the periodic ϕ structures described in the previous section seem to be related to electrons in the tails of the E_{sc}/p_{tk} distribution. In fact, as it can be seen in Figure 3.7, the effect mostly disappears when applying a selection on E_{sc}/p_{tk} in the calibration procedure. The same effect is observed in data and in the simulation as well.

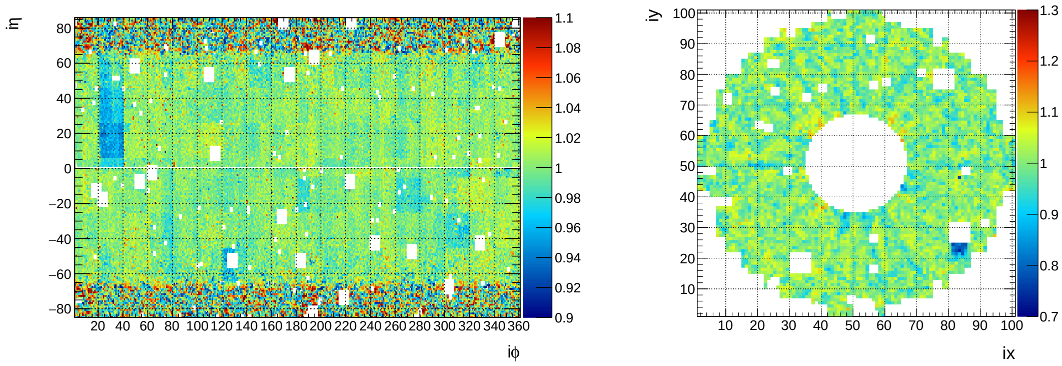

Figure 3.7: Maps of intercalibrations obtained running the algorithm on 2015 data, after applying a selection on E_{sc}/p_{tk} in the calibration. Left: EB, right: EE+.

However, the drawback here is the loss in statistics, which can results in a loss of statistical precision. Another potential issue can arise from the fact that when applying a E/p selection, a limit is also implicitly imposed on the values of IC that can be derived, because the E/p ratio is not allowed to be too far from 1. This can be a problem especially when there are crystals that are initially largely miscalibrated, i.e. their intercalibration value is far from 1, where the results of the calibration can be biased.
In order to assess the real effects of an E/p selection on the calibration, several studies

have been performed on data and simulation.
A first study has been performed using a Monte Carlo simulation of $Z \to ee$ events. The procedure is the following:

- An initial miscalibration of 30% is applied on crystals located at various ϕ regions: this means that the true intercalibration value (IC_{true}, that is available in the simulation) of a specific crystal is incremented or decremented by 30%. This is done to study the effect of the E/p selection also on largely miscalibrated crystals. The map with the initial intercalibration coefficients after applying the miscalibration is shown in Figure 3.8.

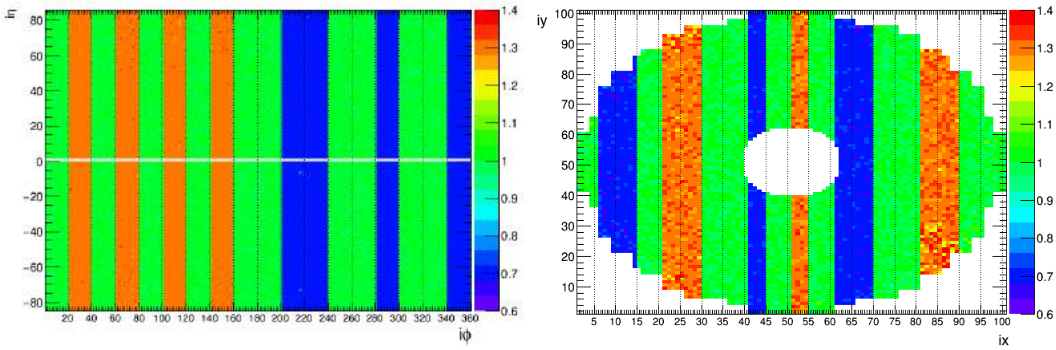

Figure 3.8: Maps of IC_{true} in the simulation, after applying a 30% miscalibration in some ϕ regions. Left: EB, right: EE+.

- The calibration algorithm is run applying a cut on the E/p ratio of the electrons, i.e. selecting only electrons whose E_{sc}/p_{tk} ratio is sufficiently close to 1. Technically, this is done by changing the distribution $f\left(\frac{E_{sc}}{p_{tk}}\right)$ used in Eq. 3.5 as follows:

$$f\left(\frac{E_{sc}}{p_{tk}}\right) = \begin{cases} f\left(\frac{E_{sc}}{p_{tk}}\right) & \text{if } |E_{sc}/p_{tk} - 1| < \beta \\ 0 & \text{otherwise} \end{cases} \tag{3.7}$$

  where β gives the size of the E/p window where electrons are accepted. Several values of β have been tested: 0.05, 0.07, 0.10, 0.15, 0.20, 0.30, 0.50. A calibration with the normal algorithm, without applying any E/p selection, has also been run as reference.

- The cut applied in Eq. 3.7 is dynamic, this means that it is re-applied at each iteration of the algorithm, in order to take into account variations in the electron energy related to the updated intercalibrations.

The results are compared by looking at the spread between the intercalibration coefficients derived with the algoritm and the true intercalibration values of the crystals (after applying the miscalibration). This is done in different pseudorapidity regions: in the barrel, four regions are defined using $i\phi$ (0-20, 20-40, 40-60, 60-85) while, in each of the two endcaps, four regions are defined by using different η-rings: 0-5, 5-15, 15-25 and 25-35. For each of these regions, and for each β-value tested for the E/p selection, the distribution of $IC - IC_{\text{true}}$ is built, where IC are the intercalibrations derived with the algorithm. This distribution generally has a Gaussian shape, centered around zero if the set of IC is unbiased. An example of this distribution is shown in Fig 3.9.

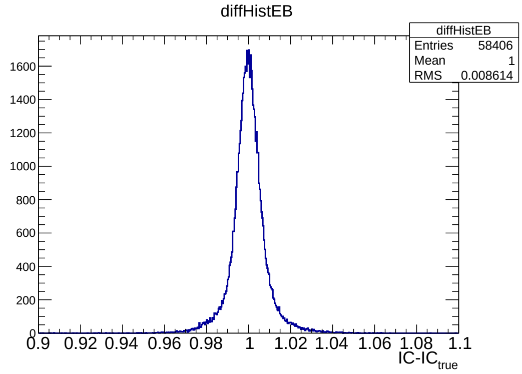

Figure 3.9: Example of the $IC - IC_{true}$ distribution, for one of the pseudorapidity regions mentioned in the text.

The width of the distribution determines how close the IC are to their true values, IC_{true}. This can be quantified by looking at the RMS of the distribution, for each of the working points and the η-regions under study. The results are shown in Figure 3.10 and 3.11 for the barrel and for one side of the endcap, respectively, where the RMS of the $IC - IC_{\mathrm{true}}$ distributions as a function of the E/p cut is shown. As it can be seen, all the curves show a similar behaviour, with a minimum located around 0.15-0.20. For larger values of the E/p cut, the RMS worsen because more and more events in the E/p distribution tails enter the calibration. For smaller values, the RMS worsen as well due to the fact that the E/p window becomes too narrow, and the electron energy cannot change much from one iteration to another; as a consequence, the algorithm is not able to recover the right value of intercalibrations for the crystals with large initial miscalibration. Therefore, this study suggests that a β value of 0.15-0.20 is the optimal one.

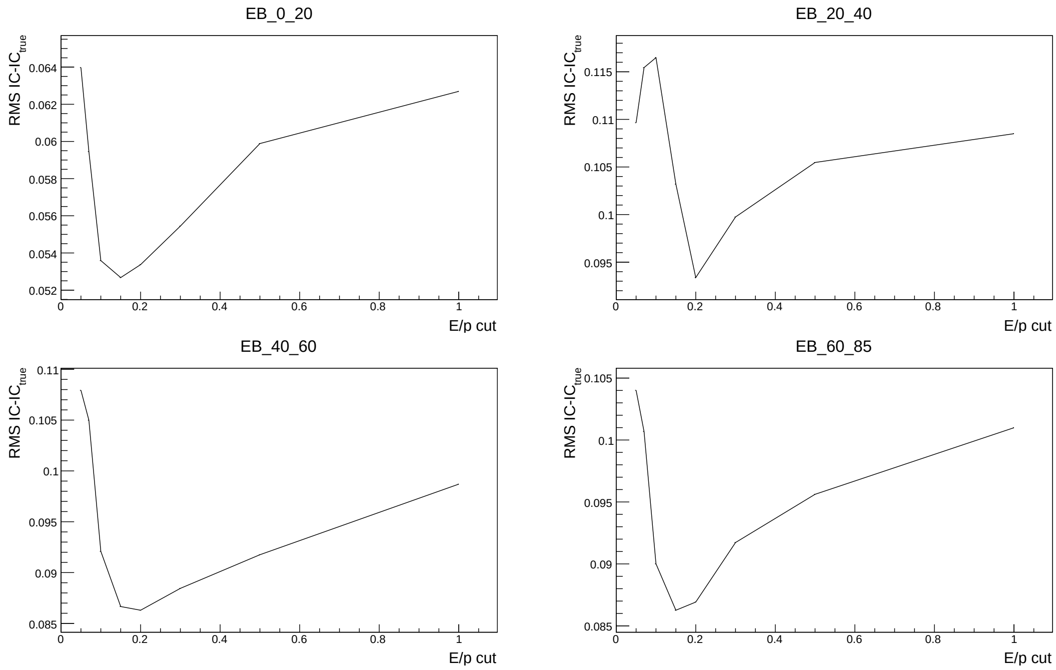

Figure 3.10: RMS of the $IC - IC_{true}$ distribution as a function of different β values, i.e. different E/p cuts, in several η regions in EB. Top line: $0 < |i\eta| < 20$ (left) and $20 < |i\eta| < 40$ (right). Bottom line: $40 < |i\eta| < 60$ (left) and $60 < |i\eta| < 85$ (right).

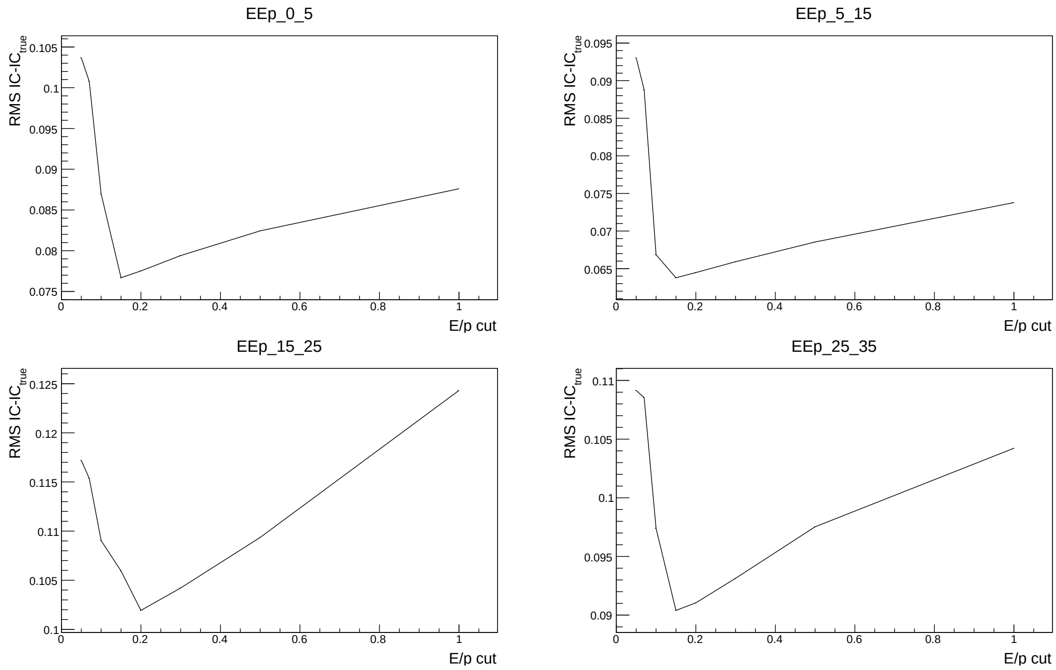

Figure 3.11: RMS of the $IC - IC_{true}$ distribution as a function of different β values, i.e. different E/p cuts, in several η regions in EE+. Top line: $0 < \eta$-ring < 5 (left) and $5 < \eta$-ring < 15 (right). Bottom line: $15 < \eta$-ring < 25 (left) and $25 < \eta$-ring < 35 (right).

Additional studies have been performed using 2015 data. As explained before, it is also necessary to quantify the impact of the loss in statistics introduced by the E/p cut. This can be done by looking at the statistical precision of the intercalibration constants derived using different working points of β. This test has been performed exploiting the full statistics of 2.3 fb^{-1} of 2015 data, and the result is shown in Figure 3.12. It can be seen that, although the number of usable events is fewer, the statistical precision improves when applying the E/p cut. In the barrel, the curve which represents $\beta = 0.15$ shows overall the best performance. $\beta = 0.10$ gives also similar results, however this working point shows a worsening of the statistical precision at $|\eta| > 75$ due to the loss in statistics. In the endcap, $\beta = 0.15$ and $\beta = 0.20$ give the best statistical precision, with the latter performing slightly better overall.
Finally, a test has been done by checking the effects of the E/p cut on the Z invariant mass resolution in $Z \to ee$ events. Once the calibration algorithm has provided a new set of intercalibrations, events can be reconstructed applying these new intercalibration coefficients to the crystal energies, and verifying if the energy resolution has improved or not. This is done by using the same events of $Z \to ee$ used in the calibration, and applying the same selections described in section 3.3.1. The invariant mass shape, m_{ee}, is reconstructed with the supercluster energy of the two electrons, and its distribution is fitted using a binned maximum Likelihood method. The fit function $f(m_{ee})$ is given by a Breit-Wigner (BW) convoluted with a Crystall Ball function (CB), to account for tail asymmetries and detector effects [72, 73]:

$$f(m_{ee}) = BW(m_{ee}, m_Z, \Gamma_Z)*CB(m_{ee}, \Delta m, \sigma_{CB}, \alpha, n)$$

The values of Breit-Wigner function parameters (m_Z and Γ_Z) are fixed to their nominal values, the fit is performed in a chosen invariant mass range $m_{ee} \in [65, 115]$ GeV, while the bin width is set to 0.25 GeV (for a total of 200 bins). A Crystal Ball pdf consists in a

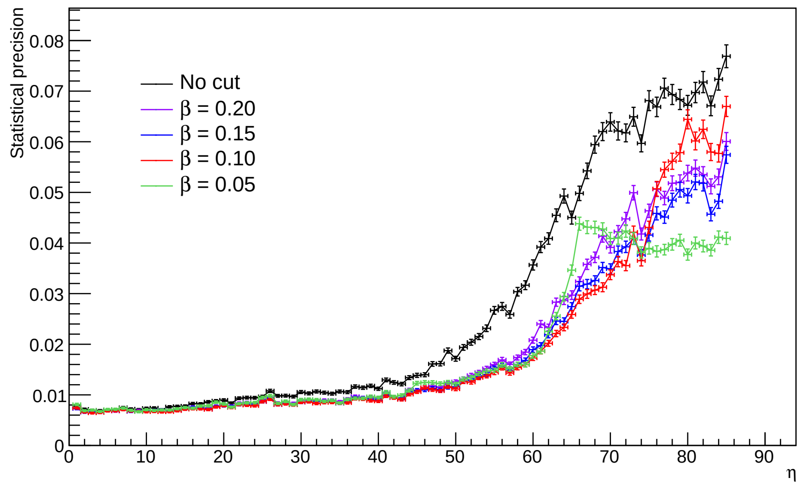

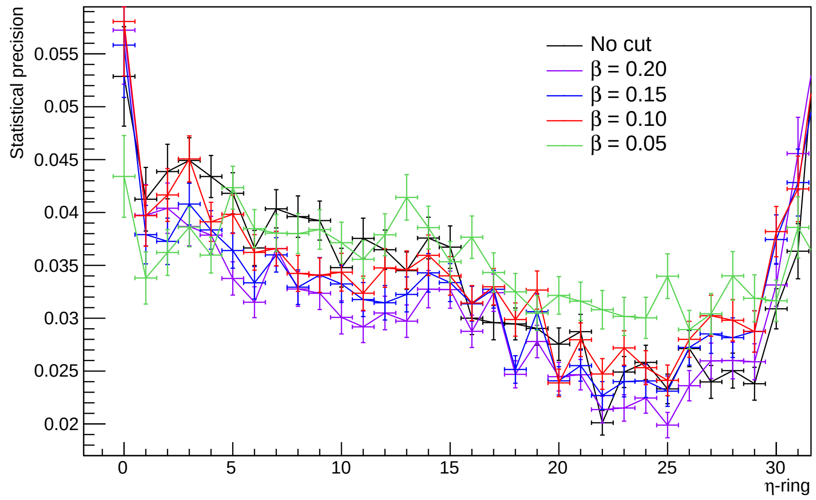

Figure 3.12: Comparison of the statistical precision for different calibrations using different β values. Top: Barrel, bottom: endcap. Black line: reference calibration (no cut applied). Purple line: $\beta = 0.20$. Blue line: $\beta = 0.15$. Red line: $\beta = 0.10$. Green line: $\beta = 0.05$.

Gaussian core and a power-law low tail, starting below a fixed threshold:

$$CB(m_{ee}, \Delta m, \sigma_C B, \alpha, n) = M \cdot \begin{cases} e^{-\frac{1}{2}\frac{(m_{ee}-\Delta m)^2}{\sigma_{CB}^2}} & \frac{m_{ee}-\Delta m}{\sigma_{CB}} > -\alpha \\ \left(\frac{n}{|\alpha|}\right)^n e^{-\frac{|\alpha|^2}{2}} \cdot \left(\frac{n}{|\alpha|} - |\alpha| - \frac{m_{ee}-\Delta m}{\sigma_{CB}}\right)^{-n} & \frac{m_{ee}-\Delta m}{\sigma_{CB}} \leq -\alpha \end{cases} \tag{3.8}$$

where Δm represents the displacement of the real peak with respect to m_Z, α and n determine the low Crystal Ball tail shape, M is a normalization factor and σ_{CB} is the Gaussian core width, which is used as estimator of the invariant mass resolution. An example of fit on the m_{ee} invariant mass distribution is shown in Figure 3.13, while in Tab. 3.2 the results on σ_{CB} are presented for barrel and endcap, for the different working points of β tested. For the inner barrel, $(|\eta| < 1)$, all the values between $\beta = 0.05$ and $\beta = 0.20$ are compatible within the uncertainty. For the outer barrel $(1 < |\eta| < 1.479)$, $\beta = 0.15$ clearly gives the best m_{ee} resolution, in agreement with the tests on data and simulation mentioned before. Slightly larger values are instead preferred in the endcap, where the best resolution is achieved using $\beta = 0.20$.

EB/EB

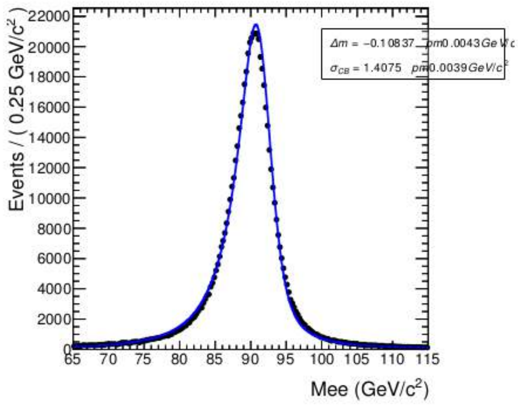

Figure 3.13: Examples of fit on the m_{ee} invariant mass distribution, which is used to extract the resolution σ_{CB}, for the barrel.

β	0.05	0.07	0.10	0.15	0.20	0.30	0.50	No cut	Uncertainty
EB $0 < \|\eta\| < 1.0$	1.38	1.38	1.37	1.38	1.38	1.39	1.42	1.44	± 0.01
EB $1.0 < \|\eta\| < 1.479$	2.92	2.95	2.62	2.55	2.62	2.86	2.99	3.03	± 0.03
EE $1.479 < \|\eta\| < 2.0$	3.06	2.99	2.93	2.91	2.91	2.92	2.97	3.09	± 0.04
EE $2.0 < \|\eta\| < 2.5$	3.40	3.38	3.33	3.27	3.23	3.27	3.39	3.87	± 0.05

Table 3.2: σ_{CB} resolution extracted from fit on the m_{ee} invariant mass in $Z \to ee$ events, in four different η regions, for the different values of the β cut.

Combining all these results, the final choice is to use $\beta = 0.15$ in the barrel and $\beta = 0.20$ in the endcap.

3.3.4 Final results on LHC Run II data

The calibration algorithm, after applying all the corrections described in the previous sections, has been run on the full statistics of 2015 data, corresponding to a luminosity of 2.3 fb^{-1}, and on a subset of 2016 data corresponding to a total integrated luminosity of 24.1 fb^{-1}. The results are presented here.

2015 data

In Figure 3.14, the intercalibration map and the statistical precision are shown for the barrel. The statistical precision achieved in the barrel varies from $0.7 - 1\%$ in the central part ($i\eta \in [0, 45]$) up to $5-6\%$ in the outer region ($i\eta \in [70, 85]$) due to the lack of statistics in this region. In Figure 3.15, the results are shown for the endcap. The statistical precision is similar for the two sides, and it goes from about 4% in the outer rings (η-ring $\approx 0 - 5$) to 2% in the central part (η-ring $\approx 20 - 25$), while it worsens in the very forward region (η-ring $\approx 30 - 35$).

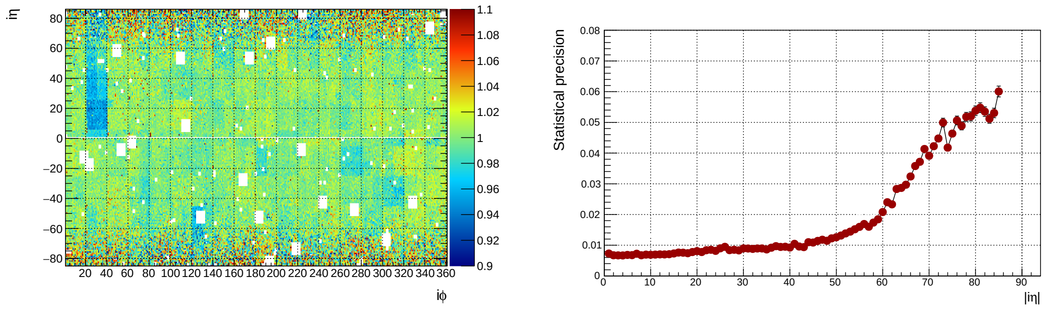

Figure 3.14: Final intercalibration results on 2015 data, in the barrel. Left: Intercalibration map, right: statistical precision for each η-ring folding EB+ and EB-.

2016 data

In Figure 3.16, the intercalibration map and the calibration precision are shown for the barrel. The statistical precision achieved in the barrel varies from 0.3% in the central part ($i\eta \in [0, 45]$) up to about 1.5% in the outer region ($i\eta \in [70, 85]$). It can be noticed that the larger statistics collected in 2016 allowed a large improvement in the precision with respect to 2015 calibrations. The same conclusion holds for the endcap, whose results are shown in Figure 3.17. The statistical precision is similar for the two sides, going from about 2% in the outer rings (η-ring $\approx 0 - 5$) to 1% in the central part (η-ring $\approx 20 - 25$), worsening again in the very forward region.

3.4 Monitoring of energy response stability

The electron sample is useful not only for calibration, but also for the monitoring of the response stability of the channels. Among the contributions to the constant term c in eq. 3.4 is the instability of the crystal responses versus time. The response of the ECAL crystals varies under irradiation due to the formation of colour centers, which cause a loss in the $PbWO_4$ transparency. This damage is partially recovered at the temperature at which ECAL operates (18°) through spontaneous annealing of the colour centers, which leads to a partial recovery of the transparency in absence of radiation. The result is a cycle of transparency changes between LHC collision runs and machine refills. A dedicated laser monitoring system [74] is used to measure and correct these transparency changes. It is based on the injection of a fixed intensity blue laser pulse with $\lambda = 447$ nm (close to the emission peak of the $PbWO_4$) into each crystal, through optical quartz fibers, in regular cycles of ≈ 40 min, and into a PN diode which is used as reference. Infrared and green light provide complementary measurements for other wavelength values. The measured transparency change (R/R_0) is not directly proportional to the scintillation light relative change (S/S_0), due to their different spectra and the different paths to reach the photodetectors, but they are related by the following relation:

$$\left(\frac{S}{S_0}\right) = \left(\frac{R}{R_0}\right)^{\alpha} \tag{3.9}$$

with α being a parameter depending on the crystal. The ECAL crystals were grown in two different facilities, one in China (SIC crystals) and the other one in Russia (BTCP crystals). A measurement of α was performed with in situ measurements during 2011 and 2012 data taking. The measured effective value of α was 1.52 for BTCP barrel crystals, 1.16 for the endcap BTCP crystals and 1.00 for the endcap SIC crystals.

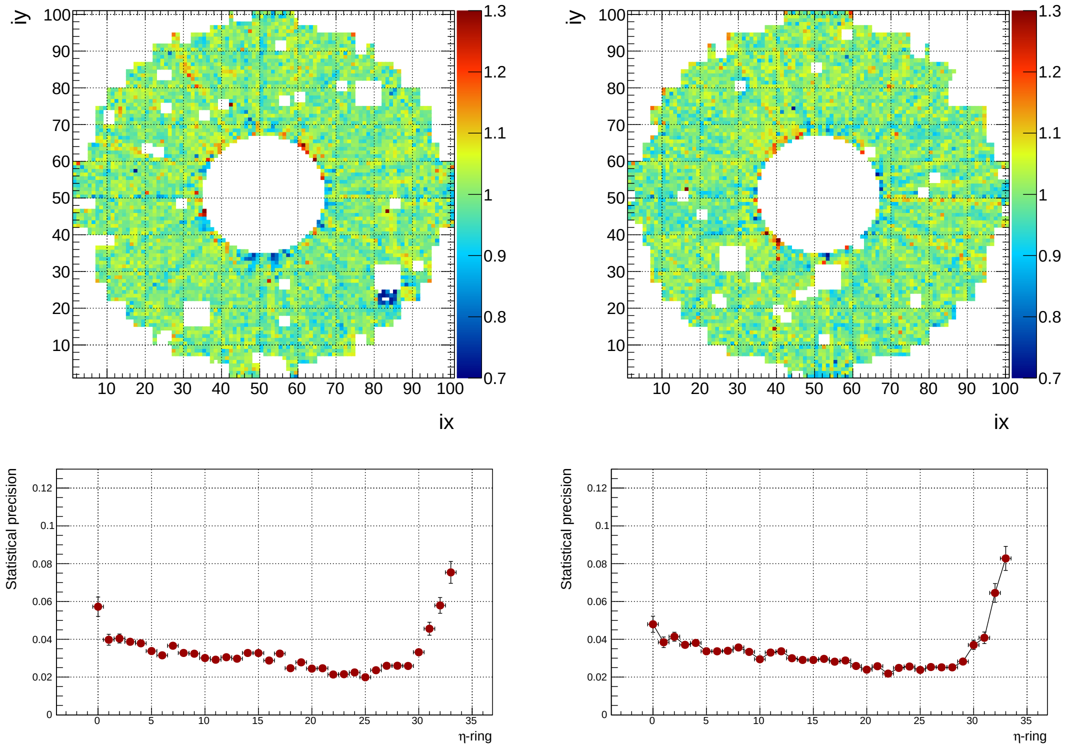

Figure 3.15: Final intercalibration results on 2015 data, in the endcap. Left: EE+, Right: EE-. Top: Intercalibration map, bottom: statistical precision for each η-ring.

The variation of the crystal response has been measured during LHC Run I and Run II, and it is shown in Figure 3.18 for crystals belonging to different pseudorapidity (η) region. The response change observed in the ECAL channels is up to 6% in the barrel and it reaches up to 30% at $\eta \approx 2.5$, the limit of the tracker acceptance. The response change is up to 70% in the region closest to the beam pipe. The recovery of the crystal response during Long-Shutdown 1 is visible, where the response was not fully recovered, particularly in the region closest to the beam pipe.

The validation of the laser corrections should be performed on high-level physics objects, such as electrons. The method discussed here exploits the same sample of isolated electrons from W and Z decays as were used for the calibration. The procedure is similar to the momentum calibration approach described in section 3.3.2, and it is the following:

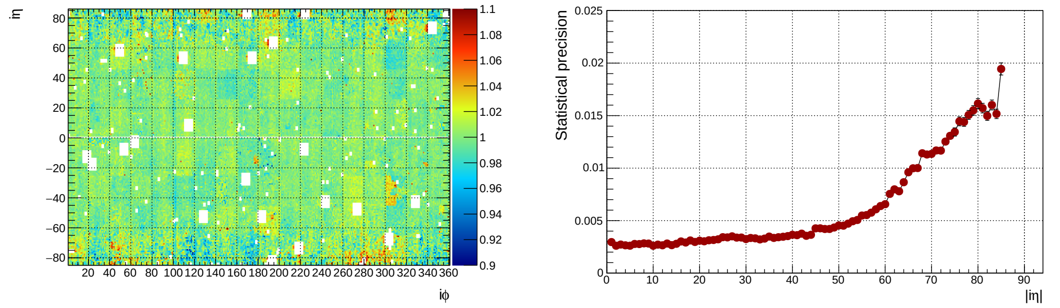

Figure 3.16: Final intercalibration results on 2016 data, in the barrel. Left: Intercalibration map, right: statistical precision for each η-ring folding EB+ and EB-.

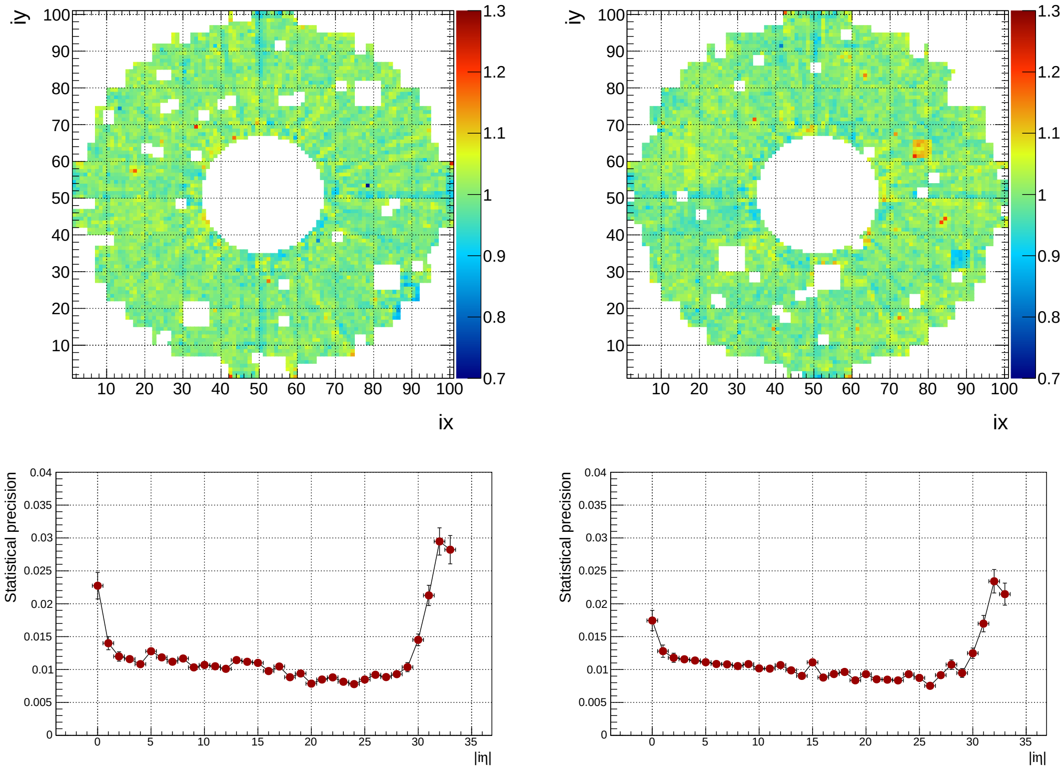

Figure 3.17: Final intercalibration results on 2016 data, in the endcap. Left: EE+, Right: EE-. Top: Intercalibration map, bottom: statistical precision for each η-ring.

- A reference distribution (referred to as "template") of $E_{sc}^{\mathrm{corr}}/p_{tk}$, where E_{sc}^{corr} is the electron supercluster energy after the laser corrections, is built using all the available events in data. Two templates are created, one for the barrel, and one for the endcap.

- Data are sorted by time and splitted into bins of 5000 events in the barrel and 10000 events in the endcaps, with the requirement that the time interval between two consecutive events should be less than 24 hours, otherwise a new bin is created.

- $E_{sc}^{\mathrm{corr}}/p_{tk}$ distributions are built for each bin.

- Each distribution is fitted using a scaled version of the template, defined as follows:

$$f(x, k) = N \cdot k \cdot F(kx)$$

  where $x = E_{sc}^{\mathrm{corr}}/p_{tk}$, N is the number of events in the bin considered, and k is a factor which tells how much the original template distribution $F(x)$ is drifting and scaling to fit the data in the subset of events considered.

- The inverse of the factor k, $1/k$, is used to monitor the stability of the E/p scale versus time.

The entire procedure is repeated by using also $E_{sc}^{\mathrm{uncorr}}/p_{tk}$, where E_{sc}^{uncorr} is the electron supercluster energy before applying the laser corrections, to check how much the transparency changes affect the stability of the E/p ratio.

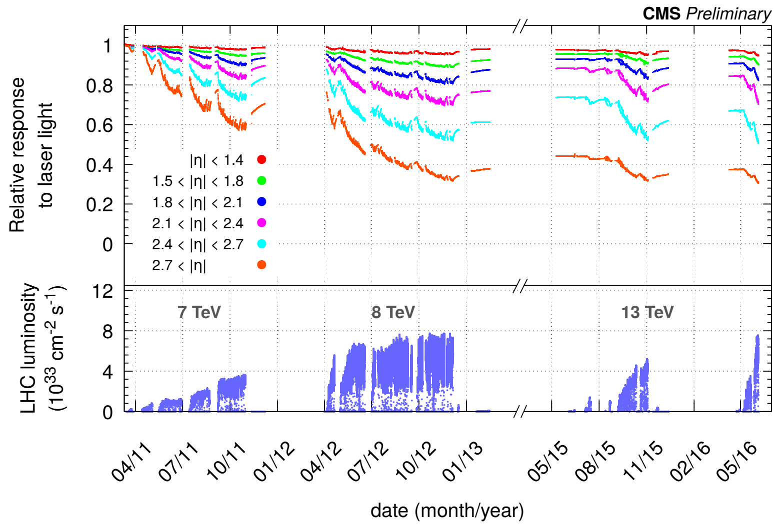

Figure 3.18: Relative response to laser light injected in the ECAL crystals, measured by the ECAL laser monitoring system, averaged over all crystals in bins of pseudorapidity, for the 2011, 2012, 2015 and 2016 data taking periods, with magnetic field at 3.8 T. The bottom plot shows the instantaneous LHC luminosity delivered during this time period.

3.4.1 Results on LHC Run II data

The procedure described in the previous section has been applied on the full statistics of 2015 data, corresponding to an integrated luminosity of 2.5 fb^{-1}. The results are presented here.

The E/p relative scale is shown in Figure 3.19 for the barrel and Figure 3.20 for the endcaps, before and after applying the laser corrections. In the barrel, an average signal loss of 3% is observed, while the stability reached with the laser corrections is 0.14%. In the endcaps, an average signal loss of 8% is observed, while the stability reached with the laser corrections is 0.54%.

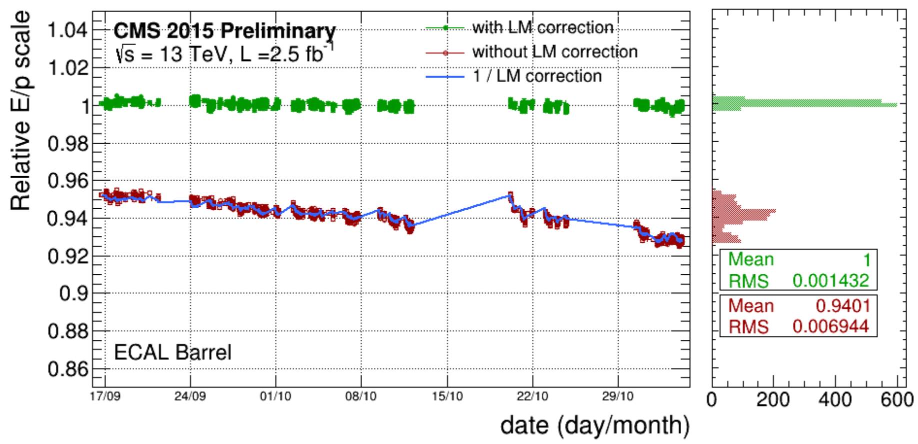

Figure 3.19: History plot for 2015 data of the ratio of electron energy E, measured in the ECAL barrel, to the electron momentum p, measured in the tracker. Green: after applying laser corrections, red: before applying laser corrections. The magnitude of the average transparency correction for each point (averaged over all crystals in the reconstructed electromagnetic clusters) is also shown with a continuous blue line.

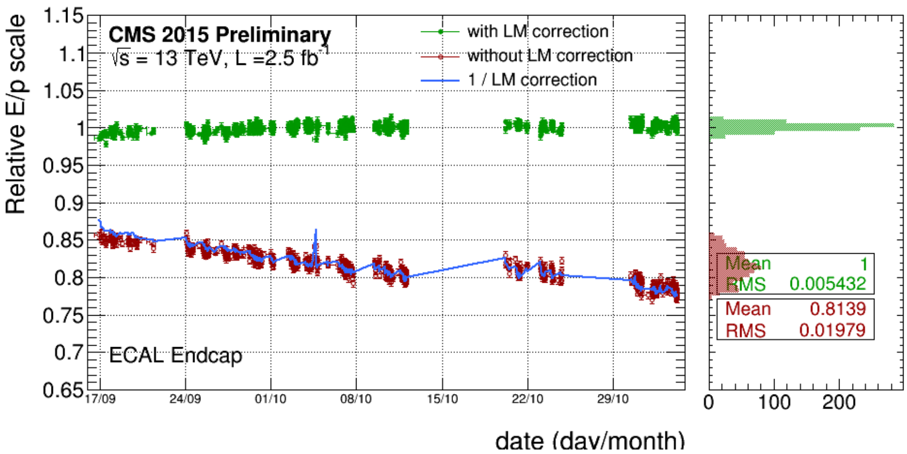

Figure 3.20: History plot for 2015 data of the ratio of electron energy E, measured in the ECAL endcap, to the electron momentum p, measured in the tracker. Green: after applying laser corrections, red: before applying laser corrections. The magnitude of the average transparency correction for each point (averaged over all crystals in the reconstructed electromagnetic clusters) is also shown with a continuous blue line.

Chapter 4

Search for high-mass resonances decaying into VW semileptonic final state

This work searches for massive resonances decaying into a VW final state, with the W boson decaying into leptons ($\ell\nu$), while V denotes either a W or a Z boson decaying hadronically ($q\bar{q}$). The theoretical models which predict the existence of heavy particles decaying to pairs of bosons are discussed in chapter 1. Figure 4.1 shows an example of a Feynman diagram for the production and decay of a generic resonance X into the final state considered.

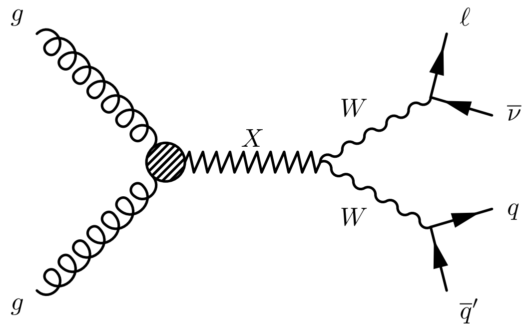

Figure 4.1: Feynman diagram for the production of a generic resonance X decaying to the final state considered in this study.

This analysis requires the reconstruction of the full kinematics of the events, in order to search for a local enhancement in the diboson invariant mass spectrum (m_{VW}). In section 4.1, the main background processes of the analysis are presented, while in section 4.2 the main selections used to isolate the signal topology are described.

One of the challenges of this analysis is the reconstruction of the highly energetic decay products. Since the resonances under study have masses of O(TeV), the vector bosons have on average transverse momenta of several hundred GeV. Therefore, the quarks from the V boson decay tend to be very collimated and they are reconstructed as a single ("merged") jet in the detector. Dedicated techniques (section 2.4) have been developed to improve the reconstruction of these merged jets, exploiting the different spatial and energy distribution of the jet constituents with respect to QCD jets. The identification of the V boson decay through these techniques in this analysis is explained in section 4.3.

The final state considered is $\ell\nu J$, i.e. events with a charged lepton, a neutrino and a merged jet. The search is limited to final states where ℓ is a muon or an electron, since τ leptons produce lower energy electrons or muons, with smaller selection efficiency for the analysis and additional missing energy in the event. Even if the analysis is not optimized for them, such events are accounted for in the signal model. Leptonically decaying W bosons are reconstructed by identifying isolated high-momentum leptons and by exploiting the measured missing transverse energy ($\not{E}_T$) in the event, which is used to reconstruct the neutrino kinematics. An estimate of the neutrino longitudinal momentum is obtained by imposing the W mass constraint on the $\ell\nu$ system invariant mass. This procedure is described in section 4.4.

The contribution of the background processes after the event selection is estimated from data, using a signal-depleted region. The details of this procedure are explained in section 4.5.

Section 4.6 briefly explaines the estimation of the signal contribution, while section 4.7 describes the procedure used to interpret the results in terms of an upper limit on the cross section of the theoretical model considered.

Finally, the analysis of LHC Run I and Run II data is presented in chapters 5 and 6 respectively, targeting different theoretical models.

4.1 Backgrounds

All the processes with one isolated lepton, missing transverse energy and additional jets in the final state are possible sources of background, and they are described in the following.

W+jets: production of a single W boson which decays leptonically, in association with quarks or gluons that lead to the presence of additional jets in the final state. The main leading-order production diagrams are shown in Figure 4.2.

In most of the phase spaces considered in this analysis, this is the dominant background.

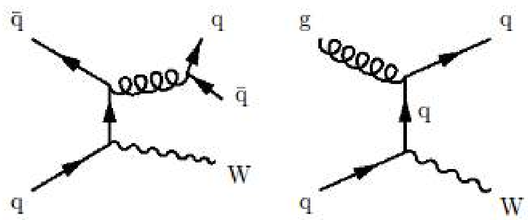

Figure 4.2: W+jets leading-order production diagrams

In the simulation, the description of the substructures in jets coming from soft radiation is not as accurate as the one for high-p_T jets that characterize the signal topology. Therefore, the estimate of this background is performed from data, as described in section 4.5.

$t\bar{t}$ **+ jets:** production of two top quarks via the gluon fusion process $gg \to t\bar{t}$ or quark annihilation $q\bar{q} \to t\bar{t}$; the leading-order production diagrams are shown in Figure 4.3.

Both top quarks decay into a b quark and a W boson; when one W decays leptonically and the other one decays hadronically, this process gives rise to the same final state as the

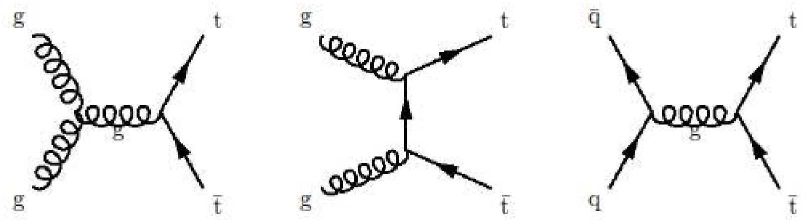

Figure 4.3: $t\bar{t}$ leading-order production diagrams

signal. This background can be reduced using b-tag algorithms to identify and veto jets originating from the hadronization of bottom quarks (b-tagged jets).

Single Top: the production of this background proceeds through different channels (Figure 4.4):

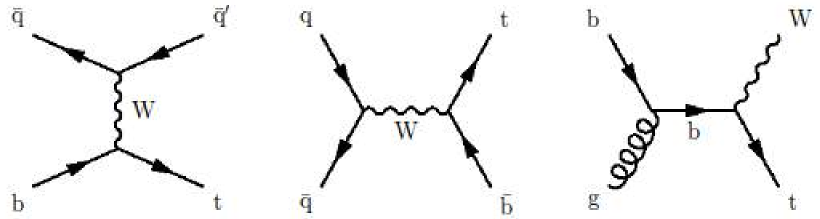

Figure 4.4: Single top leading-order production diagrams; from left to right: t-channel, s-channel and tW-channel.

- **t-channel**: a single top quark is produced after a quark-bottom interaction with the exchange of a virtual W boson. The top quark decays into a bottom quark and a W boson, and if the latter decays leptonically, it produces the same signature as the signal.

- **s-channel**: this is the production of a top-bottom pair, after the annihilation of a quark pair in a weak vertex. The W boson from the top decay or the bottom quark can decay leptonically, mimicking the final state for the signal.

- **tW-channel**: a top quark is produced in association with a charged vector boson via the weak process, from a gluon-bottom pair in the initial state. If the W boson decays leptonically and the one produced by the top fragmentation decays hadronically (or vice versa) this process can produce the same signature of the signal process.

The single top production is a non-dominant background, and can be reduced by identifying and vetoing the jets coming from the b quark, as in the case of $t\bar{t}$ + jets.

Diboson: production of two vector bosons, in association with jets (Figure 4.5). This background includes three different processes:

- **WW**: this is the non-resonant production of two W bosons. It is an irreducible background for this analysis since its topology is identical to the signal.

- **WZ**: this is the production of a W and a Z boson, where the W boson decays leptonically and the Z boson decays hadronically, or the W boson decays hadronically while the Z boson decays leptonically and one lepton is not identified in the detector.

- **ZZ**: this is the production of two Z bosons, where one of them decays hadronically and the other one decays leptonically, and one lepton is not identified in the detector.

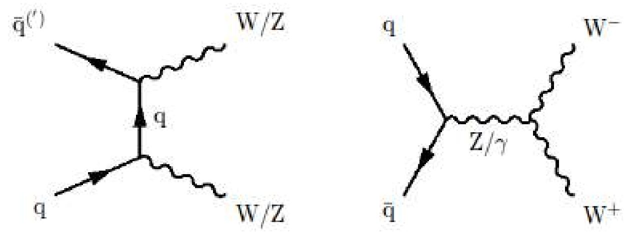

Figure 4.5: Diboson leading-order production diagrams

Z/γ+jets: production of a Z/γ boson in association with quarks or gluons, where one lepton is undetected due to acceptance or inefficiency effects. The production diagrams are the same as Figure 4.2 with the W boson replaced by a Z/γ boson. This background is not considered in this analysis, since its contribution is negligible.

QCD multijet production: this background refers to all the processes in which there is the production of several jets mediated by strong interactions. In these cases it is possible to produce a non-prompt lepton, coming from the decay of a b-quark, or a fake lepton, when a hadron is wrongly reconstructed by the detector. Even if the mis-reconstruction probability is low, the fake rate can be high, since these QCD processes have cross sections of approximately one millibarn in the kinematic region of interest of this analysis (while typical cross section values for the signal are approximately one picobarn or less). The contribution of this background is more important in the final state with an electron, since the probability of fake muon reconstruction is much lower than the probability of fake electron reconstruction. Nevertheless, the tight selections on the lepton p_T/ID/isolation and on the missing transverse energy applied in this analysis reduce this background to a negligible level.

The procedures applied for the estimate of the various backgrounds are described in detail in section 4.5.

4.2 Event selection

In order to isolate a boosted topology consistent with the VW system, events are selected requiring one energetic lepton (electron or muon), large $\not{E}_T$ and one merged jet in the final state. In this section, a general overview of the main selections used in the analysis is given. The exact working points used for the cuts, the isolation and the ID criteria are analysis-dependent and therefore are reported in chapters 5 and 6.

4.2.1 Lepton selection

Candidate signal events are selected online with triggers which require one electron or one muon above a certain p_T threshold, which ranges from $\approx$ 30 GeV to $\approx$ 100 GeV depending on the analysis and the lepton flavour. Tighter p_T cuts, ID and isolation criteria are then applied in the offline analysis, while the presence of additional low-p_T electrons or muons in the event is vetoed, to suppress Z/γ+jets and top backgrounds.

4.2.2 Jet Selection

Jets are reconstructed from the particle flow candidates in the event. Two jet collections are used:

- Large-cone jets: reconstructed using the Cambridge-Aachen (anti-k_T) algorithm in LHC Run I (Run II), with a distance parameter of R = 0.8, used to select the hadronic V boson candidate.
- Small-cone jets: reconstructed using the anti-k_T algorithm, with a distance parameter of R = 0.5 (0.4) in LHC Run I (Run II), used to require or veto the presence of b-tagged jets in the event.

To reduce contamination from pileup, a technique called Charged Hadron Subtraction (CHS) [75] is applied to the jets. This technique uses the tracking capabilities to identify and remove charged hadrons which are known to have originated from pileup vertices. Jets are also corrected using the energy corrections described in section 2.3.3.

The hadronic V boson candidate is selected as the large-cone jet with largest p_T, with the requirements $p_T > 200$ GeV and $|\eta| < 2.4$. It is also required that no electrons or muons lie inside the jet cone.

In addition, events which contain b-tagged small-cone jets outside the hadronic V boson cone are rejected, to reduce contamination from top backgrounds.

4.2.3 Angular selection

The signature of the signal process is characterized by a topology with two boosted vector bosons which are back-to-back in the transverse plane. In order to isolate such a topology, various angular selections are applied. The $\Delta R = \sqrt{(\Delta\phi)^2 + (\Delta\eta)^2}$ between the lepton and the hadronic V boson candidate must be larger than $\pi/2$. The separation in the transverse plane, $\Delta\phi$, between the hadronic V boson candidate and the missing transverse energy must be larger than 2.0. Furthermore, the $\Delta\phi$ between the hadronic V boson candidate and the reconstructed leptonic W boson must be larger than 2.0.

Summary of event selection

The event selection can be summarized as follows:

1. exactly one charged lepton;
2. missing transverse energy: events are required to have large $\not{E}_T$ (typically above 40-80 GeV) to suppress contributions from QCD;
3. leptonic W p_T: the p_T of the reconstructed leptonic W boson must be larger than 200 GeV. This is required to select the boosted W topology;
4. hadronic V p_T: the p_T of the reconstructed hadronic V boson (merged jet) must be larger than 200 GeV. This is required to select the boosted W topology;
5. b-veto: the event is required to have no small-cone jets identified as b-jets;
6. angular selections to select a diboson-like topology:

- $\Delta R(\ell, W_{had}) > \pi/2$
- $\Delta\phi(W_{had}, \not{E}_T) > 2$
- $\Delta\phi(W_{had}, W_{lep}) > 2$

4.3 Hadronic V boson reconstruction

The bosons from the heavy resonance decay are usually highly energetic and their hadronic decay products are reconstructed in the detector as a single jet [76]. The identification of such a boson (called "V-tagging") exploits the substructure topology of the merged quark pair to differentiate them from quark- and gluon-induced jets.

An observable used to discriminate between signal and background is the pruned jet mass (m_J), introduced in section 2.4. As can be observed in Figure 4.6, the distribution for the signal shows a peak around the W/Z mass, while for QCD jets it tends to smaller values. The pruned mass of the merged jet is therefore used to define a Signal Region (SR), centered around the W/Z mass, and two signal-depleted regions called respectively Lower Sideband (LSB) and Higher Sideband (HSB), which are used for the estimation of the W+jets background. The exact definition of these regions is analysis-dependent. For instance, in the analysis of Run I data, the window $65 < m_J < 105$ GeV is used as signal region while $40 < m_J < 65$ and $105 < m_J < 130$ GeV are used as lower and higher sideband region, respectively.

To discriminate between two-pronged jets from a V boson decay and QCD jets, the n-subjetiness ratio $\tau_{21} = \tau_2/\tau_1$ is also used, with τ_N defined as in section 2.4. The typical τ_{21} distributions for signal and background are shown in Figure 4.6. It can be observed that the distribution from signal-like jets from a V boson decay peaks to lower values with respect to the distribution from QCD jets. In the analysis, an additional cut on τ_{21} is applied to further reduce the background contribution. The working point values used for the τ_{21} selection are analysis-dependent and are specified in the following chapters.

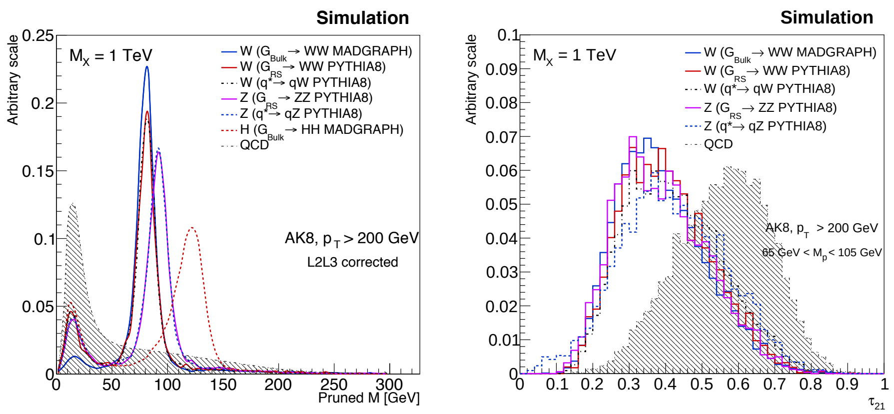

Figure 4.6: Typical pruned jet mass (left) and τ_{21} distribution (right) for signal (V-boson decay) and background (QCD jets) processes. For the purpose of presentation a signal cross section of 1.5 nb is used.

4.3.1 V-tagging scale factors and mass scale/resolution correction

Since data/simulation discrepancies in the substructure variables can bias the signal efficiency estimated using the simulation, the performance of the pruned jet mass and τ_{21} are studied in a signal-free sample with jets having characteristics similar to the ones expected for the signal. The high p_T $t\bar{t}$ events provide a sample of pure hadronic W bosons, which can be used to validate the performances of the substructure variables and to extract data/simulation scale factors for the τ_{21} selection efficiency and mass scale/resolution corrections. This $t\bar{t}$-enriched control sample is selected reversing the b-veto condition, therefore requiring the presence of at least one b-tagged small-cone jet outside the merged jet cone. To increase purity, the merged jet is choosen to be the large-cone jet with the highest mass satisfying $p_T > 200$ GeV, in the opposite hemisphere with respect to the lepton. This requirement is different from the standard analysis selection, where only $p_T > 200$ GeV is imposed. With these requirements, an almost pure sample of $t\bar{t}$ events can be obtained, with a small contamination from single top, W+jets and VV events. This control sample is used to extract data/simulation scale factors for the non-dominant backgrounds, e.g. $t\bar{t}$, single top, WW/WZ, and for the signal, whose contribution is evaluated from the simulation.

For the $t\bar{t}$ and single top contributions, a scale factor is computed as the ratio between the number of events in data and in simulation in the $t\bar{t}$ control sample. This scale factor is calculated applying the full event selection and the N-subjettiness τ_{21} selection, and considering only events in the m_J signal region.

The procedure is different for the WW/WZ and the signal contribution, since what is needed is the efficiency for pure W-jet signal. To get the correct signal efficiency scale factor, it is necessary to subtract the combinatorial background contribution in the $t\bar{t}$ control sample. In order to identify the fraction of the $t\bar{t}$ jet mass distribution which contains "real" merged W bosons and the combinatorial background, the $t\bar{t}$ simulated sample is used. The merged jet is matched at generator level with the hadronic W boson, using a cone $\Delta R < 0.3$, obtaining the shapes for the "real" merged W boson ("matched") and for the combinatorial background ("unmatched"). The m_J distributions of the matched and unmatched samples that pass and fail the N-subjettiness selection are modelled by using the following functions:

- $f_{\text{bkg}}(m_j) = F_{\text{ExpErf}} = e^{c_0 m_j} \cdot \frac{1+\text{Erf}((m_j-a)/b)}{2}$ for both the unmatched-passed and unmatched-failed sample;
- $f^{\text{sig}}(m_j) = F_{\text{Gaus}}(m_j) + F_{\text{ErfExp}}(m_j)$ for both the matched-passed and matched-failed sample, where $F_{\text{Gaus}}(m_j)$ is a Gaussian distribution.

In Figure 4.7 an example of fits to the $t\bar{t}$ jet mass distribution for the simulation, for matched/unmatched and pass/fail samples, is shown.
The W-tagger scale factor (SF) is extracted estimating the cut efficiency (ϵ) on both data and simulated samples with a simultaneous unbinned maximum-likelihood fit on the "pass" and the "fail" samples, with the following likelihoods:

$$L_{\text{pass}} = \prod_i^{N_{\text{evt}}^{pass}} \Big[N_{\text{W}} \cdot \epsilon \cdot f_{\text{pass}}^{\text{sig}}(m_j) + \\ N_2 \cdot f_{\text{pass}}^{\text{bkg}}(m_j) + N_{\text{pass}}^{\text{sTop}} \cdot f_{\text{pass}}^{\text{sTop}} + N_{\text{pass}}^{\text{VV}} \cdot f_{\text{pass}}^{\text{VV}} + N_{\text{pass}}^{\text{wjet}} \cdot f_{\text{pass}}^{\text{wjet}} \Big] \tag{4.1}$$

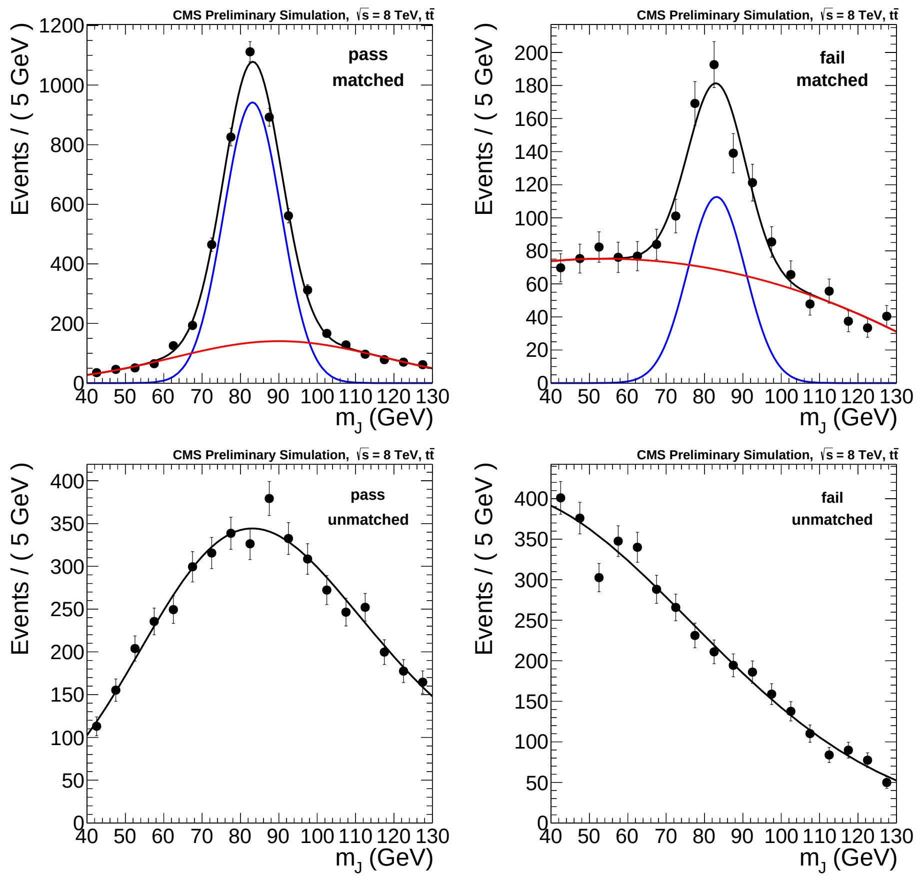

Figure 4.7: Fit to the pruned jet mass distribution in $t\bar{t}$ simulation, for events which pass (left) and fail (right) the N-subjettines selection, and where the jet is matched (top) or not matched (bottom) with the generated W boson.

$$
\begin{aligned}
L_{\text{fail}} = \prod_{i}^{N_{\text{evt}}^{fail}} \Big[& N_{\text{W}} \cdot (1-\epsilon) \cdot f_{\text{fail}}^{\text{sig}}(m_j) + N_3 \cdot f_{\text{fail}}^{\text{bkg}}(m_j) + \\
& N_{\text{fail}}^{\text{sTop}} \cdot f_{\text{fail}}^{\text{sTop}} + N_{\text{fail}}^{\text{VV}} \cdot f_{\text{fail}}^{\text{VV}} + N_{\text{fail}}^{\text{wjet}} \cdot f_{\text{fail}}^{\text{wjet}} \Big]
\end{aligned}
\tag{4.2}
$$

where N_W is the number of real W-jets, N_2 and N_3 are the number of combinatorial background events passing and failing the τ_{21} cut respectively, N_i and f_i with $i =$ single top, VW, W+jets are the normalizations and analytic shapes of the minor backgrounds. The shapes and normalizations of these minor backgrounds are estimated and fixed from the simulations, while the rates N_W, N_2 and N_3, and the mean and sigma of the W-mass distribution defined in $f_{\text{pass}}^{\text{sig}}(m_j)$ and $f_{\text{fail}}^{\text{sig}}(m_j)$ are the floating parameters of the fit. The following functions are used to describe the W+jets, single top and VV contributions:

$$
\begin{aligned}
f_{\text{pass}}^{\text{sTop}} = F_{\text{ErfExpGaus}}(x) &= \frac{1+\text{Erf}((x-a)/b)}{2} \cdot e^{-(x-x_0)^2/2\sigma^2} \\
f_{\text{fail}}^{\text{sTop}} = F_{\text{ExpGaus}}(x) &= e^{ax} \cdot e^{-(x-b)^2/2s^2} \\
f_{\text{pass}}^{\text{VV}} = F_{\text{ErfExpGaus}}(x) &= \frac{1+\text{Erf}((x-a)/b)}{2} \cdot e^{-(x-x_0)^2/2\sigma^2} \\
f_{\text{fail}}^{\text{VV}} = F_{\text{ExpGaus}}(x) &= e^{ax} \cdot e^{-(x-b)^2/2s^2} \\
f_{\text{pass}}^{\text{wjet}} = F_{\text{ErfExp}}(x) &= e^{c_0 x} \cdot \frac{1+\text{Erf}((x-a)/b)}{2} \\
f_{\text{fail}}^{\text{wjet}} = F_{\text{Exp}}(x) &= e^{c_0 x}
\end{aligned}
\tag{4.3}
$$

where the parameters of these functions are determined by a fit to the corresponding MC sample.

The ratio between data and simulation efficiencies is taken as the W-tagging scale factor:

$$
SF = \frac{\epsilon(\text{data})}{\epsilon(\text{sim})} \tag{4.4}
$$

The value for this scale factor is typically close to 1, while the exact value is analysis-dependent and it is reported in the following chapters. An example of the simultaneous fit on data and simulation to extract the W-tagging scale factor is shown in Figure 4.8, for Run I data.

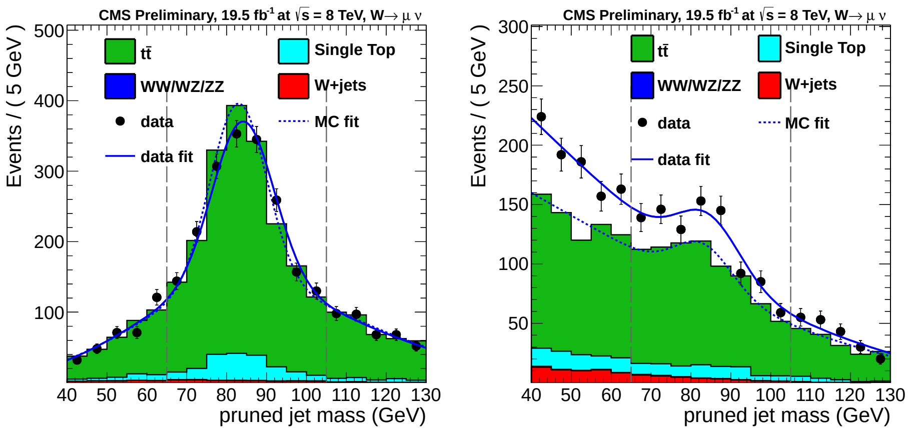

Figure 4.8: Fits to the pruned jet mass distribution in $t\bar{t}$ control sample passing (left) and failing (right) the N-subjettines cut.

In addition to the scale factors discussed above, it is possible to correct for residual data/MC differences observed in the shape of the pruned jet mass distribution. The mass scale and the resolution observed in the simulation are matched to the ones observed in data, extracted using the values of the mean and the sigma of the narrower Gaussian in $f_{\text{pass}}^{\text{sig}}(x)$ and $f_{\text{fail}}^{\text{sig}}(m_j)$, from the simultaneous fit of the "pass" and "fail" samples. Since no major differences between electron and muon channels are expected in the jet mass scale and resolution, the two channels are usually merged in this procedure.

4.4 Diboson invariant mass reconstruction

The analysis strategy is to search for a possible resonance in the invariant mass spectrum of the two bosons, M_{VW}. The experimental signature of the signal is a narrow peak in the M_{VW} spectrum, over a large falling distribution typical of the background. The two bosons are on mass shell, so it is possible to calculate the M_{VW} value despite the presence of the undetected neutrino in the final state. In fact, the transverse components of the neutrino momentum are known from the missing transverse energy, and the p_z of the neutrino can be determined by imposing a constraint on the invariant mass of the lepton-neutrino system, that should be equal to the W mass: $m_W = 80.385$ GeV. Therefore, the p_z^ν can be found solving the following equation:

$$(p_z^\nu)_{1,2} = \frac{p_Z^{lepton}(\vec{p}_T^{lepton}\vec{E}_T^{miss} + m_W^2/2) \pm \sqrt{\Delta}}{(p_T^{lepton})^2}$$

$$\Delta = (\vec{p}_T^{lepton}\vec{E}_T^{miss} + m_W^2/2)^2 - (\vec{p}_T^{lepton}\vec{E}_T^{miss})^2$$

There are three possible cases:

- The discriminant Δ is positive: two distinct solutions exist; the one yielding the smallest value for p_z^ν is chosen.
- The discriminant Δ is zero: the two real solutions coincide.
- The discriminant Δ is negative: two complex solutions exist; in this case the discriminant is forced to be equal to zero, then the unique solution for p_z is chosen and the p_T of the neutrino is corrected by re-imposing that the lepton-neutrino system mass is equal to m_W.

After the determination of the p_z^ν, M_{VW} can be computed calculating the invariant mass of the sum of the lepton, the neutrino and the merged jet.

4.5 Background estimation

After all the selections are applied, the dominant background arises from the W+jets process. The procedure used to estimate this background is based on data. The sub-dominant backgrounds ($t\bar{t}$, single top and diboson production) are estimated from the Monte Carlo simulation of the corresponding process, applying the correction factors extracted from the data top-enriched control sample as described in section 4.3.1.

The overall normalization of the W+jets background in the signal region is extracted from an unbinned maximum likelihood fit to the m_J distribution in the lower and higher sidebands of the observed data, while the contribution of the sub-dominant backgrounds is estimated from a fit to the m_J distribution in the simulation. The empirical forms used for the fits are different for each process considered. The complete list of functions used is the following:

$$
\begin{aligned}
F_{\text{ErfExp}}(x) &= e^{c_0 x} \cdot \frac{1 + \text{Erf}((x-a)/b)}{2} \\
F_{\text{ExpGaus}}(x) &= e^{ax} \cdot e^{-(x-b)^2/2s^2} \\
F_{\text{2Gaus}}(x) &= c_0 \cdot G_0(x, x^0, \sigma^0) + c_1 \cdot G_1(x, x^1, \sigma^1) \\
F_{\text{ErfExp2Gaus}}(x) &= e^{c_0 x} \cdot \frac{1 + \text{Erf}((x-a)/b)}{2} \cdot (c_0 \cdot G_0(x, x^0, \sigma^0) + c_1 \cdot G_1(x, x^1, \sigma^1))
\end{aligned}
\tag{4.5}
$$

The use of these functions for each background process is specified in chapter 5 and 6. In Figure 4.9, an example of the m_J sidebands fit to the observed data to extract the W+jets normalization is shown.

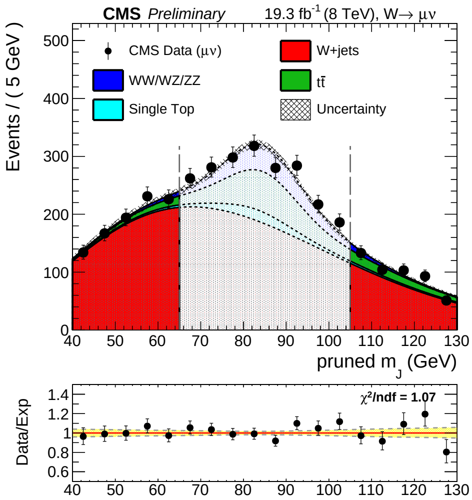

Figure 4.9: Example of fit on the observed data using the sidebands of the pruned jet mass distribution, to extract the W+jets normalization. The signal region is denoted by a hatched area. In this example, the signal region is defined as $65 < m_J < 105$ GeV, while the two sidebands are $40 < m_J < 65$ and $105 < m_J < 130$ GeV. In the bottom part of the plot, the ratio between the data and the expected total background distribution is also shown, together with its uncertainty represented with a yellow area.

The shape of the W+jets m_{VW} distribution in the signal region is determined from the lower sideband only and is corrected by a transfer function $\alpha_{MC}(m_{VW})$ derived from the W+jets simulation, defined as

$$
\alpha_{MC}(m_{VW}) = \frac{F^{W+jets}_{MC,SR}(m_{VW})}{F^{W+jets}_{MC,SB}(m_{VW})}
$$

where $F^{W+jets}_{MC,SR}(m_{VW})$ and $F^{W+jets}_{MC,SB}(m_{VW})$ are the shapes of the m_{VW} distribution extracted from a fit on the W+jets Monte Carlo sample, in the signal and the lower sideband regions, respectively.

An unbinned maximum likelihood fit is performed to the m_{VW} distribution observed in data, in the lower sideband, to extract the W+jets shape in this region, $F^{W+jets}_{DATA,SB}(m_{VW})$. In the procedure, the observed m_{VW} distribution in the lower sideband is corrected taking into account the contribution of the sub-dominant backgrounds. Events in the higher sideband are not used in this procedure, due to the different m_{VW} shape of the background in this region with respect to the lower sideband. Figure 4.10 shows an example of the extrapolation function $\alpha_{MC}(m_{VW})$ and of the fit to the data m_{VW} distribution in the lower sideband.

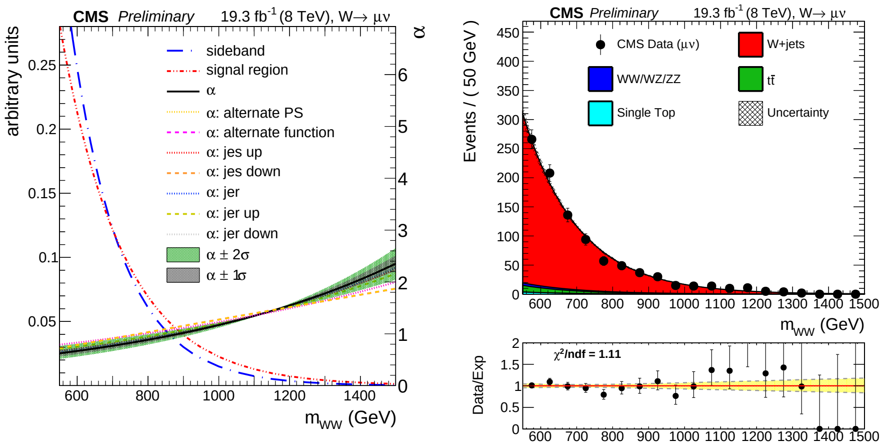

Figure 4.10: Left: example of the extrapolation function $\alpha_{MC}(m_{VW})$ (black line), represented with its 1 and 2 σ statistical uncertainty (black and green hatched area). The red and blue lines represent the results of the fits to the signal region and to the sideband m_{VW} distribution, respectively, on the W+jets simulation. Right: example of fit to the observed m_{VW} distribution in the lower sideband, to extract the W+jets shape. In the bottom part of the plot, the ratio between the data and the expected total background distribution is also shown, together with its uncertainty represented with a yellow area.

The final m_{VW} shape of the W+jets background in the signal region is then obtained by scaling $F^{W+jets}_{DATA,SB}(m_{VW})$ for the $\alpha_{MC}(m_{VW})$ function. The final prediction of the total background contribution in the signal region can be written as:

$$N^{BKG}_{SR}(m_{VW}) = C^{W+jets}_{SR} \times F^{W+jets}_{DATA,SB}(m_{VW}) \times \alpha_{MC}(m_{VW}) + \sum_k C^k_{SR} F^k_{MC,SR}(m_{VW})$$

where the index k runs over the list of sub-dominant backgrounds, C^{W+jets}_{SR} is the normalization of the W+jets in the signal region and the C^k_{SR} are the yields of the other backgrounds, corrected for the data/Monte Carlo scale factors derived as described in section 4.3.1. The $F^k_{MC,SR}(m_{VW})$ represent the m_{VW} shape of the sub-dominant backgrounds, which are estimated from fit on the corresponding Monte Carlo samples. Different parameterizations are used to model the m_{VW} spectrum of the backgrounds:

$$\begin{aligned} F_{\text{Exp}}(x) &= e^{ax} \\ F_{\text{ExpN}}(x) &= e^{ax+b/x} \\ F_{\text{ExpTail}}(x) &= e^{-x/(a+bx)} \end{aligned} \tag{4.6}$$

The different models are also used to evaluate the uncertainty due to choice of the background modeling function. The use of these models for each background is specified in chapter 5 and 6.

An example of extrapolation of the final m_{VW} total background distribution in the signal region is shown in Figure 4.11.

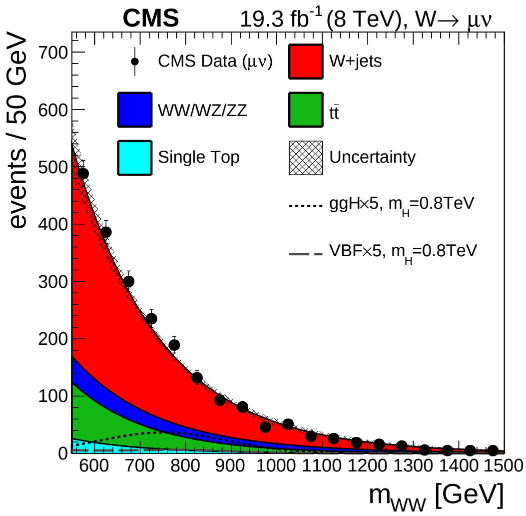

Figure 4.11: Example of extrapolation of the total m_{VW} background distribution in the signal region, compared with the observed data. The contribution of the sub-dominant backgrounds is added to the W+jets distribution derived through the α function.

4.6 Signal modeling

The normalization of the signal process is determined by the theoretical cross section of the model under study, and corrected for the W-tagger scale factor described in section 4.3.1. The m_{VW} signal shape is estimated from an unbinned maximum likelihood fit on the simulated signal samples. The parameterization used to fit the m_{VW} distribution varies depending on the theoretical model considered, therefore it is specified in chapter 5 and 6.

4.7 Statistical interpretation of the results: extraction of the upper limit

Using the estimate of the expected background and the signal contributions described in the previous sections, it is possible to infer a constraint on the validity of the considered model in the mass range under study. If no significant excess is observed in data, an upper limit on the production cross section can be set. The procedure used is based on the modified frequentist approach, often referred to as the asymptotic $\mathrm{CL_s}$ method [77].

4.7.1 Observed Limit

The method to extract the observed limit can be summarized as follows:

- A Likelihood function is defined as:

$$L(\text{data}|\mu, \theta) = \text{Poisson}(\text{data}|\mu \cdot s(\theta) + b(\theta)) \cdot p(\tilde{\theta}, \theta)$$

  where s and b denote the expected signal and background event yields, depending on some set of nuisance parameters θ with observed values $\tilde{\theta}$. In general, the limit is expressed in terms of μ, the signal strength modifier, that changes the signal cross sections of all production mechanisms by exactly the same scale: $\sigma' = \mu \cdot \sigma$.

- To compare the compatibility of the data with the background-only and signal + background hypotheses, where the signal is scaled by the factor μ, a test statistic $\tilde{q}_\mu$ is constructed as follows:

$$\tilde{q}_\mu = -\frac{L(\text{data}|\mu, \hat{\theta}_\mu)}{L(\text{data}|\hat{\mu}, \hat{\theta})}$$

with the constraint $0 \leq \hat{\mu} \leq \mu$; $\hat{\mu}$ and $\hat{\theta}$ are the parameter estimators that maximize the likelihood, while $\hat{\theta}_\mu$ is the value of θ that maximizes the likelihood for a given assumed μ.

- The values of the nuisance parameters $\hat{\theta}_0^{obs}$ and $\hat{\theta}_\mu^{obs}$ best describing the experimentally observed data (i.e. maximising the likelihood) are found, for the background-only ($\mu = 0$) and signal + background hypothesis (with strength μ) respectively. These quantities are used to generate pseudo-data to construct the probability density function (pdf) of the test statistic q_μ under both hypotheses: $f(\tilde{q}_\mu|0, \hat{\theta}_0^{obs})$ and $f(\tilde{q}_\mu|\mu, \hat{\theta}_\mu^{obs})$. Examples of these distributions are shown in Figure 4.12.

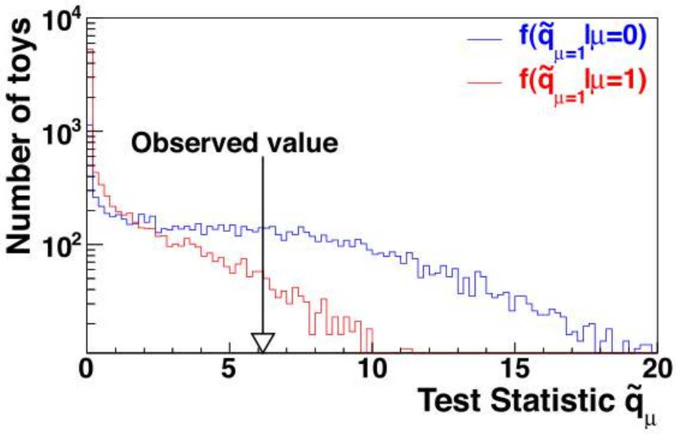

Figure 4.12: Test statistic distributions for ensembles of pseudo-data generated for the signal + background (red) and background-only (blue) hypothesis. The value of q_μ measured from real data is indicated by an arrow.

- For the observed value of the test statistic $\tilde{q}_\mu^{obs}$, two p-values are defined, one for the signal+background hypothesis and the other one for the background-only hypothesis, p_μ and p_b:

$$p_\mu = P(\tilde{q}_\mu \geq \tilde{q}_\mu^{obs}|\text{signal+background}) = \int_{\tilde{q}_\mu^{obs}}^{\infty} f(\tilde{q}_\mu|\mu, \hat{\theta}_\mu^{obs})d\tilde{q}_\mu$$

$$1 - p_b = P(\tilde{q}_\mu \geq \tilde{q}_\mu^{obs}|\text{background-only}) = \int_{\tilde{q}_0^{obs}}^{\infty} f(\tilde{q}_\mu|0, \hat{\theta}_0^{obs})d\tilde{q}_\mu$$

and the CL$_s$ is computed as

$$\text{CL}_s(\mu) = \frac{p_\mu}{1 - p_b}$$

- If, for $\mu = 1$, CL$_s \leq \alpha$, the signal is excluded with $(1 - \alpha)$ CL$_s$ confidence level. To find the 95 % confidence level upper limit on μ (denoted as $\mu^{95\%CL}$), μ is adjusted until CL$_s = 0.05$ is reached.

4.7.2 Expected Limit

The expected limit is computed for the background-only hypothesis: a large set of background-only pseudo-data are generated, and for each of them the CL_s and $\mu^{95\%CL}$ are computed, as if they were real data. Then, it is possible to build a cumulative probability distribution of results by integrating from the side corresponding to low event yields (Figure 4.13). The point at which the cumulative probability distribution crosses the quantile of 50% is the median expected value. The $\pm1\sigma$ (68%) band is defined by the crossing of the 16% and 84% quantiles, while crossings at 2.5% and 97.5% define the $\pm2\sigma$ (95%) band.

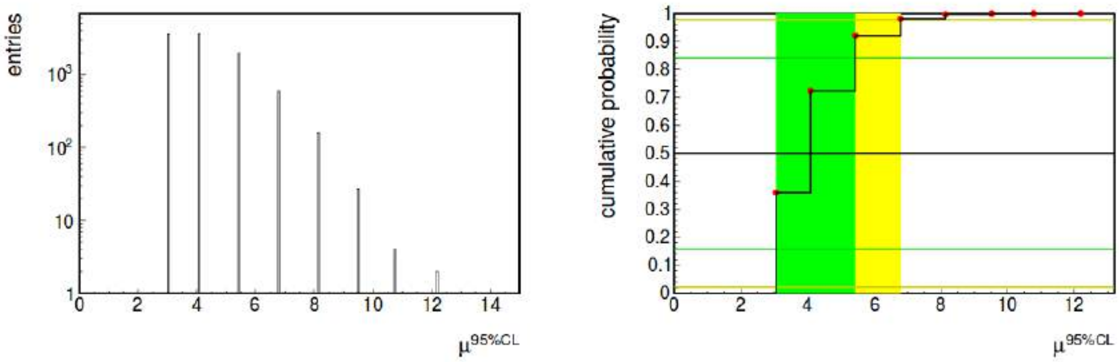

Figure 4.13: Left: an example of the differential distribution of possible limits on μ for the background-only hypothesis. Right: cumulative probability distribution of the left plot with 2.5%, 16%, 50%, 84%, 97.5% quantiles (horizontal lines) defining the median expected limit as well as the $\pm1\sigma$ (68%) and $\pm2\sigma$ (95%) bands for the expected value of μ for the background-only hypothesis.

Chapter 5

Application I: search for heavy Higgs bosons with LHC Run I data

A first analysis which makes use of the techniques described in chapter 4 is presented here. The analysis is based on the data collected at LHC during run I, in 2012. The benchmark signal model considered is a heavy Standard Model Higgs boson with a mass between 0.6 and 1.0 TeV. The results are also interpreted in the context of the Electroweak Singlet Model, described in section 1.6.1.

5.1 Datasets

This analysis is based on proton-proton collision data at $\sqrt{s} = 8$ TeV collected by the CMS experiment at the LHC during 2012 and corresponding to an integrated luminosity of 19.3 fb^{-1} for the muon channel and 19.2 fb^{-1} for the electron channel, approximately. The data have been recorded using triggers which require single electrons or single muons. The details can be found in section 5.2.1.

5.1.1 Signal and background samples

The benchmark signal model considered is a heavy Standard Model Higgs boson with a mass between 0.6 and 1.0 TeV. Several simulated samples are generated for each signal hypothesis, varying the mass of the resonance in the range $0.6-1.0$ TeV. The Monte Carlo signal events are generated with POWHEG [78, 79, 80, 81, 82, 83] with NLO accuracy. Separate samples for the gluon fusion and the vector boson fusion channels are produced.

Different Monte Carlo event generators are used to simulate the signal and the backgrounds. The W+jets processes are simulated using the leading order MADGRAPH generator. Four different W+jets samples are used, each one characterized by a different number of additional jets in the matrix element. This is done in order to ensure an adequate background statistics after the VBF selections. Diboson events are simulated with PYTHIA 6 [84, 85]. The POWHEG program with NLO accuracy is used to provide event samples for single top and $t\bar{t}$+jets processes. The parton showering and hadronization of all samples are performed with PYTHIA using the CUETP8M1 tune [86, 87]. All samples are processed using the GEANT4 [88] simulation of the CMS detector. The simulated background samples are normalized using inclusive cross sections calculated at

next-to-leading order (NLO), or next-to-next-to-leading order (NNLO) where available. The complete list of the Monte Carlo samples used is reported in table 5.1.
The ggH (VBF) signal sample is corrected for the effects of interference between the signal itself and the SM gg→WW (qq→WW) production process. In general, the effect of this correction is to shift the Higgs mass peak to lower masses. The details of this procedure are described in section 5.6.1.

Extra minimum bias interactions are added to the generated events to match the distribution of the number of additional interactions per LHC bunch crossing (pileup) observed in data. The simulated samples are also corrected for the observed differences between data and simulation in the lepton trigger efficiencies, the lepton identification/isolation, and the selection criteria to identify b-tagged jets.

Process (GeV)	σ x BR (pb)	Generator
W+1 jet	5400	MADGRAPH
W+2 jets	1750	MADGRAPH
W+3 jets	519	MADGRAPH
W+4 jets	211	MADGRAPH
$t\bar{t}$+jets	225.197	POWHEG
t-s ch.	3.79	POWHEG
$\bar{t}$-s ch.	1.76	POWHEG
t-t ch.	56.4	POWHEG
$\bar{t}$-t ch.	30.7	POWHEG
tW	11.1	POWHEG
$\bar{t}$W	11.1	POWHEG
WW	54.838	PYTHIA 6
WZ	33.21	PYTHIA 6
ZZ	8.051	PYTHIA 6
Z/γ+jets	3053.71	MADGRAPH
QCD (μ)	$\sim$ 6740000	-
QCD (e)	$\sim$ 84700	-

Table 5.1: Cross section values for every background process; the values are multiplied by the proper branching ratio for the $l\nu q\bar{q}$ final state. For every background the Monte Carlo generator used is also reported.

5.2 Event selection

In order to isolate a boosted topology consistent with the VW system, events are selected requiring one energetic lepton (electron or muon), large $\not\!\!E_T$ and one merged jet in the final state. A summary of the main selections used is given in the following.

5.2.1 Lepton selection

Two levels of selections (online and offline) are applied to select events with one energetic lepton.

Candidate signal events are selected online using triggers which require one electron or one muon. Isolation criteria are applied. For the muon channel, the presence is required of at least a single isolated muon with a p_T threshold of 24 GeV. For the electron channel, events are selected requiring at least a single isolated electron with a p_T threshold of 27 GeV.

Offline level, the muon candidates are required to have $p_T > 30$ GeV, while the requirement for the electrons is $p_T > 35$ GeV. Several ID criteria are also used to classify muon and electron candidates in the analysis. The complete description of the ID selections can be found in appendix A.
In the muon channel, events are required to have exactly one tight muon, while in the electron channel, events should have exactly one tight electron. Events with additional muons or electrons are rejected.

5.2.2 Jet selection

In this analysis, the large-cone jets used to select the boosted hadronic V boson candidate are reconstructed using the Cambridge-Aachen algorithm with distance parameter of R = 0.8 (CA8 jets). The anti-k_T jets with distance parameter of R = 0.5 (AK5 jets) are instead used as small-cone jets.

All jets used in the analysis must satisfy the loose jet ID requirements, described in appendix A. Charged hadron subtraction [75] is also applied to the jets, in order to reduce contamination from pileup. All jets are corrected applying the L1, L2, and L3 energy corrections both in data and simulation (section 2.3.3). In addition, the L2+L3 residual corrections are applied to data.

The hadronic V candidate is selected as the CA8 jet with largest p_T, with the requirement $p_T > 200$ GeV and $|\eta| < 2.4$. CA8 jets within $\Delta R < 1.0$ of any tight electron or tight muon defined as in the previous section are discarded from the analysis.

The AK5 jets with $p_T > 30$ GeV and $|\eta| < 4.7$ are also used in the analysis. The looser requirement in η of the AK5 jets with respect to the CA8 jets is needed for the VBF topology, since the tag jets have in general large pseudorapidity. These jets should not lie within the cone of the selected CA8 jet ($\Delta R > 0.8$) and they must be separated ($\Delta R > 0.3$) from any tight electron or tight muon, otherwise they are not considered. Cuts on additional heavy flavor jet activity in the event are also applied, to reduce the amount of $t\bar{t}$ background. A jet is considered to be b-tagged if it passes the medium working point (corresponding to 0.679) of the particle flow inclusive combined secondary vertex (CSV) run I algorithm [89]. The event is required to have zero b-tagged AK5 jets.

5.2.3 Angular selection

The signal is characterized by a topology with two boosted vector bosons which are back-to-back in the transverse plane. In order to isolate such a topology, the following angular selections are applied:

- The ΔR between the lepton and the hadronic V boson candidate, $\Delta R(\ell, V_{had})$, must be larger than $\pi/2$;
- The separation in the transverse plane, $\Delta\phi$, between the hadronic V boson candidate and the missing transverse energy, $\Delta\phi(V_{had}, \not{E}_T)$, must be larger than 2.0;
- The $\Delta\phi$ between the hadronic V boson candidate and the reconstructed leptonic W boson, $\Delta\phi(V_{had}, W_{lep})$, must be larger than 2.0.

Summary of event selection

The summary of the event selection is the following:

1. exactly one charged tight lepton;
2. lepton veto: no additional loose electrons or muons;
3. missing transverse energy: events are required to have $\not{E}_T > 70$ GeV in the electron channel and $\not{E}_T > 50$ GeV in the muon channel to suppress contributions from QCD multijet backgrounds;
4. leptonic W p_T: the p_T of the reconstructed leptonic W boson must be larger than 200 GeV;
5. hadronic V p_T: the p_T of the reconstructed hadronic V boson (selected as the CA8 leading jet) must be larger than 200 GeV;
6. b-tag veto: the event is required to have no AK5 jets identified as b-jets;
7. angular selections to select a diboson-like topology:
   - $\Delta R(\ell, V_{had}) > \pi/2$
   - $\Delta\phi(V_{had}, \not{E}_T) > 2.0$
   - $\Delta\phi(V_{had}, W_{lep}) > 2.0$

5.2.4 Additional selections on the hadronic V boson

A first categorization of the events is performed using the pruned jet mass. As described in chapter 4, this is in fact one of the most powerful observables between signal and background. The following disjoint pruned jet mass regions are defined:

- Low sideband (LSB): defined as $40 < m_J < 65$ GeV
- Signal Region (SR): defined as $65 < m_J < 105$ GeV
- High sideband (HSB): defined as $105 < m_J < 130$ GeV

As described in section 4.5, the sideband regions are used to extract the normalization and shape of the W+jets background.

In addition, a selection on the N-subjettiness is also applied, keeping only events with $\tau_{21} < 0.5$.

5.3 Definition of jet bin categories

In order to enhance the sensitivity of the analysis, two categories are defined, using the number of AK5 jets (which must satisfy the requirements described in section 5.2.2) in the event:

- 0-1 jet bin category: events containing 0 or 1 additional AK5 jets;
- 2 jet bin category; events containing 2 or more additional AK5 jets.

This categorization allows a dedicated search to be performed via the VBF process. Further kinematic requirements, described below, are applied in the 2-jet bin category in order to better identify the VBF production mode. Furthermore, in the 0-1 jet bin category the analysis is performed separately for the electron and the muon channels, while in the 2-jet bin case the two samples are merged together in order to recover statistics in the sidebands after applying the VBF selections.

5.3.1 Identification of the VBF topology and optimization of the VBF selections

In the 2-jet bin category, only the events with at least two AK5 jets are kept. The AK5 collection is used to identify the two tag jets which characterize the VBF process. The tag jets are chosen as the two AK5 jets with the largest p_T. From studies on simulated samples, it has been checked that this is the choice which gives the best geometrical matching between the reconstructed jets and the corresponding tag quarks at generator level, and that leads to the best signal-over-background ratio in the analysis region.

Additional selections are applied in the 2-jet bin category in order to further enhance the sensitivity of the VBF search. As stated before, the two primary observables used to discriminate the VBF topology against the background are the $\Delta\eta_{\mathrm{jj}}$ and M_{jj}. However, further selections can be applied, in particular to suppress the contribution from $t\bar{t}$ and single top backgrounds. The following two variables are defined:

- Hadronic top mass ($m_{\mathrm{W_{had}+j}}$): the invariant mass of the system constituted by the selected hadronic V boson and its closest AK5 jet.
- Leptonic top mass ($m_{\mathrm{W_{\ell}+j}}$): the invariant mass of the system constituted by the reconstructed leptonic W boson and its closest AK5 jet.

For $t\bar{t}$ and single top events, the system composed by the leptonic (or hadronic) W boson with its closest jet contains, in most cases, the products of the top quark decay, thus the distribution of these two variables shows a peak around the top quark mass. Therefore, it is possible to reject these events by requiring that the value of these observables is far from the mass of the top quark.
A simultaneous optimization is performed on these four observables ($\Delta\eta_{\mathrm{jj}}$, M_{jj}, $m_{\mathrm{W_{had}+j}}$, $m_{\mathrm{W_{\ell}+j}}$) to determine the best working points for each of them. The figure of merit used in the optimization is $\frac{S}{\sqrt{S+B}}$. The results of this study are shown in Figure 5.1 with the ROC curve, which shows the fraction of rejected background as a function of the signal efficiency, and with the curve of the significance versus signal efficiency. The final choice for the selections is the following:

- $\Delta\eta_{\mathrm{jj}} > 3$
- $m_{jj} > 250$ GeV
- $m_{W_{had}+j} > 200$ GeV
- $m_{W_{\ell}+j} > 200$ GeV

This choice corresponds to a signal efficiency of about 80% and a background rejection of about 85%.
A summary of all the selections and categories described in section 5.2.2 and section 5.3 is reported in table 5.2.

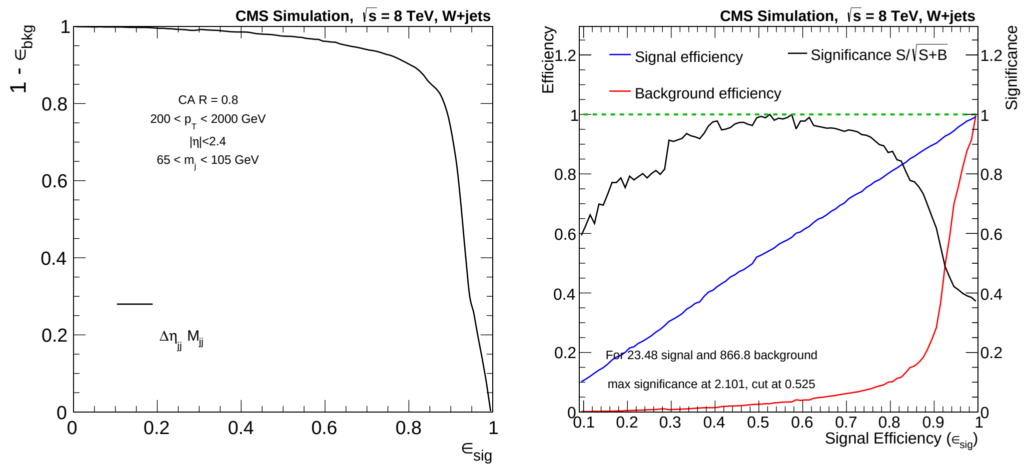

Figure 5.1: Optimization of the VBF cuts. Left: ROC curve. Right: significance versus signal efficiency (black), signal efficiency (blue), background efficiency (red).

Selection	Value	Comments
Lepton selections		
Electron	$p_T > 35$ GeV	
	$\lvert\eta\rvert < 2.5$	(except $1.44 < \lvert\eta\rvert < 1.57$)
Muon	$p_T > 30$ GeV	
	$\lvert\eta\rvert < 2.1$	
Number of electrons	exactly 1	
Number of muons	exactly 1	
AK4 jet selections		
Jet p_T	$p_T > 30$ GeV	
Jet η	$\lvert\eta\rvert < 4.7$	
Number of b-tagged AK4 jets	0	
p_T selections		
p_T (electron channel)	$p_T > 70$ GeV	
p_T (muon channel)	$p_T > 50$ GeV	
Boson selections		
W $\rightarrow \ell\nu$	$p_T > 200$ GeV	
V $\rightarrow q\bar{q}$ (AK8 jet)	$p_T > 200$ GeV	
	$\lvert\eta\rvert < 2.4$	
Back-to-back topology	$\Delta R(\ell, V_{had}) > \pi/2$	
	$\Delta\phi(V_{had}, \not{E}_T) > 2$	
	$\Delta\phi(V_{had}, W_{lep}) > 2$	
Pruned jet mass	$65 < m_J < 105$ GeV	
2- to 1-subjettiness ratio	$\tau_{21} < 0.50$	
Categories (jet bin)		
0-1 jet bin	0-1 AK4 jets	ggH category
2- jet bin	≥ 2 AK4 jets	VBF category
VBF selections (2-jet bin category)		
$\Delta\eta_{\rm jj}$	$\Delta\eta_{\rm jj} > 3$	
M_{jj}	$M_{jj} > 250$ GeV	
Hadronic top mass	$m_{W_{had}+j} > 200$ GeV	
Leptonic top mass	$m_{W_{\ell}+j} > 200$ GeV	

Table 5.2: Summary of the event selection and categories.

5.4 Data/simulation comparison

In this section different comparison plots between data and simulation for key observables are shown, for both muon and electron channels and for the different jet bin categories, in various kinematic regions.

5.4.1 Data/simulation comparison for the 0-1 jets category

The plots shown in this section are produced applying the event selection reported in section 5.2, using events in both the jet mass sidebands and the signal region.
In the plots, the number of MC events are normalized to the luminosity. Residual data/MC discrepancies in the normalization are removed by correcting the W+jets background to match the number of events in data.
Figure 5.2 shows the lepton p_T distribution and the $\not{E}_T$.
The main observables for the hadronic leg are shown in Figure 5.3: the AK8 jet p_T, the pruned mass and the N-subjettiness.
A good agreement is generally observed between data and simulation, especially in the lepton p_T distribution. Some mismodeling is observed in the distributions of the substructure variables, in particular in τ_{21}. However, since the estimate of the contribution of the main background (W+jets) is obtained from data, as described in section 4.5, the analysis is robust against these small disagreements between data and simulation.

5.4.2 Data/simulation comparison for the 2-jets category

The same plots presented in the previous section are shown here for the 2-jet category. As before, the plots are obtained applying the event selections reported in section 5.2, using events in both jet mass sideband and signal region.
In the plots, the number of MC events are normalized to the luminosity. Residual data/MC discrepancies in the normalization are removed by correcting the W+jets and the $t\bar{t}$ background to match the number of events in data.
Figure 5.4 shows the lepton p_T distribution and the $\not{E}_T$.
The main observables for the hadronic leg are shown in Figure 5.5: the AK8 jet p_T, the pruned mass and the N-subjettiness.
Finally, the main observables used for the VBF selections are shown in Figure 5.6: the $\Delta\eta$ between the two tag jets, $\Delta\eta_{jj}$, and the invariant mass of the tag jets system, M_{jj}.
The plots show in general a good agreement between data and simulation, especially in the muon channel.

5.4.3 W-tagger validation and scale factors in $t\bar{t}$ control region

As described in section 4.3.1, the performance of the substructure observables on merged V bosons can be checked using a control sample of almost-pure hadronic W bosons, which can be selected in data using $t\bar{t}$ events. In order to isolate a top-enriched region, the cuts reported in section 5.2 are applied, removing the angular selections and reversing the b-veto condition (i.e. at least one b-jet in the event). The remaining sample is an almost pure sample of $t\bar{t}$ events, with only a small contamination from the other backgrounds. The distribution of the two substructure observables used in the analysis, i.e. the pruned jet mass and the N-subjettiness, are shown in Figure 5.7 for the 0-1 jet category.
This sample of almost pure $t\bar{t}$ events is used to extract data/MC scale factors, as described in section 4.3.1. The measured data-to-simulation scale factors are reported in Table 5.3.

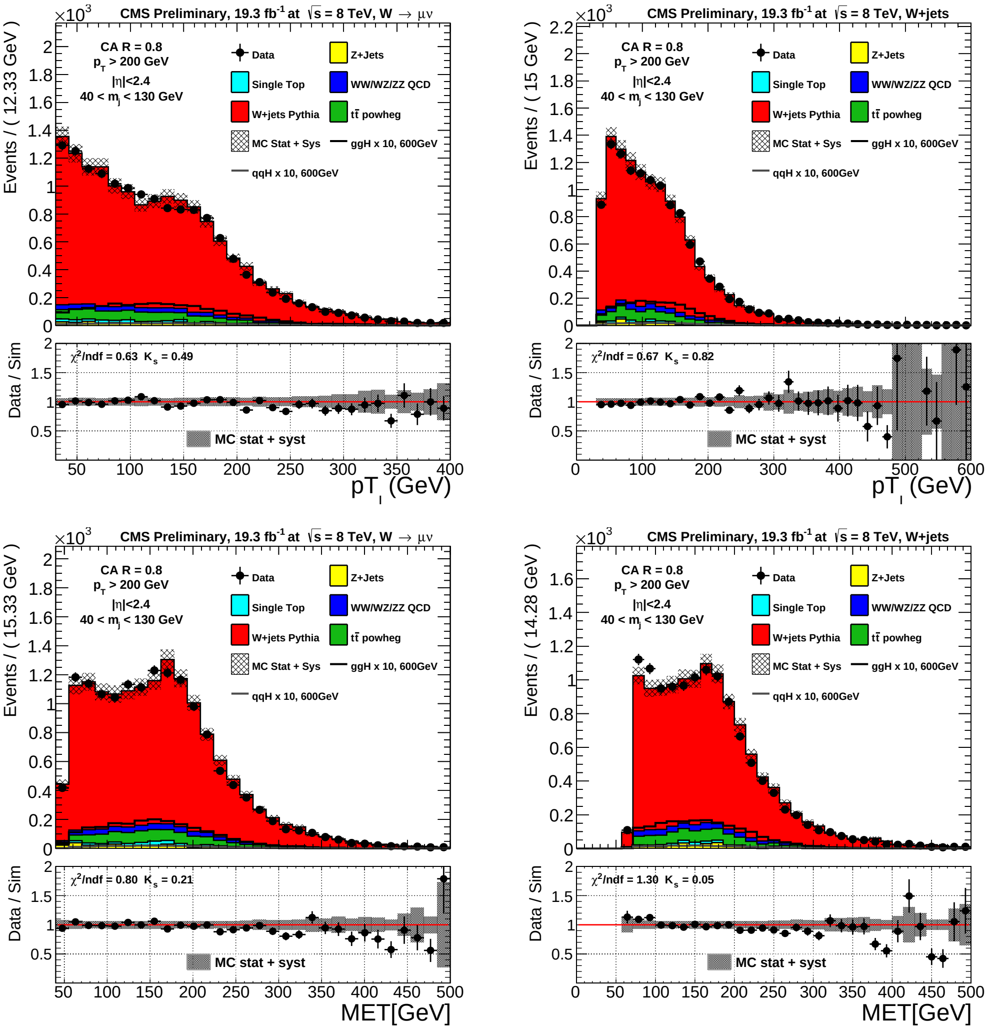

Figure 5.2: Comparison plots between data and simulation for different observables in the 0-1 jet category. From top to bottom: lepton p_T and $\not{E}_T$. Left: muon channel, right: electron channel. Data are represented by black dots. The bottom part of each plot shows the ratio between the events in data and in the MC. The statistical uncertainty of the MC is also shown by the grey area.

Definition	Top scale factor	W scale factor
$\tau_{21} < 0.50$ 0-1 jet category (μ-channel)	0.91 ± 0.08	0.93 ± 0.09
$\tau_{21} < 0.50$ 0-1 jet category (e-channel)	0.89 ± 0.08	0.93 ± 0.09
$\tau_{21} < 0.50$ 2-jet category (μ+e-channel)	1.09 ± 0.25	0.93 ± 0.09

Table 5.3: Data-to-simulation top- and W- scale factors extracted with the W-tagger procedure, for the electron and the muon channel.

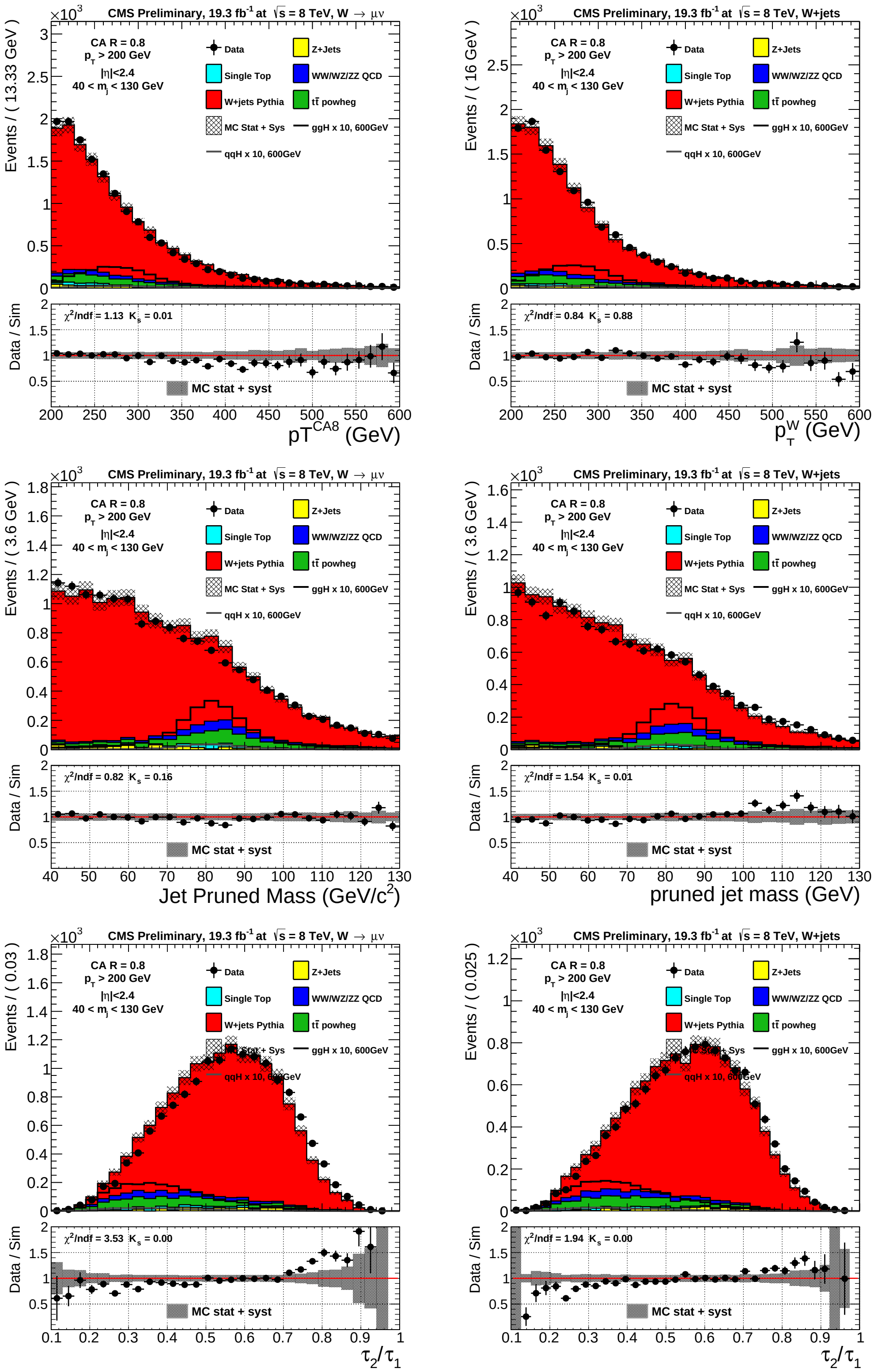

Figure 5.3: Comparison plots between data and simulation for different observables in the 0-1 jet category. From top to bottom: AK8 jet p_T, pruned jet mass and N-subjettiness τ_{21}. Left: muon channel, right: electron channel. Data are represented by black dots. The bottom part of each plot shows the ratio between the events in data and in the MC. The statistical uncertainty of the MC is also shown by the grey area.

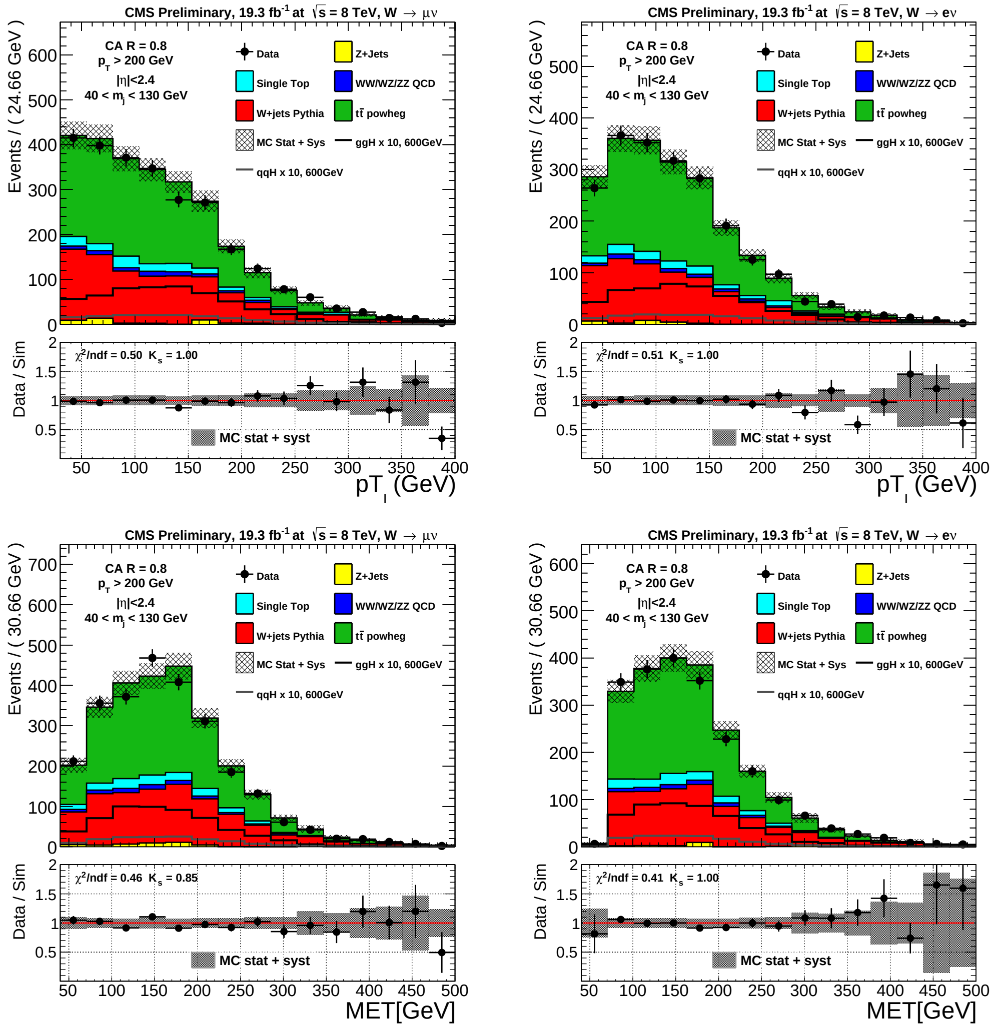

Figure 5.4: Comparison plots between data and simulation for different observables in the 2-jet category. From top to bottom: lepton p_T and $\not{E}_T$. Left: muon channel, right: electron channel. Data are represented by black dots. The bottom part of each plot shows the ratio between the events in data and in the MC. The statistical uncertainty of the MC is also shown by the grey area.

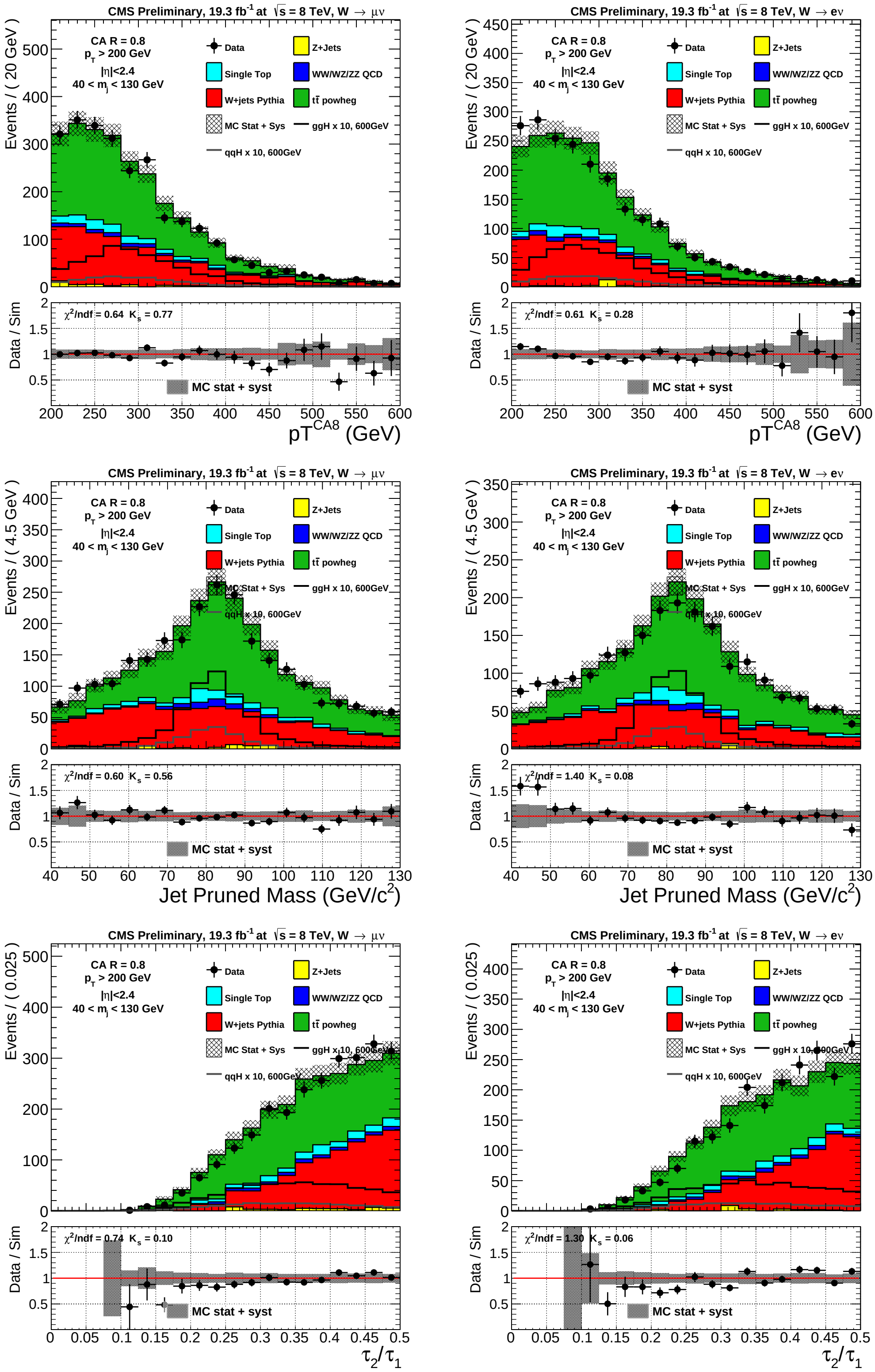

Figure 5.5: Comparison plots between data and simulation for different observables in the 2-jet category. From top to bottom: AK8 jet p_T, pruned jet mass and N-subjettiness τ_{21}. Left: muon channel, right: electron channel. Data are represented by black dots. The bottom part of each plot shows the ratio between the events in data and in the MC. The statistical uncertainty of the MC is also shown by the grey area.

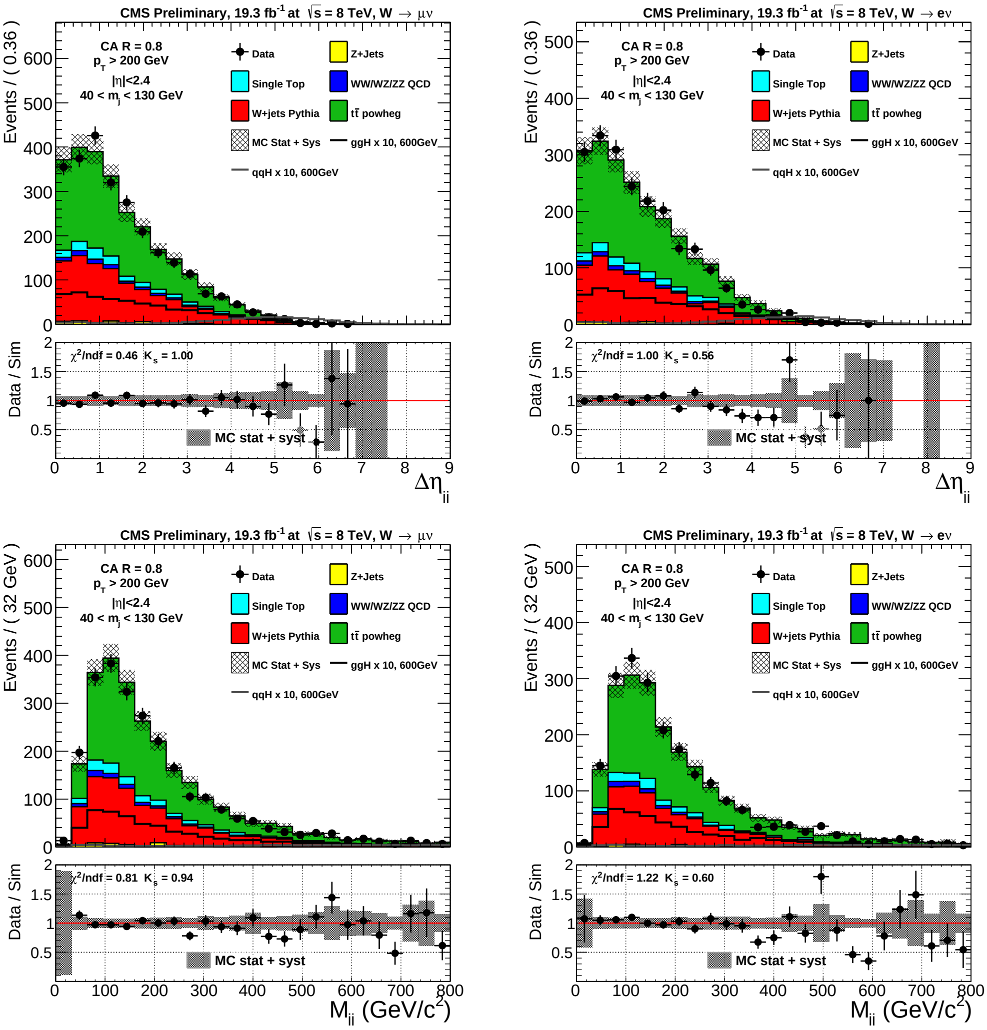

Figure 5.6: Comparisons plots between data and simulation for different observables in the 2-jet category. Top: $\Delta\eta_{jj}$, bottom: M_{jj}. Left: muon channel, right: electron channel. Data are represented by black dots. The bottom part of each plot shows the ratio between the events in data and in the MC. The statistical uncertainty of the MC is also shown by the grey area.

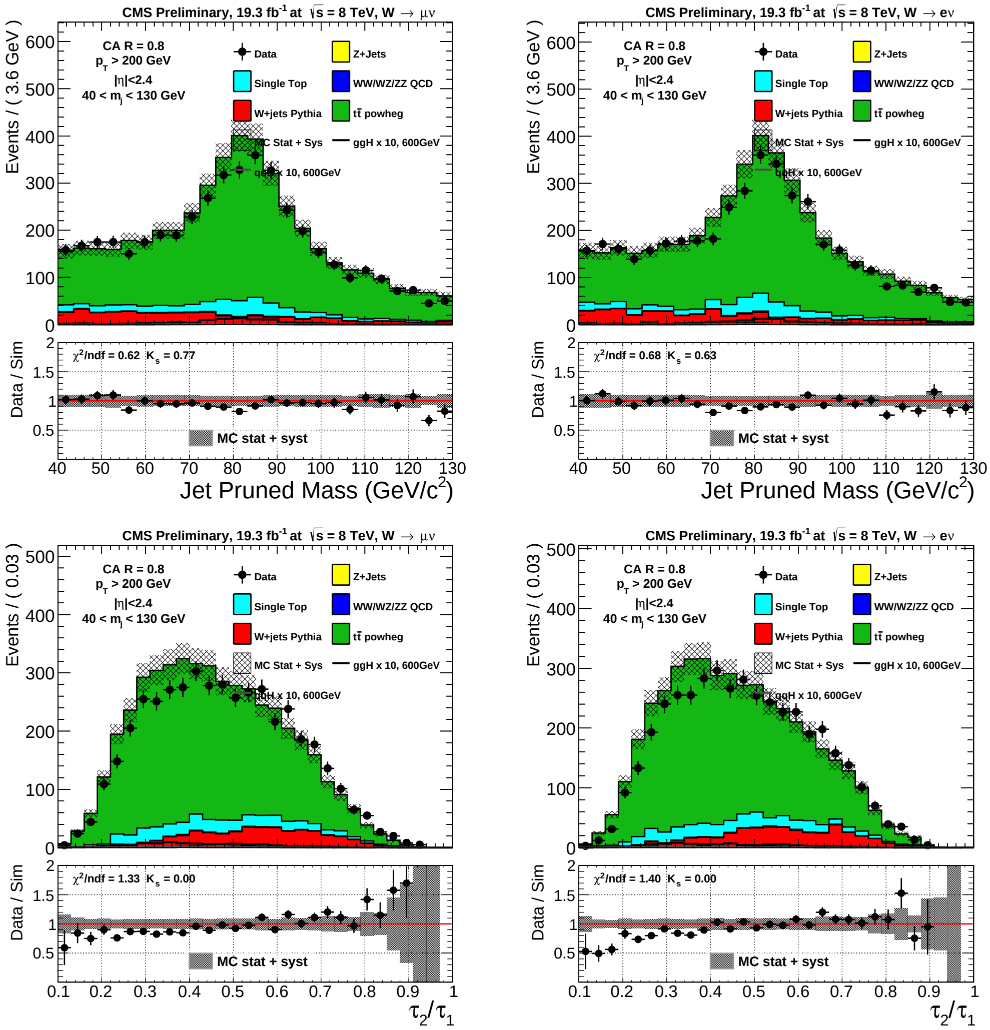

Figure 5.7: Comparison plots between data and simulation for different observables, in the $t\bar{t}$ control region. Top: pruned jet mass. Bottom: N-subjettiness. Left: muon channel, right: electron channel. Data are represented by black dots. The bottom part of each plot shows the ratio between the events in data and in the MC. The statistical uncertainty of the MC is also shown by the grey area.

In addition, the W-jet mass peak position and resolution are extracted from the same fit. The results are presented in Table 5.4. The mass peak position is slightly shifted with respect to the W-boson mass due to the presence of extra energy deposited in the jet cone coming from pileup, underlying events, and initial-state radiation not completely removed by the pruning procedure. Additional energy contributions can also come from the possible presence of a b jet close to the W boson in events with top quarks. These numbers are used to correct the mass peak position and resolution in the MC, to match the one observed in data.

$\tau_{21} < 0.45$	m [GeV]	σ [GeV]
Data	84.1 ± 0.4 GeV	8.4 ± 0.6 GeV
Simulation	82.7 ± 0.3 GeV	7.6 ± 0.4 GeV

Table 5.4: W-jet mass peak position and resolution, as extracted from a top enriched data sample and from simulation.

5.5 Background estimation

In the following the estimation of the background through the alpha method, described in section 4.5, is presented.

5.5.1 W+jets normalization

The normalization of the W+jets in the signal region is extracted from a fit to the m_J distribution in data using events in the sideband regions only. The single top, VV and $t\bar{t}$ samples are instead normalized based on the theoretical calculation of their cross sections, and corrected using the scale factors obtained in section 5.4.3, with the top scale factor being used for single top and $t\bar{t}$, while the W scale factor is used for VV. The different background contributions are described using functional forms determined through fits to the simulated samples. The complete list of analytical models used in the fits is given in section 4.5. Table 5.5 reports which function is used to model each background.

W+jets	$t\bar{t}$	Single Top	VV
F_{ErfExp}	$F_{\text{ErfExp2Gaus}}$	$F_{\text{ErfExpGaus}}$	F_{2Gaus}

Table 5.5: Summary of the shapes used for the fits to the m_j spectrum of each background component.

Figure 5.8 shows examples of the MC fits for the non-dominant backgrounds, for the muon channel, in the 0-1 jet category. The sideband fits to the m_J observed distribution to extract the W+jets normalization are shown instead in Figure 5.9.

5.5.2 W+jets shape

The functional forms chosen to fit the m_{VW} distribution are described in section 4.5. In Table 5.6 it is specified which function is used to model each background, in the different analysis regions.

In the sideband region, the contribution of the non-dominant backgrounds is extracted from a fit to the simulation. A fit to data in the lower sideband region is then performed

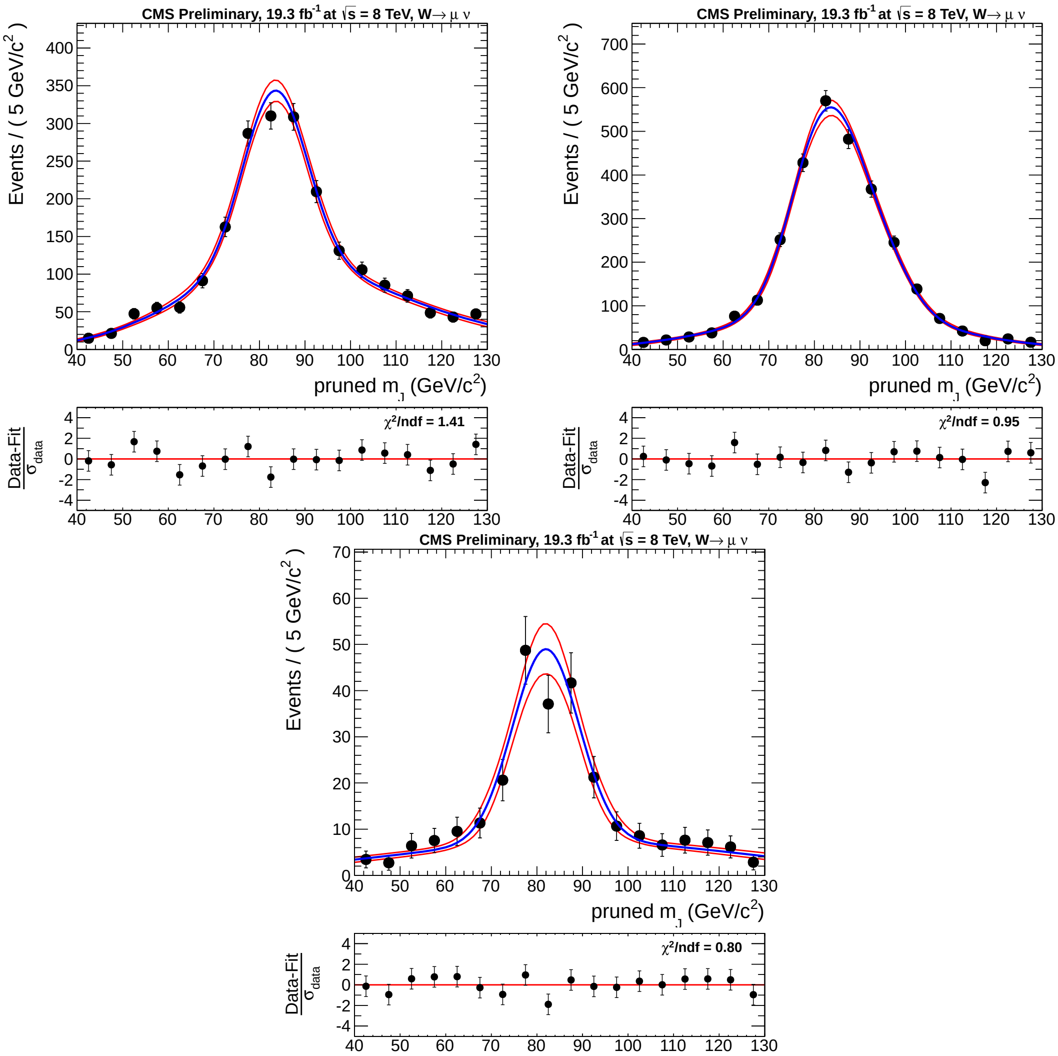

Figure 5.8: MC fits of the non-dominant background m_J spectra. On the top: $t\bar{t}$ (left) and diboson (right), on the bottom: single top. The red lines represent the contour of the uncertainty band of the fit. On the bottom of each plot, the bin-by-bin fit residuals, $(N_{Data} - N_{Fit})/\sigma_{data}$, are shown.

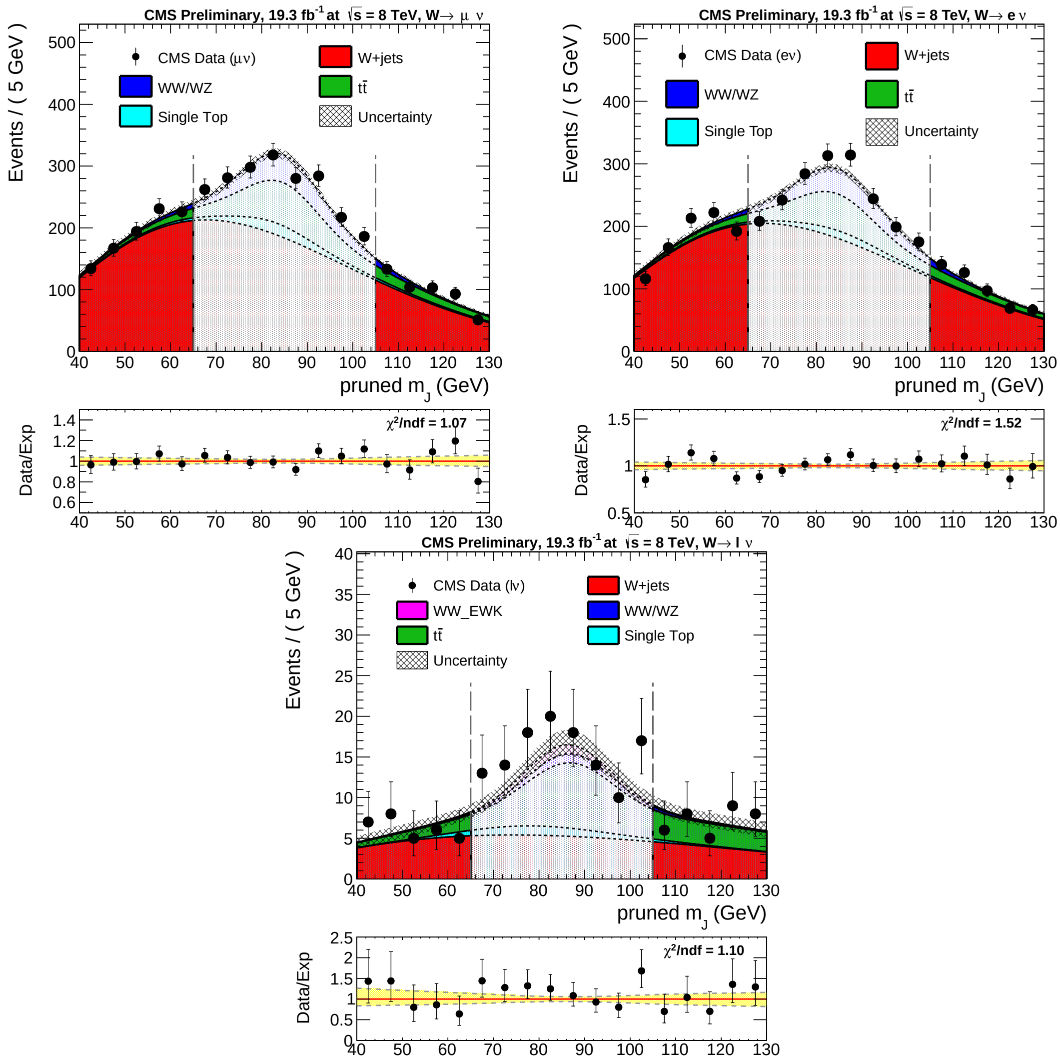

Figure 5.9: Fits to extract the relative shape and normalization of the W+jets contribution from the data in the jet mass distribution. Top: 0-1 jet category (left: muon channel, right: electron channel). Bottom: 2-jet category. Data are shown as black markers. All selections are applied except the final m_J signal window requirement. The borders of the signal region are indicated by the vertical lines. At the bottom of each plot, the bin-by-bin fit residuals, $(N_{Data} - N_{Fit})/\sigma_{data}$, are shown together with the uncertainty band of the fit normalized by the statistical uncertainty of data, σ_{data}.

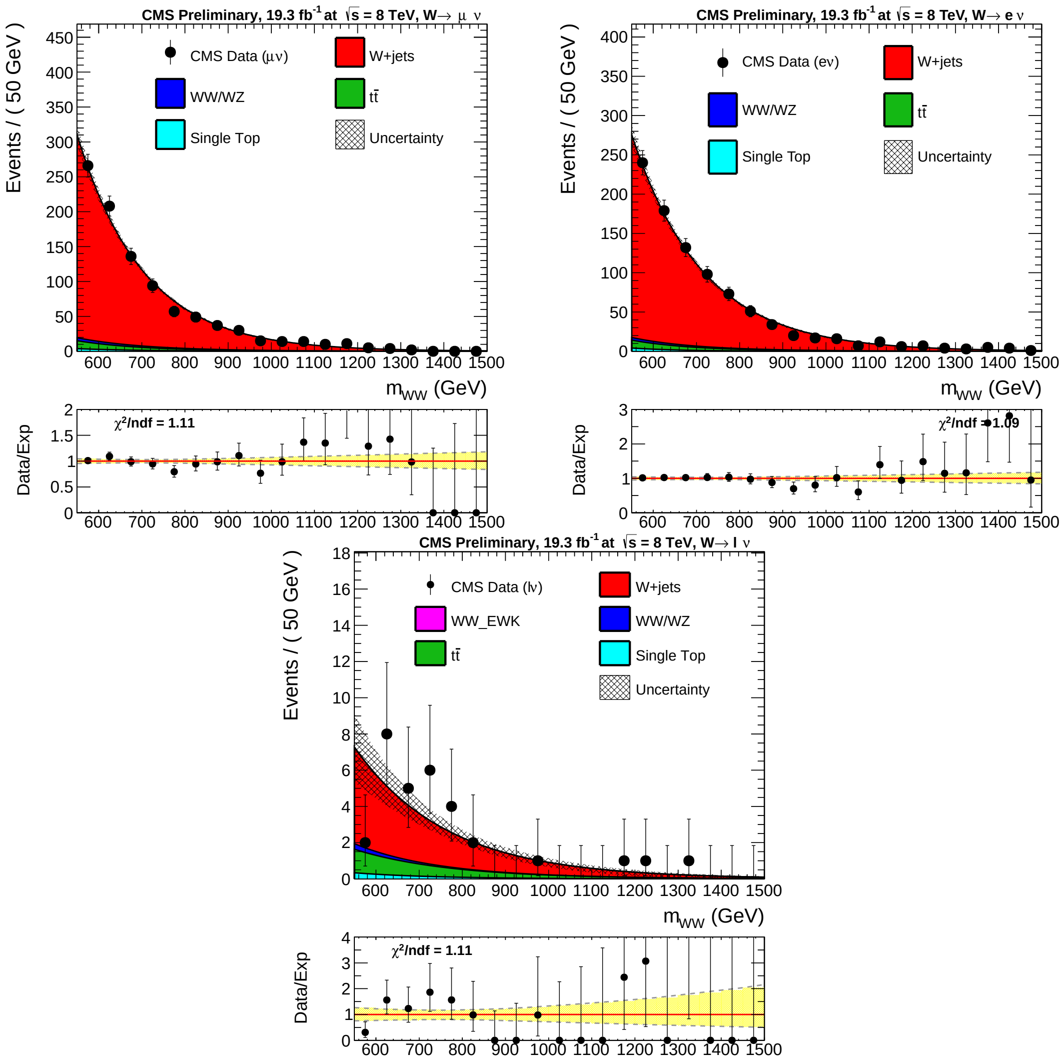

Figure 5.10: Fits to extract $F_{data,LSB}(m_{VW})$ from data. Top: 0-1 jet category (left: muon channel, right: electron channel). Bottom: 2-jet category. On the bottom of each plot, the bin-by-bin fit residuals, $(N_{Data} - N_{Fit})/\sigma_{data}$, are shown.

m_J region	W+jets	$t\bar{t}$	Single Top	VV
Sideband	F_{Exp}	F_{Exp}	F_{Exp}	F_{Exp}
Signal region	F_{Exp}	F_{Exp}	F_{Exp}	F_{Exp}

Table 5.6: Summary of the shapes used for fit the m_{VW} spectra of each background component.

to extract the W+jets shape $F_{data,LSB}(m_{VW})$, subtracting the contribution of the other backgrounds. The fit to the data in the lower sideband region is shown in Figure 5.10. The W+jets shape in the signal region is then extrapolated using the alpha method described in section 4.5, and corrected for the contribution of the sub-dominant backgrounds. The signal region fits for the non-dominant backgrounds are shown as example in Figure 5.11 for the muon channel in the 0-1 jet category. Figure 5.12 shows instead the α functions used to extrapolate the W+jets shape in the 0-1 jet (left) and the 2-jet (right) category for the muon channel. The final extrapolation of the background contribution into the signal region is presented in section 5.7.

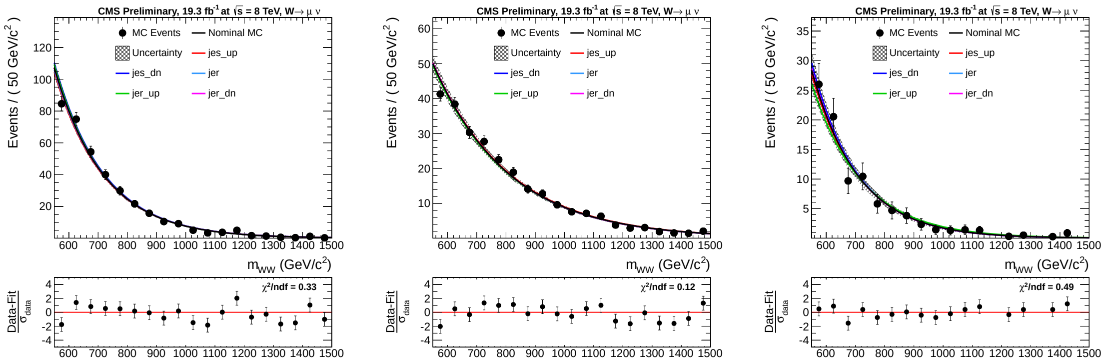

Figure 5.11: MC fits of background m_{VW} spectra in the m_J signal region for events in the 0-1 jet category. From left to right: $t\bar{t}$, diboson, single top process. On the bottom of each plot, the bin-by-bin fit residuals, $(N_{Data} - N_{Fit})/\sigma_{data}$, are shown. The variations of the fits varying up and down the jet energy scale and resolution are also shown with different colours; for details on this procedure see section 5.8.

5.5.3 Estimation of the $t\bar{t}$ background in the 2-jet category

As shown in the control plots in section 5.4.2, the fraction of background from $t\bar{t}$ becomes much larger in the 2-jet category with respect to the 0-1 jet category. In the 0-1 jet category, the top control region is used to obtain a normalization scale factor to renormalize the $t\bar{t}$ simulation, while the m_{VW} shape in the m_J signal region is taken directly from simulation. In order to adopt the same procedure also in the 2-jet category, a new top control region should be defined, starting from the default one (with the different requirement on the number of jets) and adding the selections of the 2-jet category (VBF and top mass cuts). However, the statistics is not sufficient in order to extract scale factors with a reasonable uncertainty.

The solution adopted is to check the behaviour of the normalization scale factors and the m_{VW} shape in different control regions, starting from the default one and adding one by one various selections to approach the 2-jet category signal region. If the scale factors and the shapes do not change significantly when moving from one region to the others, it is

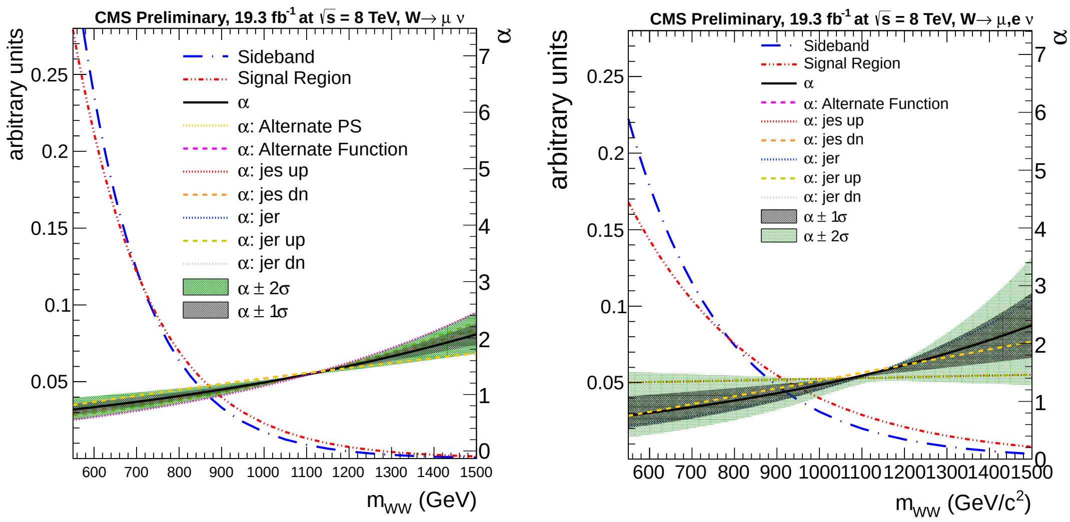

Figure 5.12: The $\alpha_{MC}(m_{VW})$ functions used to extrapolate the W+jets m_{VW} shape in the 0-1 jet category (left) for the muon channel and in the 2-jet category (right). The black and the green hatched areas represent the 1 and 2 σ statistical uncertainty band. The red and blue lines represent the results of the fits to the signal region and to the sideband m_{VW} distribution, respectively, on the W+jets simulation. The variations of the $\alpha_{MC}(m_{VW})$ using an alternative model and varying up and down the jet energy scale and resolution are also shown with different colours; for details on this procedure see section 5.8.

justified to use the scale factor from the default region (where the uncertainty is small), and the m_{VW} shape in the signal region can be taken directly from the simulation.

For this procedure, the following regions are defined:

{a}: Standard top-enriched control region (with $N_{jets} > 2$)

{b}: {a} + VBF cuts ($\Delta\eta_{jj} > 3$ && $M_{jj} > 250$ GeV)

{c}: {a} + top mass veto ($m^{top}_{W_{\rm had}+j} > 200$ GeV && $m^{top}_{W_{\rm lep}+j} > 200$ GeV)

{d}: {a} + top mass tag ($m^{top}_{W_{\rm had}+j} < 200$ GeV && $m^{top}_{W_{\rm lep}+j} < 200$ GeV)

{e}: {a} + {b} + {c}

{f}: {a} + {b} + {d}

In order to have a significant amount of data and MC in the regions with the tightest cuts, events from electron and muon channels are merged together. In addition, two different $t\bar{t}$ simulation samples are compared (Powheg + Pythia and MC@NLO + Herwig). Figure 5.13 shows the m_{VW} distributions in the m_J signal region, for each of the different regions defined above.

The data/MC normalization scale factors are evaluated for each of the six regions. Their values are summarized in Figure 5.14, and it can be seen that the numbers are compatible with each other within their statistical error. Therefore, it is possible to use the scale factors (together with their uncertainty) derived in the standard top control region in the signal region as well, after applying the VBF and the top mass selections.

The m_{VW} shape is also checked through the different control regions, and by comparing the two different generators, Powheg + Pythia and MC@NLO + Herwig. Figure 5.13 shows that the shapes do not show significant changes moving from one region to the other, with a general reasonable data/MC agreement. Moreover, the two generators give similar results, despite different matrix element level and parton shower simulations. Therefore, it is reasonable to extract the shapes of the $t\bar{t}$ background directly from the simulation.

5.6 Signal modeling

The signal benchmark considered in this analysis is a heavy Higgs boson, with Standard Model properties, with a mass ranging between 0.6 and 1.0 TeV. In addition, results are interpreted in the Electroweak Singlet Model (EWSM), described in section 1.6.1. Both the production via gluon fusion and via vector boson fusion are taken into account, therefore two different signal samples are used for each mass point. The normalization of the signal is taken from the cross section value of the corresponding process, and corrected for the efficiency after applying the analysis selections. The m_{VW} shape of the signal processes is instead extracted from a fit on the simulation, and corrected for interference effects of the signal process with the SM background. This procedure is described in section 5.6.1, while the results of the fits to extract the final shape are presented in section 5.6.2.

5.6.1 Interference effects

In order to obtain the correct m_{VW} lineshape for the signal, the quantum interference between signal and background diagrams must be taken into account, since they can modify significantly the resonance shape. The interference effects between the Higgs production and the background processes are estimated in a different way in the ggH and the VBF channels.

In the gluon fusion case, the interference process considered is the one between the non-resonant gg→WW background and the H→WW production via gluon fusion. The contribution of the interference is assumed to scale according to the modified coupling of the Higgs boson as:

$$\mu(I)_{BSM} = \mu_{SM} \cdot C'^2 + I_{SM} \cdot C'$$

where $\mu(I)$ is the signal+interference strength in the EWSM case, μ_{SM} is the Standard Model signal strength, C' is the scale factor of the coupling of the heavy Higgs with respect to the SM one, and I_{SM} is the contribution of the interference process. This assumption is based on the hypothesis that the couplings are similar to the SM case and simply rescaled due to unitarity constraints.

In the VBF case, the interference effect is simulated by reweighting the signal-only m_{WW} shape, so to reproduce the trend expected when also the presence of the continuum qq→WW is accounted for in the simulation. The reweighting factor is calculated with the PHANTOM generator, that allows for the production of signal-only events (S), as well as the total calculation, including signal, background (B) and interference with the background (I). The scale factor is obtained as:

$$w(m_{WW}) = \frac{(S + I + I_{125})(m_{WW})}{S(m_{WW})} \tag{5.1}$$

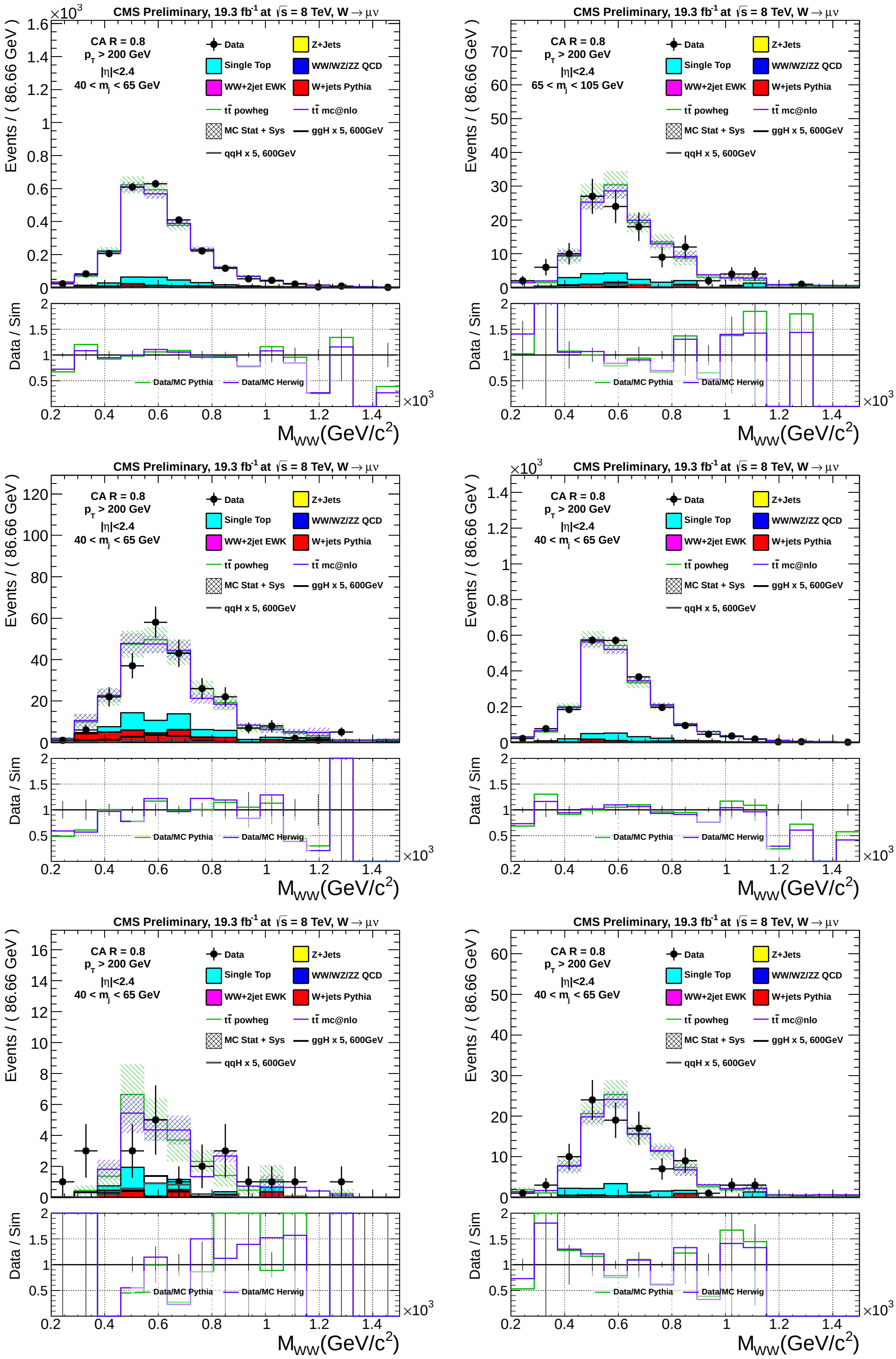

Figure 5.13: Invariant mass distribution m_{VW}, in the six different top enriched control regions obtained adding various selections to the default control region. Top left is region {a}, top right is {b}, middle left is {c}, middle right is {d}, bottom left is {e}, bottom right is {f}.

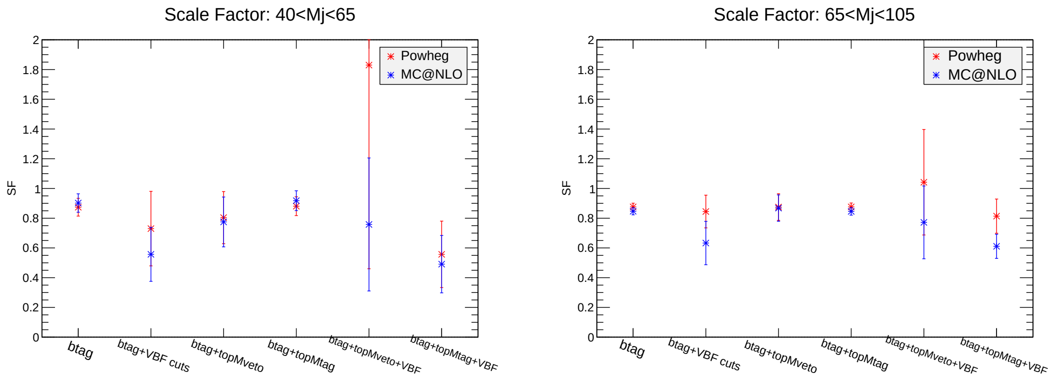

Figure 5.14: Normalization scale factors after several variations of the cuts for the m_J sideband (top) and signal (bottom) regions.

in the correction factor, I_{125}, the interference between the signal and the SM Higgs boson with m=125 GeV (h_1 in the EWSM scenario), is also taken into account. PHANTOM generator allows the introduction of the C' scale factor to the Higgs coupling, the same as done in the gluon fusion case. Before the calculation of the reweighting factor, the distributions are fitted in order to smooth them. This allows the production of the reweighting factor over the whole (mass, C', BR_{new}) space by interpolating the fitting function parameters.
Example of fits performed on the S+I and S distributions are shown in Figure 5.15, for a signal generated with a mass of 800 GeV, $C'^2 = 0.5$ and $\text{BR}_{\text{new}} = 0$. In Figure 5.16, the respective distribution of the interference weights is also shown.

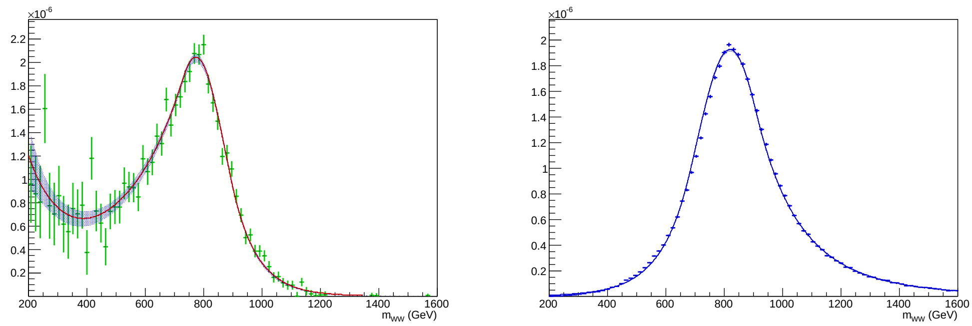

Figure 5.15: Fit on the S+I distribution (left) and fit on the signal distribution (right) for a SM Higgs boson with m= 800 GeV, $C'^2 = 0.5$ and $\text{BR}_{\text{new}} = 0$.

In Figure 5.17, the interference weight distributions are shown, for a mass of 650 GeV, as a function of different C'^2 and BR_{new} values.

5.6.2 Reconstructed signal shape

After applying the reweighting procedure described in the previous section to correct for the interference effects, the reconstructed signal shape is extracted from a fit to the Monte Carlo samples using the following analytical parameterizations:

- A Crystal-Ball function is used to model the gluon fusion Higgs signal.

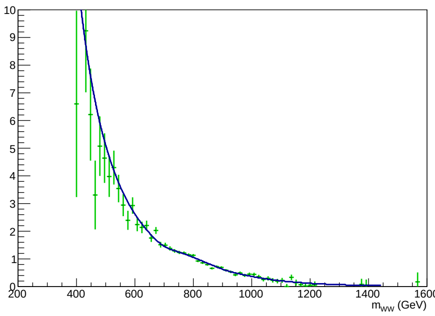

Figure 5.16: Distribution of the interference weights for a SM Higgs boson with m= 800 GeV, $C'^2 = 0.5$ and $\mathrm{BR}_{\mathrm{new}} = 0$. Green: ratio of the S+I and S distribution. Blue: ratio of the fitted functions obtained from S+I and S distributions.

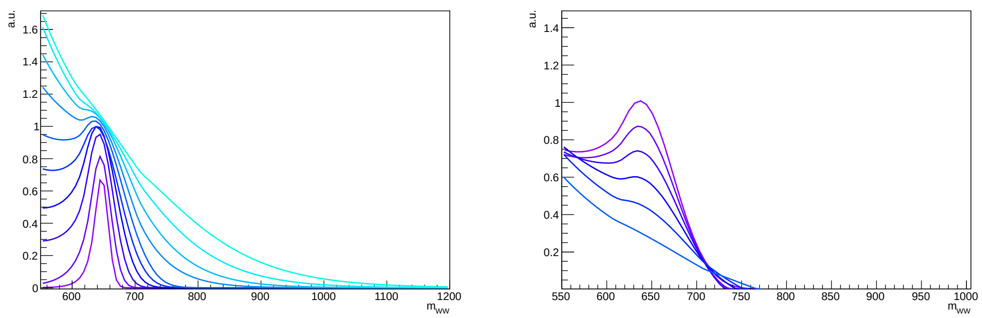

Figure 5.17: Left: Interference weight distributions for fixed $\mathrm{BR}_{\mathrm{new}} = 0$ varying $\mathrm{C'}^2$ from 0.1 to 1, in steps of 0.1 Light blue line corresponds to $\mathrm{C'}^2 = 1.0$, purple line corresponds to $\mathrm{C'}^2 = 0.1$. Right: interference weight distributions for a fixed $\mathrm{C'}^2 = 0.5$ varying $\mathrm{BR}_{\mathrm{new}}$ from 0 to 0.5, in steps of 0.1. Purple line corresponds to $\mathrm{BR}_{\mathrm{new}} = 0$, blue line corresponds to $\mathrm{BR}_{\mathrm{new}} = 0.5$.

- A composite model, formed by a Crystal-Ball function plus an exponential shape, is used for the invariant mass shape of the VBF Higgs signal, since the original resonance shape is strongly modified by the interference effect especially at high mass.

As an example, fits for the muon channel in the 0+1 jet category are shown in Figure 5.18.

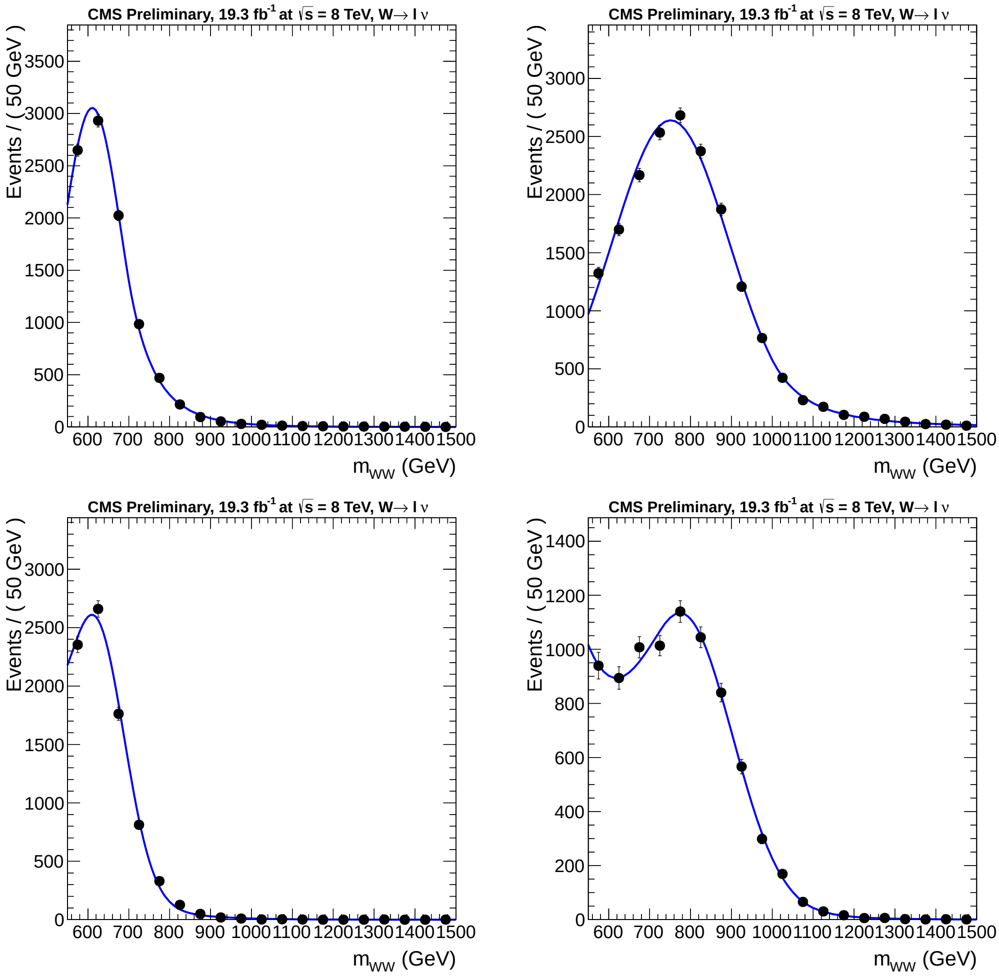

Figure 5.18: Fits on the SM Higgs reconstructed shape for the muon channel in the 0+1 jet bin category: top line are the ggH fits for a higgs mass of 600 (left) and 800 GeV (right); bottom line same fits for the qqH signal.

5.7 Results

The final extrapolation of the background shape into the signal region follows the procedure described in section 4.5, combining both the $\alpha(m_{VW})$ function and the W+jets sideband shape extracted from data in section 5.5.2. The contribution from the non-dominant backgrounds, whose m_{VW} shape in the signal region is obtained from fits on simulation, is then added to the obtained W+jets shape in the signal region. Examples of the fits to the sub-dominant backgrounds are shown in Figure 5.11.

The total m_{VW} distributions in the signal region for the 0-1 jet and the 2-jet category are shown in Figure 5.19 and 5.20. The expected shape for a Higgs signal of mass $m_H = 0.8$ TeV is also shown. No significant deviations from the standard model predictions are observed.

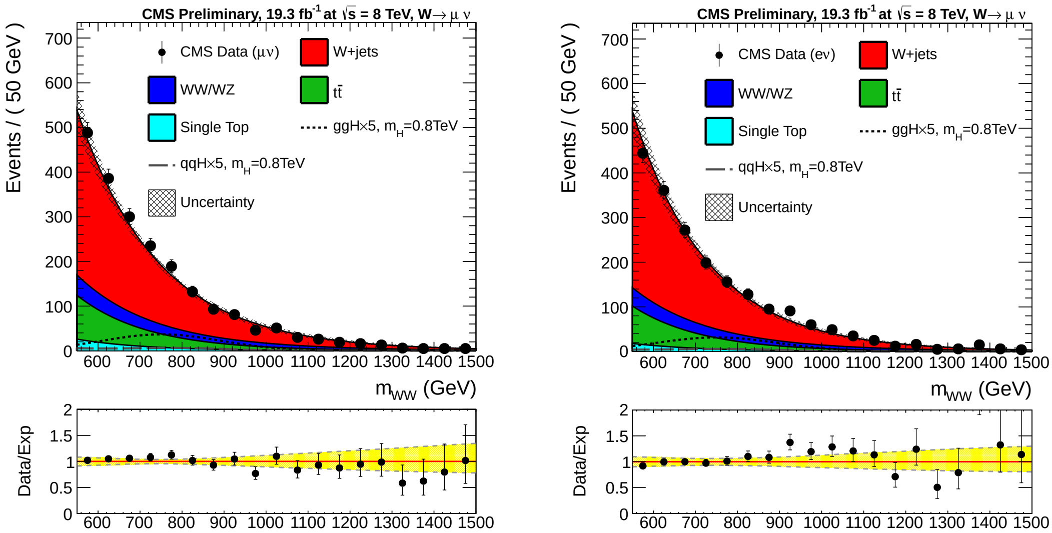

Figure 5.19: Final m_{VW} distributions for data and expected backgrounds in the signal region for the 0-1 jet category. Left: muon channel, right: electron channel. In each plot the solid curve represents the background estimation provided by the alpha ratio method. The hatched band includes both statistical and systematic uncertainties. The data are shown as black markers. The expected shapes for a Higgs signal with mass of 0.8 TeV is also shown. At the bottom of each plot, the bin-by-bin fit residuals, $(N_{\text{Data}} - N_{\text{Fit}})/\sigma_{\text{data}}$, are shown together with the uncertainty band of the fit normalized by the statistical uncertainty of data, σ_{data}.

5.8 Systematic uncertainties

The systematic uncertainties considered in the analysis are discussed in this section, separately for the background (section 5.8.1) and the signal (section 5.8.2).

5.8.1 Systematic uncertainties on the background

The systematic uncertainties on the background can affect the normalization or the shape, or both.

The uncertainty on the W+jets background normalization is dominated by the fit uncertainty related to the number of data events in the m_J sideband regions. Residual biases due to the choice of the functional parametrization are also taken into account: a second analytical model is used to perform the m_J fit, and the difference between the W+jets normalization obtained with this function and the one obtained from the default function is added in quadrature to the statistical uncertainty. The total value of the uncertainty on the W+jets background normalization is 5(8)% in 0+1 jet category for the muon (electron) channel, while it is of 25% in the 2-jet category.

The uncertainty on the $t\bar{t}$ normalization comes from the uncertainty on the data-to-simulation scale factors derived in the top-enriched control sample, and it is estimated to be $8-10\%$ in the 0+1 jet category and 25% in the 2 jet category due to the lower

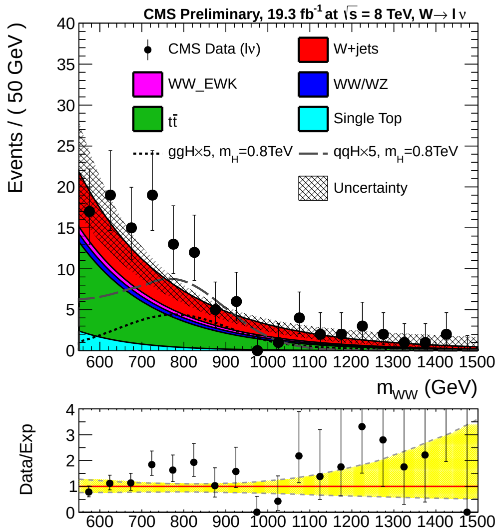

Figure 5.20: Final m_{VW} distributions for data and expected backgrounds in the signal region for the 2-jet category. Electron and muon channels are merged together. In each plot the solid curve represents the background estimation provided by the alpha ratio method. The hatched band includes both statistical and systematic uncertainties. The data are shown as black markers. The expected shapes for a Higgs signal with mass of 0.8 TeV is also shown. At the bottom of each plot, the bin-by-bin fit residuals, $(N_{\rm Data} - N_{\rm Fit})/\sigma_{\rm data}$, are shown together with the uncertainty band of the fit normalized by the statistical uncertainty of data, $\sigma_{\rm data}$.

statistics.

The theoretical uncertainty on the WW inclusive cross section is assigned to be 20%, based on the diboson CMS measurements at 8 TeV [90]. An additional systematic uncertainty on the WW normalization comes from the uncertainty on the W-tag scale factors, which is at the order of 8%.

A conservative uncertainty of 30% is assigned to the single top process, which has a negligible effect due to the fact that the contribution of this background is small.

The normalization of the backgrounds is also affected by the uncertainty on the energy of the reconstructed jets. The four-momenta of the jets are rescaled (smeared) according to the uncertainties on the jet energy-momentum scale (jet energy-momentum resolution). The background contributions are then recalculated, and for each process an additional systematic error is assigned by evaluating the difference in the event yields between the nominal samples and these modified samples.

A similar uncertainty is related to the lepton energy and momentum scale. Changes in the lepton energy and momentum are propagated to the reconstructed $\not{E}_T$ and to the entire analysis. The relative variation in the number of the selected background events is taken as a systematic uncertainty on the yields. The uncertainties on the lepton energy and momentum scale are generally smaller than 1%.

Other experimental uncertainties affecting the background normalization are the following:

- luminosity: assigned to each of the non-W+jets backgrounds as well as to the signal, equal to 2.6%.

- single lepton trigger, scale, resolution and reconstruction efficiency: estimated with dedicated "tag-and-probe" studies [91] on $Z \to \mu^+\mu^-$ and $Z \to e^+e^-$ events, they are typically 1 to 2% and represent a negligible contribution to the final results.
- uncertainty on the b-tagging efficiency: this is typically a few % and this also has a small effect on the final results.

The systematic uncertainties are summarized for each background component in Table 5.7.

Syst. uncertainty	W+jets	$t\bar{t}$	single t	VV	W+jets	$t\bar{t}$	single t	VV	WW$_{ewk}$
Luminosity	-	2.6%	2.6%	2.6%	-	-	2.6%	2.6%	2.6%
Bkg. Cross section	-	-	30%	20%	-	-	30%	20%	20%
Trigger Eff.	-	1%	1%	1%	-	1%	1%	1%	1%
Lepton Eff.	-	2%	2%	2%	-	2%	2%	2%	2%
B-Tagging	-	1.7%	3.3%	0.6%	-	1.5%	3%	0.5%	0.7%
W-Tagging	-	-	-	9.3%	-	-	-	9.3%	9.3%
Top Normalization	-	6.5%	-	-	-	26.5%	-	-	-
W+jet Normalization	5-8%	-	-	-	22%	-	-	-	-
Lepton Scale	-	0.4%	-	1%	-	0.5%	-	1.5%	1%
Lepton Res.	-	-	-	-	-	-	-	-	0.8%
Jet Scale (JES)	2.7%	4%	4.1%	3%	2.1%	4.1%	7.1%	7.5%	4.6%
Jet Res. (JER)	1%	0.4%	0.9%	0.7%	1.9%	3.1%	8.3 %	4.3%	6.3%

Table 5.7: List of systematic uncertainties on the background normalization: the left part of the table refers to 0+1 jet bin, the right part refers to 2-jet bin category.

The systematic uncertainties on the W+jets m_{VW} shape in the signal region come from two separate contributions: the uncertainty on the extrapolation function $\alpha_{MC}(m_{VW})$ and the uncertainty of the fit to the m_{VW} spectrum in the low-mass sideband region of data. The uncertainty on $\alpha_{MC}(m_{VW})$, computed using the default W+jets simulated sample, is related to the uncertainties on the m_{VW} fit parameters for the numerator and the denominator of the α ratio and it is shown in Figure 5.12 as a function of the reconstructed invariant mass. The pink and the yellow dashed lines denote, respectively, the $\alpha_{MC}(m_{VW})$ functions derived from the alternative parton shower model (PYTHIA) and an alternative fit parametrization. To account for these additional shape variations, the uncertainty from the fit is increased by a factor of 2 for all the mass points, which is enough to cover the variations. In the same way, in order to reduce potential biases in the final limit extraction due to a possible wrong description of the W+jet shape, the uncertainty band of the W+jet shape fitted in the sideband region is also increased by a factor 2.

5.8.2 Systematic uncertainties on the signal

Theoretical uncertainties on the signal normalization come from the QCD scale and PDF uncertainties on the production of the signal SM Higgs. The values are taken directly from [26].

Additionally, the uncertainty on the evaluation of the interference effects between the signal and the SM background is taken into account. In the gluon fusion production case, a prescription is given in [26]. In the VBF signal production case, the uncertainty is evaluated by varying up and down the renormalization scale and computing the effect on the S+I and S distributions (see Section 5.6.1).

An additional systematic error arises due to the uncertainty introduced by binning the analysis in number of jets.
The uncertainty on the integrated luminosity of the sample (2.6%) is also considered, as it is done for the backgrounds.

Both signal efficiency and shape are also affected by the uncertainty on the energy of the reconstructed jets. Using the same procedure used for the backgrounds, the four-momenta of the jets are rescaled (smeared) according to the uncertainties on the jet energy-momentum scale (jet energy-momentum resolution). The selection efficiencies are then recalculated, and an additional systematic error is assigned evaluating the difference in the event yields between the nominal sample and these modified samples. The value of this uncertainty is strongly dependent on the resonance mass. Furthermore, the induced changes on the shape of the reconstructed resonances are propagated as uncertainties on the signal lineshape, namely on the mean and resolution of the m_{VW} peak.

A similar procedure is also used for the uncertainty related to the lepton energy and momentum scale. Changes in the lepton energy and momentum are propagated to the reconstructed $\not{E}_T$ and to the entire analysis. The relative variation in the number of the selected signal events is taken as a systematic uncertainty on the signal yield; for both lepton flavours, these uncertainties are smaller than 1%. In addition, when fitting the nominal signal lineshape and the scaled lineshapes, the observed variation of the peak position (mean of the m_{VW} distribution) and of the width (RMS of the m_{VW} distribution) are added as a systematic uncertainty on the fitted signal shape. Again, for both lepton flavours, those uncertainties are smaller than 1%.

Other systematics which affect the signal efficiency are related to the uncertainties on data-to-simulation scale factors for the W-tag identification (derived from the top-enriched control sample, section 5.4.3), lepton trigger, identification and isolation (derived from Z→ $\ell^+\ell^-$ events via tag-and-probe technique), and b-tag identification efficiencies, already described in the previous section.

A summary of the impact of all sources of systematic uncertainty on the signal is presented in Table 5.8. The dominant systematic uncertainty on the signal normalization is related to the theoretical uncertainty on the interference with SM processes (gg→WW [26] and qq→WW) and the theoretical uncertainty on the gluon fusion cross section due to the splitting in jet categories. The dominant systematic uncertainty on the m_{VW} signal shape comes instead from the jet energy scale and resolution.

5.9 Statistical interpretation

Since no significant excesses are observed in the final m_{VW} spectra presented in Figure 5.19 and 5.20, it is possible to infer 95% C.L. exclusion limits on the production cross section of the considered models, using the procedure described in section 4.7.

5.9.1 Upper limits for a heavy SM-like Higgs boson

Exclusion limits at a 95% confidence level are presented on the production cross section times branching fraction to WW of a SM-like Higgs boson, normalized to the SM Higgs

Syst. uncertainty	ggH	VBF	ggH	VBF
Luminosity	2.6%	2.6%	2.6%	2.6%
PDF gg	-	9.1%*	-	9.1%*
PDF qq	-	5%*	-	5%*
Jet binning (0 jets)	26%	-	-	-
Jet binning (2 jets)	6%	-	19%	-
Int ggH	10%	-	10%	-
Int vbfH	-	10%	-	10%
Trigger eff.	1%	1%	1%	1%
Lepton eff.	2%	2%	2%	2%
B-Tagging	0.5%*	0.2%*	0.5%*	0.2%*
W-Tagging	9.3%	9.3%	9.3%	9.3%
Lepton Scale	2.1%*	1.5%*	3.5%*	1.8%*
Jet Scale (JES)	3.9%*	4.4%*	5.0%*	4.5%*
Jet Res (JER)	2.5%*	3.5%*	8.0%*	10.6%*

Table 5.8: List of systematic uncertainties on signal (ggH and VBF) normalisation: left part of the table refers to 0+1 jet category, right to 2-jet bin category. (* stands for mass dependent systematics)

cross section, in Figure 5.21. On the left, the exclusion limit obtained from the combination between gluon fusion and VBF channels is shown, while on the right the comparison between the combined sensitivity and the one coming from the individual 0+1 and 2 jet bin categories is presented. The expected sensitivity to exclude the presence of a SM-like Higgs boson varies from 1.1 times the SM Higgs cross section at 600 GeV to 3.3 times the SM Higgs cross section at 1000 GeV. Local excesses of 2.64 σ and 2.56 σ are observed in the mass range between 700 and 800 GeV. These excesses are due to the small bumps observed in data in the final m_{VW} spectra, visible in Figure 5.19 and 5.20, especially in the 2-jet category.

5.9.2 Upper limits in the Electroweak singlet interpretation

The exclusion limit in the electroweak singlet model has been investigated in a limited parameter space, where $C^{'} \leq \sqrt{1 - \mathrm{BR}_{\mathrm{new}}}$, in order to remain in the region where the resonance width is narrower than the SM-like Higgs ones ($\Gamma \leq \Gamma_{SM}$). Since the maximum value considered for $\mathrm{BR}_{\mathrm{new}}$ is 0.5, $C^{'}$ is constrained to be less than 0.7.

Figure 5.22 shows the 2D scan of the observed upper limits as a function of the parameters $\mathrm{C}^{'}$ and BR_{new} for the different mass hypotheses considered.
The results can be summarized in a set of contour plots as a function of (Higgs mass, $\mathrm{C}^{'}$) or ($\mathrm{C}^{'}$, $\mathrm{BR}_{\mathrm{new}}$), as reported in Figure 5.23.
Since the sensitivity of the analysis is not enough to exclude the predicted signal, the observed exclusion contours corresponding to three and four times the expected strength are shown.

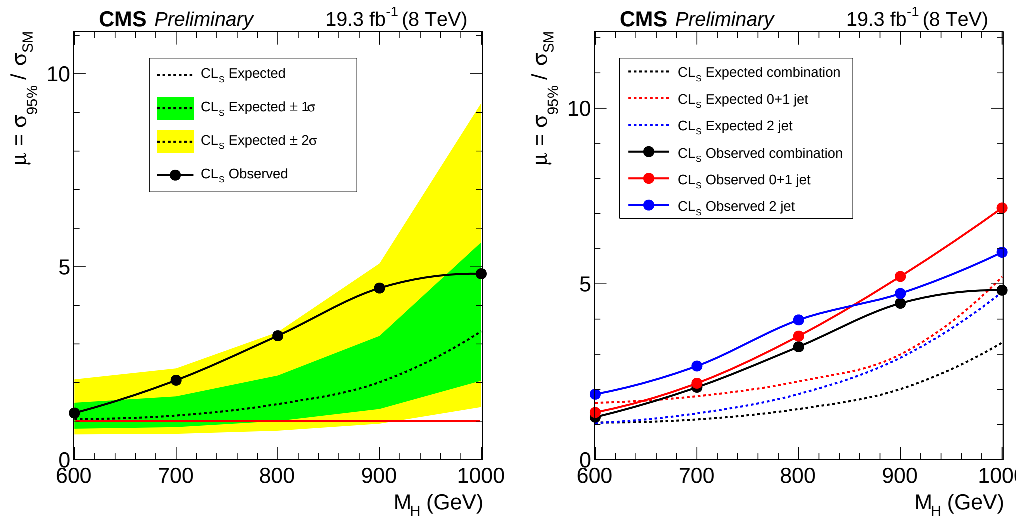

Figure 5.21: Left: observed (solid) and expected (dashed) 95% CL upper limit on $\sigma/\sigma_{\mathrm{SM}}$, obtained via asymptotic CL$_s$ technique, for a SM-like Higgs boson decaying to WW $\to l\nu q\bar{q}'$. The 68% and 95% ranges of expectation for the background-only model are also shown with green and yellow bands, respectively. The solid horizontal red line at unity indicates the expectation for a SM-like Higgs boson. (Right) Comparison between exclusion limits in each bin category.

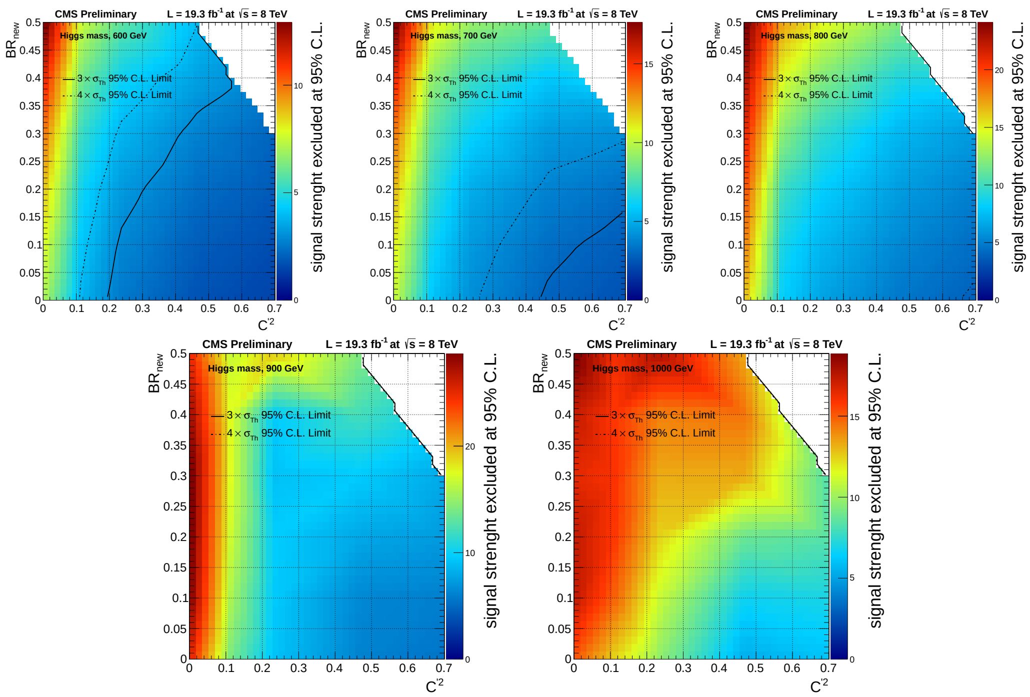

Figure 5.22: 2D Scan of the observed upper limit at 95% CL for BSM electroweak singlet heavy Higgs boson as a function of C$'$ and BR_{new} for a fixed Higgs mass value, from 600 GeV up to 1 TeV. (On top, from left to right: 600, 700, 800 GeV; on bottom, from left to right: 900 and 1000 GeV.) Intermediate points are obtained by Delaunay interpolation and contour lines at a sensitivity equal to 3 and 4 times the expected cross section are reported too.

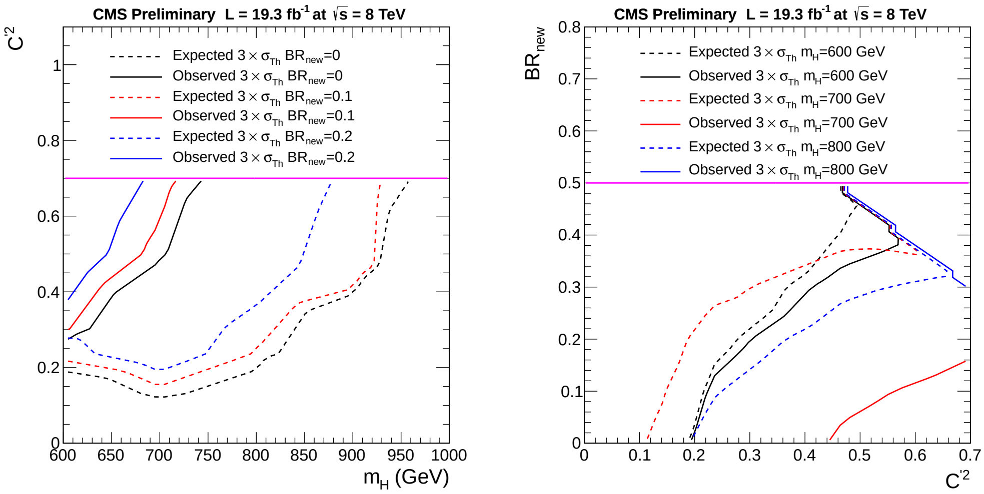

Figure 5.23: Left: observed and expected contour lines, related to a sensitivity equal to three times the theoretical expectation, in the (m_H, $\mathrm{C}^{'2}$) plane for three fixed $\mathrm{BR}_{\mathrm{new}}$ values (0, 0.1, 0.2, represented with different colours). The horizontal magenta lines stands as upper limit for the $\mathrm{C}^{'2}$ values considered in the analysis. Right: observed and expected contour lines, related to a sensitivity equal to three times the theoretical expectation, in the ($\mathrm{C}^{'2}$, $\mathrm{BR}_{\mathrm{new}}$) plane for three fixed m_H values (600, 700, 800 GeV, represented with different colours). The horizontal magenta lines stands as upper limit for the $\mathrm{BR}_{\mathrm{new}}$ values considered in the analysis.

Chapter 6

Application II: search for BSM resonances with LHC Run II data

The same techniques described in chapter 4 have also been applied to LHC Run II data. The models under study are the bulk graviton and the HVT model, described in chapter 1. Contrary to the previous analysis, the main assumption is that the natural width of the resonance is much smaller than the experimental resolution (narrow-width approximation). This assumption leads to a different modeling of the signal, with respect to the previous chapter. This search addresses the mass spectrum [0.6 − 4.0] TeV and consists of two exclusive analyses, separately optimized for the two mass ranges [0.6 − 1.0] TeV ("low-mass") and [1.0 − 4.0] TeV ("high-mass"). The strategy of the two searches is based on the same procedure, although the event selection and the category definition are slightly different in order to maximize the sensitivity in the relevant mass range. In each section, the relevant differences between the two searches are highlighted.

6.1 Datasets

This analysis is based on proton-proton collision data at $\sqrt{s} = 13$ TeV collected by the CMS experiment at the LHC during 2015 and corresponding to an integrated luminosity of 2.3 fb^{-1}. The data are recorded using triggers requiring single electrons or single muons. The details can be found in section 6.2.1.

6.1.1 Signal and background samples

The bulk graviton model and the HVT model (W′ and Z′ bosons) are used as benchmark signal processes. Several simulated samples are generated for each signal hypothesis, varying the mass of the resonance in the range 0.6 − 4.0 TeV. The Monte Carlo simulations of the signal processes are generated with the leading-order (LO) mode of MADGRAPH5_AMC@NLO v5.2.2.2 [92].

Concerning the backgrounds, W+jets events are generated with MADGRAPH5_AMC@NLO. Several W+jets simulated samples are used, each of them covering a different H_T region, with H_T defined as the scalar sum of the transverse energies of all jets in the event. The $t\bar{t}$ and single top processes are simulated using both POWHEG v2 [78, 79, 80, 81, 82, 83] and MADGRAPH5_AMC@NLO, while diboson (WW, WZ, and ZZ) processes are produced with PYTHIA v8.205 [84, 85]. The parton showering and hadronization are performed with PYTHIA using the CUETP8M1 tune [86, 87]. The NNPDF 3.0 [93] parton distribution functions (PDF) are used for all simulated samples. All samples are processed using the GEANT4 [88] simulation of the CMS detector. The simulated background samples are normalized using inclusive cross sections calculated at next-to-leading order (NLO), or next-to-next-to-leading order (NNLO) where available, calculated with MCFM v6.6 [94, 95, 96, 97] and FEWZ v3.1 [98].

Extra minimum bias interactions are added to the generated events to match the distribution of the number of additional interactions per LHC bunch crossing (pileup) observed in data. The simulated samples are also corrected for the observed differences between data and simulation in the lepton trigger efficiencies, the lepton identification/isolation, and the selection criteria to identify b-tagged jets.

In Tab. 6.1, the list of samples used to simulate the background processes, with their corresponding cross sections, is reported.

Sample	**Cross section[pb]**
W+Jets→ $\ell\nu$ HT-binned (100-200 GeV)	1630
W+Jets→ $\ell\nu$ HT-binned (200-400 GeV)	435.6
W+Jets→ $\ell\nu$ HT-binned (400-600 GeV)	59.2
W+Jets→ $\ell\nu$ HT-binned (600-800 GeV)	14.62
W+Jets→ $\ell\nu$ HT-binned (800-1200 GeV)	6.36
W+Jets→ $\ell\nu$ HT-binned (1200-2500 GeV)	1.61
W+Jets→ $\ell\nu$ HT-binned (> 2500 GeV)	0.0374
WW	118.7
WZ	16.5
ZZ	47.13
$t\bar{t}$	831.76
Single top s-channel	47.13
Single top t-channel	43.8
Single top $\bar{t}$-channel	26.07
Single top tW-channel	35.6
Single top $\bar{t}$W-channel	35.6

Table 6.1: Samples used to simulate the backgrounds processes, with their corresponding cross sections.

6.2 Event selection

In order to isolate a topology compatible with a boosted VW system, typical of the signal, events are required to have exactly one energetic lepton (electron or muon), large $\not{E}_T$ and one merged jet in the final state. A summary of the main selections used is given in the following.

6.2.1 Lepton selection

Two levels of selections (online and offline) are applied to select events with one energetic lepton.

Candidate signal events are selected online using triggers which require one electron or one muon, without isolation requirements. For the high-mass analysis, the lepton p_T measured online must be larger than 45 GeV in the muon case, while the threshold is 105 GeV in the electron channel. The efficiency for the single-muon trigger varies between 90% and 95% depending on the pseudorapidity of the muon, while the efficiency is around 98% for the single-electron trigger. For the low-mass case, the thresholds used are looser in order to recover efficiency in the mass range considered. For muon candidates, the online threshold is 27 GeV in p_T, with $|\eta| < 2.1$ and isolation requirements. The same selections are applied in the electron case. The trigger efficiency varies between 95% and 100% for single muons, and between 94% and 100% for single electrons, depending on the p_T and η value of the candidate.

For the offline selections, the p_T thresholds used are 53 GeV and 120 GeV for muons and electrons, respectively, in the high-mass analysis. The p_T thresholds used in the low-mass case are instead 40 (45) GeV for muons (electrons), to recover efficiency at low masses. These values correspond to the point where the plateau is reached in the trigger efficiency curve. In both analyses, muons also satisfies the requirement $|\eta| < 2.1$.

Several ID criteria are also used to classify muon and electron candidates in the analysis. The complete description of the ID selections can be found in appendix B.

In the high-mass analysis, in addition to the p_T and η requirements mentioned before, muon candidates must satisfy the HighPT muon ID. An isolation requirement is also applied to suppress the background from QCD events where jet constituents are identified as muons. For this purpose, a cone of radius $\Delta R = 0.3$ is built around the muon direction, and the isolation parameter is defined as the scalar sum of the transverse momenta of all the additional tracks reconstructed within the cone, divided by the muon p_T. This isolation parameter is required to be less than 0.1. In the following, muon candidates which pass all these requirements will be referred to as “tight” muons. In order to reject events which contain more than one lepton, “loose” muon candidates are also defined. They are required to pass the HighPT muon ID and must have $p_T > 20$ GeV and $|\eta| < 2.4$. They should also satisfy the same isolation criteria described above for the tight muons. In the low-mass analysis, the tight muons are required instead to pass the Tight muon ID criteria, with $p_T > 40$ GeV and same isolation requirements, while loose candidates are defined as the muons passing the Loose muon ID with $p_T > 20$ GeV and $|\eta| < 2.4$.

For the electron identification, candidates must pass the HEEP electron ID with isolation requirements applied and must satisfy the p_T requirements mentioned before. These electrons will be referred to as “tight” electrons. “Loose” electron candidates (used to veto additional leptons, as in the muon case) are required to pass the HEEP electron ID with isolation requirements and must have $p_T > 35$ GeV and the same η range as the tight electrons. In the low-mass analysis, tight electrons must satisfy the Tight electron ID and $p_T > 45$ GeV, while loose candidates should pass the Loose ID criteria and must have $p_T > 20$ GeV.

6.2.2 Jet selection

In this analysis, the large-cone jets used to select the boosted hadronic V boson candidate are reconstructed using the anti-k_T algorithm with distance parameter of R = 0.8 (AK8 jets). The anti-k_T jets with distance parameter of R = 0.4 (AK4 jets) are instead used as small-cone jets.

All jets used in the analysis must satisfy the loose jet ID requirements, described in appendix B. Charged hadron subtraction [75] is also applied to the jets, in order to reduce contamination from pileup. All jets are corrected applying the L1, L2, and L3 energy corrections both in data and simulation (section 2.3.3). In addition, the L2+L3 residual corrections are applied in data. Furthermore, the pruned jet mass is corrected as well using L2 and L3 (and L2+L3 residual) in simulation (data).

The hadronic V candidate is selected as the AK8 jet with largest p_T, with the requirement $p_T > 200$ GeV and $|\eta| < 2.4$. AK8 jets within $\Delta R < 1.0$ of any tight electron or tight muon defined as in the previous section are discarded from the analysis.

The AK4 jets with $p_T > 30$ GeV and $|\eta| < 2.4$ are also used in the analysis. These jets should not lie within the cone of the selected AK8 jet ($\Delta R > 0.8$) and they must be separated ($\Delta R > 0.3$) from any tight electron or tight muon, otherwise they are not considered. These jets are used to veto the presence of b-tagged jets in the event, in order to reduce the $t\bar{t}$ and single top background contribution. A jet is considered to be b-tagged if it passes the medium working point (corresponding to 0.891) of the particle flow inclusive combined secondary vertex (CSV) run II algorithm [89].

6.2.3 Angular selection

The signal is characterized by a topology with two boosted vector bosons which are back-to-back in the transverse plane. In order to isolate such a topology, the following angular selections are applied:

- The ΔR between the lepton and the hadronic V boson candidate, $\Delta R(\ell, V_{had})$, must be larger than $\pi/2$;
- The separation in the transverse plane, $\Delta\phi$, between the hadronic V boson candidate and the missing transverse energy, $\Delta\phi(V_{had}, \not{E}_T)$, must be larger than 2.0;
- The $\Delta\phi$ between the hadronic V boson candidate and the reconstructed leptonic W boson, $\Delta\phi(V_{had}, W_{lep})$, must be larger than 2.0.

Summary of event selection

The summary of the event selection is the following:

1. exactly one charged tight lepton;
2. lepton veto: no additional loose electrons or muons;
3. missing transverse energy: events are required to have $\not{E}_T > 80$ GeV in the electron channel and $\not{E}_T > 40$ GeV in the muon channel to suppress contributions from QCD multijet background;
4. leptonic W p_T: the p_T of the reconstructed leptonic W boson must be larger than 200 GeV;
5. hadronic V p_T: the p_T of the reconstructed hadronic V boson (selected as the AK8 leading jet) must be larger than 200 GeV;
6. b-tag veto: the event is required to have no AK4 jets identified as a b-jet;

7. angular selections to select a diboson-like topology:
   - $\Delta R(\ell, V_{had}) > \pi/2$
   - $\Delta\phi(V_{had}, \not{E}_T) > 2.0$
   - $\Delta\phi(V_{had}, W_{lep}) > 2.0$

6.3 Definition of categories

Different categories are defined in order to maximize the sensitivity to different signal models or mass regions. The two observables used for this purpose are the pruned jet mass m_J and the N-subjettiness τ_{21}.

6.3.1 Mass categories

A first categorization is performed using the pruned jet mass. As described in chapter 4, this is in fact one of the most powerful observable to discriminate the signal from the background. The following orthogonal pruned jet mass regions are defined:

- Low sideband (LSB): defined as $40 < m_J < 65$ GeV
- Signal Region (SR): defined as $65 < m_J < 105$ GeV ($65 < m_J < 95$ GeV) in the high-mass (low-mass) analysis
- High sideband (HSB): defined as $135 < m_J < 150$ GeV

As described in section 4.5, the sideband regions are used to extract the normalization and shape of the W+jets background. The region $105 < m_J < 135$ GeV corresponds to the signal region of analyses searching for final states with a boosted Higgs boson which decays hadronically, and therefore it is not used for the background estimation.

In the high-mass analysis, a further categorization is considered. In fact, the signal models under study have different behaviours in the signal region: in the G→WW and Z'→WW cases, the merged jet comes from the decay of a W boson ("W-jet"), while in the W'→WZ case the merged jet comes from the decay of a Z boson ("Z-jet"). Figure 6.1 shows the m_J distributions of merged W-jets and merged Z-jets expected in G→WW→ $l\nu qq$ and W'→WZ→ $l\nu qq$ signals, respectively.

With the default signal region window, $65 < m_J < 105$ GeV, it is not possible to discriminate between the two signal hypotheses. This separation can instead be achieved splitting the m_J window into two exclusive categories, to maximize the discrimination between a merged W-jet and a merged Z-jet. The categorization has been studied investigating the potential separation between the G→WW→ $l\nu qq$ and W'→WZ→ $l\nu qq$ signals and the effects on the expected analysis sensitivity.

This feasibility study has been performed before applying L2+L3 corrections to the pruned jet mass, therefore the listed cut windows on the uncorrected pruned jet mass are shifted with respect to the corrected pruned jet mass windows used in the analysis. Two mass categories are defined:

- **WW category**: 60-80 GeV on the uncorrected pruned mass (65-85 on the corrected pruned mass), optimized for a signal with a merged W-jet (G→WW→ $l\nu qq$)

- **WZ category**: 80-95 GeV on the uncorrected pruned mass (85-105 on the corrected pruned mass), optimized for a signal with a merged Z-jet (W'→WZ→ $l\nu qq$)

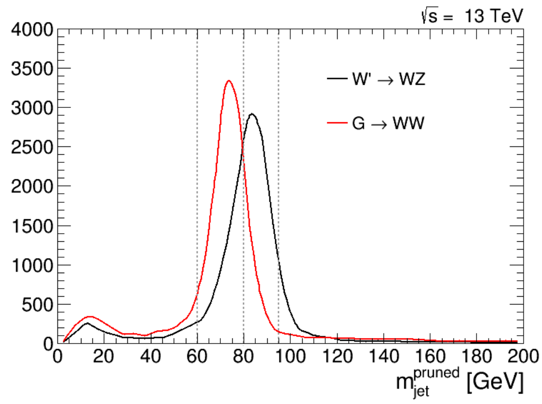

Figure 6.1: Pruned jet mass distributions of merged W-jets and merged Z-jets expected in G→WW→ $l\nu qq$ (red) and W'→WZ→ $l\nu qq$ (black) signals, respectively. The outer vertical lines show the boundaries of the "default" signal region, while the central vertical line shows the optimal separation point between the two distributions.

The efficiencies for the two considered signals in the two mass categories and in the default mass category are shown in Figure 6.2. The large pruned mass window gives the maximum efficiency (about 80%) for both the signals as expected, but in this case the overlap between the two signals is maximal, and the ratio between the two efficiencies is near to 1. Hence, it is possible to maximize this ratio using the categories: from Figure 6.2 it can be noticed that the W' signal efficiency in the Z-mass category is about 4 times larger than the graviton efficiency, while the graviton efficiency in the W-mass category is about 2 times larger than the W' efficiency. Therefore, an excess in the Z-mass category is more likely to come from a spin-1 W' resonance than from a spin-2 graviton and vice-versa for the W-mass category.

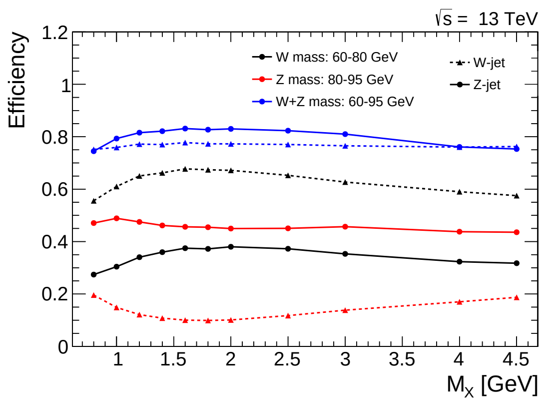

Figure 6.2: Efficiencies of a W-jet signal (G→WW) (dashed lines) and of a Z-jet signal (W'→WZ) (solid lines) as a function of the resonance mass for different pruned jet mass windows: W-mass category (black), Z-mass category (red) and the default single mass category (blue).

A combination of the two mass categories is then adopted to use all the available data and recover the loss in signal efficiency and sensitivity due to the smaller mass windows. A comparison is shown in Figure 6.3, where the expected 95% CL upper limits on the production cross section for a W' signal multiplied by the branching ratio W'→WZ and for a graviton signal multiplied by the branching ratio G→WW are shown as a function of the resonance mass for the different categories. The combination of the two categories (red curve) allows an improvement ($\sim 10\%$) in sensitivity with respect to the default single category (blue curve).

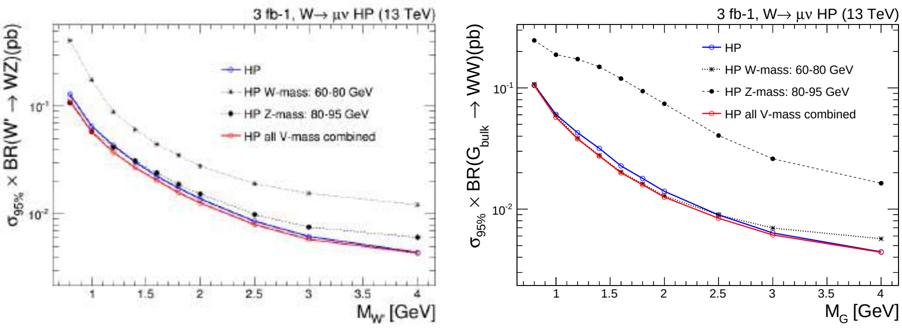

Figure 6.3: Expected 95% CL upper limits on the production cross section of a W' signal multiplied by the branching fraction of W'→WZ (left) and a graviton signal multiplied by the branching fraction of G→WW (right) as function of the resonance mass for the different mass categories. Blue line: default mass category; black-dashed line: W-mass category; black-solid line: Z-mass category; red line: combination of W- and Z-mass category.

No categorization is performed in the low-mass analysis.

6.3.2 Optimization of the N-subjettiness selection

In order to enhance the discrimination power between jets coming from hadronic V boson decays and from QCD processes, additional selections are introduced on the 2- to 1-subjetiness ratio τ_{21}.

An optimization on the τ_{21} selection is performed using Punzi significance as figure of merit, which is defined as [99]:

$$S = \frac{\epsilon_S}{1 + \sqrt{B}}$$

where ϵ_S is the signal efficiency, while B is the total number of background events after applying all the selections described in section 6.2 and the additional requirement on the reconstructed m_{VW} to be within $\pm 15\%$ of the resonance mass under study. The Punzi significance is then calculated for different values of τ_{21} in the range 0–1. The result is shown in Figure 6.4 for Bulk graviton masses between 1 and 3 TeV. From the plot, it can be seen that the optimal cut on τ_{21} depends on the graviton mass.

Figure 6.5 shows instead the ratio of the significances between several fixed upper values of τ_{21} and the optimal value taken from Figure 6.4.

The optimal τ_{21} selection is mass-dependent, with lower values $(0.45-0.5)$ slightly preferred by the low-mass region while higher values $(0.6-0.7)$ are preferred by the high-mass region. The working point chosen for the τ_{21} selection is therefore $\tau_{21} < 0.60$ for the high-mass analysis and $\tau_{21} < 0.45$ for the low-mass case.

A summary of all the selections and categories described in section 6.2 and section 6.3 is reported in table 6.2.

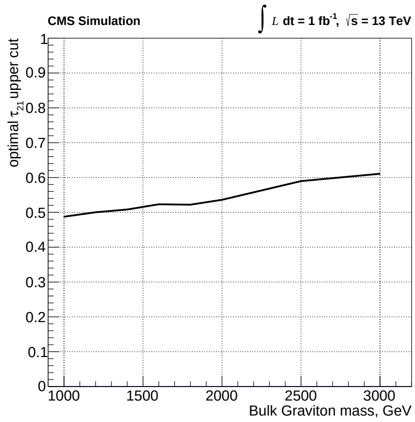

Figure 6.4: Optimal upper cut on τ_{21} as a function of Bulk graviton mass. The optimal τ_{21} selection for W' (HTV model) is similar to the Bulk graviton selection.

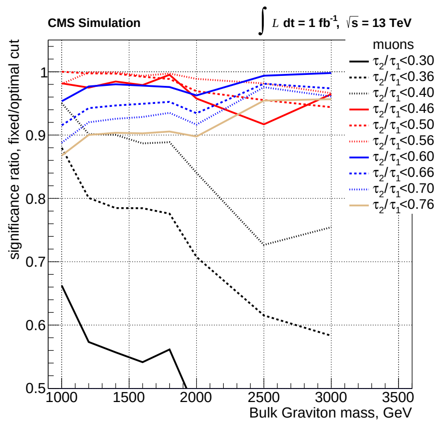

Figure 6.5: Ratio of the Punzi significance between the fix and the mass-dependent optimal upper cut on the τ_{21} as a function of the Bulk graviton mass in the muon channel.

6.4 Data/simulation comparison

In this section comparison plots between data and simulation for key observables are shown, for both muon and electron channels, in various kinematic regions.

6.4.1 Data/MC comparison in the analysis region

The plots shown in this section are obtained by applying the event selection of the high-mass analysis reported in section 6.2, using events in both jet mass sidebands and signal regions.

In the plots, the number of MC events are normalized to the luminosity. Additional scale factors of 1.18 (1.01) for the muon (electron) channel are applied to the W+jets background, in order to correct residual discrepancies in the normalization between data and MC. These scale factors are applied only in these plots, while they are not applied in the rest of the analysis, since the contribution of the W+jets background is extracted from data.

Figure 6.6 shows the lepton p_T distribution and the $\not{E}_T$. The agreement between data and

Selection	Value	Comments
Lepton selections		
Electron	$p_T > 120$ (45) GeV	in the high-mass (low-mass) analysis
	$\|\eta\| < 2.5$	(except $1.44 < \|\eta\| < 1.57$)
Muon	$p_T > 53$ (40) GeV	in the high-mass (low-mass) analysis
	$\|\eta\| < 2.1$	
Number of electrons	exactly 1	
Number of muons	exactly 1	
AK4 jet selections		
Jet p_T	$p_T > 30$ GeV	
Jet η	$\|\eta\| < 2.4$	
Number of b-tagged AK4 jets	0	
$\not{E}_T$ selections		
p_T (electron channel)	$p_T > 80$ GeV	
p_T (muon channel)	$p_T > 40$ GeV	
Boson selections		
$W \to \ell\nu$	$p_T > 200$ GeV	
$V \to q\bar{q}$ (AK8 jet)	$p_T > 200$ GeV	
	$\|\eta\| < 2.4$	
Back-to-back topology	$\Delta R(\ell, V_{had}) > \pi/2$	
	$\Delta\phi(V_{had}, \not{E}_T) > 2$	
	$\Delta\phi(V_{had}, W_{lep}) > 2$	
Pruned jet mass	$65 < m_J < 105$ (95) GeV	in the high-mass (low-mass) analysis
2- to 1-subjettiness ratio	$\tau_{21} < 0.60$ (0.45)	in the high-mass (low-mass) analysis
Categories (pruned jet mass)		
WW	$65 < m_J < 85$ GeV	only in the high-mass analysis
WZ	$85 < m_J < 105$ GeV	only in the high-mass analysis

Table 6.2: Summary of the event selection and categories.

simulation is good especially in the electron channel, while in the muon case some small discrepancies in the modelling of the shape are observed.
The main observables for the hadronic leg are shown in Figure 6.7: the AK8 jet p_T, the pruned mass and the N-subjettiness. The p_T distribution is well-modeled by the simulation in both channels, with a reasonable data/simulation agreement also for the pruned mass and the N-subjettiness shapes.
The analysis is designed to be robust against small differences between data and simulation, since the estimate of the contribution of the main background (W+jets) is obtained from data, as described in section 4.5.

6.4.2 W-tagger validation and scale factors in $t\bar{t}$ control region

As described in section 4.3.1, the performance of the substructure observables on merged V bosons can be checked by using a control sample of almost-pure hadronic W bosons, which can be selected in data using $t\bar{t}$ events. In order to isolate a top-enriched region, the cuts reported in section 6.2 are applied, but removing the angular selection cuts and reversing the b-veto condition (i.e. at least one b-jet in the event). The remaining sample is almost pure of $t\bar{t}$ events, with only a small contamination from the other backgrounds. The distributions of the two substructure observables used in the analysis, i.e. the pruned jet mass and the N-subjettiness, are shown in Figure 6.8 for the high-mass search.
This sample of almost pure $t\bar{t}$ events is used to extract data/MC scale factors, as described in section 4.3.1. The measured data-to-simulation scale factors are reported in Tab. 6.3.
In addition, the W-jet mass peak position and resolution are extracted from the same

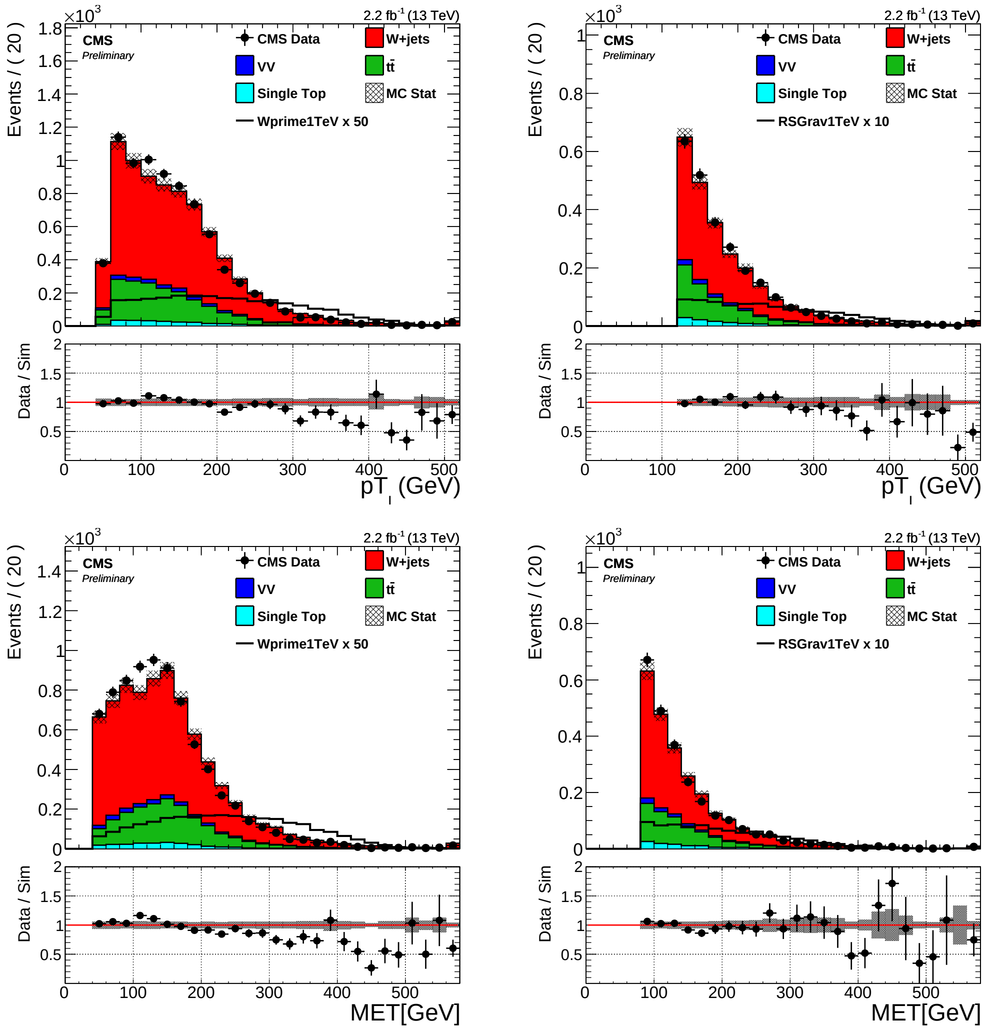

Figure 6.6: Comparison plots between data and simulation for different observables in the high-mass analysis. From top to bottom: lepton p_T and $\not{E}_T$. Left: muon channel, right: electron channel. Data are represented by black dots. The bottom part of each plot shows the ratio between the events in data and in the MC. The statistical uncertainty of the MC is also shown by a grey area. The shape of a W' (graviton) signal with mass of 1 TeV is also shown by a black line in the muon (electron) channel.

Definition	Top scale factor	W scale factor
$\tau_{21} < 0.45$ (low-mass)	0.85 ± 0.04	0.95 ± 0.06
$\tau_{21} < 0.60$ (high-mass)	0.86 ± 0.04	1.01 ± 0.03

Table 6.3: Data-to-simulation top- and W- scale factors extracted with the W-tagger procedure, for the two different τ_{21} working points used in the analysis.

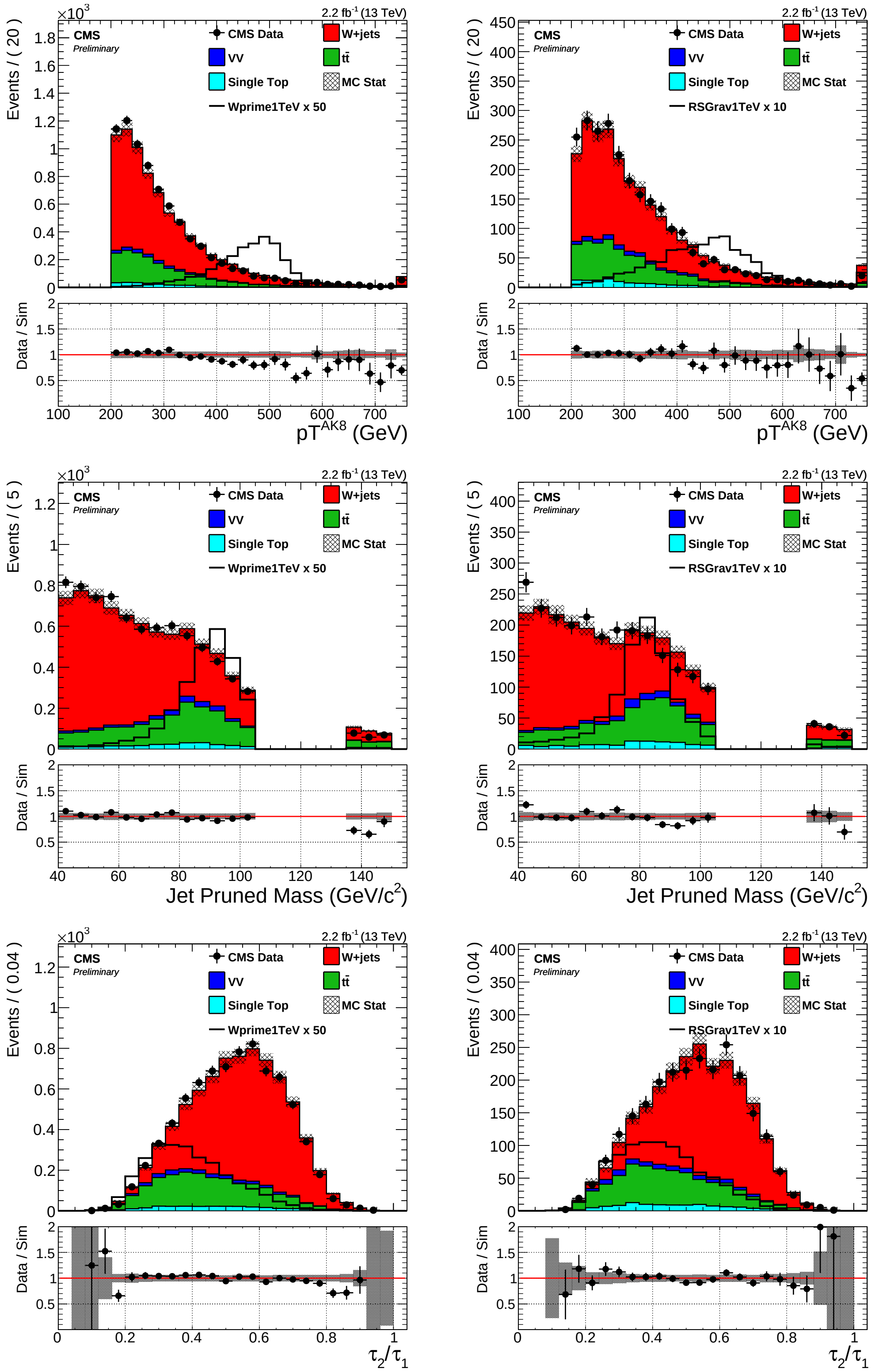

Figure 6.7: Comparison plots between data and simulation for different observables in the high-mass analysis. From top to bottom: AK8 jet p_T, pruned jet mass and N-subjettiness τ_{21}. Left: muon channel, right: electron channel. Data are represented by black dots. The bottom part of each plot shows the ratio between the events in data and in the MC. The statistical uncertainty of the MC is also shown by a grey area. The shape of a W' (graviton) signal with mass of 1 TeV is also shown by a black line in the muon (electron) channel.

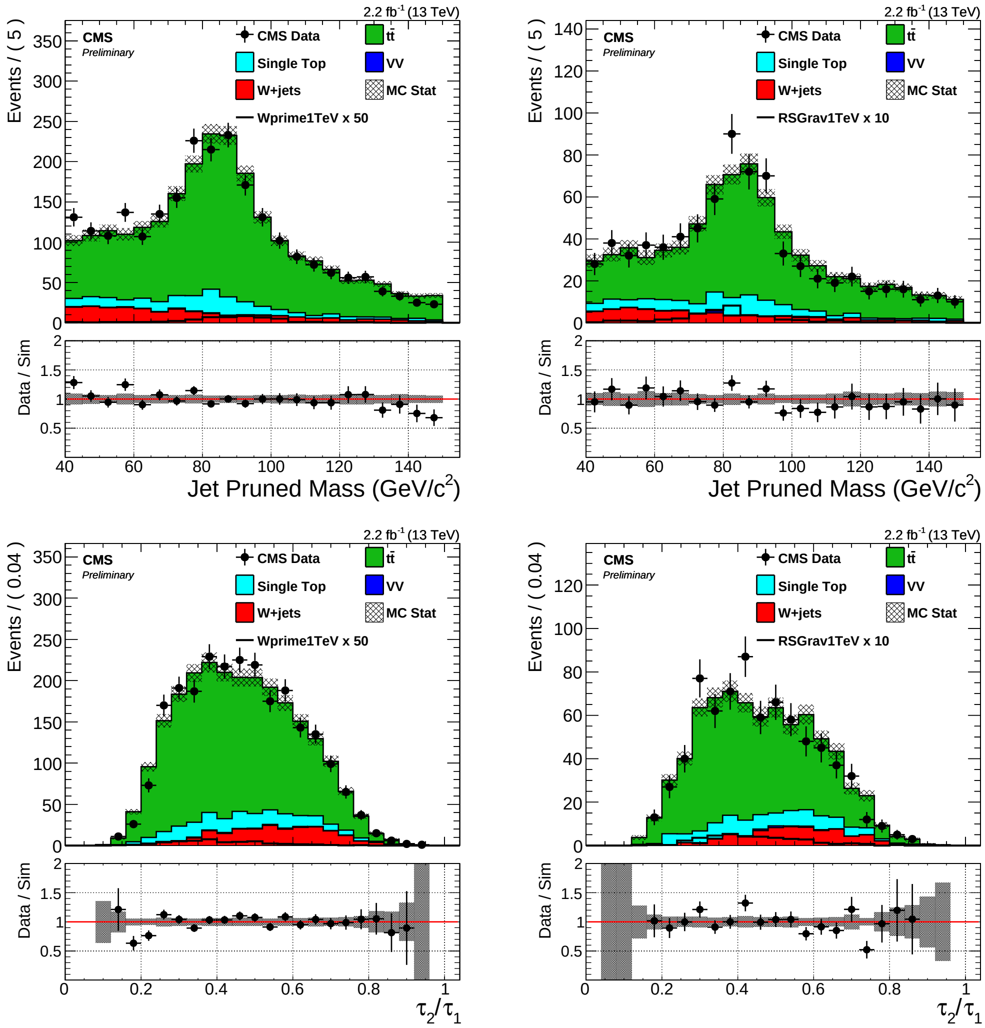

Figure 6.8: Comparison plots between data and simulation for different observables, in the $t\bar{t}$ control region. Top: pruned jet mass. Bottom: N-subjettiness. Left: muon channel, right: electron channel. Data are represented by black dots. The bottom part of each plot shows the ratio between the events in data and in the MC. The statistical uncertainty of the MC is also shown by a grey area. The shape of a W' (graviton) signal with mass of 1 TeV is also shown by a black line in the muon (electron) channel.

fit. The results are presented in Tab. 6.4. The mass peak position is slightly shifted with respect to the W-boson mass due to the presence of extra energy deposited in the jet cone coming from pileup, underlying events, and initial-state radiation not completely removed by the pruning procedure. Additional energy contributions can also come from the possible presence of a b jet close to the W boson in events with top quarks. These numbers are used to correct the mass peak position and resolution in the MC, to match the one observed in data. Because the kinematic properties of W-jets and Z-jets are very similar, the same corrections are used in both cases.

$\tau_{21} < 0.45$	m [GeV]	σ [GeV]
Data	84.6 ± 0.7 GeV	8.2 ± 0.7 GeV
Simulation	85.1 ± 0.2 GeV	7.8 ± 0.3 GeV

Table 6.4: W-jet mass peak position and resolution, as extracted from a top enriched data sample and from simulation.

6.5 Background estimation

The estimation of the background through the alpha method, described in section 4.5, is described in the following.

6.5.1 Normalization

The normalisation of the W+jets in the signal region is extracted from fitting the m_J distributions in data using events in the sideband regions only. The single top, VV and $t\bar{t}$ backgrounds are instead normalised to the theory prediction, and corrected using the scale factors obtained in section 6.4.2, with the top scale factor being used for single top and $t\bar{t}$, while the W scale factor being used for VV. The different background contributions are described using functional forms determined with fits to the corresponding simulated samples. The complete list of functional forms used in the fits is given in section 4.5. Tab. 6.5 reports which function is used to model each background process.

W+jets	$t\bar{t}$	Single Top	VV
F_{ErfExp}	$F_{\text{ErfExp2Gaus}}$	F_{ExpGaus}	F_{2Gaus}

Table 6.5: Summary of the analytical shapes used to fit the m_j spectrum of each background component.

Figure 6.9 shows examples of the MC fits for the non-dominant backgrounds, for the muon channel, in the high mass analysis. The sideband fits to the m_J observed distribution to extract the W+jets normalisation are shown instead in Figure 6.10.

6.5.2 Shape

The functional forms chosen to fit the m_{VW} distribution are described in section 4.5. In Tab. 6.6 it is specified which function is used to model each background, in the different analysis regions.

In the sideband region, the contribution of the non-dominant backgrounds is extracted from a fit to the simulation. The W+jets shape, $F_{data,LSB}(m_{VW})$, is extracted by fitting the m_{VW} distribution in the data in the lower sideband region, subtracting the contribution

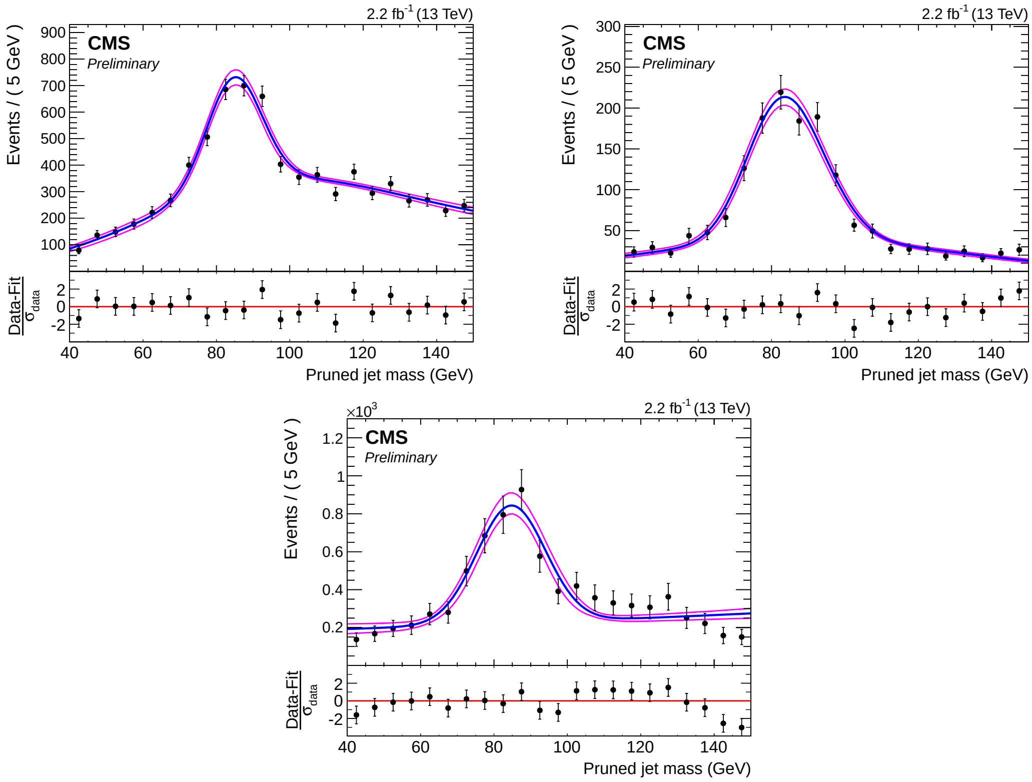

Figure 6.9: MC fits of the non-dominant background m_J spectra. On the top: $t\bar{t}$ (left) and diboson (right), on the bottom: single top. On the bottom of each plot, the bin-by-bin fit residuals, $(N_{Data} - N_{Fit})/\sigma_{data}$, are shown.

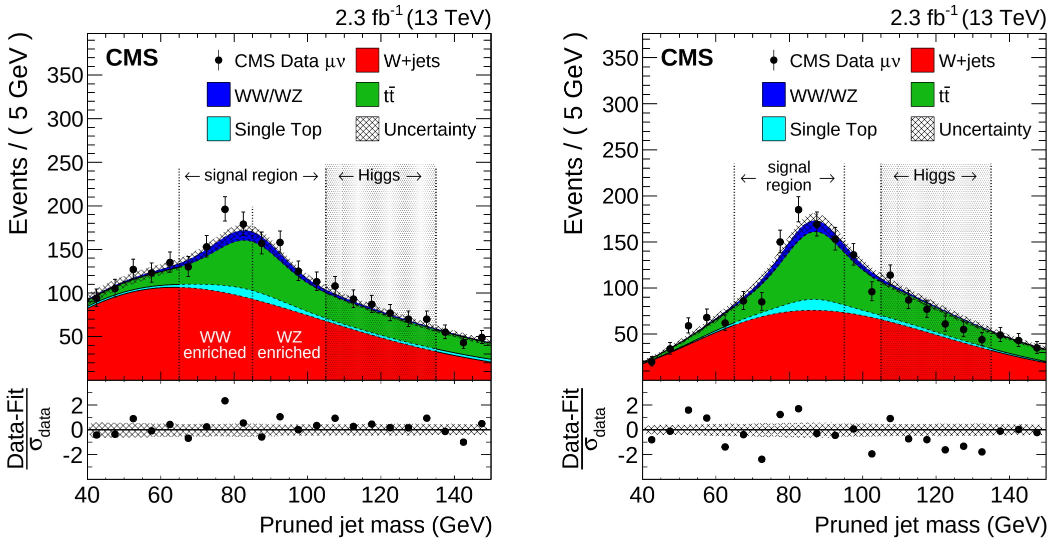

Figure 6.10: Fits to extract the relative shape and normalization of the W+jets contribution from the data in the jet mass distribution, for the high-mass (left) and for the low-mass (right) analysis, in the muon channel. Data are shown as black markers. All selections are applied except the final m_J signal window requirement. The signal regions and mass categories of the analyses are indicated by the vertical lines. The Higgs region 105–135 GeV is not used in the analyses. At the bottom of each plot, the bin-by-bin fit residuals, $(N_{Data} - N_{Fit})/\sigma_{data}$, are shown together with the uncertainty band of the fit normalized by the statistical uncertainty of data, σ_{data}.

m_J region	W+jets	$t\bar{t}$	Single Top	VV
Sideband	F_{ExpN}	F_{Exp}	F_{Exp}	F_{Exp}
Signal region	F_{ExpN}	F_{Exp}	F_{Exp}	F_{ExpN}

Table 6.6: Summary of the shapes used to fit the m_{VW} spectra of each background component.

of the other backgrounds. The fit to the data in the lower sideband region is shown in Figure 6.11.

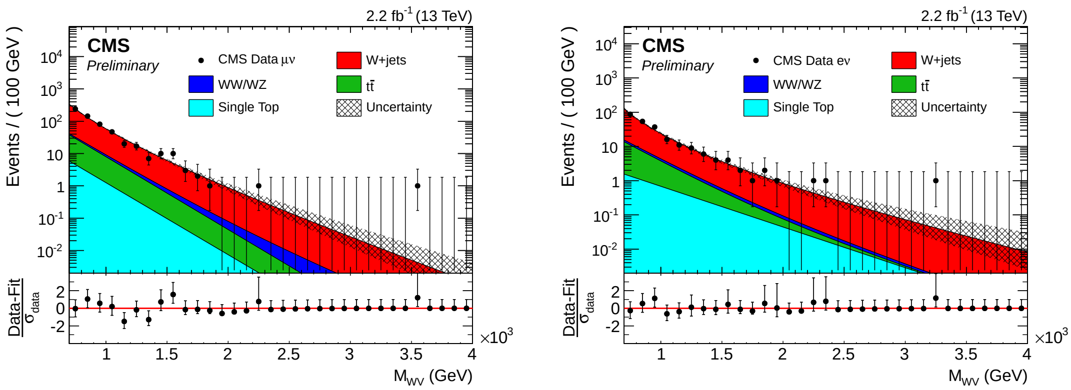

Figure 6.11: The fits to extract $F_{data,LSB}(m_{VW})$ for both muon (left) and electron (right) channels, in the high-mass analysis. On the bottom of each plot, the bin-by-bin fit residuals, $(N_{Data} - N_{Fit})/\sigma_{data}$, are shown.

The W+jets shape in the signal region is then extrapolated using the alpha method described in section 4.5, and corrected for the contribution of the sub-dominant backgrounds. The signal region fits for the non-dominant backgrounds are shown as example in Figure 6.12 for the muon channel in the WW category, for the high-mass analysis. Figure 6.13 shows instead the α functions used to extrapolate the W+jets shape in the WW (left) and WZ (right) signal regions for the muon channel. The final extrapolation of the background contribution into the signal region is presented in section 6.7.

6.6 Signal modeling and efficiency

The signal benchmarks considered in this analysis are the bulk graviton, G $\rightarrow$ WW, and the HVT model, with both charged and neutral resonances W' $\rightarrow$ WZ and Z $\rightarrow$ WW.

The analytical description of the signal shape is extracted from a fit on the simulated samples, using a double-sided Crystal-Ball function [100] for all the resonance mass hypotheses. As examples, fits for the W' (left) and Bulk graviton (right) models for the 2 TeV mass point in the muon channel are shown in Figure 6.14.

The normalization of the signal samples is taken from the cross section of the corresponding theoretical models, and rescaled by the efficiency after applying all the analysis selections. Tab. 6.7 summarizes the efficiencies for the different signal models for various mass points.

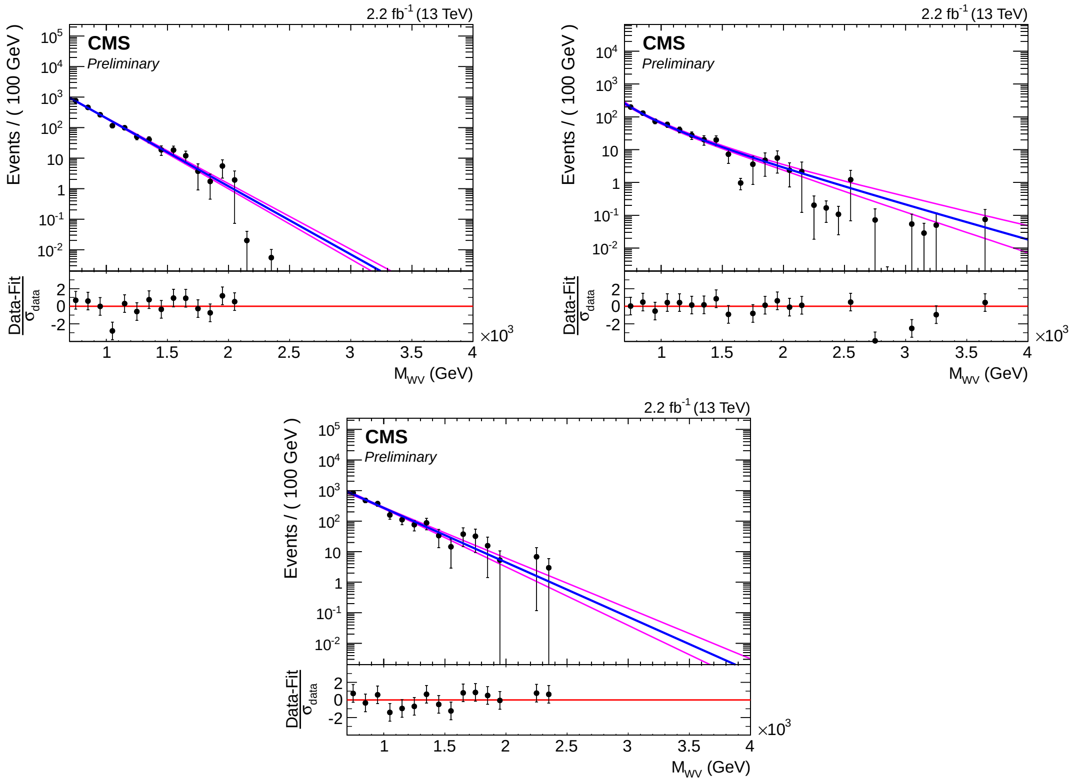

Figure 6.12: MC fits of background m_{VW} spectra in the m_J signal region for events in the WW category. Top: $t\bar{t}$ (left) and diboson (right), bottom: single top process. The pink lines represent the contour of the uncertainty band of the fit. On the bottom of each plot, the bin-by-bin fit residuals, $(N_{Data} - N_{Fit})/\sigma_{data}$, are shown.

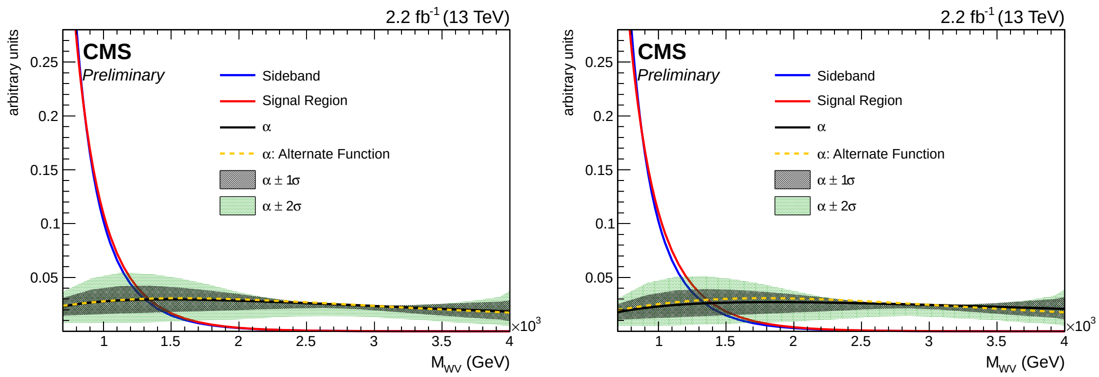

Figure 6.13: The $\alpha_{MC}(m_{VW})$ functions used to extrapolate the W+jets m_{VW} shape in the WW (left) and WZ (right) signal regions, for the muon channel, in the high-mass analysis. The black and the green hatched areas represent the 1 and 2 σ statistical uncertainty bands. The red and blue lines represent the results of the fits to the signal region and to the sideband m_{VW} distribution, respectively, on the W+jets simulation.

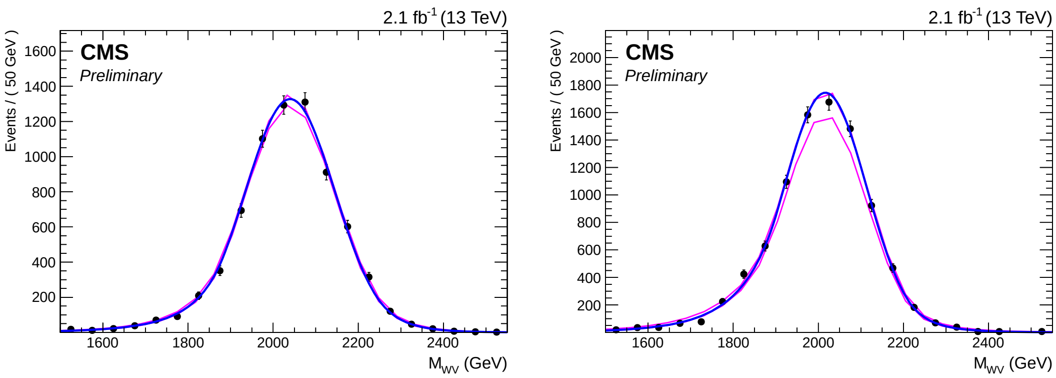

Figure 6.14: Modeling of the signal shape with a Double Crystal Ball function in the muon channel. Left: W' resonance, right: bulk graviton resonance. The pink lines represent the contour of the uncertainty band of the fit. The pruned jet mass Z-mass cut is applied for the W' case, while the W-mass cut is applied for the bulk graviton case.

		WW		WZ	
Signal	Mass	e (%)	μ (%)	e (%)	μ (%)
G $\rightarrow$ WW	0.75 TeV	4.4	5.3	-	-
G $\rightarrow$ WW	1.2 TeV	5.7	7.4	1.7	2.1
G $\rightarrow$ WW	2.0 TeV	7.3	8.0	1.4	1.5
G $\rightarrow$ WW	3.0 TeV	7.0	7.5	1.5	1.7
G $\rightarrow$ WW	4.0 TeV	7.0	7.0	2.0	1.9
W' $\rightarrow$ WZ	0.75 TeV	1.3	1.6	-	-
W' $\rightarrow$ WZ	1.2 TeV	1.2	1.6	2.8	3.4
W' $\rightarrow$ WZ	2.0 TeV	1.8	2.0	3.0	3.3
W' $\rightarrow$ WZ	3.0 TeV	1.9	2.0	3.1	3.2
W' $\rightarrow$ WZ	4.0 TeV	1.9	2.0	3.1	3.0
Z' $\rightarrow$ ZZ	0.75 TeV	4.1	5.1	-	-
Z' $\rightarrow$ ZZ	1.2 TeV	6.0	7.7	1.6	2.0
Z' $\rightarrow$ ZZ	2.0 TeV	7.9	8.8	1.3	1.5
Z' $\rightarrow$ ZZ	3.0 TeV	7.5	8.1	1.6	1.5
Z' $\rightarrow$ ZZ	4.0 TeV	7.4	7.6	1.9	1.9

Table 6.7: Summary of the efficiencies of the different signal models after the full analysis selection. The quoted signal efficiencies are in percent and include the branching ratios of the two vector bosons to the final state $\ell\nu J$

6.7 Results

To extrapolate the W+jets shape into the signal region, both the $\alpha(m_{VW})$ function shown in Figure 6.13, and the W+jets shape extracted from data in the sideband shown in Figure 6.11, are used. The obtained W+jets shape is then combined with the contribution from the non-dominant backgrounds, whose m_{VW} shape in the signal region is obtained from fits on simulation. Examples of these fits are shown in Figure 6.12.

The total m_{VW} distributions in the signal region for the high-mass and the low-mass analyses are then shown in Figure 6.15 combining the electron and muon channels. The expected shape for a bulk graviton (W') signal with mass of 2 (0.75) TeV is also shown in the high-mass (low-mass) case. No significant deviations from the standard model predictions are observed.

6.8 Systematic uncertainties

Systematic uncertainties can affect the final prediction on the background and the signal contribution. These uncertainties can affect the normalization or the shape of these processes, or both. In the following, a summary of the main systematic uncertainties is presented.

6.8.1 Systematic uncertainties in the background prediction

The dominant systematics affecting the background normalization are:

- Uncertainty on the W+jets component. Since the normalization of this background is extracted from the m_J fit on data (section 4.5), the uncertainty is dominated by the amount of statistics in data in the jet mass sideband. It varies between $5 - 9\%$ depending on the category.

- Uncertainty on the $t\bar{t}$ /single top component, dominated by the scale factor derived in the top control region. The value of this systematic uncertainty is about 5% for both high-mass and low-mass analysis.

- Uncertainty on the diboson (WW/WZ/ZZ) component. This uncertainty is dominated by the V-tagger uncertainty, and its value is 3 (6)% in the high-mass (low-mass) analysis.

The dominant shape uncertainties are instead related to the W+jets background, and they consist of two elements:

- The fit uncertainty on the m_{VW} shape extracted from data in the sideband region. This is dominated by the amount of statistics in data in the sideband region.

- The uncertainty in the modelling transfer function $\alpha(m_{VW})$ between the sideband region and the signal region.

The effect of the two uncertainties is about the same size.

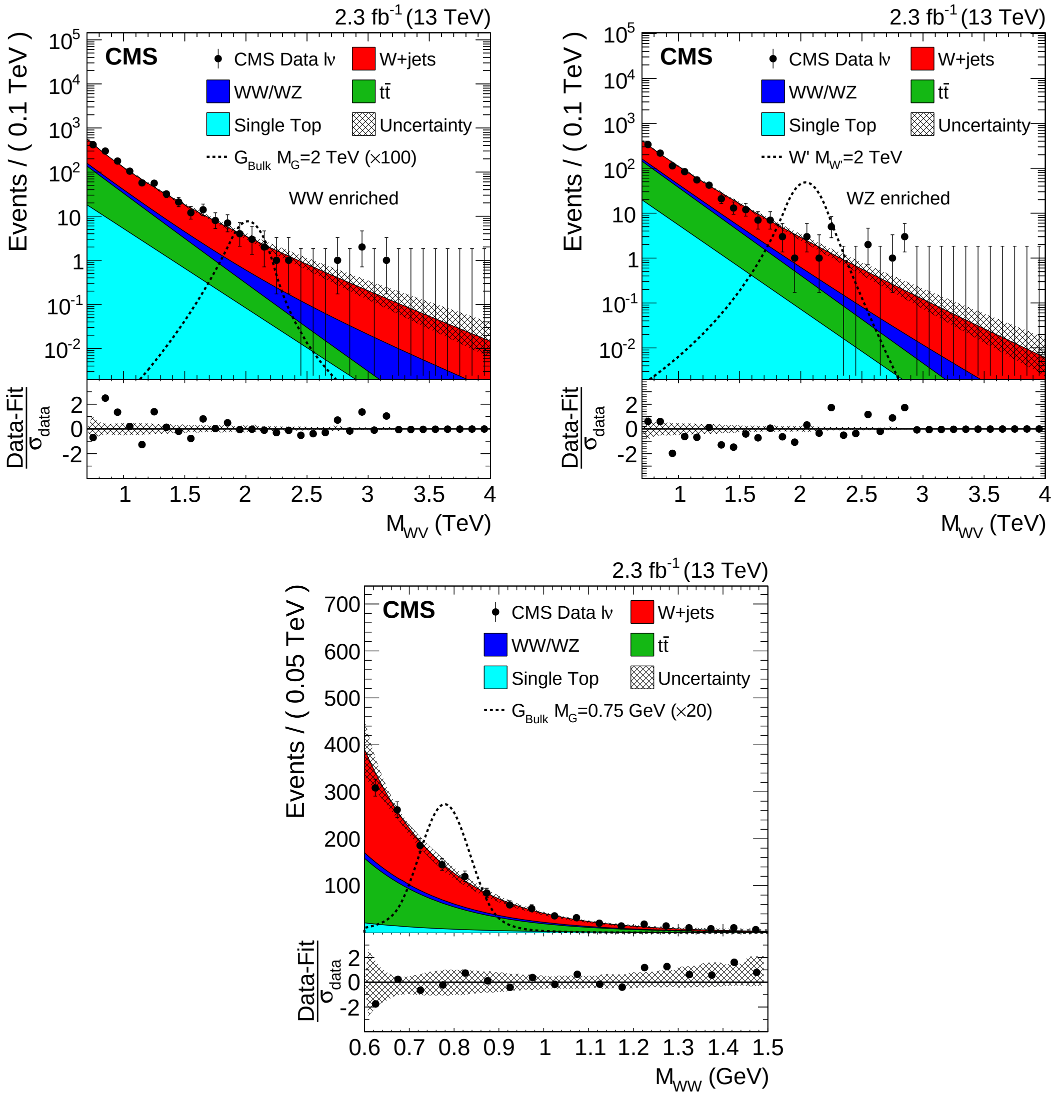

Figure 6.15: Top: final m_{VW} distributions for data and expected backgrounds in the high-mass analysis obtained combining the muon and electron channels, in the WW-enriched (left) and WZ-enriched (right) signal regions. Bottom: final m_{VW} distributions for data and expected backgrounds in the signal region in the low-mass analysis obtained combining the muon and electron channels. In each plot the solid curve represents the background estimation provided by the alpha ratio method. The hatched band includes both statistical and systematic uncertainties. The data are shown as black markers. The expected shapes for a bulk graviton (W') signal with mass of 2 (0.75) TeV is also shown in the high-mass (low-mass) case. At the bottom of each plot, the bin-by-bin fit residuals, $(N_{\mathrm{Data}} - N_{\mathrm{Fit}})/\sigma_{\mathrm{data}}$, are shown together with the uncertainty band of the fit normalized by the statistical uncertainty of the data, σ_{data}.

6.8.2 Systematic uncertainties in the signal prediction

Concerning the normalization, the predicted yield for the signal process is affected by several systematics:

- Uncertainty in tagging the merged jet as W/Z boson (i.e. uncertainty on the W-tagger scale factor).
- Uncertainty due to the parton distribution functions, which ranges from 0.5 to 45% depending on the resonance mass, type and production mechanism.
- Uncertainty due to the choice of factorization and renormalization scales, which ranges from 2 to 23% depending on the resonance mass, type and production mechanism.

Both signal efficiency and shape are also affected by the uncertainty on the energy of the reconstructed jets. The four-momenta of the jets are rescaled (smeared) according to the uncertainties on the jet energy-momentum scale (jet energy-momentum resolution). The selection efficiencies are then recalculated, and an additional systematic error is assigned considering the difference in the event yields between the nominal sample and these modified samples. The value of this uncertainty is strongly dependent on the resonance mass. In addition, the induced relative migrations of events among WW and WZ mass categories (for the high-mass analysis) and outside the m_J signal region (for both high- and low- mass analyses) are evaluated, and assigned as additional systematic uncertainty. Furthermore, the induced changes on the shape of the reconstructed resonances are propagated as uncertainties on the signal lineshape, namely on the mean and the resolution of the m_{VW} peak. The effect of this systematic uncertainty on the background is found to be negligible.

A similar uncertainty is related to the lepton energy and momentum scale. Changes in the lepton energy and momentum are propagated to the reconstructed $\not{E}_T$ and to the entire analysis. The relative variation in the number of the selected signal events is taken as a systematic uncertainty on the signal yield; for both lepton flavours, these uncertainties are smaller than 1%. These uncertainties are uncorrelated for the different lepton flavours, but are correlated for the different pruned jet mass categories. In addition, when fitting the nominal signal lineshape and the scaled lineshapes, the observed variation of the peak position (mean of the m_{VW} distribution) and of the width (RMS of the m_{VW} distribution) are added as a systematic uncertainty on the fitted signal shape. Again, for both lepton flavours, those uncertainties are smaller than 1%. The effect of this systematics on the background is found to be negligible.

6.8.3 Common systematics

Both signal and background yield prediction are affected by the uncertainty on the knowledge of the integrated luminosity, which has been estimated to be 2.6%, and by the uncertainty related to the pileup reweighing process, which is about 2%.

Additional systematic uncertainties are related to the lepton trigger, the identification, and the isolation efficiencies. All of them are derived using a "tag-and-probe" technique in $Z \to \ell\ell$ events [91]. An uncertainty of 1% is assigned to the trigger efficiency for both lepton flavours, while for the lepton identification and isolation, the systematic uncertainty is estimated to be 1% (3%) for the muon (electron) flavour.

Tab. 6.8 summarizes the systematic uncertainties for the signal, while in Tab. 6.9 the systematic uncertainties for the background are reported.

Source	Relevant quantity	muon channel	electron channel
Lepton trigger	Yield	1%	1%
Lepton identification	Yield	1%	3%
B tag	Yield	$1-2\%$	
Jet energy and m_J scale	Yield	0.2%–4%	
Jet energy scale	Shape (mean)	1%–3%	
Jet energy scale	Shape (width)	2%–3%	
Jet energy and m_J resolution	Yield	0.1%–2%	
Jet energy resolution	Shape (mean)	0.1%	
Jet energy resolution	Shape (width)	4%	
Pileup	Yield	2%	2%
Integrated luminosity	Yield	2.6%	
PDF and scales (W',Z')	Yield	2%–23%	
PDF and scales (G_{bulk})	Yield	0.5%–45%	
Jet energy and m_J scale	Migration	2%–24%	
W-tagging	Migration/yield	3%–6%	

Table 6.8: Summary of the systematic uncertainties affecting the signal normalization or the reconstructed m_{VW} shape (mean and width). It is also specified which is the relevant quantity affected by the uncertainty: yield, shape (the mean or the width of the Gaussian core of the Double-Crystall Ball function) or migration of events between the mass categories.

Source	$\mu\nu$+jet uncertainty	$e\nu$+jet uncertainty
Lepton trigger	1%	1%
Lepton identification	1%	3%
B tag	1–2%	
Pileup	2%	2%
Integrated luminosity	2.6%	
W+jets Normalization	5–9%	
Diboson cross section	3%	
Single top cross section	5%	
Top normalization	5%	
W tagging	3%–6%	

Table 6.9: Systematic uncertanties affecting the background normalization. The last uncertainty results in migrations between event categories in the high-mass analysis, while it affects only the yield in the low-mass case.

6.9 Statistical interpretation

Since no significant excesses are observed, it is possible to infer 95% C.L. exclusion limits on the production cross section of the considered models, using the procedure described in section 4.7.

The results are interpreted in the context of the bulk graviton and the HVT (W' and Z') model.

6.9.1 Upper Limits for the bulk graviton model

The expected and observed upper limits on the spin-2 bulk graviton production cross section times the branching fraction of $G_{bulk} \rightarrow$WW are shown in Figure 6.16. The limits are obtained combining together mass categories, lepton channels and high-mass with low-mass analysis. The theoretical prediction for a Bulk graviton model with $\tilde{k} = k/\bar{M}_{Pl} = 0.5$ is also shown. The achieved sensitivity is not sufficient to exclude this particular model, although it is possible to set upper limits which span from 2 to 0.02 pb in the mass range $0.6 - 4.0$ TeV.

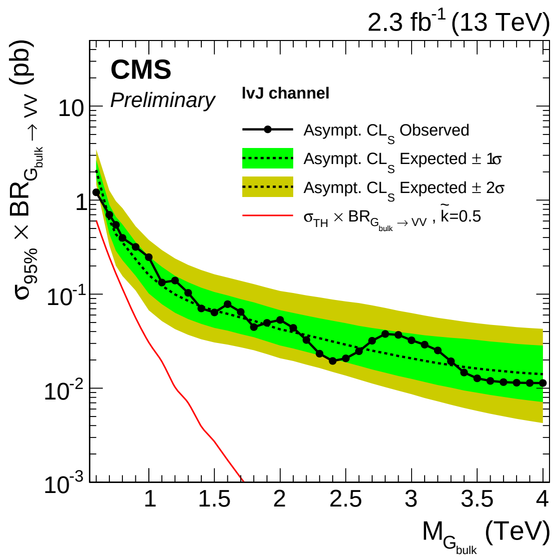

Figure 6.16: Expected and observed 95% CL upper limit on the bulk graviton production cross section times the branching fraction of $G_{bulk} \rightarrow$WW, combining together all the categories and channels, and low-mass with high-mass analysis. The 68% and 95% ranges of expectation are also shown by green and yellow bands. The expected product of the bulk graviton production cross section and the branching fraction to WW is shown as a red solid curve for $\tilde{k} = 0.5$.

6.9.2 Upper Limits for the HVT model

Upper limits for the HVT model are produced for different scenarios: singlet hypothesis (with production of a charged spin-1 W' boson or a neutral spin-1 Z' boson), or in the triplet hypothesis (with production of both W' and Z' bosons). The expected and observed upper limits on the W' (Z') production cross section times the branching fraction of W' $\rightarrow$ WZ (Z' $\rightarrow$ WW) are shown in Figure 6.17 in the singlet hypothesis, while the expected and observed upper limits in the triplet hypothesis are shown in Figure 6.18. The limits are computed combining all the mass categories, lepton channels and high-mass and low-mass analysis together. For the HVT model A (B), with the statistical combination it is possible to exclude the existence of W' and Z' resonances below 1.6 (1.9) and 1.5 (1.6) TeV, respectively, in the singlet hypothesis. Under the triplet hypothesis, spin-1 resonances are excluded below 1.9 and 2.0 TeV for the HVT model A and B, respectively.

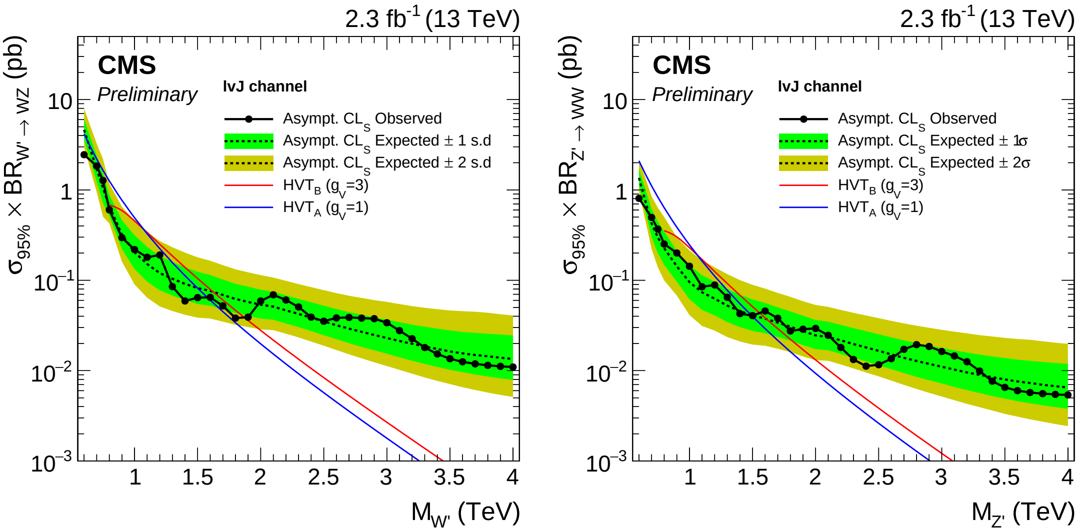

Figure 6.17: Left: expected and observed 95% CL upper limits on the W' production cross section times the branching fraction of W' → WZ in the singlet HVT hypothesis. Right: expected 95% CL upper limits on the Z' production cross section times the branching fraction of Z' → WW in the singlet HVT hypothesis. The 68% and 95% ranges of expectation are also shown by green and yellow bands. The theoretical prediction for the HVT model A and B are also shown by blue and red lines, respectively.

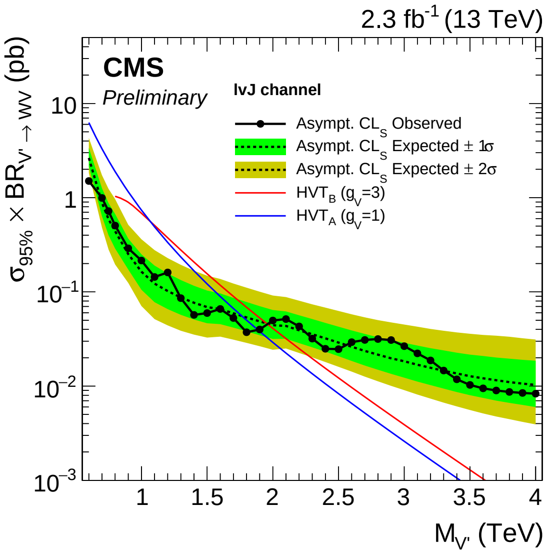

Figure 6.18: Expected and observed 95% CL upper limits in the triplet HVT hypothesis. The 68% and 95% ranges of expectation are also shown by green and yellow bands. The theoretical prediction for the HVT model A and B are also shown by blue and red lines, respectively.

6.10 Analysis of 2016 data

After a technical stop foreseen for machine improvements, LHC has restarted collisions in April 2016, with the same center-of-mass energy ($\sqrt{s} = 13$ TeV) but with higher instantaneous luminosity. The new machine conditions allowed to surpass already in the first few months of 2016 the amount of data collected in 2015. Therefore, the analysis described in the previous sections has been re-run using the 2016 data, in order to exploit the gain in statistics and improve the results. Since most of the selections and the background estimation procedure are the same as the 2015 analysis, only the relevant changes, described in section 6.10.1, are highlighted in the following, while the results and the limits are presented in section 6.10.2 and 6.10.4, respectively.

6.10.1 Differences with respect to the 2015 analysis

The analysis is based on 12.9 fb^{-1} of pp collision data collected in 2016 by the CMS experiment at a center-of-mass energy of $\sqrt{s} = 13$ TeV. The range of masses investigated is [0.6-4.5] TeV. The benchmark models are the bulk graviton and the HVT model A with the W'→WZ interpretation only. As in 2015, two separate searches are performed in the low-mass ([0.6-1.0] TeV) and the high-mass ([1.0-4.5] TeV) regions.
The Monte Carlo samples used for the background estimation are simulated using the same generators described in section 6.1.1, while the simulation of the reconstruction within CMS is performed taking into account the different pileup conditions of 2016.
The event selection is exactly the same as in the previous analysis, except for the following differences:

- A trigger with p_T tresholds of 45 GeV is used for both electrons and muons, and for both low and high mass searches;
- The offline p_T cut is moved to 50 (55) GeV for the muon (electron) category, for both low and high mass searches;
- To suppress possible QCD contamination in the muon channel, a selection is applied on the W transverse mass, defined as $m_T = \sqrt{(2\not{E}_T E_T^e) \cdot (1 - cos\Delta\phi)}$. Events are required to have m_T larger than 40 GeV.
- The definition of the jet pruned mass window for the signal region is changed to 65-95 GeV for the W-jet interpretation and to 75-105 GeV for the Z-jet interpretation, and the two regions are no longer combined.

The top and W-tagger scale factors have been re-derived on 2016 data using the same procedure described in section 4.3.1. The values of the new scale factors and the mass peak/resolution corrections are reported in Tab. 6.10 and Tab. 6.11, respectively.

Definition	Top scale factor	W scale factor
$\tau_{21} < 0.45$ (low-mass)	0.81 ± 0.02	0.98 ± 0.05
$\tau_{21} < 0.60$ (high-mass)	0.83 ± 0.01	1.00 ± 0.02

Table 6.10: Data-to-simulation top- and W- scale factors extracted with the W-tagger procedure on 2016 data, for the two different τ_{21} working points used in the analysis.

$\tau_{21} < 0.45$	m [GeV]	σ [GeV]
Data	84.9 ± 0.2 GeV	7.9 ± 0.2 GeV
Simulation	83.8 ± 0.2 GeV	7.5 ± 0.2 GeV

Table 6.11: W-jet mass peak position and resolution, as extracted from a top enriched data sample and from simulation, for the 2016 analysis.

6.10.2 Results

The background estimate is performed using the same procedure as for the 2015 analysis, described in section 4.5, and using the same analytical forms for the fit functions.
The fit to the m_j distribution in the lower and upper sidebands of the observed data to extract the overall normalization of the W+jets background in the signal region is shown in Figure 6.19.

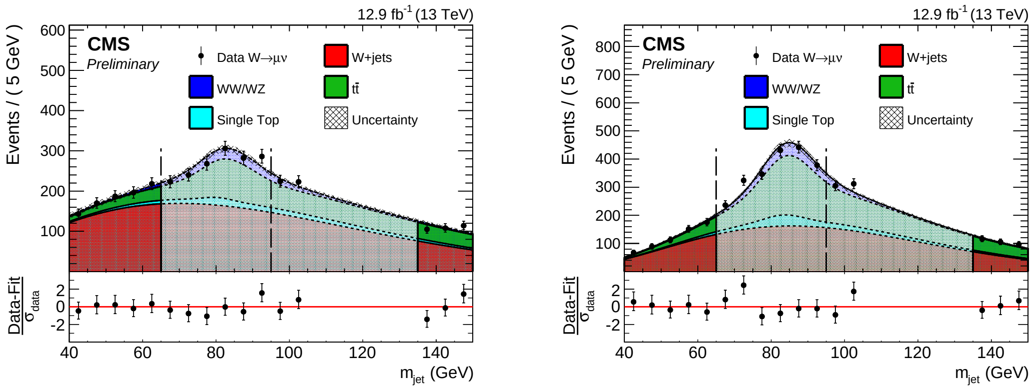

Figure 6.19: Fits to extract the relative shape and normalization of the W+jets contribution from the data in the jet mass distribution, for the high-mass (left) and for the low-mass (right) analysis, in the muon channel. Data are shown as black markers. All selections are applied except the final m_J signal window requirement. The signal regions and mass categories of the analyses are indicated by the vertical lines. The Higgs region 105–135 GeV is not used in the analyses. At the bottom of each plot, the bin-by-bin fit residuals, $(N_{Data} - N_{Fit})/\sigma_{data}$, are shown together with the uncertainty band of the fit normalized by the statistical uncertainty of data, σ_{data}.

The final observed m_{VW} spectra, obtained correcting the m_{WV} distribution observed in the lower sideband region by the transfer function $\alpha_{MC}(m_{VW})$, is shown in Figure 6.20. The observed data and the predicted background agree with each other, and no significant excesses are observed.

6.10.3 Systematic uncertainties

The systematic uncertainties considered in this analysis are the same of the 2015 analysis. Some of their values, however, are different, therefore the summary of the systematic uncertainties affecting the signal and the background for 2016 data is reported in Tab. 6.12 and 6.13, respectively. The relevant differences with respect to the 2015 analysis concern the W+jets and top normalization uncertainties: the larger amount of data collected in 2016 allows in fact to reduce the uncertainties on these backgrounds, given the larger statistics available in the sidebands and in the top-enriched control regions.

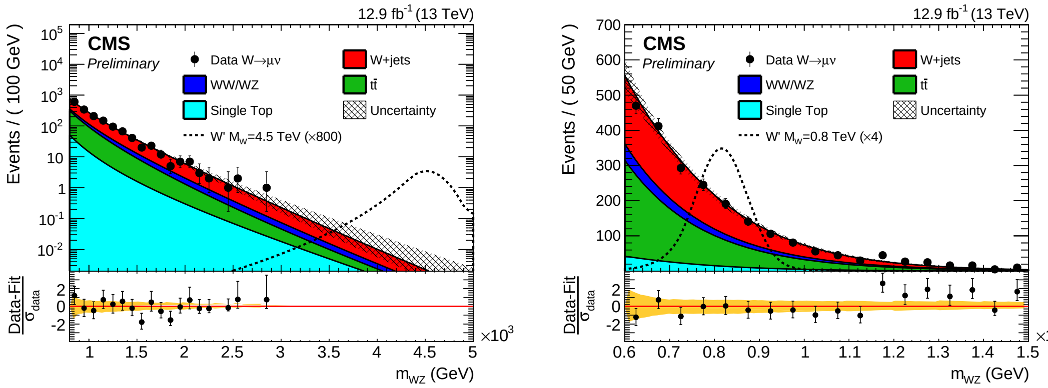

Figure 6.20: Final m_{VW} distributions for data and expected backgrounds in the high-mass (left) and low-mass (right) analysis in the muon channel, in the WW-enriched signal region. In each plot the solid curve represents the background estimation provided by the alpha ratio method. The hatched band includes both statistical and systematic uncertainties. The data are shown as black markers. The expected shapes for a bulk graviton signal with mass of 4.5 (0.75) TeV is also shown in the high-mass (low-mass) case. At the bottom of each plot, the bin-by-bin fit residuals, $(N_{\rm Data} - N_{\rm Fit})/\sigma_{\rm data}$, are shown together with the uncertainty band of the fit normalized by the statistical uncertainty of data, $\sigma_{\rm data}$.

Source	Relevant quantity	muon channel	electron channel
Lepton trigger	Yield	5%	5%
Lepton identification	Yield	5%	5%
B tag	Yield	0.6%	
Jet energy and m_J scale	Yield	1%–2%	
Jet energy scale	Shape (mean)	1%–3%	
Jet energy scale	Shape (width)	2%–3%	
Jet energy and m_J resolution	Yield	0.1	
Jet energy resolution	Shape (mean)	0.1%	
Jet energy resolution	Shape (width)	4%	
Pileup	Yield	2%	2%
Integrated luminosity	Yield	6.2%	
PDF and scales (W',Z')	Yield	1%–30%	
PDF and scales (G$_{bulk}$)	Yield	10%–80%	
Jet energy and m_J scale	Yield	1%–4%	
W-tagging	Yield	5%	

Table 6.12: Summary of the systematic uncertainties affecting the signal normalization or the reconstructed m_{VW} shape (mean and width). It is also specified which is the relevant quantity affected by the uncertainty: the yield or the shape (the mean or the width of the Gaussian core of the Double-Crystall Ball function).

Source	$\mu\nu$+jet uncertainty	$e\nu$+jet uncertainty
Lepton trigger	1%	1%
Lepton identification	1%	3%
B tag	0.6–6%	
Pileup	2%	2%
Integrated luminosity	6.2%	
W+jets Normalization	3–5%	
Diboson cross section	20%	
Single top cross section	2%	
Top normalization	2%	
W tagging	5%	

Table 6.13: Systematic uncertanties affecting the background normalization.

6.10.4 Statistical interpretation

The comparison between the m_{WV} distribution observed in data and the standard model background prediction is used to test the hypothesis of the presence of a new resonance decaying to vector bosons.
Upper limits are set combining together the two lepton channels and high-mass with low-mass analyses.

Exclusion limits are set in the context of the bulk graviton model, in the narrow-width approximation. Figure 6.21 shows the 95% CL expected and observed exclusion limits as a function of the resonance mass for the statistical combination of the electron and muon channels. The limit is compared with the cross section times the branching fraction to WW for a bulk graviton with $k/M_{Pl} = 0.5$. The achieved sensitivity is not sufficient to exclude this particular model. However, the larger statistics of 2016 data sample allows to improve the upper limits from 2 to 0.4 pb at a mass of 0.6 TeV and from 0.02 to 0.003 pb at a mass of 4.0 TeV.

Exclusion limits are also set in the context of the HVT model A, for a W' resonance decaying to WZ. Figure 6.22 shows the 95% CL expected and observed exclusion limits as a function of the resonance mass for the combination of the electron and muon channels. The limits are compared with the cross section times the branching fraction to WZ for a W' boson from HVT model A. The existence of a W' resonance decaying to WZ in the HVT model A is excluded up to 2.0 TeV.

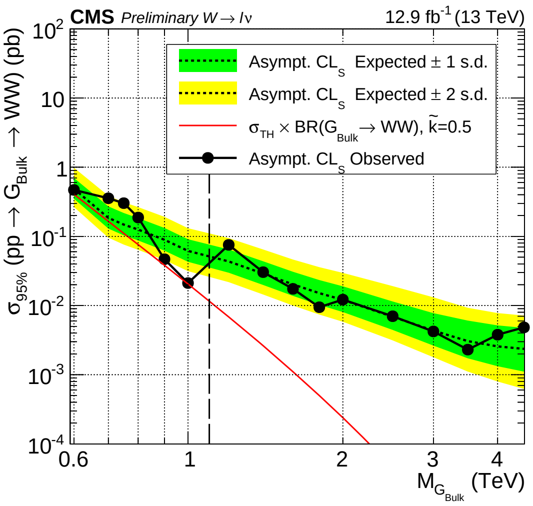

Figure 6.21: Expected and observed 95% CL upper limit on the product of the bulk graviton production cross section and the branching fraction of G_{bulk} →WW, combining together both electron and muon channels, and low-mass with high-mass analysis. The 68% and 95% ranges of expectation are also shown by green and yellow bands. The expected product between the bulk graviton production cross section and the branching fraction to WW is shown as a red solid curve for $\tilde{k} = 0.5$. The dashed vertical line delineates the transition between the low and high mass searches.

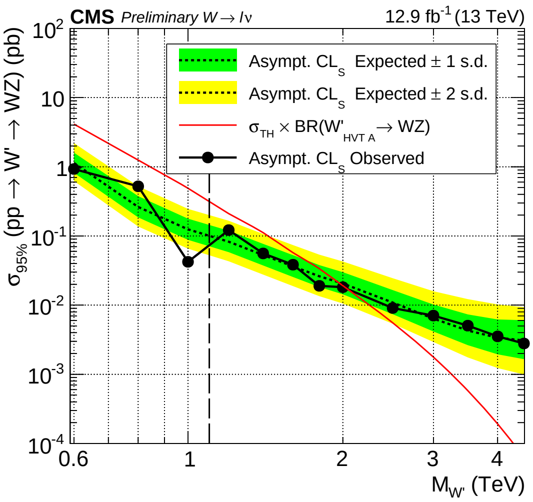

Figure 6.22: Expected and observed 95% CL upper limits on the product of the W' production cross section and the branching fraction of W' → WZ, combining together both electron and muon channels, and low-mass with high-mass analysis. The 68% and 95% ranges of expectation are also shown by green and yellow bands. The theoretical prediction for the HVT model A and B are also shown by blue and red lines, respectively. The dashed vertical line delineates the transition between the low and high mass searches.

Chapter 7

Conclusion

In the previous chapters, the relevant topics of the work performed during my PhD have been presented.

On the detector side, the work has focused on the calibration of the single-channel response of the ECAL crystals using high-energy electrons from W and Z boson decays. This method, already used during Run I, has been improved by implementing a dynamic selection on the E/p ratio of the electrons, which lead to an improvement of the precision of the method itself. The new algorithm has been run on LHC run II data. The large amount of data collected in 2016 allowed a statistical precision of about 0.3% (1.5%) to be reached in the inner (outer) part of the barrel, while the precision in the endcap goes from 1% to 2%, improving the results of 2015 and Run I. Furthermore, electrons from W/Z bosons have been used to monitor the stability of the energy response of the ECAL.

On the physics side, several analyses have been conducted probing different theoretical models, searching for heavy resonances decaying into a VW final state, where the W boson decays to a lepton-neutrino pair while the V boson decays hadronically. Dedicated substructure techniques have been used to improve the identification of the two-prong jets coming from the V boson decay, to better discriminate them from QCD jets.

A first search using Run I data has been performed searching for a heavy Higgs boson, with properties predicted by the SM. Two separate searches, which targeted different Higgs production modes (gluon fusion and vector boson fusion) have been conducted and combined together. Upper limits have been set on the presence of a SM-like Higgs boson, with cross sections larger than 1.1 (3.3) times the SM one for a mass of 0.6 TeV (1.0 TeV). The same analysis has been interpreted in the context of the Electroweak Singlet Model, where upper limits have been set scanning different values of the model parameters (C',$\mathrm{BR}_{\mathrm{new}}$).

A similar analysis strategy has been adopted with Run II data, targeting different theoretical frameworks, such as the WED models and the HVT model. Upper limits have been set on the cross section of spin-2 bulk graviton resonances, ranging from 0.4 pb for a mass of 0.6 TeV to 0.003 pb for a mass of 4.0 TeV, using the full statistics of 2015 and part of the data collected in 2016. Furthermore, the sensitivity of the analysis is sufficient to exclude the existence of W' resonances predicted from the HVT model up to masses of 2.0 TeV.

Appendix A

Description of the lepton and jet ID of run I

Tight electron ID

Electrons are reconstructed as described in section 2.3, and are required to pass some ID cuts; these requirements on the electron candidates are:

- The electron reconstruction should be driven by ECAL deposits.
- Number of inner tracker layers hit greater than two.
- Transverse momentum $p_T > 35$ GeV.
- Supercluster pseudorapidity $|\eta_{SC}| < 2.5$; there is also an exclusion range in pseudorapidity $1.4442 < |\eta_{SC}| < 1.566$ due to the ECAL barrel-endcap transition region.
- $|\Delta\eta_{in}|$ smaller than 0.005 (0.007) for barrel (endcap) electrons, where $\Delta\eta_{in}$ is the difference between the η of the supercluster back-propagated to the vertex and the η of the track.
- $|\Delta\Phi_{in}|$ smaller than 0.006 for both barrel and endcap electrons, where $\Delta\Phi_{in}$ is the difference between the Φ of the supercluster back-propagated to the vertex and the Φ of the track.
- $\sigma_{i\eta}$ smaller than 0.003 (only for endcap electrons), where $\sigma_{i\eta}$ is the η width of the electron candidate supercluster.
- H/E smaller than 0.05, where H/E is the ratio between the energy depositions in the hadronic and electromagnetic calorimeters.
- $E_{2\times5}/E_{5\times5}$ larger than 0.94 or $E_{1\times5}/E_{5\times5}$ larger than 0.83, where $E_{m\times n}$ is the energy deposited in a matrix of $m \times n$ crystals.
- Transverse impact parameter $|d_{xy}|$, respect to the selected primary vertex, smaller than 0.02 (0.05) cm for barrel (endcap) electrons, in order to ensure the selected electrons come from the interaction vertex and not from one of the pileup vertices.
- Isolation- the electron candidates have to be isolated: since they come from weak decays, the expected hadronic activity around them has to be very low. In general,

the isolation can be defined by summing the energy deposits of the other particles inside a cone in the $\eta - \phi$ plane around the electron track; the cone is defined by $\Delta R = \sqrt{(\Delta\eta)^2 + (\Delta\phi)^2} \leq 0.3$.
The tracker isolation I_{tk} is defined summing the p_T of all the tracks coming from the primary vertex and contained inside the cone. For electron candidates, I_{tk} should be less than 5 GeV.

- Furthermore, the electron is required also to be isolated simultaneously in the ECAL and in the HCAL. A fraction of energy deposited in the calorimeters within the isolation cone by particles may come from pileup interactions; therefore, a correction is applied, consisting of subtracting from the isolation cone the average pileup energy. Then, the combined isolation is defined as:

$$I_{\text{comb}} = I_{em} + I_{had} - 0.28 \cdot \rho$$

where I_{em} and I_{had} are the ECAL and HCAL isolation, and ρ is the average neutral particle energy density of the event. It is required that I_{comb} is smaller than $2 + 0.003 \cdot E_T$ for electrons in the barrel and I_{comb} smaller than $2.5 + 0.003 \cdot (E_T - 50)$ (2.5) for electrons in the endcaps with $E_T > 50$ ($E_T < 50$) GeV.

Tight muon ID

Muons are reconstructed as described in section 2.3, and are required to pass some ID cuts; the selection criteria on the muon candidates are:

- The muon candidates have to be reconstructed both in the tracker and in the muon chambers;
- Transverse momentum $p_T > 30$ GeV;
- Pseudorapidity $|\eta| < 2.1$;
- The muon track impact parameter and the primary vertex have to lie within a distance of less than 0.2 cm; also, the distance between the z coordinate of the PV and of the muon's inner track should be smaller than 0.5 cm, in order to make sure that the muon does not originate from one of the pileup vertices.
- Cuts on some track quality parameters, to reject fake muons coming from QCD jets In particular, at least one pixel hit found for the inner track of the muon, at least one muon station hit by the global track and a total number of tracker hits larger than 5 are required. In addition, the global track reduced chi-square must be smaller than 10.
- Isolation- the selected muon candidates must be isolated from charged hadron activity in the detector, requiring that the sum of tracks transverse momentum (I_{tk}), within an isolation cone of $\Delta R = 0.3$ around the muon track, should be $I_{tk}/p_T < 0.1$.

Loose electron ID

In order to reject events with more than one lepton, loose electrons are defined relaxing some of the previous requirements; the loose electron satisfy $p_T > 20$ GeV, $|\eta| < 2.5$ and the other cuts previously described.

Loose muon ID

As in the previous case, loose muons are defined too, with the requirements $p_T > 10$ GeV, $|\eta| < 2.5$ and satisfying the isolation and ID cuts previously described.

Loose jet ID

The selection criteria on the jet candidates are:

- The energy fraction carried by neutral hadrons should be less than 0.99.
- The energy fraction carried by photons should be less than 0.99.
- The number of constituents should be larger than 1.
- The energy fraction carried by charged hadrons should be larger than 0.
- The charged particle multiplicity should be larger than 0.
- The energy fraction carried by electrons should be less than 0.99.

Appendix B

Description of the lepton and jet ID of run II

High p_T muon ID

- The muon candidate must be reconstructed as a Global Muon
- At least one muon-chamber hit should be present in the global-muon track fit
- Muon segments in at least two muon stations
- The p_T relative error of the muon best track should be less than 30%
- Transverse impact parameter of the tracker track $d_{xy} < 2$ mm with respect to the primary vertex
- Longitudinal distance of the tracker track with respect to the primary vertex should be $d_z < 5$ mm
- Number of pixel hits > 0
- Number of tracker layers with hits > 5

Tight muon ID

- The muon candidate must be reconstructed as a Global Muon
- The muon candidate must be reconstructed as a PF Muon
- χ^2/ndof of the global-muon track fit less than 10
- At least one muon-chamber hit should in the global-muon track fit
- Muon segments in at least two muon stations
- Transverse impact parameter of the tracker track $d_{xy} < 2$ mm with respect to the primary vertex
- Longitudinal distance of the tracker track with respect to the primary vertex should be $d_z < 5$ mm
- Number of pixel hits > 0
- Number of tracker layers with hits > 5

Loose muon ID

- The muon candidate must be reconstructed as a PF Muon
- The muon candidate must be reconstructed as a Global Muon or a Tracker Muon

HEEP electron ID

- At least two inner tracker layers hit
- Transverse energy $E_T > 35$ GeV
- Supercluster pseudorapidity $|\eta_{SC}| < 2.5$; there is also an exclusion range in pseudorapidity $1.4442 < |\eta_{SC}| < 1.566$ due to the ECAL barrel-endcap transition region
- The electron reconstruction should be driven by ECAL deposits
- $|\Delta\eta_{in}|$ smaller than 0.004 (0.006) for barrel (endcap) electrons, where $\Delta\eta_{in}$ is the difference between the η of the supercluster back-propagated to the vertex and the η of the track
- $|\Delta\Phi_{in}|$ smaller than 0.06 for both barrel and endcap electrons, where $\Delta\Phi_{in}$ is the difference between the Φ of the supercluster back-propagated to the vertex and the Φ of the track
- H/E smaller than $1/E+0.05$ ($5/E+0.05$), where H/E is the ratio between the energy depositions in the hadronic and electromagnetic calorimeters
- Only for barrel electrons: $E_{2\times5}/E_{5\times5}$ larger than 0.94 or $E_{1\times5}/E_{5\times5}$ larger than 0.83, where $E_{m\times n}$ is the energy deposited in a matrix of $m \times n$ crystals
- Only for endcap electrons: $\sigma_{i\eta i\eta}$ smaller than 0.03, where $\sigma_{i\eta i\eta}$ is the η width of the electron candidate supercluster
- Transverse impact parameter $|d_{xy}|$, respect to the selected primary vertex, smaller than 0.02 (0.05) cm for barrel (endcap) electrons, in order to ensure the selected electrons come from the interaction vertex and not from one of the pileup vertices.
- Isolation- the electron candidates have to be isolated: since they come from weak decays, the expected hadronic activity around them has to be very low. In general, the isolation can be defined by summing the energy deposits of the other particles inside a cone in the $\eta - \phi$ plane around the electron track; the cone is defined by $\Delta R = \sqrt{(\Delta\eta)^2 + (\Delta\phi)^2} \leq 0.3$.
  The tracker isolation I_{tk} is defined summing the p_T of all the tracks coming from the primary vertex and contained inside the cone. For electron candidates, I_{tk} should be less than 5 GeV.

- Furthermore, the electron is required also to be isolated simultaneously in the ECAL and in the HCAL. A fraction of energy deposited in the calorimeters within the isolation cone by particles may come from pileup interactions; therefore, a correction is applied, consisting of subtracting from the isolation cone the average pileup energy. Then, the combined isolation is defined as:

$$I_{\text{comb}} = I_{em} + I_{had} - 0.28 \cdot \rho$$

where I_{em} and I_{had} are the ECAL and HCAL isolation, and ρ is the average neutral particle energy density of the event. It is required that I_{comb} is smaller than $2 + 0.003 \cdot E_T$ for electrons in the barrel and I_{comb} smaller than $2.5 + 0.03 \cdot (E_T - 50)$ (2.5) for electrons in the endcaps with $E_T > 50$ ($E_T < 50$) GeV.

Tight electron ID

- Supercluster pseudorapidity $|\eta_{SC}| < 2.5$; there is also an exclusion range in pseudorapidity $1.4442 < |\eta_{SC}| < 1.566$ due to the ECAL barrel-endcap transition region
- $\sigma_{i\eta i\eta}$ smaller than 0.0101 (0.0287) for barrel (endcap) electrons, where $\sigma_{i\eta i\eta}$ is the η width of the electron candidate supercluster
- $|\Delta\eta_{in}|$ smaller than 0.00864 (0.00762) for barrel (endcap) electrons, where $\Delta\eta_{in}$ is the difference between the η of the supercluster back-propagated to the vertex and the η of the track
- $|\Delta\Phi_{in}|$ smaller than 0.0286 (0.0439) for barrel (endcap) electrons, where $\Delta\Phi_{in}$ is the difference between the Φ of the supercluster back-propagated to the vertex and the Φ of the track
- H/E smaller than 0.0342 (0.0544), where H/E is the ratio between the energy depositions in the hadronic and electromagnetic calorimeters
- $|1/E - 1/p|$ less than 0.0116 (0.01) for barrel (endcap) electrons
- Transverse impact parameter $|d_{xy}|$, respect to the selected primary vertex, smaller than 0.0103 (0.0377) cm for barrel (endcap) electrons, in order to ensure the selected electrons come from the interaction vertex and not from one of the pileup vertices.
- Longitudinal impact parameter $|d_z|$, respect to the selected primary vertex, smaller than 0.170 (0.571) cm for barrel (endcap) electrons, in order to ensure the selected electrons come from the interaction vertex and not from one of the pileup vertices.
- Number of missing inner tracker layers less than 3 (2) for barrel (endcap) electrons
- The electron is required to be isolated simultaneously in the ECAL and in the HCAL. The isolation parameter is defined as:

  $$I = (I_n + I_{ch})/p_T$$

  where I_n is the neutral isolation, defined as $I_n = max(0, I_{nh} + I_{em} - \rho * A_{eff})$ with I_{nh} being the E_T sum if neutral hadrons, I_{em} the E_T sum of photons, ρ the average neutral particle energy density of the event and A_{eff} is the electron effective area, defined as a different number depending on the η region, while I_{ch} is the p_T sum of the charged hadrons in the event. It is required that I is smaller than 0.0591 (0.0759) for electrons in the barrel (endcap).

Loose electron ID

- Supercluster pseudorapidity $|\eta_{SC}| < 2.5$; there is also an exclusion range in pseudorapidity $1.4442 < |\eta_{SC}| < 1.566$ due to the ECAL barrel-endcap transition region
- $\sigma_{i\eta i\eta}$ smaller than 0.0105 (0.0318) for barrel (endcap) electrons, where $\sigma_{i\eta i\eta}$ is the η width of the electron candidate supercluster

- $|\Delta\eta_{in}|$ smaller than 0.00976 (0.00952) for barrel (endcap) electrons, where $\Delta\eta_{in}$ is the difference between the η of the supercluster back-propagated to the vertex and the η of the track
- $|\Delta\Phi_{in}|$ smaller than 0.0929 (0.181) for barrel (endcap) electrons, where $\Delta\Phi_{in}$ is the difference between the Φ of the supercluster back-propagated to the vertex and the Φ of the track
- H/E smaller than 0.0765 (0.0824), where H/E is the ratio between the energy depositions in the hadronic and electromagnetic calorimeters
- $|1/E - 1/p|$ less than 0.184 (0.125) for barrel (endcap) electrons
- Transverse impact parameter $|d_{xy}|$, respect to the selected primary vertex, smaller than 0.0227 (0.242) cm for barrel (endcap) electrons, in order to ensure the selected electrons come from the interaction vertex and not from one of the pileup vertices.
- Longitudinal impact parameter $|d_z|$, respect to the selected primary vertex, smaller than 0.379 (0.921) cm for barrel (endcap) electrons, in order to ensure the selected electrons come from the interaction vertex and not from one of the pileup vertices.
- Number of missing inner tracker layers less than 3 (2) for barrel (endcap) electrons
- It is required that I is smaller than 0.118 (0.118) for electrons in the barrel (endcap), where the definition of the isolation I is the same of the tight electron ID case.

Loose jet ID

The selection criteria on the jet candidates are:

- The energy fraction carried by neutral hadrons should be less than 0.99.
- The energy fraction carried by photons should be less than 0.99.
- The number of constituents should be larger than 1.
- The energy fraction carried by charged hadrons should be larger than 0.
- The charged particle multiplicity should be larger than 0.
- The energy fraction carried by electrons should be less than 0.99.

Bibliography

[1] CMS Collaboration. Observation of a new boson at a mass of 125 GeV with the CMS experiment at the LHC. *Phys.Lett.*, B30, 2012.

[2] ATLAS Collaboration. Observation of a new particle in the search for the Standard Model Higgs boson with the ATLAS detector at the LHC. *Phys.Lett.*, Ba, 2012.

[3] Vernon Barger, Paul Langacker, Mathew McCaskey, Michael J. Ramsey-Musolf, and Gabe Shaughnessy. LHC Phenomenology of an Extended Standard Model with a Real Scalar Singlet. *Phys. Rev.*, D77:035005, 2008.

[4] Kaustubh Agashe, Hooman Davoudiasl, Gilad Perez, and Amarjit Soni. Warped Gravitons at the LHC and Beyond. *Phys.Rev.*, D76:036006, 2007.

[5] A. Liam Fitzpatrick, Jared Kaplan, Lisa Randall, and Lian-Tao Wang. Searching for the Kaluza-Klein Graviton in Bulk RS Models. *JHEP*, 0709:013, 2007.

[6] Oleg Antipin, David Atwood, and Amarjit Soni. Search for RS gravitons via W(L)W(L) decays. *Phys.Lett.*, B666:155–161, 2008.

[7] D. Pappadopulo, A. Thamm, R. Torre, and A. Wulzer. Heavy vector triplets: Bridging theory and data. 2014.

[8] Search for a Standard Model-like Higgs boson decaying into WW to l nu qqbar in pp collisions at sqrt s = 8 TeV. Technical Report CMS-PAS-HIG-13-008, CERN, Geneva, 2013.

[9] Search for a Standard Model-like Higgs boson decaying into WW to l nu qqbar in exclusive jet bins in pp collisions at sqrt s = 8 TeV. Technical Report CMS-PAS-HIG-14-008, CERN, Geneva, 2015.

[10] Vardan Khachatryan et al. Search for a Higgs Boson in the Mass Range from 145 to 1000 GeV Decaying to a Pair of W or Z Bosons. *JHEP*, 10:144, 2015.

[11] Search for WW in semileptonic final states: low mass extension. Technical Report CMS-PAS-B2G-16-004, CERN, Geneva, 2016.

[12] Search for massive resonances decaying into pairs of boosted W and Z bosons at $\sqrt{s}$ = 13 TeV. Technical Report CMS-PAS-EXO-15-002, CERN, Geneva, 2015.

[13] S. Schael et al. Precision electroweak measurements on the Z resonance. *Phys. Rept.*, 427:257–454, 2006.

[14] Serguei Chatrchyan et al. Measurement of inclusive W and Z boson production cross sections in pp collisions at $\sqrt{s} = 8$ TeV. *Phys. Rev. Lett.*, 112:191802, 2014.

[15] Vardan Khachatryan et al. Measurements of jet multiplicity and differential production cross sections of $Z+$ jets events in proton-proton collisions at $\sqrt{s} = 7$ TeV. *Phys. Rev.*, D91(5):052008, 2015.

[16] Vardan Khachatryan et al. Differential cross section measurements for the production of a W boson in association with jets in proton–proton collisions at $\sqrt{s} = 7$ TeV. *Phys. Lett.*, B741:12–37, 2015.

[17] D.Perkins. *Introduction to high energy physics.* Cambridge univ., 2000.

[18] S. Eidelman et al. Review of particle physics. Particle Data Group. *Phys. Lett.*, B592(1-4):1–5, 2004.

[19] F.Mandl and G.Shaw. *Quantum field theory.* Wiley, 1984.

[20] Jeffrey Goldstone, Abdus Salam, and Steven Weinberg. Broken Symmetries. *Phys.Rev.*, 127:965–970, 1962.

[21] Englert, F. and Brout, R. Broken Symmetry and the Mass of Gauge Vector Mesons. *Phys. Rev. Lett.*, 13:321–323, Aug 1964.

[22] Higgs, Peter W. Broken Symmetries and the Masses of Gauge Bosons. *Phys. Rev. Lett.*, 13:508–509, Oct 1964.

[23] S. Dittmaier et al. Handbook of LHC Higgs Cross Sections: 1. Inclusive Observables. 2011.

[24] Tao Han and S. Willenbrock. QCD correction to the pp $\rightarrow$ WH and ZH total cross-sections. *Phys.Lett.*, B273:167–172, 1991.

[25] W. Beenakker, S. Dittmaier, M. Kramer, B. Plumper, M. Spira, et al. NLO QCD corrections to t anti-t H production in hadron collisions. *Nucl.Phys.*, B653:151–203, 2003.

[26] J R Andersen et al. Handbook of LHC Higgs Cross Sections: 3. Higgs Properties. 2013.

[27] Vardan Khachatryan et al. Precise determination of the mass of the Higgs boson and tests of compatibility of its couplings with the standard model predictions using proton collisions at 7 and 8 TeV. *Eur. Phys. J.*, C75(5):212, 2015.

[28] ATLAS collaboration. Measurements of the Higgs boson production and decay rates and coupling strengths using pp collision data at $\sqrt{\mathrm{s}} = 7$ and 8 TeV in the ATLAS experiment. 2015.

[29] Georges Aad et al. Measurements of the Higgs boson production and decay rates and coupling strengths using pp collision data at $\sqrt{s} = 7$ and 8 TeV in the ATLAS experiment. *Eur. Phys. J.*, C76(1):6, 2016.

[30] Matts Roos. Dark Matter: The evidence from astronomy, astrophysics and cosmology. 2010.

[31] S. Alekhin, A. Djouadi, and S. Moch. The top quark and Higgs boson masses and the stability of the electroweak vacuum. *Phys. Lett.*, B716:214–219, 2012.

[32] Daniel Baumann and Hiranya V. Peiris. Cosmological Inflation: Theory and Observations. *Adv. Sci. Lett.*, 2:105–120, 2009.

[33] Brian Patt and Frank Wilczek. Higgs-field portal into hidden sectors. 2006.

[34] Sebastian Bock, Remi Lafaye, Tilman Plehn, Michael Rauch, Dirk Zerwas, and Peter M. Zerwas. Measuring Hidden Higgs and Strongly-Interacting Higgs Scenarios. *Phys. Lett.*, B694:44–53, 2011.

[35] Christoph Englert, Tilman Plehn, Dirk Zerwas, and Peter M. Zerwas. Exploring the Higgs portal. *Phys. Lett.*, B703:298–305, 2011.

[36] Christoph Englert, Tilman Plehn, Michael Rauch, Dirk Zerwas, and Peter M. Zerwas. LHC: Standard Higgs and Hidden Higgs. *Phys. Lett.*, B707:512–516, 2012.

[37] Lisa Randall and Raman Sundrum. A Large mass hierarchy from a small extra dimension. *Phys.Rev.Lett.*, 83:3370–3373, 1999.

[38] Lisa Randall and Raman Sundrum. An Alternative to Compactification. *Phys.Rev.Lett.*, 83:4690–4693, 1999.

[39] Brando Bellazzini, Csaba Csáki, and Javi Serra. Composite Higgses. *Eur.Phys.J.*, C74(5):2766, 2014.

[40] Roberto Contino, Duccio Pappadopulo, David Marzocca, and Riccardo Rattazzi. On the effect of resonances in composite higgs phenomenology. *Journal of High Energy Physics*, 2011(10), 2011.

[41] Davide Greco and Da Liu. Hunting composite vector resonances at the LHC: naturalness facing data. *JHEP*, 1412:126, 2014.

[42] Martin Schmaltz and David Tucker-Smith. Little Higgs review. *Ann.Rev.Nucl.Part.Sci.*, 55:229–270, 2005.

[43] N. Arkani-Hamed, A.G. Cohen, E. Katz, and A.E. Nelson. The Littlest Higgs. *JHEP*, 0207:034, 2002.

[44] G. Altarelli, B. Mele, and M. Ruiz-Altaba. Searching for new heavy vector bosons in $p\bar{p}$ colliders. *Zeitschrift für Physik C Particles and Fields*, 45(1):109–121, 1989.

[45] Michael S. Chanowitz and Mary K. Gaillard. The TeV Physics of Strongly Interacting W's and Z's. *Nucl. Phys.*, B261:379–431, 1985.

[46] O. S. Bruning, P. Collier, P. Lebrun et al. Lhc design report. CERN, Geneva, 2004.

[47] CMS Collaboration. Cms, the compact muon solenoid: technical proposal. *LHC Tech. Proposal*, CERN-LHCC-94-38, 1994.

[48] ATLAS Collaboration. Atlas: technical proposal for a general-purpose pp experiment at the large hadron collider at cern. *LHC Tech. Proposal*, CERN-LHCC-94-43, 1994.

[49] LHCb Collaboration. Lhcb: Technical proposal. *Tech. Proposal*, CERN-LHCC-98-004, 1998.

[50] ALICE Collaboration. Alice: Technical proposal for a large ion collider experiment at the cern lhc. *LHC Tech. Proposal*, CERN-LHCC-95-71, 1995.

[51] CMS Collaboration. The CMS tracker system project: Technical Design Report. *Technical Design Report CMS*, CMS-TDR-005, 1997.

[52] CMS Collaboration. The CMS electromagnetic calorimeter project: Technical Design Report. *Technical Design Report CMS*, CMS-TDR-004, 1997.

[53] CMS Collaboration. The CMS muon project : Technical Design Report. *Technical Design Report CMS*, CMS-TDR-003, 1997.

[54] CMS Collaboration. CMS TriDAS project : Technical Design Report; 1, the trigger systems. *Technical Design Report CMS*, CMS-TDR-006-, 2000.

[55] CMS Collaboration. CMS Physics Technical Design Report Volume I : Detector Performance and Software. *Technical Design Report CMS*, CMS-TDR-008-1, 2006.

[56] Emilio Meschi, T. Monteiro, Christopher Seez, and Pratibha Vikas. Electron Reconstruction in the CMS Electromagnetic Calorimeter. *CMS Notes*, CMS-NOTE-2001-034, 2001.

[57] H. Bethe and W. Heitler. On the Stopping of fast particles and on the creation of positive electrons. *Proc.Roy.Soc.Lond.*, A146:83–112, 1934.

[58] W. Adam, R. Fruhwirth, A. Strandlie, and T. Todorov. Reconstruction of electrons with the Gaussian sum filter in the CMS tracker at LHC. *eConf*, C0303241:TULT009, 2003.

[59] CMS Collaboration. Commissioning of the Particle-flow Event Reconstruction with the first LHC collisions recorded in the CMS detector. *CMS Physics Analysis Summaries*, PFT-10-001, 2010.

[60] CMS Collaboration. Commissioning of the Particle-Flow reconstruction in Minimum-Bias and Jet Events from pp Collisions at 7 TeV. *CMS Physics Analysis Summaries*, PFT-10-002, 2010.

[61] Matteo Cacciari, Gavin P. Salam, and Gregory Soyez. The Anti-k_T jet clustering algorithm. *JHEP*, 0804:063, 2008.

[62] Stan Bentvelsen and Irmtraud Meyer. The Cambridge jet algorithm: features and applications. *Eur. Phys. J.*, C4:623–629, 1998.

[63] Matteo Cacciari and Gavin P. Salam. Pileup subtraction using jet areas. *Phys.Lett.*, B659:119–126, 2008.

[64] Nhan Tran et al. Identifying hadronically decaying W bosons merged into a single jet. *cms-an-2013/72*.

[65] CMS collaboration. Searches for new physics in the WW$\to$lνj final state with hadronic W bosons merged into a single jet. *cms-an-2012/381*.

[66] S.D.Ellis C.K.Vermilion and J.R.Walsh. Recombination Algorithms and Jet Substructure: Pruning as a Tool for Heavy Particle Searches. *Phys.Rev.D*, 81, (2010) 094023.

[67] Andrew J. Larkoski, Simone Marzani, Gregory Soyez, and Jesse Thaler. Soft Drop. *JHEP*, 05:146, 2014.

[68] D.Krohn J.Thaler and L.-T.Wang. Jet Trimming. *JHEP*, 1002, (2010) 084.

[69] J. Thaler and K. Van Tilburg. Identifying Boosted Objects with N-subjettiness. *JHEP*, 1103, (2011) 015.

[70] P. Adzic et al. Reconstruction of the signal amplitude of the CMS electromagnetic calorimeter. *Eur. Phys. J.*, C46S1:23–35, 2006.

[71] P. Adzic et al. Energy resolution of the barrel of the CMS electromagnetic calorimeter. *JINST*, 2:P04004, 2007.

[72] M. Oreglia. *A study of the reactions $\psi' \rightarrow \gamma\gamma\psi$.* PhD thesis, SLAC, 1980.

[73] T. Skwarnicki. *A study of the radiative CASCADE transitions between the Upsilon-Prime and Upsilon resonances.* PhD thesis, Cracow, INP, 1986.

[74] M. Anfreville et al. Laser monitoring system for the CMS lead tungstate crystal calorimeter. *Nucl. Instrum. Meth.*, A594:292–320, 2008.

[75] Henning Kirschenmann. Jet performance in CMS. Technical Report CMS-CR-2013-325, CERN, Geneva, Oct 2013.

[76] Maxime Gouzevitch, Alexandra Oliveira, Juan Rojo, Rogerio Rosenfeld, Gavin P. Salam, and Veronica Sanz. Scale-invariant resonance tagging in multijet events and new physics in Higgs pair production. *JHEP*, 07:148, 2013.

[77] LHC Higgs Combination Group, ATLAS Collaboration, CMS Collaboration. Procedure for the LHC Higgs boson search combination in summer 2011. *CMS Notes, ATLAS Notes*, ATL-PHYS-PUB-2011-011, 2011.

[78] Paolo Nason. A New method for combining NLO QCD with shower Monte Carlo algorithms. *JHEP*, 11:040, 2004.

[79] Stefano Frixione, Paolo Nason, and Carlo Oleari. Matching NLO QCD computations with Parton Shower simulations: the POWHEG method. *JHEP*, 11:070, 2007.

[80] Simone Alioli, Paolo Nason, Carlo Oleari, and Emanuele Re. A general framework for implementing NLO calculations in shower Monte Carlo programs: the POWHEG BOX. *JHEP*, 06:043, 2010.

[81] Simone Alioli, Paolo Nason, Carlo Oleari, and Emanuele Re. NLO single-top production matched with shower in POWHEG: s- and t-channel contributions. *JHEP*, 09:111, 2009. [Erratum: JHEP02,011(2010)].

[82] Emanuele Re. Single-top Wt-channel production matched with parton showers using the POWHEG method. *Eur. Phys. J.*, C71:1547, 2011.

[83] Simone Alioli, Sven-Olaf Moch, and Peter Uwer. Hadronic top-quark pair-production with one jet and parton showering. *JHEP*, 01:137, 2012.

[84] Torbjorn Sjostrand, Stephen Mrenna, and Peter Z. Skands. PYTHIA 6.4 Physics and Manual. *JHEP*, 05:026, 2006.

[85] Torbjorn Sjostrand, Stephen Mrenna, and Peter Z. Skands. A Brief Introduction to PYTHIA 8.1. *Comput. Phys. Commun.*, 178:852–867, 2008.

[86] Peter Skands, Stefano Carrazza, and Juan Rojo. Tuning PYTHIA 8.1: the Monash 2013 Tune. *Eur. Phys. J.*, C74(8):3024, 2014.

[87] CMS Collaboration. Underlying Event Tunes and Double Parton Scattering. CMS Physics Analysis Summary CMS-PAS-GEN-14-001, 2014.

[88] S. Agostinelli et al. GEANT4: A Simulation toolkit. *Nucl. Instrum. Meth.*, A506:250–303, 2003.

[89] Christian Weiser. A combined secondary vertex based b-tagging algorithm in cms. (CMS-NOTE-2006-014), Jan 2006.

[90] Serguei Chatrchyan et al. Measurement of W+W- and ZZ production cross sections in pp collisions at sqrt(s) = 8 TeV. *Phys. Lett.*, B721:190–211, 2013.

[91] Serguei Chatrchyan et al. Measurement of the Inclusive W and Z Production Cross Sections in pp Collisions at $\sqrt{s} = 7$ TeV. *JHEP*, 10:132, 2011.

[92] J. Alwall, R. Frederix, S. Frixione, V. Hirschi, F. Maltoni, O. Mattelaer, H. S. Shao, T. Stelzer, P. Torrielli, and M. Zaro. The automated computation of tree-level and next-to-leading order differential cross sections, and their matching to parton shower simulations. *JHEP*, 07:079, 2014.

[93] Richard D. Ball, Valerio Bertone, Francesco Cerutti, Luigi Del Debbio, Stefano Forte, Alberto Guffanti, Jose I. Latorre, Juan Rojo, and Maria Ubiali. Impact of Heavy Quark Masses on Parton Distributions and LHC Phenomenology. *Nucl. Phys.*, B849:296–363, 2011.

[94] John M. Campbell, R. Keith Ellis, and David L. Rainwater. Next-to-leading order QCD predictions for $W + 2$ jet and $Z + 2$ jet production at the CERN LHC. *Phys. Rev.*, D68:094021, 2003.

[95] John M. Campbell, R. Keith Ellis, and Ciaran Williams. Vector boson pair production at the LHC. *JHEP*, 07:018, 2011.

[96] John M. Campbell and R. Keith Ellis. Top-quark processes at NLO in production and decay. *J. Phys.*, G42(1):015005, 2015.

[97] John M. Campbell, R. Keith Ellis, and Francesco Tramontano. Single top production and decay at next-to-leading order. *Phys. Rev.*, D70:094012, 2004.

[98] Ye Li and Frank Petriello. Combining QCD and electroweak corrections to dilepton production in FEWZ. *Phys. Rev.*, D86:094034, 2012.

[99] Giovanni Punzi. Sensitivity of searches for new signals and its optimization. *eConf*, C030908:MODT002, 2003. [,79(2003)].

[100] Mark Joseph Oreglia. *A study of the reactions $\psi' \to \gamma\gamma\psi$*. PhD thesis, Stanford University, 1980. SLAC Report SLAC-R-236.